

**UTILIZING THE CONNECTED POWER ELECTRONIC
CONVERTER FOR IMPROVED CONDITION MONITORING OF
INDUCTION MOTORS AND CLAW-POLE GENERATORS**

A Dissertation
Presented to
The Academic Faculty

by

Siwei Cheng

In Partial Fulfillment
Of the Requirements for the Degree
Doctor of Philosophy in the
School of Electrical and Computer Engineering

Georgia Institute of Technology
May 2012

Copyright © Siwei Cheng 2012

**UTILIZING THE CONNECTED POWER ELECTRONIC
CONVERTER FOR IMPROVED CONDITION MONITORING OF
INDUCTION MOTORS AND CLAW-POLE GENERATORS**

Approved by:

Dr. Thomas G. Habetler, Advisor
School of Electrical and Computer
Engineering
Georgia Institute of Technology

Dr. J. Rhett Mayor
School of Mechanical Engineering
Georgia Institute of Technology

Dr. Ronald G. Harley
School of Electrical and Computer
Engineering
Georgia Institute of Technology

Dr. Ying Zhang
School of Electrical and Computer
Engineering
Georgia Institute of Technology

Dr. Santiago Grijalva
School of Electrical and Computer
Engineering
Georgia Institute of Technology

Date Approved: March 20, 2012

*Dedicated to my parents Mr. Li Cheng and Mrs. Ping Xiao
for their love and support*

ACKNOWLEDGEMENTS

First and foremost, I would like to thank my advisor, Professor Thomas G. Habetler, whose guidance and support have made all this work possible. Professor Habetler has been a wise advisor to me. Working with him is a rewarding experience both technically and non-technically. His great personality is like an eternal source of inspiration and encouragement that helps me go through tough times with my projects. His trust in my abilities allows me to freely explore research ideas that eventually result in interesting and fulfilling work. I am deeply grateful for his guidance.

I am also grateful to Professor Ronald G. Harley and Professor J. Rhett Mayor. Professor Harley is like a co-advisor to me. I am honored to work with him on several projects and benefit greatly from his profound knowledge on electric machine design and his serious attitude towards research. I have the pleasure to work with Professor Mayor in several projects as well. His interdisciplinary perspective helps me to better understand the thermal and structural aspects of electric machine design. I am also very thankful to both Professor Grijalva and Professor Zhang for being my dissertation committee members and for their time in evaluating my thesis and providing valuable feedback.

I would like to thank Professor Jose A. Restrepo visiting from Universidad Simón Bolívar. I have the honor to design and build an inverter with him from the ground up. The hands-on experience I obtained through this process is invaluable. Professor Restrepo is always happy to answer my various questions. I have also learned from him a great deal on control of power electronics.

Among numerous staff members I should mention here, I wish to especially thank Louis Boulanger and James Steinberg for helping me with numerous experimental setups.

It is very fortunate for me to have the opportunity to work with so many exceptional fellow students at Georgia Tech. Among them, I wish to especially thank Yi Du, Dr. Pinjia Zhang, Dr. Stefan Grubic, Dr. Yao Duan, Dr. Jiaqi Liang, Dr. Yi Yang, and Jacob Kunz, for the helpful discussions and pleasant collaborations. I would also like to thank Andrew Paquette, Andrew Semidey, Dr. Anish Prasai, Dawei He, Dr. Debrup Das, Diogenes Molina, Dongbo Zhao, Dustin Howard, Frank Kreikebaum, Jie Dang, Jing Dai, Jorge Hernandez, Dr. Jyoti Sastry, Liang Du, Lijun He, Nathan Ainsworth, Qin Sun, Rohit Moghe, Sangtaek Han, Yi Deng, Zhaoyu Wang, Dr. Long Wu, Dr. Bin Lu, Dr. Zhi Gao, and Dr. Wei Qiao for their friendship and support.

I also want to express my most sincere gratitude to all the close friends I made at Georgia Tech. During the past five years, we lived together, played together, smiled together, and cried together. It is you that make the years at Georgia Tech a memorable experience for us all.

Lastly, I would like to dedicate this thesis to my parents. It is their love and support throughout my entire life that makes me the man I am today. Here I wish them good health and happy living.

TABLE OF CONTENTS

	Page
ACKNOWLEDGEMENTS	iv
LIST OF TABLES	xii
LIST OF FIGURES	xiii
SUMMARY	xxi
CHAPTER 1 Introduction and Objective of the Research	1
1.1 Background	1
1.2 Induction Motors Fed by Closed-loop Inverter Drives	4
1.3 Claw-pole Generators with Built-in Rectifiers	5
1.4 Problem Statement	7
1.5 Dissertation Outline	7
CHAPTER 2 Previous Work on Insulation and Thermal Monitoring of Induction Machines Fed by Closed-loop Inverter Drive	9
2.1 Overview	9
2.2 Detection of the Stator Turn Fault	9
2.2.1 Stator Turn-fault Detection for Grid-connected Induction Machines.....	11
2.2.2 Stator Turn-fault Detection for Open-loop Inverter-fed Induction Machines	12
2.2.3 Stator Turn-fault Detection for Closed-loop Inverter-fed Induction Machines	16
2.3 Thermal Monitoring of Stator Winding.....	22
2.3.1 Thermal Monitoring for Grid-connected Induction Machines	24

2.3.2	Thermal Monitoring for Open-loop Inverter-fed Induction Machines ...	26
2.3.3	Thermal Monitoring for Closed-loop Inverter-fed Induction Machines.	28
2.4	Chapter Summary	29
 CHAPTER 3 Previous Work on Condition Monitoring of Claw-pole Generators with Built-in Rectifiers31		
3.1	Overview.....	31
3.2	Detection of External Faults	32
3.3	Detection of Internal Faults	35
3.4	Chapter Summary	36
 CHAPTER 4 Stator Turn-fault Detection for Induction Machines Fed by Closed-loop Inverter Drives.....37		
4.1	Overview.....	37
4.2	Closed-loop Impact on Stator Turn-Fault Detection	38
4.3	Proposed Method to Detect Stator Turn Fault	39
4.4	A Special Case of Multiple Motors Connected to a Single Closed-loop Inverter – Fault Location	43
4.5	Signal Processing Techniques.....	47
4.5.1	A Post-processing Workflow for the Lab	47
4.5.2	Goertzel Algorithm for Real-time Implementations.....	50
4.6	Experimental Validation on Commercial Closed-loop Inverter	51
4.6.1	Experimental Setup.....	51
4.6.2	Experimental Results	54
4.7	Practical Considerations for Real-time Implementation.....	59
4.7.1	Terminal Voltage Estimation.....	59

4.7.2	Bandwidth of the Current Controller	60
4.7.3	Real-time Implementation	61
4.8	Chapter Summary	65
 CHAPTER 5 Stator Thermal Monitoring for Induction Machines Fed by Closed-loop Inverter Drives.....67		
5.1	Overview.....	67
5.2	Principle of Stator Winding Temperature Estimation	68
5.3	Simulation Validation	70
5.4	Terminal Voltage Estimation.....	71
5.4.1	Effect of Dead Time on DC Voltage Estimation	73
5.4.2	Effect of Device Voltage Drop on DC Voltage Estimation.....	76
5.4.3	Effect of Different Device Turn-on and Turn-off Time Delay	78
5.4.4	Over Modulation and Discontinuous PWM Methods	80
5.5	Real-time Signal Processing Technique	80
5.6	Temperature Estimation Error Analysis	82
5.6.1	Errors Introduced by the Current Measurement	82
5.6.2	Errors Introduced by the DC Bus Voltage Measurement	83
5.6.3	Errors Introduced During Inverter-nonideality Compensation.....	83
5.6.4	Errors in the Estimated Temperature	85
5.7	Experimental Validation	86
5.7.1	Experiment Setup.....	86
5.7.2	Measured Motor Waveforms	87
5.7.3	Temperature Estimation at a Single Operating Condition.....	90
5.7.4	Temperature Estimation with Variable Operating Conditions	91

5.8	Chapter Summary	94
CHAPTER 6	Fundamental Aspects of Condition Monitoring of Claw-pole Generators	96
6.1	Overview	96
6.2	Failure Types and Failure Mechanisms	97
6.3	Finite-element Model of the Claw-pole Generator	102
6.4	Test Bench Setup	107
6.5	Spectral Analysis	111
6.5.1	Voltage-regulator Switching Harmonics	111
6.5.2	Rectifier Ripple Harmonic	112
6.5.3	Harmonics at Integral Factors of the Rectifier Ripple Frequency	113
6.5.4	Harmonics related to the Belt Cycle	113
6.5.5	Harmonics related to the Torque Oscillations of the Prime Mover	114
6.6	Chapter Summary	115
CHAPTER 7	Detection of External Faults for Claw-pole Generators.....	117
7.1	Overview	117
7.2	Generator Speed Tracking and Detection of Belt Slip.....	117
7.2.1	Principle of the Belt-slip Detector	117
7.2.2	Interpolated FFT for Ripple Frequency Extraction	119
7.2.3	Frequency Locking	121
7.2.4	Spectrum Aliasing.....	122
7.2.5	Experimental Results	123
7.3	Detection of Belt Defects.....	125

7.3.1	Principle of the Belt-defect Detector	125
7.3.2	Real-time Signal Processing Technique	128
7.3.3	Experimental Results	129
7.4	Chapter Summary	131
CHAPTER 8 Detection of Internal Faults for Claw-pole Generators.....		133
8.1	Overview	133
8.2	Detection of the Stator Turn-to-turn Fault	134
8.2.1	Modeling of Claw-pole Generator with Stator Turn Faults.....	135
8.2.2	Parameter Identification for the Generator Model	140
8.2.3	Fault Signature	142
8.2.4	Finite-element Model of Generators with Stator Turn Faults.....	148
8.2.5	Experimental Validation of the Stator Turn-fault Detector	151
8.3	Fault-severity Evaluation and Post-fault Protection of the Stator Turn-to-turn Short Circuit	157
8.3.1	Validation of the Generator Model for Fault-severity Evaluation.....	158
8.3.2	Fault-severity Evaluation	160
8.3.3	Post-fault Protection Strategy	163
8.4	Detection of the Rotor Eccentricity	165
8.4.1	Fault Signature	166
8.4.2	Finite-element Simulation.....	168
8.4.3	Experimental Validation	170
8.5	Detection of the Generalized Bearing Roughness Fault	172
8.5.1	Accelerated Bearing Aging Tests	172

8.5.2	Evaluation of Noise-cancellation Methods for Bearing Roughness Detection	175
8.5.3	Shift of Rectifier Ripple Frequency Caused by the Bearing Fault	178
8.5.4	Experimental Validation	182
8.6	Chapter Summary	189
CHAPTER 9 Conclusions, Contributions, and Recommended Future Work		191
9.1	Conclusions.....	191
9.2	Contributions.....	195
9.3	Recommended Future Work	198
9.3.1	Stator Turn-fault Detection during Transient Operation of Induction Motors	199
9.3.2	Fault-severity Evaluation of Stator Turn-to-turn Short circuits for Inverter-fed Induction Machines.....	199
9.3.3	Thermal Monitoring of Induction Motors with Direct Torque Control (DTC).....	200
9.3.4	Further Study and Verification of the Mechanism for Pulley Diameter Change	201
APPENDIX A Derivation of the Equivalent Circuit of the Short-circuit Path.....		202
BIBLIOGRAPHY		205
VITA		215

LIST OF TABLES

	Page
Table 2.1: Temperature limits for different insulation classes [68].....	23
Table 4.1: Parameters and ratings of the test machine for stator turn-fault detection	53
Table 4.2: Operating conditions and fault levels considered in the experiment.....	54
Table 4.3: Sequence components extracted by the inverter controller in real time.....	64
Table 5.1: Parameters and ratings of the test machine for thermal monitoring	87
Table 6.1: Physical quantities that may be monitored in a claw-pole generator	107
Table 8.1: Identified parameters for the generator model.....	140
Table 8.2: Experimental results for bearing aging tests and control tests.	188

LIST OF FIGURES

	Page
Figure 2.1: Electric machine stator failures [29].	10
Figure 2.2: Experimental setup for unbalancing the three-phase supply voltage [44].	14
Figure 2.3: High-frequency voltage injection for stator turn-fault detection [53].	14
Figure 2.4: Current waveform before and after high-frequency voltage injection [53]. ..	15
Figure 2.5: Neural-network-based stator turn-fault detection scheme [56].	18
Figure 2.6: Experimental setup for inducing voltage unbalances for a inverter-fed induction machine [56].	19
Figure 2.7: Overall scheme for testing the stator turn-fault detection scheme [44].	20
Figure 2.8: Representation of the flux hysteresis band and stator flux locus imposed by a DTC induction motor drive [57].	22
Figure 2.9: Four-nodes second-order thermal model for induction machine [70].	24
Figure 2.10: Soft-starter-based DC current injection for stator thermal monitoring [60].	25
Figure 2.11: Modified voltage space vector for DC signal injection [73].	27
Figure 3.1: Illustration of an automotive EPGS system.	32
Figure 3.2: Model-based fault diagnostic scheme for claw-pole generator [16].	33
Figure 3.3: Illustration of the linear relationship between battery voltage V_b and field voltage F_{dc} for a given voltage set point [20].	34
Figure 4.1: A simplified diagram of a closed-loop induction motor drive.	38
Figure 4.2: A torque-distribution scheme using multiple motors fed by a single closed- loop inverter.	43

Figure 4.3: A torque-distribution scheme using a mechanical differential and a single large motor fed by a single closed-loop inverter.	44
Figure 4.4: Signal processing workflow to extract sequence components.	47
Figure 4.5: A magnitude spectrum of the current space vector.	49
Figure 4.6: DFT bins of the current space vector calculated by Goertzel Algorithm.....	51
Figure 4.7: Experimental setup for validating stator turn-fault detection and location in a closed-loop multiple-motor drive.	52
Figure 4.8: A comparison of extracted sequence components from various tests.	54
Figure 4.9: Scatter plot of ΔZ_{np} at different operating conditions and fault levels.	55
Figure 4.10: Scatter plot of Z_{nn} at 300 rpm and 0.03 slip with various fault levels.	57
Figure 4.11: Scatter plot of Z_{nn} at 300 rpm and no load with various fault levels.	58
Figure 4.12: Scatter plot of Z_{nn} at 600 rpm and various load levels with 1-turn fault.	59
Figure 4.13: Current controller enhanced with negative-sequence-current suppressor....	61
Figure 4.14: Photographs of the inverter built for validating real-time condition monitoring methods of electric machines.	62
Figure 4.15: Control architecture of the inverter built for validating real-time condition monitoring methods of electric machines.	63
Figure 5.1: A simple method to inject DC current into induction motors fed by closed-loop inverters.	68
Figure 5.2: Simulink simulation of a field-oriented controlled induction motor with DC current injection.	71
Figure 5.3: Estimated stator winding temperature given by the simulation of the DC injection method.	71
Figure 5.4: Illustration of the effect of the dead time.	73

Figure 5.5: Contribution of dead time on terminal voltage – No DC current offset.....	74
Figure 5.6: Contribution of dead time on terminal voltage – Positive DC current offset.....	75
Figure 5.7: Contribution of dead time on terminal voltage – Positive DC current offset and smaller current amplitude.	75
Figure 5.8: Illustration of device voltage drop.....	77
Figure 5.9: Contribution of device voltage drop on terminal voltage.....	78
Figure 5.10: Contribution of different turn-on/turn-off delay on terminal voltage.	79
Figure 5.11: Signal process techniques for extracting DC current and voltage.....	81
Figure 5.12: Device voltage drop curve at different temperature.	84
Figure 5.13: Experimental setup for DC-injection based stator resistance estimation.	87
Figure 5.14: D- and Q- axis current before and during DC current injection.....	89
Figure 5.15: Stator voltage and current before and during DC current injection.	89
Figure 5.16: DC components of stator voltage and current.	89
Figure 5.17: Motor torque and speed before and during DC current injection.....	90
Figure 5.18: Stator winding temperature estimation at constant operating condition.	91
Figure 5.19: Stator winding temperature estimation with variable load level (error band of estimated temperature removed for clarity).	92
Figure 5.20: Stator winding temperature estimation with variable motor speed (error band of estimated temperature removed for clarity).	93
Figure 5.21: Stator winding temperature estimation with variable DC bus voltage (error band of estimated temperature removed for clarity).	94
Figure 6.1: Illustration of the automotive EPGS system.	97
Figure 6.2: Mechanical structure and electrical circuits of a claw-pole generator [87]. ..	99

Figure 6.3: Comparison of the bar-wound and wire-wound stator winding [88].	100
Figure 6.4: Major types of faults of generators replaced by auto dealerships under warranty (Courtesy: General Motors).	101
Figure 6.5: Finite-element model of the claw-pole generator.	103
Figure 6.6: Measured DC B-H curve of the rotor material.	104
Figure 6.7: Experimental and simulated open-circuit voltage waveforms.	105
Figure 6.8: Magnetic flux distribution in the rotor core.	106
Figure 6.9: Magnetic flux distribution in the stator core.	106
Figure 6.10: Test bench for claw-pole generators.	108
Figure 6.11: EPGS test facilities at General Motors.	109
Figure 6.12: Generator field voltage and field current.	110
Figure 6.13: Generator line voltage and phase current.	110
Figure 6.14: Generator output voltage and output current.	111
Figure 6.15: Spectrum of generator field voltage.	112
Figure 6.16: Spectrum of generator output voltage.	112
Figure 6.17: Spectrum of generator output current.	112
Figure 6.18: Zoom-in plot of the output current spectrum around the rectifier ripple frequency	114
Figure 6.19: Zoom-in plot of the output current spectrum around 200 Hz.	115
Figure 7.1: Comparison of the generator output voltage spectrum with different FFT sizes.	120
Figure 7.2: Major procedures for generator speed tracking and belt-slip detection.	123

Figure 7.3: Experiment results of generator speed tracking and belt-slip detection.....	124
Figure 7.4: Illustration of aging serpentine belt with torn rubber in the grooves	126
Figure 7.5: Artificially induced belt defect.....	126
Figure 7.6: Generator current spectrum around the rectifier ripple frequency without any belt defect	127
Figure 7.7: Generator current spectrum around the rectifier ripple frequency with the belt defect	127
Figure 7.8: Experimental results of belt-defect detection at different speeds.....	130
Figure 7.9: Fault-signature variations between different serpentine belts	130
Figure 8.1: Circuit representation of a healthy claw-pole generator.	135
Figure 8.2: Simplified equivalent circuit of the short-circuit path.....	136
Figure 8.3: Circuit representations of fault-current-induced back-EMFs in three-phase windings.	137
Figure 8.4: A circuit model of claw-pole generator with stator turn faults.	139
Figure 8.5: Thevenin model of a lead-acid battery.	139
Figure 8.6: Claw-pole generator test results.	141
Figure 8.7: Finite-element simulation result for calculating mutual inductances.....	142
Figure 8.8: Simulink model of the generator with stator turn fault – part 1.	142
Figure 8.9: Simulink model of the generator with stator turn fault – part 2.	143
Figure 8.10: Experimental generator with artificially induced stator turn fault	143
Figure 8.11: Comparison of the simulated and measured fault currents in the shorted path.	144
Figure 8.12: Comparison of the simulated and measured line currents.....	145

Figure 8.13: Comparison of the simulated generator output current without and with stator turn fault.	146
Figure 8.14: Illustration of harmonic at one third of rectifier ripple frequency caused by unbalanced rectifier inputs.	146
Figure 8.15: Dependencies of fault-related current and voltage harmonics on battery internal resistance.	148
Figure 8.16: Finite-element model for a generator with stator turn faults.....	149
Figure 8.17: Simulated generator output current with stator turn fault.	150
Figure 8.18: Simulated generator output current without stator turn fault.	150
Figure 8.19: Generator output current waveforms.....	152
Figure 8.20: Generator output current spectrum.....	152
Figure 8.21: Fault signatures at various operating conditions.	154
Figure 8.22: Fault signatures for three healthy generators.	155
Figure 8.23: Fault signatures and the fault threshold.....	155
Figure 8.24: Simulated and measured fault signatures with a 0.230- Ω current-limiting resistor.	159
Figure 8.25: Simulated and measured fault signatures with a 0.131- Ω current-limiting resistor.	160
Figure 8.26: Additional Fault signatures given by the generator model (from top surface to bottom surface, current-limiting resistors are 0.066 Ω , 0.033 Ω , and 0.016 Ω)......	162
Figure 8.27: RMS short-circuit currents given by the generator model (from top surface to bottom surface, current-limiting resistors are 0.066 Ω , 0.033 Ω , and 0.016 Ω)......	162
Figure 8.28: Illustration of the post-fault protection strategy with fault signatures classified into three categories.	165

Figure 8.29: Illustration of the static eccentricity.	167
Figure 8.30: Illustration of the dynamic eccentricity.	167
Figure 8.31: Illustration of the mixed eccentricity.	168
Figure 8.32: Simulated electromagnetic torque of a generator with mixed eccentricity.	169
Figure 8.33: Simulated output current of a generator with mixed eccentricity.	170
Figure 8.34: Low-frequency spectrum of the generator output current.	171
Figure 8.35: Experimental setup for accelerated bearing aging.	173
Figure 8.36: Pictures of bearings after the aging tests.	174
Figure 8.37: Comparison of generator current spectra before and after Bearing 3 develops roughness.	176
Figure 8.38: Notch-filtering-based bearing fault detection for Bearing 3.	177
Figure 8.39: Pictures of bearings after the aging tests.	178
Figure 8.40: Generator shaft positions and belt-segment force analysis with and without bearing fault.	179
Figure 8.41: Frequencies of major current harmonics before and after the bearing aging test.	183
Figure 8.42: Frequencies of major current harmonics before and after the control test.	184
Figure 8.43: Ripple frequency and vibration during aging test on Bearing 1.	185
Figure 8.44: Ripple frequency and vibration during aging test on Bearing 2.	186
Figure 8.45: Ripple frequency and vibration during aging test on Bearing 3.	186
Figure 8.46: Ripple frequency and vibration during control test on Bearing 4.	187
Figure 8.47: Ripple frequency and vibration during control test on Bearing 5.	187

Figure A.1: Stator winding with turn-to-turn faults.....202

Figure A.2: Equivalent circuit of the short-circuit path.....204

SUMMARY

The objective of this PhD research is to develop simple, robust, and non-intrusive condition monitoring methods for induction motors fed by closed-loop inverters and claw-pole generators with built-in rectifiers. While the flexible energy forms synthesized by these connected power electronic converters greatly enhance the performance and expand the operating region of induction motors and claw-pole generators, they also significantly alter the fault behavior of these electric machines and complicate the fault detection and protection. A comprehensive literature survey suggests that the current art of condition monitoring of power-converter-fed electric machines is underdeveloped compared to the maturing condition monitoring techniques for grid-connected electric machines.

In this work, special characteristics of the connected closed-loop inverter and rectifier have been thoroughly analyzed, with particular interest in their impact on fault behaviors of the induction motor and the claw-pole generator. Based on the understanding obtained from the theoretical and experimental analysis, several sensorless thermal, mechanical, and insulation monitoring methods are proposed by smartly utilizing special features and capabilities of the connected power electronic converter.

This thesis first investigates the stator turn-to-turn fault detection for induction motors fed by closed-loop inverter drives. A comprehensive survey of existing stator turn-fault detectors reveals that the major disadvantage of conventional methods is that the process of learning the inherent asymmetry of the induction motor is highly complicated. Such complexity directly limits the practicability of these methods in real world applications. In this work, it is discovered that motor current controllers in the

closed-loop inverter can keep the three-phase current symmetrical no matter a stator turn fault exists or not. This unique feature is utilized to essentially eliminate the learning process of the motor inherent asymmetry during stator turn-fault detection. The proposed method is evaluated experimentally and the results show that the proposed fault detector is highly sensitive and easy to implement.

In addition to detecting a solid stator turn fault, an early warning of the stator insulation degradation is also highly desired. A stator thermal monitoring method is thus proposed in this work to protect the closed-loop inverter-fed induction motor from insulation degradation caused by thermal overload. The stator temperature is indirectly estimated from the stator resistance. The closed-loop inverter is used to inject a DC current into the motor windings in an online fashion. Since only the DC bus voltage sensor is available in typical closed-loop inverter drives, the major challenge of this method is how to accurately estimate the DC component of the motor terminal voltage despite inverter nonidealities. The proposed method is finally implemented in real time in a custom-built programmable inverter drive. The experimental results demonstrate that the method gives accurate and robust stator temperature estimation regardless the operating condition of the induction motor.

The health monitoring of claw-pole generators with built-in rectifiers is also studied in this thesis. Despite the limited literatures on the major failure modes of claw-pole generators, several common types of faults are successfully identified and studied in detail. Different from grid-connected AC generators, the built-in rectifier of the claw-pole generator makes it difficult to access the three-phase voltage and current measurements. Hence, conventional condition monitoring methods based on AC signals can no longer be

used. To overcome this challenge, an experimental analysis is performed to better understand the overall waveforms and spectra of the voltage and current of the claw-pole generator. Several harmonic components in the output current spectrum are identified to be related to various faults of the claw-pole generator.

Faults of claw-pole generators are classified into two categories: External faults (or system-related faults) and internal faults. Specifically, the external faults of claw-pole generators studied in this thesis include the serpentine belt slip and serpentine belt defect. For the serpentine belt slip, the speed of the claw-pole generator is estimated indirectly by tracking the rectifier ripple frequency in the output voltage signal. Hence, the fault is reliably detected by comparing the estimated generator speed with the measured speed of the prime mover (vehicle engine). The defects on the serpentine belt, on the other hand, modulate the transmitted torque and speed of the claw-pole generator every belt cycle. It is therefore detected by monitoring some specific side-band current harmonics near the rectifier ripple frequency.

The internal faults of claw-pole generators studied in this thesis include the stator turn-to-turn fault, the rotor eccentricity, and the worn bearing. It is discovered that with unbalanced three-phase inputs, the output current of the rectifier will exhibit increased harmonic at one third of the rectifier ripple frequency. This signature is used to detect stator turn faults. Once the stator turn fault is detected, an analytical model of the claw-pole generator with fault is also derived to establish an accurate mapping relationship between the observed fault signature and the fault severity. The experimentally validated model enables the design of well-informed post-fault protection strategies, which prevent the stator turn fault from progressing into catastrophic generator failures while

maintaining maximum limp-home capability of the vehicle. The effect of rotor eccentricity on the rectifier output current is also discussed. It is found that the rotor eccentricity will produce an additional reluctance torque oscillation, which will give rise to current harmonic at the shaft frequency of the generator. This signature is successfully utilized to detect rotor eccentricity. Finally, the detection of generalized bearing roughness is investigated. It is found that the bearing wear in a belt-driven claw-pole generator can lead to slight change of the effective generator pulley diameter through one or more possible fault mechanisms. The change of effective pulley diameter of the generator is going to further shift the frequency of rectifier ripple harmonic in the generator output current. Through multiple accelerated bearing aging tests and control tests, it is confirmed that the frequency deviation of the rectifier ripple harmonic is strongly correlated to the bearing wear in claw-pole generators and can be used as a fault indicator of the generalized bearing roughness.

Whereas this PhD research only focuses on the condition monitoring of two specific types of electric machine systems, the fundamental ideas behind each proposed condition monitoring technique is quite universal and appeals to a much wider variety of electric machines connected to power electronic converters. The two main categories of power-converter-fed electric machines that benefit from this research are,

- Inverter-fed electric machines for motoring and generation applications
- Rectifier-connected electric machines for generation applications

To sum up, this PhD research has a broad beneficial impact on a wide spectrum of power-converter-fed electric machines and is thus of practical importance.

CHAPTER 1 Introduction and Objective of the Research

1.1 Background

As the most commonly used electromechanical energy-conversion device in the modern civilization, AC electric machines have played indispensable roles in electric power generation, transportation, industrial processes, and residential applications. In many applications, electric machines are subjected to environmental stresses, such as high ambient temperature, high moisture, and a corrosive and dusty environment. These environmental stresses, combined with machines' internal electrical, mechanical, and thermal stresses, could seed faults in electric machines. These incipient faults can develop into catastrophic machine failures if left undetected. Such failures result in not only costly repairs, but also significant financial loss because of unscheduled downtime in industrial plants or safety hazards in transportation applications.

The history of condition monitoring and diagnostics of electric machines is almost as old as electric machines themselves. Initially, the electric machines are only protected in a very crude way against a misuse such as over current or over voltage [1]. With advancements in sensor technology, digital processors, and signal processing techniques, it has now become possible to detect machine faults at their very inception, well before material machine failures occur [2-4]. The detection of incipient faults of electric machines allows time for preventive maintenance to be scheduled, which greatly improves the overall system reliability, availability, and maintainability in a wide range of sensitive applications.

To detect and isolate specific incipient faults, different types of sensors are added to electric machines. These include search coils for stator or rotor faults [5], infrared sensors

for bad electrical connection [6], thermal and accelerometers for bearing faults [7], etc. However, sensors and associated installations and wirings are costly and intrusive for many applications. Hence, only very large and expensive electric machines nowadays are equipped with some of these sensor-based condition monitoring schemes.

In the last two decades, the research on the so-called sensorless condition monitoring of electric machines has gained a lot of momentum. Instead of deploying expensive special-purpose sensors for fault detection, existing sensors and hardware can provide rich wellness information of the machine that has traditionally not been utilized. For example, in industrial plants, the voltage and current measurement available in the motor control center can be used for condition monitoring purposes. In motor drives, the existing current sensors and DC bus measurement can provide useful information about the wellness of the electric machines.

However, due to historic reasons, most fault-detection methods available nowadays are designed with only grid-connected electric machines in mind. With the growing emphasis on energy efficiency and inexpensive availability of power electronics, more and more electric machines are now interfaced with various types of power electronic converters, some of which even have sophisticated control. While the flexible energy forms synthesized by these power electronic converters greatly enhance the performance of electric machines in a much expanded operating region, they also have a significant impact on fault behaviors of electric machines and introduce a lot more complexity in terms of fault detection and protection. In most cases, conventional fault-detection methods for grid-connected electric machines cannot be applied to power-converter-fed machines anymore. This necessitates detailed analyses of the effects of power converters

on various faults of electric machines so that simple and reliable fault-detection schemes can be developed.

The large number of power electronic converters and electric machines available nowadays makes it unrealistic to study every possible combination of them. *The scope of this PhD research* is thus focused on the condition monitoring of two exemplary types of power-converter-fed electric machines:

- Induction motors fed by closed-loop inverter drives
- Claw-pole synchronous generators connected to output rectifiers

Whereas only these two specific types of electric machine systems are studied in detail, the fundamental principles of proposed condition monitoring techniques are quite universal and can benefit a much wider array of electric machines connected to power electronic converters. Even with so many combinations of electric machines and power electronic converters nowadays, most of them can be classified in to one of the following two broad categories:

1. Inverter-fed electric machines for motoring and generation applications
2. Rectifier-connected electric machines for generation applications

The condition monitoring techniques proposed for induction motors fed by closed-loop inverters can be easily extended to benefit the electric machines in Category 1. The condition monitoring methods proposed for claw-pole generators with built-in rectifiers, on the other hand, can be adapted to benefit the electric machines in Category 2. Therefore, this PhD research has a broad beneficial impact on a wide spectrum of power-converter-fed electric machines and is thus of practical importance.

1.2 Induction Motors Fed by Closed-loop Inverter Drives

The induction machine is one of the most prevailing types of electric machines used nowadays thanks to its relatively low cost, low maintenance, and simple construction. Induction machines are used as motors in most applications, which earn its name as the workhorse of the modern industry.

Induction motors can be connected to the grid directly, or connected to power converters such as open-loop inverter drives or closed-loop inverter drives. This study mainly focuses on the condition monitoring of closed-loop inverter-fed induction machines.

Closed-loop inverters are power converters with current or torque feedback control capabilities. Closed-loop induction motor drives find many applications in high-performance motion control and traction system, such as cranes and hoists, elevators, winding process, material handling, hybrid and electric vehicles, modern railway system, diesel-electric ships, and rolling steel mills, where zero-speed torque capability and highly dynamic torque response are required. Compared to the grid-connected or open-loop inverter-fed electric machines, the machines fed by closed-loop inverters are generally connected to the most important types of loads. Equipped with current sensors and digital processors, the inverter drives are also ideal platforms for implementing the sensorless condition monitoring schemes. In reality, however, closed-loop controlled machines turn out to be the least studied category in terms of fault detection, mainly because the closed-loop control dramatically changes the fault behaviors of the electric machines and complicates the fault analysis [8].

As one of the weakest components in induction machines, the stator winding insulation failures accounts for about 30~40% of induction machine failures in industrial applications [1, 9-12]. In closed-loop induction motor drives, the large dv/dt caused by the pulse width modulation (PWM) of the inverter will result in even higher electric stress on the induction machine, especially on the first few turns in the terminal end of the stator winding [13]. Therefore, the condition monitoring of the stator insulation of inverter-fed induction machine is the primary focus of this work. The thesis will propose methods that not only detect solid stator insulation faults but also monitor the insulation degradation through indirect thermal monitoring.

1.3 Claw-pole Generators with Built-in Rectifiers

A claw-pole generator is essentially a wound-rotor synchronous generator with a built-in rectifier and voltage regulator. The DC side of rectifier is often connected to a DC-link energy storage device, such as a capacitor, an ultra-capacitor, or a battery. The unique claw-pole shape of the rotor makes the generator inexpensive to manufacture in mass scale and caters to applications where low cost is the paramount. In fact, the claw-pole type synchronous alternator (or generator) is the dominant type of machine used in automotive electric power systems and some small marine electric power systems.

In the past few decades, the push to improve fuel economy, address increased safety and emission regulations, and provide consumers with a luxury driving experience has resulted in a rapid increase in the demand for electric power in automobiles [14]. The power consumption of an average vehicle grows to twice what it was a couple of decades back [15]. Today's passenger vehicles use up to 120 motors, up to 70 Electronic Control

Units (ECUs), and a whole host of sensors and electro-mechanical actuators, all of which require a reliable and efficient power source.

A failure of the claw-pole generator is considered to be a so-called “walk-home” incident or a very severe case of failure that can leave a motorist stranded [16, 17]. Timely and accurate detection of alternator problems will not only decrease “walk-home” incidences but will also significantly decrease misdiagnoses, thereby resulting in significant warranty cost savings for auto manufacturers [16-23].

While there has been active academic research on the condition monitoring of large wound-rotor synchronous generators that are directly connected to the grid [24-26], the literatures on the detection of incipient faults for claw-pole generators are extremely limited. The primary reason is that the built-in rectifier and the stringent cost constraint make it difficult to monitor the three-phase AC quantities of the generator. Hence, conventional fault-detection methods based on three-phase current or voltage measurements can no longer be used.

Faults of claw-pole generators are classified into two categories: External faults (or system-related faults) and internal faults. Specifically, the external faults of claw-pole generators studied in this thesis include the serpentine belt slip and serpentine belt defect. The internal faults of claw-pole generators studied in this thesis include the stator turn-to-turn fault, the rotor eccentricity, and the worn bearing.

In addition to conventional automotive applications, an AC generator with a rectified DC link is also a standard arrangement in many standalone electric power systems, such as hybrid/electric vehicles, electric ships, aircraft, and wind turbines. Therefore, the

research on claw-pole generators with built-in rectifiers can also be carried over to many other similar applications, which results in a much broader impact.

1.4 Problem Statement

Condition monitoring of AC electric machines fed by power electronic converters is of great importance to ensure the overall system reliability, availability and maintainability in a wide range of sensitive applications.

The objective of this PhD research is to develop simple, robust and non-intrusive condition monitoring methods for two exemplary types of power-converter-fed electric machines: closed-loop inverter-fed induction motors and claw-pole generators with built-in rectifiers.

The study proposes to undertake several important aspects of condition monitoring of these two types of machines, which include stator turn-to-turn fault detection and stator thermal monitoring for induction machines; and the detection of important external faults (serpentine belt slip and serpentine belt defects) and internal faults (stator turn-to-turn fault, rotor eccentricity, and worn bearing) for claw-pole generators.

1.5 Dissertation Outline

Chapter 2 reviews the previous work on the condition monitoring of closed-loop inverter-fed induction machines, with a special focus on the stator turn-fault detection and stator temperature estimation. The chapter also discusses the disadvantages and limitations of the present techniques. Chapter 3 reviews the previous work on condition monitoring and fault diagnostics for claw-pole generators with built-in rectifiers, also with their limitations discussed. The proposed stator turn fault detector and stator temperature estimator for closed-loop drive-fed induction motors are presented in

Chapter 4 and Chapter 5, respectively. The modeling and a general spectral analysis of the claw-pole generator is presented in Chapter 6. Chapter 7 presents methods to detect external faults for claw-pole generator. The methods to detect internal faults are presented in Chapter 8. Experimental results are presented to validate all proposed condition monitoring schemes. The conclusions, contributions, and the recommendation for future work are summarized in Chapter 9.

CHAPTER 2 Previous Work on Insulation and Thermal Monitoring of Induction Machines Fed by Closed-loop Inverter Drive

2.1 Overview

According to several industrial surveys, conducted by IEEE Industry Application Society (IAS) [1, 10, 11], Electric Power Research Institute (EPRI) [9], and Thorson [12, 27], the stator winding insulation failure is a major failure mode for induction machines in industrial applications, which accounts for about 30~40% of total induction machine failures. In closed-loop induction motor drives, the large dv/dt caused by the pulse width modulation (PWM) of the inverter will result in even higher electric stress on the induction machine, especially on the first few turns in the terminal end of the stator winding [13]. This may result in even higher failure rate of the winding insulation if the induction machine is not specially designed for inverter operation.

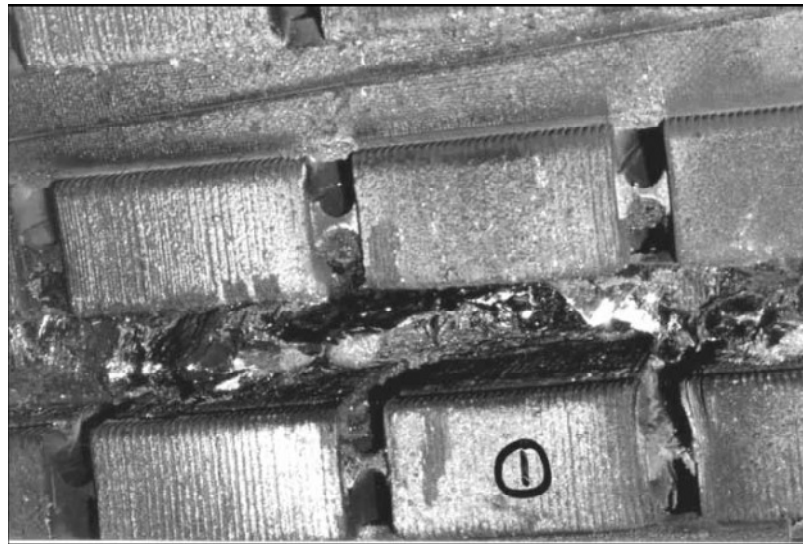
As a major root cause to stator insulation degradation [28], the thermal overload of induction machines also demands special research attention.

In this chapter, the methods for stator turn-fault detection and stator temperature estimation for induction machines are reviewed. The condition monitoring techniques for induction machines fed by different power sources (namely the grid, open-loop inverters, and closed-loop inverters) are thoroughly discussed and compared

2.2 Detection of the Stator Turn Fault

Among various types of faults in electric machines, the stator fault is one of the most commonly encountered faults and receives arguably the most research attention. Most stator failures start with a breakdown of the turn-to-turn insulation of the stator winding. Large circulating current will then flow in the shorted turns, overheating or even melting

the adjacent winding insulations. If left undetected, the incipient stator turn fault can develop into severe stator winding or stator core failures [29], as shown in Figure 2.1. The time to disaster varies from a third of a second for random-wound machine to several minutes or longer for large form-wound machines [30].



(a) Stator winding failure



(b) Stator core damage

Figure 2.1: Electric machine stator failures [29].

2.2.1 Stator Turn-fault Detection for Grid-connected Induction Machines

Numerous researches have already been published in an attempt to detect the incipient stator turn fault before the catastrophic stator failure occurs. The dominant majority of the existing methods are aimed at electric machines connected directly to the grid.

It was first proposed in [31] to use the negative-sequence component of the machine's three-phase currents as the fault signature for a stator turn fault. The method is well received and various techniques are consequently proposed to extract the negative-sequence components or its equivalence from the stator current and/or voltage, which includes phase-shift analysis [32], current-envelop analysis [33], Park's vector approach [34], the extended Park's vector approach [35], the stator current in multiple reference frames [36, 37], negative-sequence impedance [38], and the wavelet transform of the stator current [39, 40].

Moreover, the fault induced negative-sequence current, when coupled with the positive-sequence supply voltage, produces a torque (or power) oscillation at twice the stator frequency. This frequency component in the instantaneous power [41] and the air gap torque [42] was also used to detect the stator turn fault.

For grid connected machines, however, it was soon realized that [30] the negative-sequence current can also be caused by other factors, such as the inherent asymmetry of the electric machine, the time-varying three-phase unbalance of the grid voltage supply, or slightly different gains in the three-phase measurement channels. Hence, the negative-sequence current alone is not a reliable fault indicator. As a result, a large portion of the research efforts has been devoted to how to deal with these non-ideal factors. Neural-

network-based methods [43], sequence-impedance-matrix-based methods [44], and purely data-based (look-up table) methods [30] have all been proposed to compensate for such unbalanced voltage and machine inherent asymmetry. Some of the methods [44] have already achieved very high detection sensitivity (detecting a 1-turn fault). However, industry adoptions of these state-of-the-art turn-fault detectors are still extremely limited, mainly because of the high implementation complexity of such methods. All these compensation techniques [30, 43, 44] require complicated calibrations or lengthy learning processes of the machine inherent asymmetry with different amount of voltage unbalance conditions. Some methods may also demand high computational effort [43]. This significantly increases the implementation complexity of the fault-detection methods and hampers their popularity in real-world applications.

Other than stator turn-fault detectors based on negative-sequence components, methods using other fault signatures, such as the zero-sequence voltage [45], slot harmonics [46], angular fluctuation of the current's space vector [47, 48], and induced voltage during machine turn-off [49, 50], are also proposed. Observer-based parameter-identification methods are also investigated in [51, 52]. However, most of these methods [45-52] are still less sensitive compared to the state-of-the-art negative-sequence-based methods [44], and some of the methods [49, 50] does not provide continuous protection of the electric machines against stator turn faults.

2.2.2 Stator Turn-fault Detection for Open-loop Inverter-fed Induction Machines

Open-loop inverters are power converters capable to generate variable-frequency poly-phase voltages. Open-loop inverters find many applications in low-cost motor drive systems, such as fans, pumps, conveyors, mixers, and centrifuges, where energy

efficiency is important but the dynamic performance of the machine is not a major concern. Since different IGBT bridges in an open-loop inverter share the same DC bus voltage and identical switching patterns, the fundamental poly-phase output voltages are generally balanced and symmetric.

Electric machines connected to open-loop inverters usually behave similarly with their grid-connected counterparts in the case of faults. Theoretically, most fault-detection methods that work for grid-connected machines should also be applicable to machines fed by open-loop inverter after some modification. However, many of those methods are extremely inconvenient to use in practice because inverter-fed machines have variable fundamental frequencies and consequently much more complicated operating conditions. The inherent asymmetry of the induction machine thus must be learned as a function of the fundamental frequency in addition to the load level.

It was discussed in [44] that the stator turn-fault detector for grid-connected induction machines may also be applied to open-loop inverter-fed induction machines if the inherent asymmetry of the induction machine is sufficiently learned. However, the learning process involves an experimental setup shown in Figure 2.2, in which a resistor or variac is used to artificially introduce voltage supply unbalance.

This learning process is very intrusive for grid-connected induction machines already. It becomes even more inconvenient and intrusive for inverter-fed machines because the inherent asymmetry of the machine needs to be learned as a function of the fundamental frequency in addition to the load level.

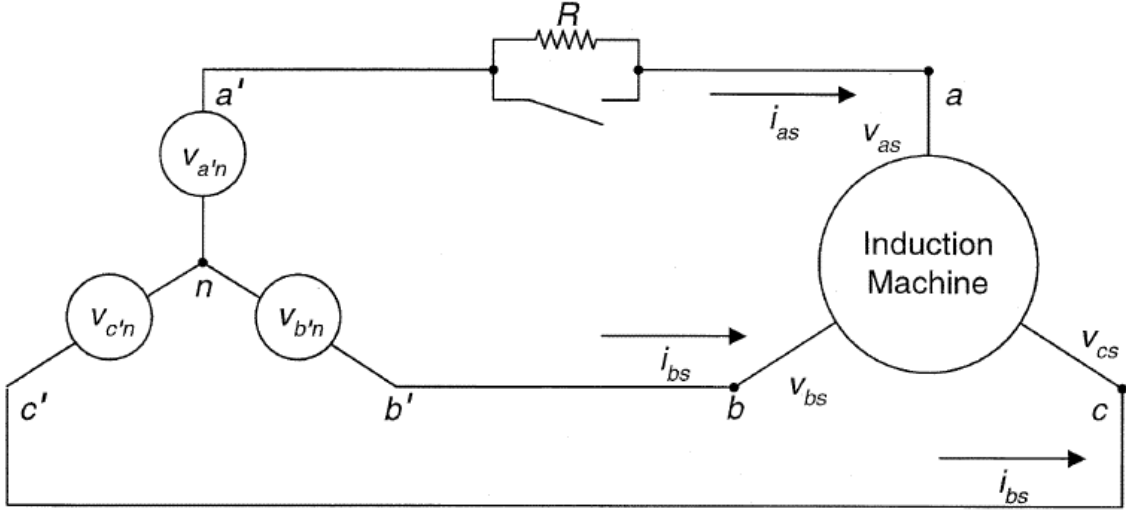


Figure 2.2: Experimental setup for unbalancing the three-phase supply voltage [44].

To reduce the dependency of the baseline fault signature (or healthy characteristic) of the induction machine on its operating conditions, a high-frequency signal injection method is proposed in [53] to detect stator turn faults, as shown in Figure 2.3.

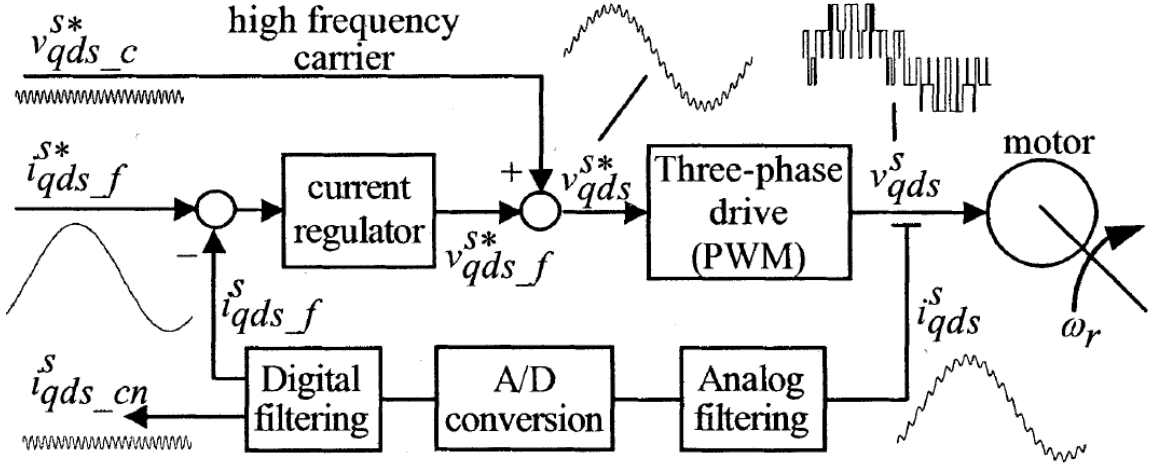


Figure 2.3: High-frequency voltage injection for stator turn-fault detection [53].

By injecting a fixed high-frequency voltage signal into the induction machine, the fault is detected by monitoring the high-frequency negative-sequence current, as illustrated in Figure 2.4. The method is capable to detect a 2-turn stator short circuit with reduced sensitivity to the operating condition of the machine.

However, the method also has several critical downsides. First, because of the inductive nature of any induction machine, only very small high-frequency negative-sequence current (1~3 mA) can be observed even in the presence of the stator turn fault. The detection of such small current component requires high-precision A/D converters, which may not be available in many open-loop inverter drives. Second, the high-frequency signal also demands very high sampling frequency in data acquisition (as high as 200 kHz in some cases) [54], which is too expensive for most inverter drives. Lastly, high-frequency signal injection may also have unwanted effects such as increased vibration and core losses.

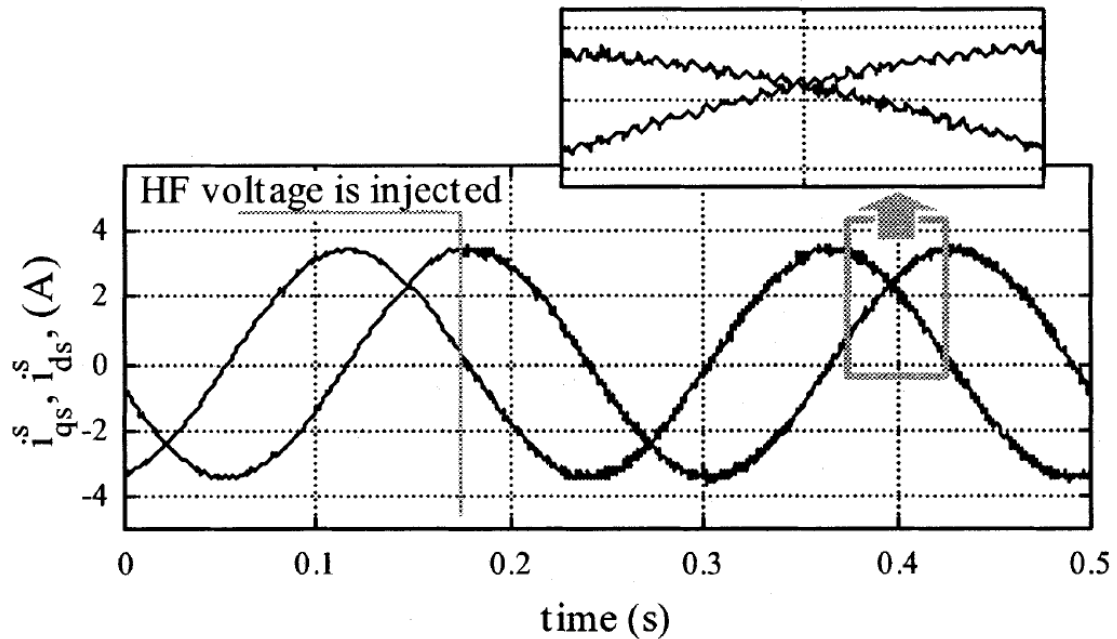


Figure 2.4: Current waveform before and after high-frequency voltage injection [53].

To address the sensitivity issue of the high-frequency negative-sequence current, it is proposed in [54] to use the high-frequency zero-sequence voltage to detect the stator turn faults. In [54], it is shown that in the presence of a stator turn fault, the injected high-frequency voltage signal will interact with the saliencies in the stator transient inductance

to produce a high-frequency zero-sequence voltage for a Y-connected induction machine. The experimental result in [54] verifies that the high-frequency zero-sequence voltage is a more sensitive fault signature compared to the high-frequency negative-sequence current. However, monitoring such zero-sequence high-frequency voltage requires additional voltage sensors, A/D converter and access to the neutral terminal of the induction machine, which are typically not available in either open-loop or closed-loop induction motor drives.

2.2.3 Stator Turn-fault Detection for Closed-loop Inverter-fed Induction Machines

Closed-loop inverters are power converters with current or torque feedback control capabilities. Closed-loop inverters find many applications in high-performance motor drive system, such as cranes and hoists, elevators, winding process, material handling, and vehicle traction, where zero-speed torque capability and highly dynamic torque response are required. The controller in a closed-loop inverter tries to regulate the machines' current or torque to follow some reference value by cleverly synthesizing an appropriate voltage space vector. The reference torque or the reference current, on the other hand, is either predetermined, or is the output of a higher-level control loop, such as the speed regulator or the voltage regulator.

Compared to grid-connected or open-loop inverter-fed electric machines, machines fed by closed-loop inverters are generally connected to the most important types of loads. Equipped with current sensors and digital signal processors, the closed-loop inverters are also ideal platforms for implementing the sensorless condition monitoring schemes. In reality, however, closed-loop controlled machines turn out to be the least studied category in terms of fault detection. There are mainly two reasons for this.

- (1) Similar with open-loop induction motor drives, closed-loop induction motor drive has variable fundamental frequency which greatly expands the operating conditions of the induction machine. Therefore, many fault detection methods developed for grid-connected machines are practically inconvenient to use for closed-loop inverter-fed machines.
- (2) More importantly, the current or torque regulator in a closed-loop inverter dramatically changes the fault behaviors of the induction machine and complicates the fault analysis [8]. Current regulators with a bandwidth of a few hundred Hertz are not uncommon in today's motor drives. Such high-bandwidth current regulators will suppress the negative sequence current in induction machines and render conventional negative-sequence-current-based methods useless.

The fault detection for closed-loop controlled induction machines was first discussed in [8, 55]. It was discovered that under very severe stator unbalance conditions (16.6% of one of the phase winding being shorted), the negative-sequence current due to the fault will exhibit itself in the currents in the synchronous reference frame, i_d and i_q , as harmonic components at twice the stator frequency. It is claimed in [8] that the harmonic component in i_d does not vary too much with the control gains of the current regulator and is therefore a proper fault signature. However, [8] considers only very severe stator unbalance conditions which make the observations not suitable to detect subtle unbalance such as stator turn faults. Moreover, the current regulators considered in [8] are simple proportional compensators. These kinds of controllers are likely to have poor control

performance and are not realistic representations of current regulators used in real-world closed-loop drives.

The impact of closed-loop control on the stator turn-fault detection was discussed more thoroughly in [56]. It was discovered in [56] that a reasonably well-tuned current regulator migrates most of the fault-related negative-sequence component from the current to the voltage. Based on this observation, [56] proposes a fault detector that uses the negative-sequence voltage as the fault indicator, as shown in Figure 2.5. An artificial neural network is employed to learn the inherent asymmetry of the induction under various operating conditions. The experimental results demonstrate that the method is able to detect a 2-turn fault at about 60% of the motor's rated speed.

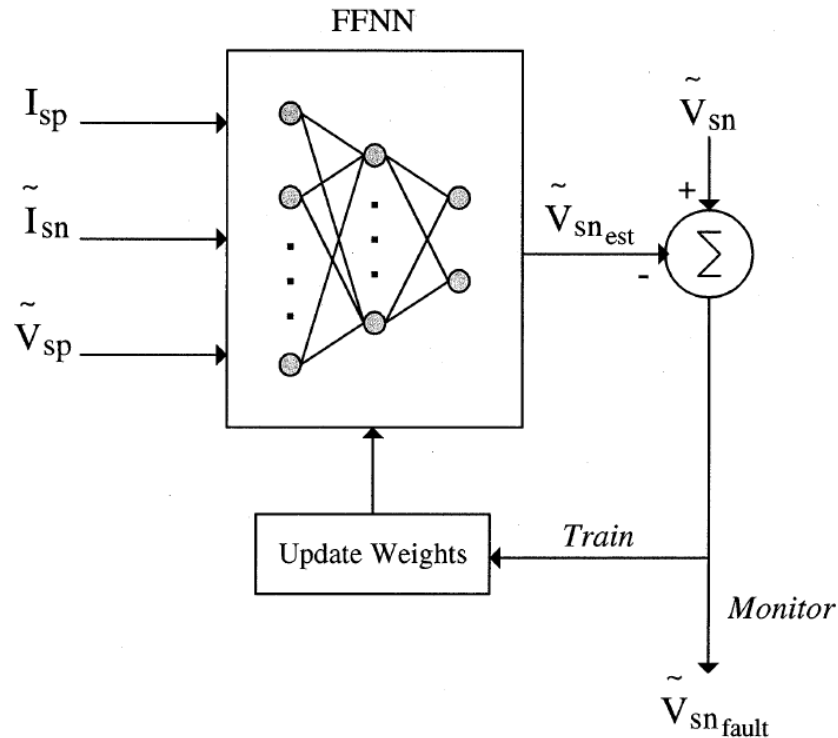


Figure 2.5: Neural-network-based stator turn-fault detection scheme [56].

However, the training of the neural-network (NN) detector for a closed-loop controlled induction machine was inconvenient and intrusive for many applications. To

sufficiently learn the inherent asymmetry of the induction machine, not only are the training data obtained at different motor speeds and load conditions, but they are also acquired at different levels of voltage unbalance. Two autotransformers are inserted in series with two phases of the induction machine to arbitrarily adjust the magnitude and phase of the negative-sequence voltage, as shown in Figure 2.6. Such additional hardware makes the training of the neural network a strictly off-line process and significantly reduces the practicability of the method.

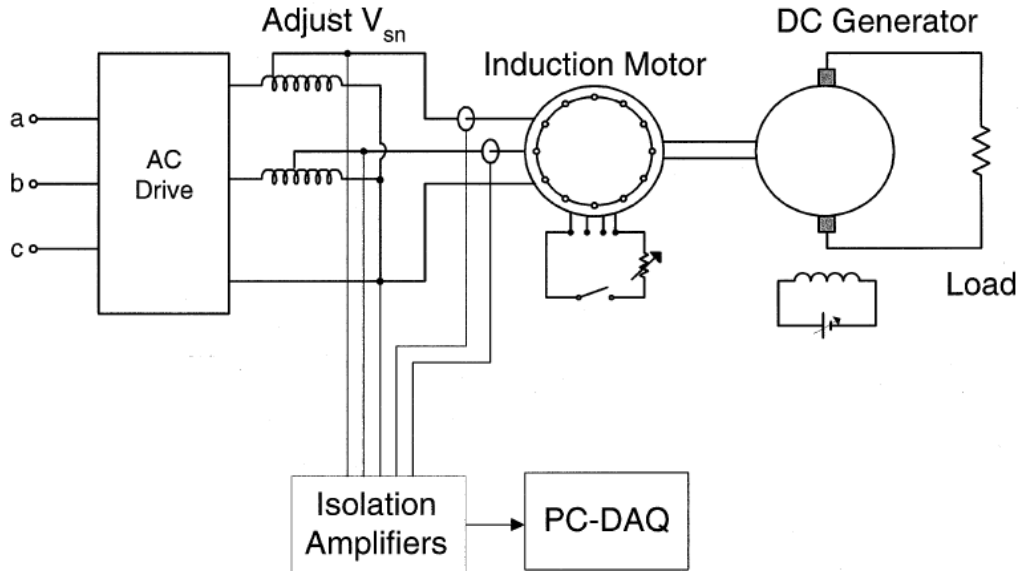


Figure 2.6: Experimental setup for inducing voltage unbalances for a inverter-fed induction machine [56].

A robust stator turn-fault detector was proposed in [44] for grid-connected induction machines. The proposed fault detector achieves very high sensitivity of reliably detecting 1-turn fault out of 216 turns per phase. Since the method is derived from a physical impedance-matrix model of the induction machine as shown in equation (2.1), it is claimed in [44] that the method should be equally effective for open-loop or closed-loop inverter-fed induction machines.

$$\begin{bmatrix} V_p \\ V_n \\ V_z \end{bmatrix} = \begin{bmatrix} Z_{pp} & Z_{pn} & Z_{pz} \\ Z_{np} & Z_{nn} & Z_{nz} \\ Z_{zp} & Z_{zn} & Z_{zz} \end{bmatrix} \cdot \begin{bmatrix} I_p \\ I_n \\ I_z \end{bmatrix}, \quad (2.1)$$

where the subscript p , n and z indicate the positive sequence, negative-sequence and zero-sequence respectively.

However, just like the previous stator turn-fault detector, the method in [44] also requires injecting different voltages unbalance into the induction machine in order to learn its inherent asymmetry. As shown in the experimental setup in Figure 2.7, the artificially voltage unbalance is introduced by a resistor or a variac. For closed-loop drives which have variable fundamental frequency and load levels, such learning stage is too inconvenient and intrusive for many applications.

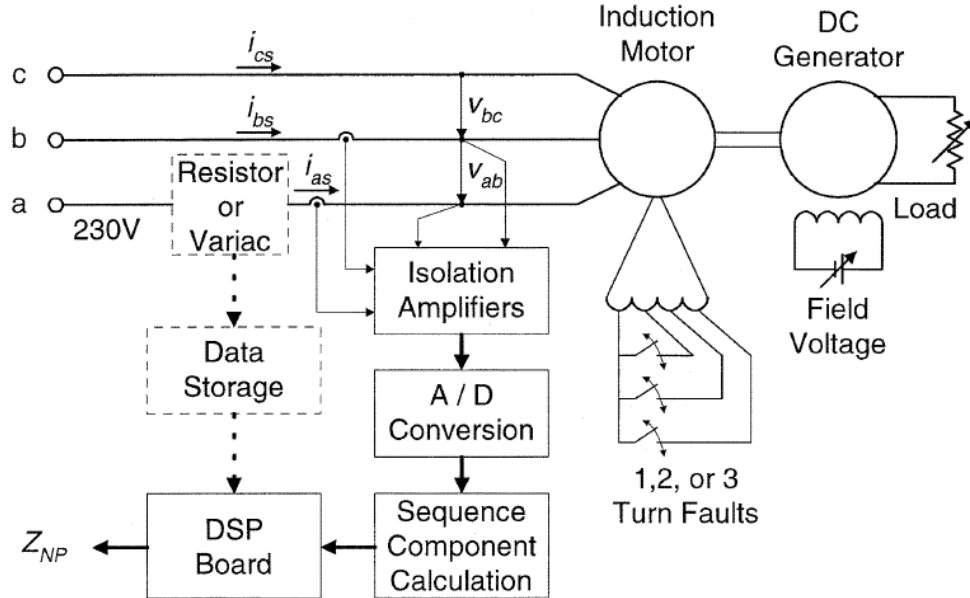


Figure 2.7: Overall scheme for testing the stator turn-fault detection scheme [44].

In spite of all the complexities introduced by the closed-loop control, the fully controlled inverter also opens up new possibilities for active stator turn-fault detection for induction machines. The same high-frequency voltage injection methods [53, 54]

described in section 2.2.2 for open-loop induction motor drive can be applied to closed-loop induction motor drive as well. If the frequency of the injected voltage signal (1~2 kHz) is chosen well beyond the bandwidth of the current control loop, the current regulator is not able to react fast enough to cancel the high-frequency voltage injection. Hence, a closed-loop inverter will behave similarly with an open-loop inverter in the high-frequency domain and the same stator turn-fault detector can be applied. However, drawbacks of the turn-fault detector for open-loop induction motor drives also apply to closed-loop versions, namely the small amplitude of fault signature and the demanding requirement on the precision and sampling frequency of the data acquisition devices.

[57] proposes a stator turn-fault detector that is exclusively designed for direct-torque-controlled (DTC) induction motor drive. It is well known that a stator turn fault in an induction machine introduces torque oscillations at twice the stator frequency. The detailed analysis in [57] shows that the fast torque controller in a DTC motor drive will react to cancel these torque oscillations, thus introducing negative-sequence component and third-order harmonic in the stator flux of the machine. Moreover, in a DTC drive the stator flux is forced to follow a round locus with a narrow hysteresis band as shown in Figure 2.8 (a). Thus the negative-sequence flux component can only be very small because any significant negative-sequence component in the stator flux will make the flux locus an ellipse as shown in Figure 2.8 (b). Therefore, the main signature of the stator fault shifts to the third-order harmonic in the stator flux, and further exhibits itself in the three-phase stator currents.

Experimental results demonstrate that the method is able to detect a 3-turn short circuit of an induction machine. Unfortunately, the fault detector is only demonstrated at a single operating point.

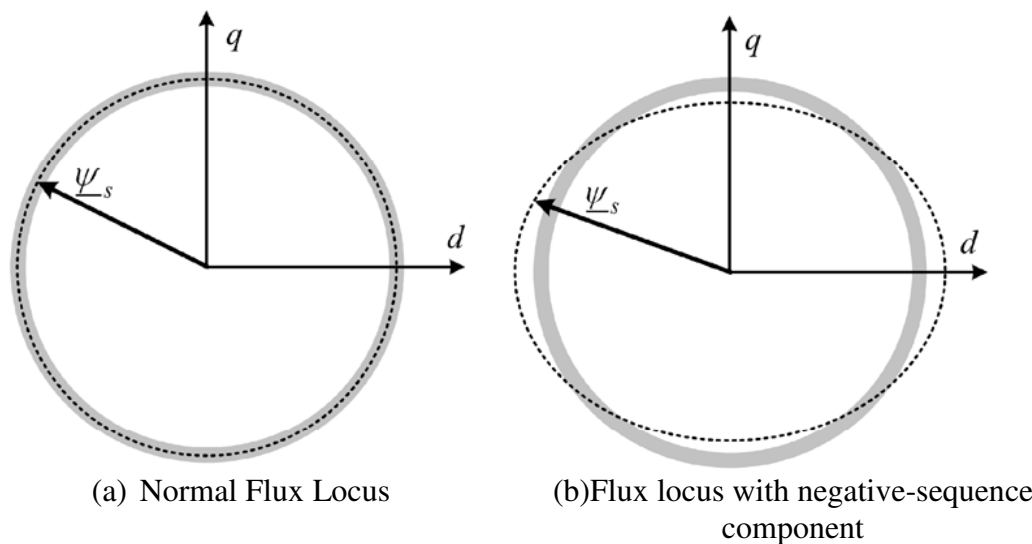


Figure 2.8: Representation of the flux hysteresis band and stator flux locus imposed by a DTC induction motor drive [57].

2.3 Thermal Monitoring of Stator Winding

In addition to aforementioned methods that detect solid stator turn faults of induction machines, it is also desirable, in many applications, to monitor the health of stator insulation before actual short circuit occurs. The insulation surge testing is one such example that is widely accepted in the industry [58]. By applying some high-voltage surge to the machine terminals, the weak spot in the stator insulation can be briefly broken down and exhibit itself in the surge waveform. Therefore, the health of the stator insulation can be roughly evaluated. However, such testing usually requires specialized hardware or instrument, which is beyond the scope of this study.

Another technique for monitoring the machine insulation condition is to measure the differential leakage currents of each phase winding [28] of the machine. However, the

method requires one pair of high performance current sensors installed in the machines' terminal box for each phase winding. The high cost of the sensors and additional wirings makes the solution economically feasible only for very large and expensive electric machines.

A quite different perspective to approach the stator insulation-degradation problem is through the stator temperature monitoring. As a major root cause to stator insulation degradation, the thermal overload of electric machines receives widespread research attention [59-67]. The typical thermal limits for different stator insulation classes are summarized in Table 2.1 [68].

Table 2.1: Temperature limits for different insulation classes [68].

Insulation	Ambient	Rated Temperature	Hot Spot
Class	Temperature (°C)	Rise (°C)	Temperature (°C)
<i>A</i>	40	60	105
<i>B</i>	40	80	130
<i>F</i>	40	105	155
<i>H</i>	40	125	180

As a rule of thumb, it is widely believed that a machine's life is reduced by 50% for every 10°C increase above the stator winding temperature limit [69]. As opposed to insulation surge testing or differential leakage current measurement, the stator temperature estimation does not provide a direct monitoring of the stator insulation condition. However, accurate stator temperature monitoring does allow the electric machine to operate safely within its thermal limits without being too conservative on machine load levels. This prevents the stator insulations from deteriorating due to the over temperature but still maximize the availability and performance of the electric machine. This section reviews several state-of-the-art stator temperature estimators for

Parameter-based methods estimate the temperature from the variation of the resistance. The accuracy of this method is not affected by the running condition and the cooling mode. The methods to identify the resistance can be further divided into induction motor model-based approaches and signal-injection-based approaches. Motor model-base approaches calculate the resistance of the stator and rotor using the induction motor equivalent circuit. Algorithms have been proposed to calculate the rotor and stator resistance under the steady state [61] or the transient state [64]. These approaches don't require offline experiment and can respond to changes in the cooling conditions. However, the stator resistance is usually so small compared to motor inductances that accurate resistance estimation is very difficult. The signal-injection-based temperature estimator calculates the stator resistance from the DC components of the voltage and current. The DC bias can be created by an extra injection circuit connected in series with one phase of the machine [65] or by using a soft starter [59, 60], as illustrated in Figure 2.10.

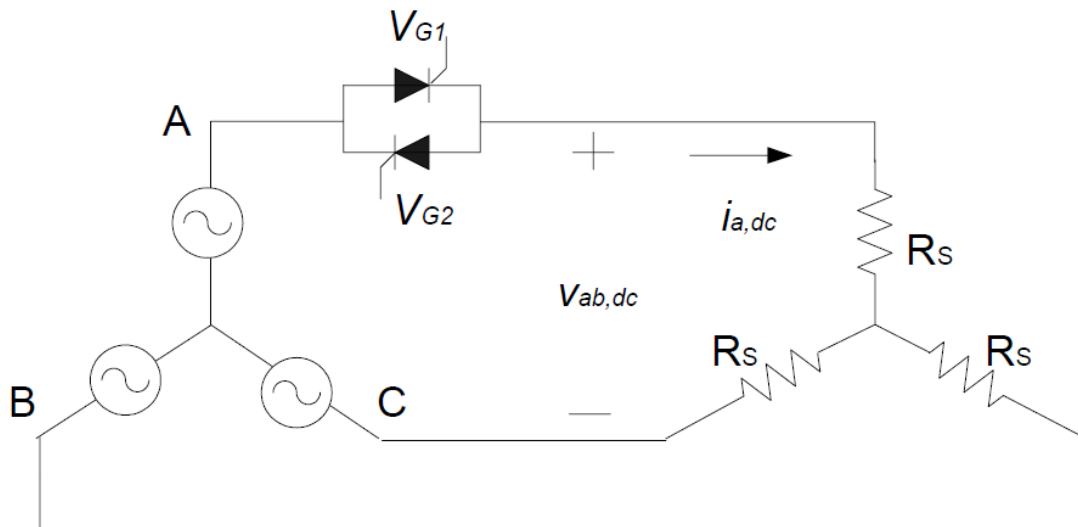


Figure 2.10: Soft-starter-based DC current injection for stator thermal monitoring [60].

2.3.2 Thermal Monitoring for Open-loop Inverter-fed Induction Machines

In inverter-fed induction machines, motor losses are functions of input frequency, voltage magnitude, motor speed, and etc. Therefore, it is more difficult to estimate the stator temperature using the thermal-model-based methods because these models can show significant parameter sensitivity, with their performance dependent on the operating condition of the machine.

On the other hand, signal-injection-based thermal monitoring methods estimate the machine stator resistance directly, with reduced sensitivity to the operating conditions of the machine. However, most inverter drives are only equipped with current sensors and one voltage sensor that measures the DC bus voltage. It is difficult to estimate the stator resistance accurately without requiring additional machine terminal voltage measurement. Despite the challenge, several signal-injection-based methods have been developed for stator temperature estimation.

In [71], a temperature estimation method based on high-frequency voltage signal injection is proposed. The transient impedance of the induction machine, which is related to the stator and rotor resistance, is identified to estimate the temperature of the machine. The method could ideally reduce the sensitivity of the thermal estimation scheme to operating conditions. However, in almost all induction machines, the inductance in the transient impedance dominates the resistance in the high-frequency region. This greatly limits the accuracy of the method.

The DC-injection-based thermal monitoring method for open-loop induction motor drive is first reported in [72]. The method injects a DC bias in the voltage command and measures the corresponding DC current response using the current sensors. In the

absence of any terminal voltage measurement in a typical inverter drive, the voltage reference command was initially used in [72] to calculate the injected DC voltage. However, it was soon realized that inverter non-idealities, such as the dead time and conduction voltage drop of the power electronic switches will distort the injected DC voltage [72]. Thus, the injected DC voltage is generally different from the commanded DC voltage.

To work around the effect of dead time and other inverter non-idealities, [72] employs a look-up table to store the true injected DC voltage at different load levels of the induction machines given the same voltage reference command. However, this compensation technique requires complicated calibrations, and even then it only reduces the resistance dependency on load levels at a single motor speed [72].

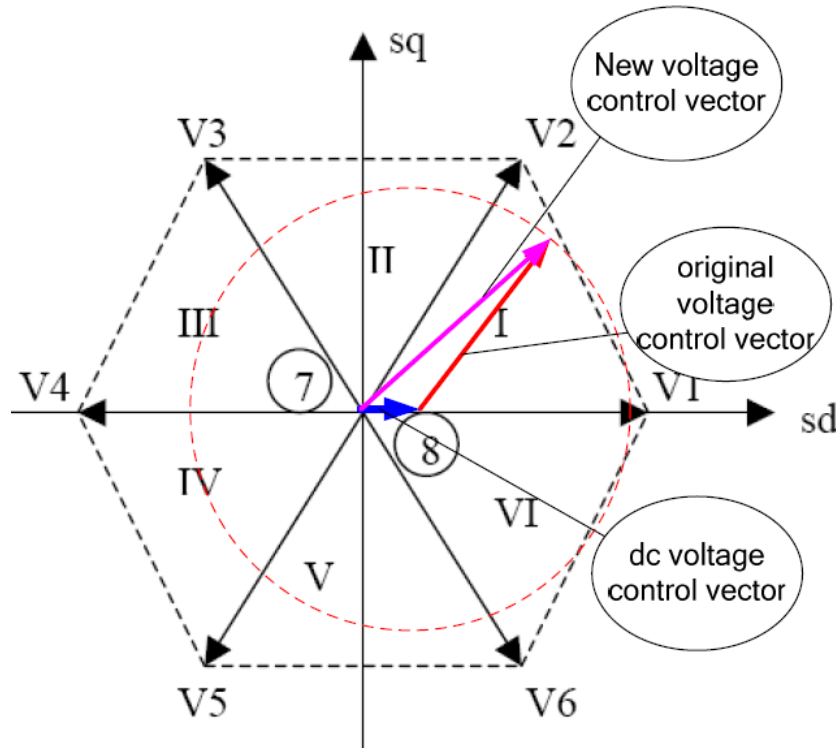


Figure 2.11: Modified voltage space vector for DC signal injection [73].

A variant of above method to estimate the stator winding resistance for open-loop induction motor drive is reported in [73]. The DC voltage is created by offsetting the origin of the voltage vector by a certain amount in a standard space-vector modulation (SVM) scheme, as shown in Figure 2.11. The method still suffers from the same problem in [72], i.e. the actual injected voltage varies with load levels even with the same reference DC voltage. A slightly different approach is proposed to work around this problem in [73]. A look-up table was constructed to store the injected DC current at different load conditions at a reference temperature. Satisfactory stator temperature estimation has been achieved at several predetermined load levels. However, the method is still not able to provide reliable stator temperature estimation at load levels and speed conditions other than those pre-calibrated ones. Since both the speed and the load level vary greatly in a drive-fed induction machine, complete calibrations of either the DC voltage or DC current are cumbersome and beat the original purpose of using DC-injection-based methods over thermal-model-based methods.

2.3.3 Thermal Monitoring for Closed-loop Inverter-fed Induction Machines

Thermal monitoring methods that are exclusively designed for closed-loop induction motor drives are very limited in literature. It is discussed in a PhD thesis [74] that if the current control loop can be disconnected briefly during the steady-state operation of the closed-loop drive, the DC voltage can then be injected in a similar fashion as did in open-loop inverter. However, no simulation or experimental results were given for the proposed method. Moreover, the loss of current control of the induction motors, even for a short period of time, is unacceptable in many applications.

In performance-sensitive or safety-critical applications, such as the electric traction motors for electric/hybrid vehicles, the winding temperature of the electric machine are still predominantly measured by thermal couples. However, thermal couples and associated wiring and measurement circuit increases the overall system cost.

2.4 Chapter Summary

This chapter provides an up-to-date review of methods to detect stator turn faults and methods to estimate the stator temperature of the induction machines. Condition monitoring schemes for grid-connected, open-loop inverter-fed, and closed-loop inverter-fed machines have all been reviewed and discussed.

Among numerous literatures published in detecting stator turn-faults for grid-connected machines, negative-sequence-component-based methods still have the highest detection sensitivity granted that the voltage unbalance and inherent machine asymmetry are properly compensated for. However, the use of these methods towards inverter-fed induction machines is extremely inconvenient in practice because of the much expanded operating region of the inverter-fed induction machines. To reduce the sensitivity of the detection scheme on machines' operating conditions, high-frequency signal-injection based methods are proposed. The impact of closed-loop control on the detection of stator turn faults is also reviewed and discussed in this chapter. However, most existing stator turn fault detectors for closed-loop induction motor drives require intrusive calibration of the machines' inherent asymmetry, which greatly limits their practical use in industry.

As for the preventive monitoring of stator insulations, the on-line monitoring of the stator winding temperature is a viable solution. Both the thermal model-based methods and machine-parameter based methods have been reviewed and compared in this chapter.

As one of the machine-parameter based methods, the signal-injection-based active temperature estimation is the preferred method for thermal management for inverter-fed induction machine because it is generally more accurate than other methods and less sensitive to various operating conditions of the machine. The major challenge to implement these methods in inverter drives, however, is that most inverters lack the terminal voltage sensors and power switches have some non-ideal characteristics. Such effects make it difficult to estimate the actually injected DC voltage from the voltage command.

CHAPTER 3 Previous Work on Condition Monitoring of Claw-pole Generators with Built-in Rectifiers

3.1 Overview

The claw-pole generator is the heart of virtually all automotive electric power generation and storage (EPGS) systems. Many critical systems in modern vehicles, such as braking, steering, engine control, and vehicle stabilization, all depend on a reliable and efficient supply of electric energy.

In a typical automotive EPGS system as shown in Figure 3.1, the vehicle engine is coupled to the claw-pole generators through pulley-serpentine belt assemblies. The claw-pole generator is essentially a wound-rotor synchronous machine with a built-in rectifier. A pulse-width-modulation (PWM) regulator connected to the field winding regulates the output voltage of the generator at an appropriate level to maintain the state of charge of the battery and to supply sufficient electric power to different electric loads in the vehicles. Since the generator is directly coupled to the vehicle engine, both the speed and the load level of the claw-pole generator vary greatly during a typical urban driving cycle. This is different from a grid-connected synchronous machine whose speed stays mostly constant.

While there has been active and systematic research on the sensorless condition monitoring of induction and synchronous machines in the past several decades [2-4, 24-26], research on the condition monitoring of claw-pole generators is still in its early stage. So far, virtually no published statistics are available on common failure modes or failure mechanisms of claw-pole generators. Related literature on the detection of generator faults is also very limited and far from systematic [16-23]. Nevertheless, it is widely

accepted that the faults of claw-pole generators can be broadly classified into external faults and internal faults. Faults that occur in systems external to the generator but have an impact on its operation are denoted as external faults, or system-related faults. Faults that happen inside the machine are called internal faults.

This chapter reviews the existing condition monitoring methods for both categories of faults for claw-pole generators. The merits and limitations of each method are thoroughly discussed.

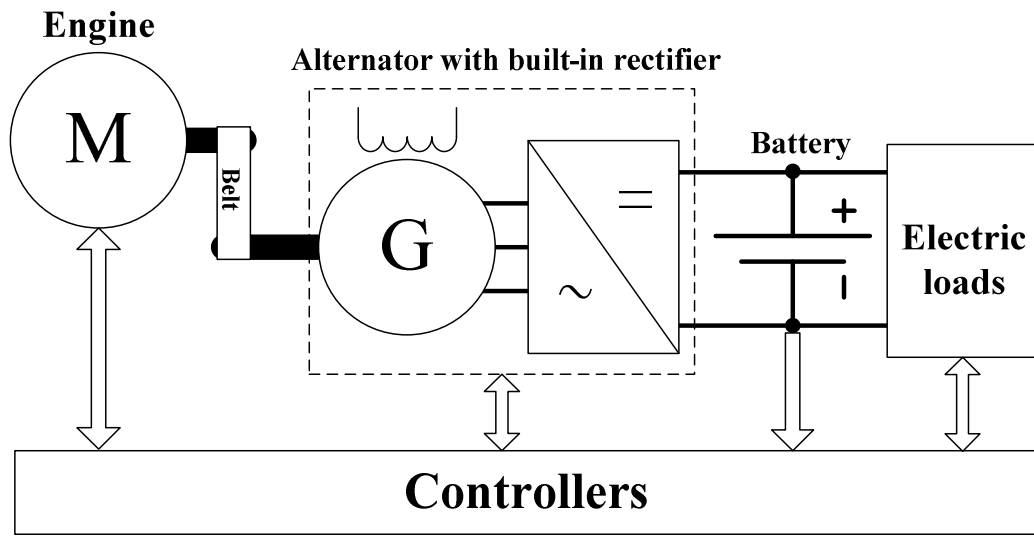


Figure 3.1: Illustration of an automotive EPS system.

3.2 Detection of External Faults

In [16], a model-based fault-detection scheme was proposed to detect three types of external faults for claw-pole generators, including the belt-slip fault, the diode fault, and the voltage-regulator fault. The schematic of the model-based generator-fault detector is shown in Figure 3.2.

An equivalent input-output model of a healthy claw-pole generator is formulated and parameterized in [16]. The model is based on a set of simplified state-space equations of

the generator. The inputs to the model are the generator speed and the voltage setpoint, and the outputs of the model are the generator field voltage and the output current.

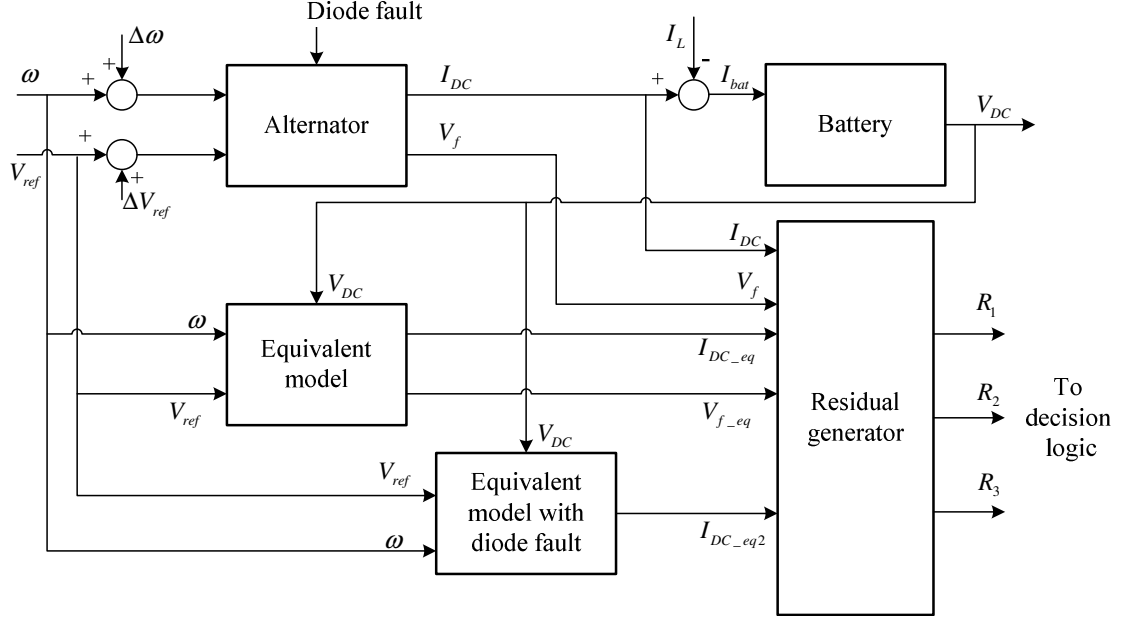


Figure 3.2: Model-based fault diagnostic scheme for claw-pole generator [16].

The belt-slip fault and the voltage-regulator fault are detected by comparing the outputs of the model to the outputs of the claw-pole generator being monitored. The differences between the two outputs form a residual vector with two elements. Very large residuals indicate a fault in the claw-pole generator. The belt-slip fault and voltage-regulator fault can be further discriminated by examining the individual elements in the residual vector in more detail.

To detect a diode fault, a simplified generator model with the diode fault was built. The diode fault is detected if the outputs of the monitored generator match the outputs of generator model with the diode fault.

However, the method proposed in [16] suffers from several major flaws. First, the simplified generator model in [16] is unlikely to represent the real claw-pole generator very well under any operating conditions. Thus the modeling errors of the generator alone

can result in large residuals that may falsely trigger the fault alarms. Second, no electric load except for the battery is modeled in this method. The variations of the electric load in vehicles can change the generator output current considerably. Such variation in output current will also cause false alarms.

A similar approach was undertaken in [17] by the same authors to detect the faults at a higher level of the vehicle EPS system, such as the loose connection fault and the battery fault. However, the method still suffers from the same problems of modeling inaccuracies and electric-load variations. No experimental results were given for either of the methods [16, 17].

A different approach to the detection of belt slip was proposed in [20]. Instead of modeling the claw-pole generator using the state-space equations, the method utilized the linear input-output relationship of the field voltage and battery voltage (equivalent to the cable voltage drop or the load current) in the steady state to detect the belt-slip fault. An illustration of the linear relationship is shown in Figure 3.3.

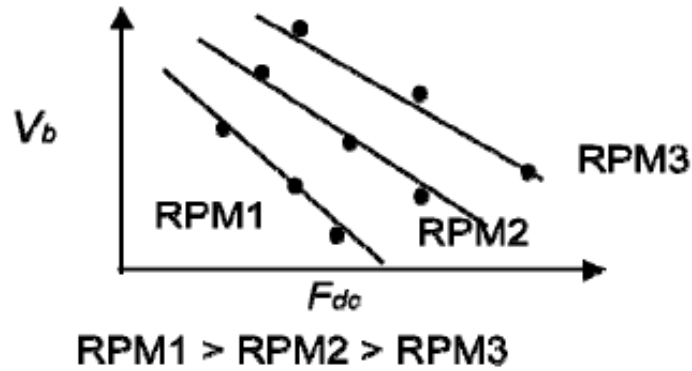


Figure 3.3: Illustration of the linear relationship between battery voltage V_b and field voltage F_{dc} for a given voltage set point [20].

One advantage of the method is that it requires only very low sampling rate. However, the disadvantage is that the method requires complicated calibrations of field

voltage and battery voltage under various operating conditions. Moreover, when the generator speed is low, the method may fail because the output of the voltage regulator may become saturated.

3.3 Detection of Internal Faults

The modeling of claw-pole generators with internal faults is usually much more difficult than the modeling of generators with only external faults. This is because internal faults have significant impact on the generators' electromagnetic structure, which necessitate major modifications to the detailed generator model and generator parameters.

To avoid the difficulty in modeling a faulty machine, neural networks (NNs) are employed to directly learn the mapping relationship between the fault symptoms and the fault types of claw-pole generators [22]. The faults investigated in [22] are as follows:

- (1) Stator-winding grounding fault and stator turn-to-turn fault
- (2) Rotor-winding one-point grounding fault, two-point grounding fault, and broken winding fault
- (3) Voltage-regulator short-circuit fault and open-circuit fault
- (4) Rectifier open-diode fault

To diagnose these faults in the claw-pole generator, the three-phase voltages, three-phase currents, field current and neutral-point voltage of the faulty generator are compared with those of a known healthy generator. The eight residuals are then compressed into 24 fuzzy-logic variables, which are fed to a neural network. The neural network used in [22] is a multi-layer-perception neural network (MLPNN) with one input layer, one hidden layer and one output layer. The simulation results demonstrate that the fuzzy neural network can diagnose the aforementioned types of generator faults.

However, the method is strictly an offline diagnostic method. Not only do some of the measurements (three-phase voltages and currents) difficult to access in an online environment, but the performance of the method is also heavily dependent on the training data available to the neural network. In a less controlled online environment, sufficient training of the neural network at various generator speed and load levels is not realistic.

In addition to aforementioned fault-detection schemes for claw-pole generators, some other methods are also proposed to monitor the condition of the entire automotive EPGS system. However, most of those methods emphasize on the condition monitoring of the battery, which is beyond the scope of this study.

3.4 Chapter Summary

This chapter reviews several methods to detect external and internal faults of claw-pole generators. Compared to the systematic research on the condition monitoring of conventional AC electric machines, the condition monitoring of claw-pole generators remains largely unexplored. One major reason is that the complicated claw-pole geometry makes it difficult to accurately model a faulty generator using conventional state-space equations. The other reason is that the built-in rectifier of the generator makes it difficult to access the three-phase voltage and current measurements that are essential in the condition monitoring of conventional AC electric machines.

The existing research on fault detection of claw-pole generator is very preliminary and few of the proposed condition-monitoring schemes have actually been validated by experiments. Nevertheless, the discussions in the literatures reveal useful information about the common failure modes of claw-pole generators, which is helpful for future research.

CHAPTER 4 Stator Turn-fault Detection for Induction Machines Fed by Closed-loop Inverter Drives

4.1 Overview

As discussed in Chapter 2, considerable amount of research have been done on the sensorless detection of stator turn-to-turn faults for induction machines in the past two decades. However, industry adoptions of these stator turn-fault detectors are still quite limited. The major hurdle lies in the implementation complexity of the methods. This problem becomes even more challenging for closed-loop inverter-fed induction motors, which have a much wider speed range than that of conventional grid-connected induction motors. Therefore, simple implementation is a crucial requirement of the proposed fault-detection scheme in this study.

The incipient stator turn fault can develop into serious stator winding failures or core failures in minutes or even seconds [30]. The fast-propagating nature of the stator turn fault requires that the proposed condition monitoring scheme is capable to detect the fault soon after it happens. Therefore, very fast real-time signal processing routine is required to achieve this goal.

In addition to above challenges, the closed-loop inverter connected to the induction motor also opens up new possibilities for advanced condition monitoring of electric machines. The onboard current sensors, the DC bus voltage sensor, and the DSP controller make it possible to integrate the condition monitoring algorithm as part of the normal control routine of the inverter. The capability to control the power switches freely also makes the active condition monitoring possible by injecting signals into the

machines. Therefore, the proposed method should take full advantage of closed-loop inverter to achieve improved condition monitoring performance.

4.2 Closed-loop Impact on Stator Turn-Fault Detection

The stator turn fault in a grid-connected induction motor typically introduces some asymmetry to the three phase windings and consequently gives rise to the negative-sequence current of the machine. This fault-induced negative-sequence current, combined with the positive-sequence voltage, results in small torque (speed) oscillations at twice the line frequency.

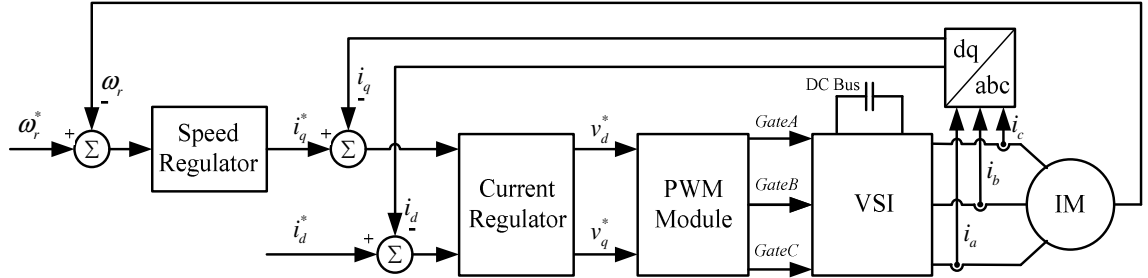


Figure 4.1: A simplified diagram of a closed-loop induction motor drive.

For closed-loop controlled induction motors, however, the effect of stator turn faults is quite different. As shown in Fig. 1, a typical closed-loop motor drive contains an outer, low-bandwidth speed-regulating loop, which generates a current (torque) command for the inner, high-bandwidth current-regulating loop. In most cases, the current regulator is implemented in the synchronous reference frame. Thus, the negative-sequence current will represent itself as a harmonic component at twice the stator frequency [56]. Generally, the speed oscillation caused by the incipient turn fault is very small because of the inertia of the motor and mechanical load. Moreover, the oscillating frequency is in most cases well above the bandwidth of the speed loop. Therefore, the stator turn fault is actually “invisible” to the speed loop of the motor drive. As a result, the output of the

speed regulator, which is the current (torque) command, is hardly affected by the stator turn fault.

The bandwidth of the inner current loop, on the other hand, is usually higher than the frequency of the negative-sequence current at twice the stator frequency for a reasonably well-tune current controller [56]. Ideally, if the current regulating effect is perfect, the actual current of the induction machine is forced to be exactly the same with the current command no matter the stator turn fault has occurred or not. That is, the current regulator will suppress any extra negative-sequence current induced by the stator turn fault. This important observation is the basic assumption of the proposed stator turn-fault detector and locator.

4.3 Proposed Method to Detect Stator Turn Fault

It is well known that the negative-sequence voltage of a healthy induction machine in steady state can be expressed by the equation as follows,

$$V_n^h = Z_{np} \cdot I_p + Z_{nn} \cdot I_n^h, \quad (4.1)$$

where superscript h indicates the machine is healthy. I_n and I_p are the negative- and positive- sequence currents. Z_{nn} is the negative-sequence impedance of the machine at a certain operating condition.

Ideally, if the machine and all measurement channels are perfectly symmetric, the transfer impedance (Z_{np}) from I_p to V_n should be zero. In reality, Z_{np} is never exactly zero due to the inherent asymmetry of the machine.

If a stator turn fault occurs in the induction machine, it will change the asymmetric behavior of the induction machine. This effect can be modeled by introducing another term ΔZ_{np} into the expression of the negative-sequence voltage [44],

$$V_n^f = (Z_{np} + \Delta Z_{np}) \cdot I_p + Z_{nn} \cdot I_n^f, \quad (4.2)$$

where superscript f indicates the machine has stator turn faults, and ΔZ_{np} is the change of the transfer impedance Z_{np} resulting from the fault. Note that equation (4.1) and (4.2) share the same I_p and Z_{nn} if their operating conditions are the same. In addition, all the quantities here are complex numbers, with phase angles referring to the same basis, typically the phase angle of the positive-sequence voltage.

Dividing equation (4.1) by I_n^h and dividing equation (4.2) by I_n^f yields,

$$\frac{V_n^h}{I_n^h} = \frac{Z_{np}}{I_n^h} \cdot I_p + Z_{nn}, \quad (4.3)$$

$$\frac{V_n^f}{I_n^f} = \frac{Z_{np} + \Delta Z_{np}}{I_n^f} \cdot I_p + Z_{nn}. \quad (4.4)$$

Eliminating Z_{nn} in equation (4.3) and (4.4) gives,

$$\frac{V_n^f}{I_n^f} - \frac{V_n^h}{I_n^h} = I_p \left(\frac{Z_{np} + \Delta Z_{np}}{I_n^f} - \frac{Z_{np}}{I_n^h} \right). \quad (4.5)$$

Finally,

$$\Delta Z_{np} + \left(1 - \frac{I_n^f}{I_n^h} \right) Z_{np} = \frac{V_n^f - V_n^h \frac{I_n^f}{I_n^h}}{I_p}. \quad (4.6)$$

Equation (4.6) is a fundamental relationship that can be utilized to detect the stator turn fault. The left-hand side of the equation contains the quantities that indicate the faulty conditions, and the right-hand side of the equation only consists of the quantities that can be directly monitored.

If an induction machine being monitored is still healthy, then the characteristic of the entire drive system is never changed. Therefore, $I_n^h = I_n^f$ and $V_n^h = V_n^f$. Equation (4.6) will collapse to $\Delta Z_{np} = 0$, which means no change in Z_{np} can be observed.

If a stator turn fault does occur in the induction machine, in general, there will be $I_n^h \neq I_n^f$ and $V_n^h \neq V_n^f$. Equation (4.6) therefore becomes

$$\Delta Z_{np} + \left(1 - I_n^f / I_n^h\right) Z_{np} = A \neq 0, \quad (4.7)$$

where A is the evaluated value of the right-hand side of equation (4.6).

For mains-fed induction machines, the non-zero value A does not offer much useful information because I_n^h can be easily different from I_n^f just due to the time-varying voltage unbalance conditions in the power grid. Thus, it is difficult to tell the true value of ΔZ_{np} from A . But for induction machines connected to closed-loop motor drives, according to the analysis in section 4.2, there will be $I_n^h \approx I_n^f$ even if stator turn fault occurs, which means $\left(1 - I_n^f / I_n^h\right) Z_{np}$ is always much smaller than ΔZ_{np} . Therefore, $\Delta Z_{np} \approx A$, i.e., the non-zero value A calculated from measurements is basically the change of Z_{np} .

To summarize, the stator turn fault in a closed-loop drive can be detected by evaluating the right-hand side of equation (4.6). If there is no stator turn fault,

$$\Delta Z_{np} = \frac{V_n^f - V_n^h \frac{I_n^f}{I_n^h}}{I_p} = 0. \quad (4.8)$$

If there is a stator turn fault,

$$\Delta Z_{np} \approx \frac{V_n^f - V_n^h \frac{I_n^f}{I_n^h}}{I_p} \neq 0. \quad (4.9)$$

Note that the proposed method monitors the fault signature ΔZ_{np} directly. Thus, it eliminates the complicated process to learn the inherent asymmetry (Z_{np}) of the healthy machine, which requires multiple sets of test data under different voltage unbalance conditions [44]. In contrast, the proposed fault detector needs only one set of baseline current and voltage measurements when the machine is healthy, greatly reducing the complexity of implementation. This is especially advantageous for drive-fed induction machines whose stator frequency and slip are both varying.

Moreover, if the slight difference between I_n^h and I_n^f is completely ignored, or if the magnitude of I_n^h and I_n^f are both very small to begin with, then equation (4.6) can be further simplified to,

$$\Delta Z_{np} = \frac{V_n^f - V_n^h}{I_p}. \quad (4.10)$$

Strictly speaking, equation (4.10) can be used only when the following condition is satisfied,

$$BW_{speed} \ll 2f_e \ll BW_{current}, \quad (4.11)$$

where BW_{speed} refers to the speed-loop bandwidth, $BW_{current}$ refers to the current-loop bandwidth and f_e refers to the stator frequency.

Equation (4.10) reveals the fact that it is the negative-sequence voltage that contains the most information of the stator turn fault for a closed-loop controlled induction machine. This observation agrees well with the opinions in [56]. However, method in

[56] only uses the magnitude of V_n as the fault indicator. Whereas equation (4.6) and (4.10) has inherently taken into account the phase difference of V_n^h and V_n^f , making itself a more reliable and sensitive turn-fault detector.

4.4 A Special Case of Multiple Motors Connected to a Single Closed-loop Inverter – Fault Location

In industrial applications such as steel processing, or in traction systems, a single closed-loop inverter is sometimes driving two or more parallel-connected motors to distribute the traction torque [75, 76], as shown in Figure 4.2.

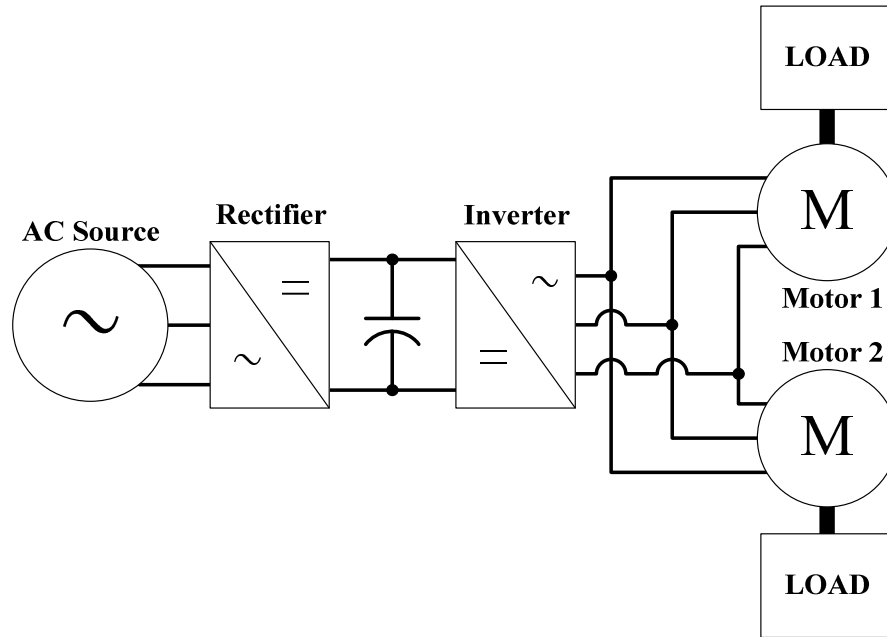


Figure 4.2: A torque-distribution scheme using multiple motors fed by a single closed-loop inverter.

This special arrangement of motors and inverters generally has a lower cost, smaller package size and lighter weight compared to a single-inverter, single-motor and mechanical-differential alternative [75, 76], as illustrated in Figure 4.3.

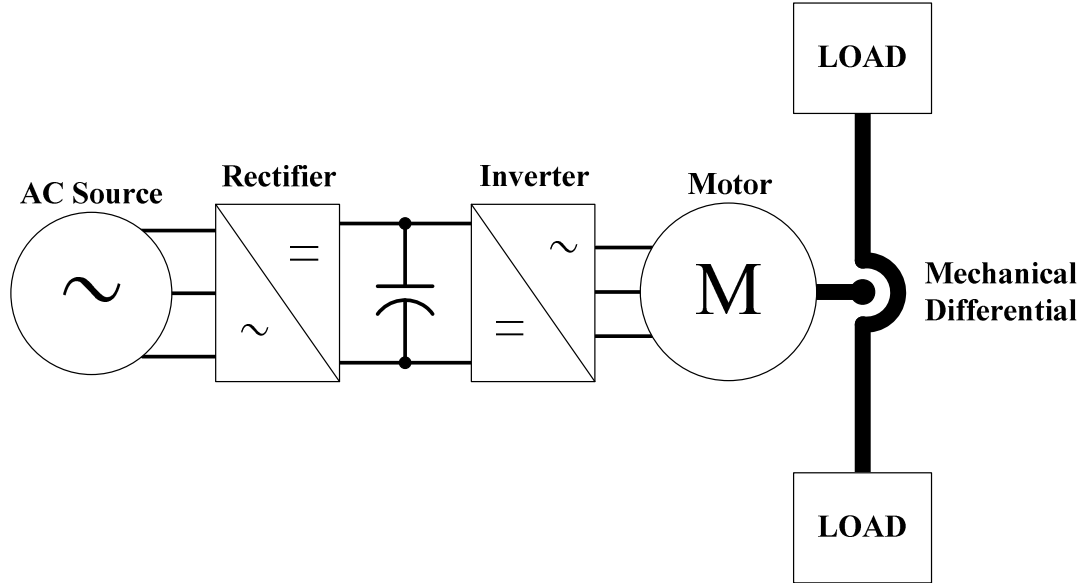


Figure 4.3: A torque-distribution scheme using a mechanical differential and a single large motor fed by a single closed-loop inverter.

For such a closed-loop multiple-motor drive in Figure 4.2, it is often not good enough to just tell whether there is a stator turn fault or not, but is also desirable to know which one of the multiple motors has the fault. This additional step is denoted as fault location in this study.

This section thus deals with the location of stator turn fault for such closed-loop multiple-motor drives. Whereas the proposed fault locator has rather specialized applications, the process to derive such fault locator sheds helpful insights into the fault behaviors of closed-loop controlled machines. The experimental results of the fault locator also further validate the analysis in section 4.3.

To locate the stator turn fault in a closed-loop multiple-motor drive, it is necessary to have independent current measurement for each parallel-connected machine. Fortunately, this is indeed the case for many high-performance closed-loop multiple-motor drives [75, 76]. Hence, no extra hardware is needed if the fault-locating feature is to be implemented

in these drives. For drives with only one set of current sensors that monitors the sum current of all the motors, the location of the stator turn fault is difficult unless additional current sensors are installed.

In case of a stator turn fault, the negative-sequence current flowing into the two individual machines will both change considerably. However, the underlying mechanisms for the current changes are quite different.

For the healthy machine, the change of I_n is solely caused by the change in V_n . Without losing any generality, let's assume Motor No. 1 is healthy, then

$$V_n^h = Z_{np1} \cdot I_{p1} + Z_{nn1} \cdot I_{n1}^h, \quad (4.12)$$

$$V_n^f = Z_{np1} \cdot I_{p1} + Z_{nn1} \cdot I_{n1}^f. \quad (4.13)$$

Note that the superscript f and h only denotes that the entire drive system has stator turn fault or not. Motor No. 1 is always healthy.

Subtracting equation (4.12) from (4.13) yields

$$\frac{V_n^f - V_n^h}{I_{n1}^f - I_{n1}^h} = Z_{nn1}. \quad (4.14)$$

Equation (4.14) is very useful. It shows how to obtain the negative sequence impedance of the healthy machine from voltage and current measurements.

For the machine with stator turn fault, however, the change of I_n is caused by a combination of the change of V_n and the change of Z_{np} , i.e.,

$$V_n^h = Z_{np2} \cdot I_{p2} + Z_{nn2} \cdot I_{n2}^h, \quad (4.15)$$

$$V_n^f = (Z_{np2} + \Delta Z_{np2}) \cdot I_{p2} + Z_{nn2} \cdot I_{n2}^f. \quad (4.16)$$

Subtracting equation (4.15) from equation (4.16) gives,

$$\frac{V_n^f - V_n^h}{I_{n2}^f - I_{n2}^h} = Z_{nn2} + \frac{\Delta Z_{np2} \cdot I_{p2}}{I_{n2}^f - I_{n2}^h}. \quad (4.17)$$

Compared to equation (4.14), equation (4.17) has a similar form on the left side of equation but has an extra term $\frac{\Delta Z_{np2} \cdot I_{p2}}{I_{n2}^f - I_{n2}^h}$ on the right due to the added stator turn fault.

Hence, $\frac{V_n^f - V_n^h}{I_{n2}^f - I_{n2}^h}$ will not yield the negative sequence impedance of the faulty machine.

The true value of $\frac{V_n^f - V_n^h}{I_{n2}^f - I_{n2}^h}$ can be obtained, again, by utilizing the relationship, $I_n^h \approx I_n^f$,

or,

$$I_{n1}^h + I_{n2}^h \approx I_{n1}^f + I_{n2}^f \quad (4.18)$$

$$I_{n1}^f - I_{n1}^h \approx -(I_{n2}^f - I_{n2}^h). \quad (4.19)$$

The left-hand side of equation (4.17) becomes,

$$\frac{V_n^f - V_n^h}{I_{n2}^f - I_{n2}^h} \approx -\frac{V_n^f - V_n^h}{I_{n1}^f - I_{n1}^h}. \quad (4.20)$$

Considering equation (4.14), equation (4.20) finally becomes,

$$\frac{V_n^f - V_n^h}{I_{n2}^f - I_{n2}^h} \approx -Z_{nn1}. \quad (4.21)$$

The result given by equation (4.21) is very interesting. It reveals the fact that no matter how severe the stator turn fault is, the value of equation (4.21) only depends on the negative sequence impedance of the healthy machine Z_{nn1} . While the impedance Z_{nn1} may vary with the operating conditions of the induction machine, it is always resistive and inductive.

The above analysis leads to the design of a simple yet reliable fault locating algorithm: once a stator turn fault is detected in a multiple-motor drive, the expression $(V_n^f - V_n^h)/(I_n^f - I_n^h)$ can be evaluated for every single machine. Then if the evaluated result lies in the first quadrant of the complex plane, the machine is healthy. If the evaluated result turns out to be abnormal, lying in the third quadrant of the complex plane, the machine has stator turn faults.

Since $(V_n^f - V_n^h)/(I_n^f - I_n^h)$ typically yields the negative sequence impedance for a healthy machine, this fault-locating method is denoted as Z_{nn} evaluation method for short in the following sections.

4.5 Signal Processing Techniques

4.5.1 A Post-processing Workflow for the Lab

Proper signal processing is vital to ensure the high sensitivity and short response time of the stator turn-fault detector and locator. To validate the proposed method in the lab, the signal processing follows a post-processing fashion. Figure 4.4 shows a workflow that extracts the positive- and negative- sequence components from the three-phase current measurements. The three-phase voltages are processed in a similar approach.

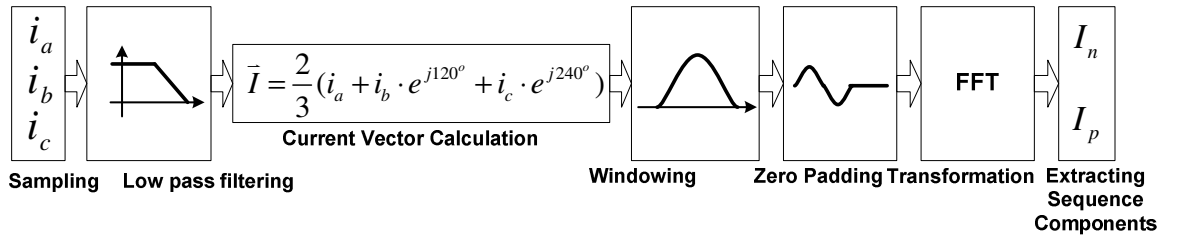


Figure 4.4: Signal processing workflow to extract sequence components.

As shown in Figure 4.4, the three-phase currents are first sampled at 5000 Hz. Then the current samples are passed through a second-order digital low-pass filter with a cut-off frequency of 1000 Hz, eliminating any aliasing distortion in the sampled current data. The filtered three-phase currents are used to calculate the current space vector,

$$\bar{I} = \frac{2}{3}(i_a + i_b \cdot e^{j2\pi/3} + i_c \cdot e^{j4\pi/3}). \quad (4.22)$$

It has been shown in [77] that the discrete Fourier transform (DFT) of the current space vector \bar{I} can automatically separate the positive- and negative- sequence currents for all frequency components. This feature is very useful in the sequence-component analysis of drive-fed machines whose stator frequency is not exactly known. In other words, DFT of \bar{I} not only locates the stator frequency but also separates the sequence components simultaneously.

The length of the signal being processed each time is an important design trade-off for the turn-fault detector. With longer signal duration, the sequence components can be extracted more accurately. But this results in slower response of the detector. In the experiment, the signal is processed in the block of roughly 5 cycles of current waveforms, or 0.25 s when the motor speed is 600 rpm and 0.5 s when the speed is 300 rpm.

Before applying DFT to the current space vector, it is necessary to window the current signal first to reduce the leakage effect. In this study, a Blackman window is used. As mentioned earlier, the sampling duration is about 0.25~0.5 seconds. If the sampled data are transformed to frequency domain directly, the resolution of the current spectrum will be about 2~4 Hz. This frequency resolution is not good enough to accurately locate the fundamental frequency. Hence, the complex current signal is zero padded by a multiple of 32~64 in this experiment. Since zero padding is equivalent to band-limited

interpolation in the frequency spectrum, the fundamental frequency can therefore be located more accurately.

Figure 4.5 shows an example of an experimental current spectrum given by the above signal processing routine. The positive-sequence current is located at 10.11 Hz with a magnitude of 20.45 dB. Hence, the negative-sequence current must be at -10.11 Hz and its magnitude is -24.88 dB. The phase angles of positive- and negative- sequence current can be extracted in a similar fashion from the phase spectrum.

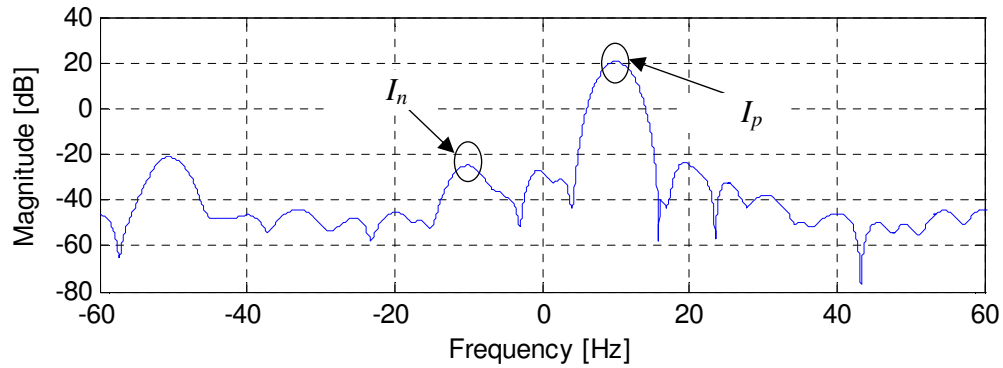


Figure 4.5: A magnitude spectrum of the current space vector.

The signal processing workflow for the three-phase voltages is almost exactly the same with that of the currents described above. The only difference lies in the calculation of the voltage space vector. The voltage space vector is defined as,

$$\bar{V} = \frac{2}{3}(v_{an} + v_{bn} \cdot e^{j2\pi/3} + v_{cn} \cdot e^{j4\pi/3}). \quad (4.23)$$

In practice, however, the terminal-to-neutral voltages v_{an} , v_{bn} and v_{cn} are hardly accessible for a 3-wire machine. Thus equation (4.23) is rewritten as,

$$\bar{V} = \frac{2}{3}[(v_{an} - v_{cn}) + (v_{bn} - v_{cn}) \cdot e^{j2\pi/3} + (v_{cn} - v_{cn}) \cdot e^{j4\pi/3}], \quad (4.24)$$

which yields a very simple result as,

$$\bar{V} = \frac{2}{3}(v_{ac} + v_{bc} \cdot e^{j2\pi/3}). \quad (4.25)$$

Hence, the voltage space vector can be obtained using any two measurements of line-to-line voltage.

4.5.2 Goertzel Algorithm for Real-time Implementations

The above signal processing scheme employs zero-padded FFT to determine the stator frequency and extract sequence components. However, such calculations may be difficult to implement in real time due to the limited computational capability of the digital signal processors in many motor drives.

Fortunately, virtually all motor drives know exactly what the stator frequency is. Hence, there is no need to calculate the entire voltage or current spectrum but only several spectral bins.

To identify the frequency components in a signal at predetermined frequencies, the definition of DFT can be directly used. But a more delicate approach is to use the Goertzel algorithm, which calculates the DFT bins as recursive difference equations [78],

$$s(n) = x(n) + 2\cos(2\pi\omega)s(n-1) - s(n-2), \quad (4.26)$$

$$y(n) = s(n) - e^{-2\pi i\omega}s(n-1), \quad (4.27)$$

where $x(n)$ is the input signal in time domain, ω is frequency of interest, in cycles per sample, $s(n)$ is an intermediate sequence and $y(n)$ is the DFT bin at the frequency ω .

By setting the frequency ω at exactly the positive or negative of the stator frequency, I_p and I_n can be calculated with no need for zero-padding as that in Figure 4.5. Moreover, since the Goertzel algorithm updates the estimation of the DFT bin recursively at each time step, it can be easily integrated into the existing control routine of the motor drive

with trivial computational effort and virtually no additional memory requirement.

Figure 4.6 shows a current spectrum given by the proposed real-time signal processing routine. The two DFT bins calculated by the Goertzel algorithm match the results in Figure 4.6 perfectly.

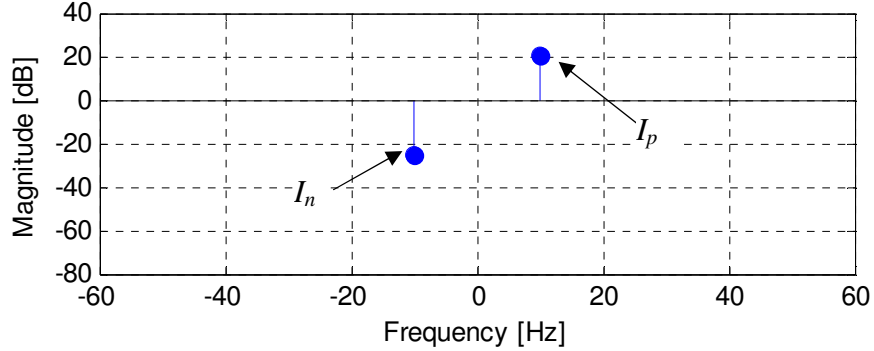


Figure 4.6: DFT bins of the current space vector calculated by Goertzel Algorithm.

4.6 Experimental Validation on Commercial Closed-loop Inverter

4.6.1 Experimental Setup

Figure 4.7 shows a special test bench which is custom made for experimentally validating the stator turn-fault detection method for closed-loop induction motor drives as well as the fault location method for closed-loop multiple-motor drive.

Two identical induction motors (5, 6), whose ratings and parameters are summarized in Table 4.1, are supplied by a commercial closed-loop inverter drive (2). A customized test bed (3) is built to couple the shafts of both motors and transfer the motoring torque to the mechanical load, a DC generator (8), through a transmission belt (4). The field winding of the DC generator is connected to a 120 V DC voltage source (7) and generated power is dissipated on a resistor bank (9). The three-phase voltages and currents of both machines are monitored by two sensor boards (10, 11). The measured

signals are then passed on to the computer through a NI data acquisition device (12). Finally, a LabVIEW program (13) running on the computer monitors and records the voltage and current waveforms.

In the experiment setup, the separate current measurements of both motors are just for validating the fault-location method. Only the sum current is used for fault detection.

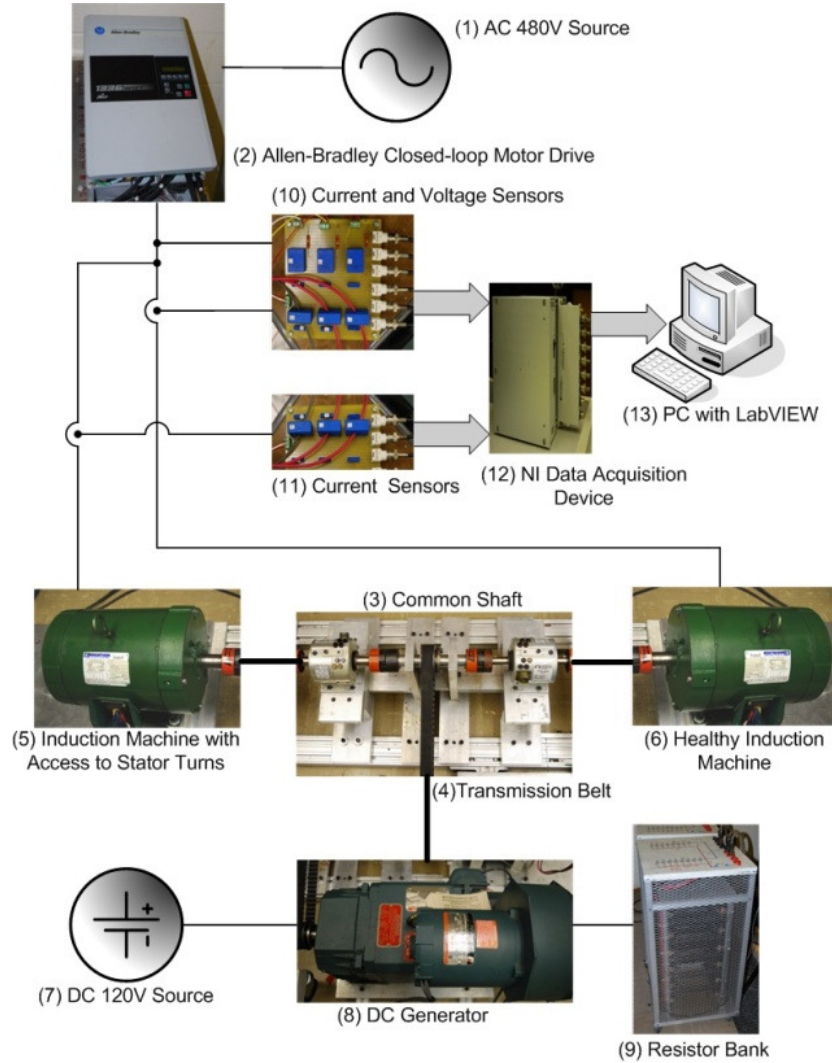


Figure 4.7: Experimental setup for validating stator turn-fault detection and location in a closed-loop multiple-motor drive.

In order to induce a stator turn-fault, one of the induction machines (5) is modified such that four adjacent turns of the stator winding are attached with taps, which are then

brought outside stator housing. The four taps are numbered 1, 2, 3 and 4 respectively. Any two of them can be shorted through a 50-A/50-MV fuse to create a stator turn fault. A short circuit of tap 1 and 2 is denoted as a 1-turn fault. A short circuit of tap 1 and 4, on the other hand, is a more severe 3-turn fault.

Table 4.1: Parameters and ratings of the test machine for stator turn-fault detection

Parameter	Value
P_{rated}	5 (hp)
$Poles$	4
V_{rated}	230 (V)
I_{rated}	12.4 (A)
$N_{m,rated}$	1745 (rpm)
R_s	0.47 (ohm)
R_r	0.33 (ohm)
L_m	73.1 (mH)
L_{ls}	2.5 (mH)
L_{lr}	3.8 (mH)
No. of turns per phase	Two parallel windings each with 108 turns

To prevent the shorted turns from overheating, the drive is running well below its nominal speed in the experiment. For 1-turn fault, the drive is running at a maximum of 600 rpm. For 2-turn and 3-turn fault, the drive is running only at a maximum of 300 rpm. In this way, the output voltage of the drive is well below its nominal value. Thus the circulating current in the shorted turns is always kept within 3 times of the motor rated current.

The motor drive in Figure 4.7 is a commercial Allen-Bradley 1336 drive operating in field-oriented control. The bandwidth of the speed loop is set to the maximum achievable value, or 30 rad/s (4.78 Hz). Still the bandwidth of the speed loop is far lower than the frequency of the torque oscillation, which is about 20 Hz when the motor is running at 300 rpm.

4.6.2 Experimental Results

The detection and location of the stator turn fault in a multiple-motor drive system involve two stages. In the first stage, all the sequence components, such as V_p , V_n , I_p and I_n (I_{p1} , I_{p2} , I_{n1} and I_{n2} if the fault are also to be located), are calibrated for different operating conditions when the drive is known healthy. In the second stage, the condition of the drive is being continuously monitored and compared with the calibrated values using the aforementioned techniques. The calibrated operating conditions and induced fault levels are summarized in Table 4.2.

Table 4.2: Operating conditions and fault levels considered in the experiment

Speed (rpm)	Load	Induced Faults
300	Zero load	Healthy, 1-turn, 2-turn, 3-turn
300	0.03 slip	Healthy, 1-turn, 2-turn, 3-turn
600	Zero load	Healthy, 1-turn
600	0.03 slip	Healthy, 1-turn

A. Fault Detection

Before calculating the ΔZ_{np} , it is worthwhile taking a look at how the stator turn fault actually impacts the extracted sequence components of voltage and current.

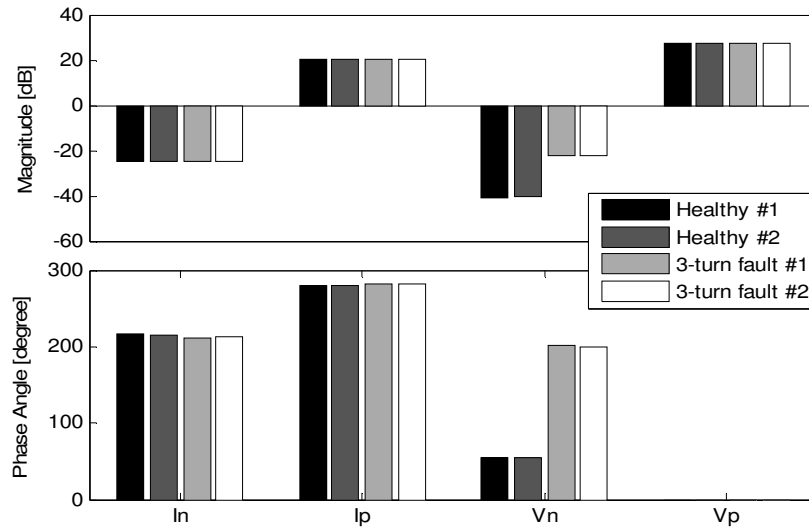


Figure 4.8: A comparison of extracted sequence components from various tests.

Figure 4.8 shows four sets of current and voltage sequence components when the multiple-motor drive is running at 300 rpm with no mechanical load. Among the four sets of measurements, two of them are taken when the motors are healthy and the other two are taken when one of the motor has a 3-turn fault. The magnitude and phase angle of the total negative-sequence current of the induction machines only changes slightly after the stator turn fault occurs. On the contrary, both the magnitude and phase angle of the negative-sequence voltage have changed substantially as a result of the stator turn fault. This observation experimentally validates the theoretic analysis that the regulating effect of closed-loop drive will keep the negative-sequence current almost unchanged.

The experimental result for fault detection is shown in Figure 4.9. The estimated ΔZ_{np} from equation (4.6) are plotted in the complex plane for various operating conditions and fault levels.

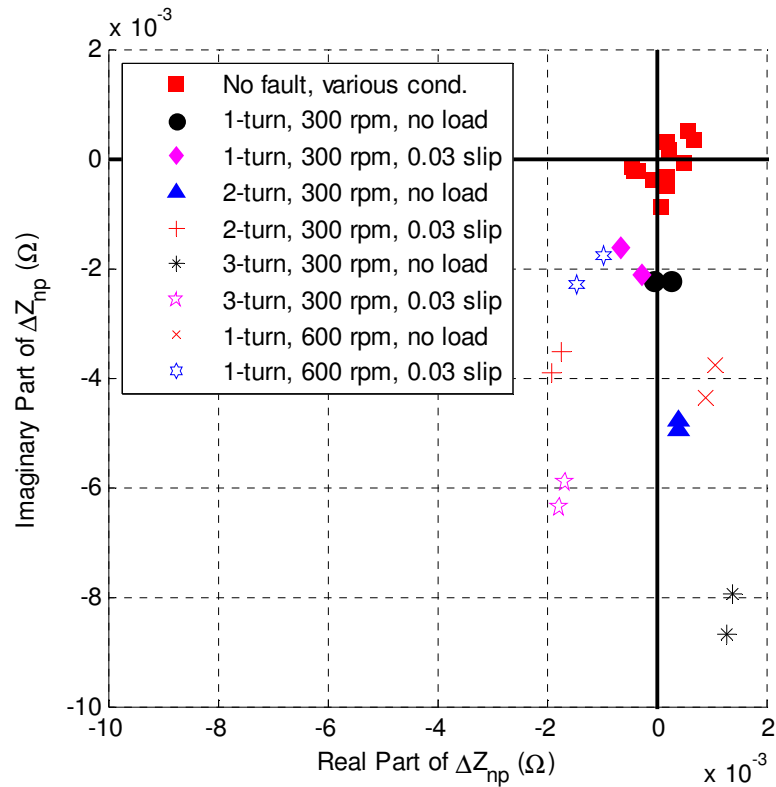


Figure 4.9: Scatter plot of ΔZ_{np} at different operating conditions and fault levels.

As can be seen from Figure 4.9, when the drive is healthy, the corresponding ΔZ_{np} is within the vicinity of the origin. For all the other faulty cases, the ΔZ_{np} obviously deviate from the origin of the complex plane, clearly indicating the existence of the stator turn fault. Figure 4.9 not only separates the faulty conditions from the healthy conditions, but it also reveals several interesting facts as follows:

The magnitude of ΔZ_{np} increases as the stator turn fault becomes more severe. This result is not surprising since 1-turn fault generally creates less amount of asymmetry than the 3-turn fault does.

As the load level goes up, the phase angle of ΔZ_{np} tends to decrease and the magnitude of ΔZ_{np} generally becomes smaller. This result agrees well with the simulation result in [44] and is backed by the theoretic analysis in [79].

Moreover, the magnitude of ΔZ_{np} also increases with the motor speed. The 1-turn fault at 600 rpm yields larger magnitude of ΔZ_{np} than it does at 300 rpm. This is because higher motor speed usually means higher output voltage of the inverter drive. As a result, the circulating current in the shorted turns will become larger, which gives rise to the level of asymmetry of the stator winding. However, even when the motor speed is merely 300 rpm and there is only 1 out of 432 turns (216 turns per phase per machine) being shorted per phase, the detecting scheme still has no problem separating the fault from normal operating conditions.

B. Fault Detection

The fault-location method is first tested when the multiple-motor drive is running at 300 rpm with a slip of 0.03. The negative-sequence impedances of the two individual

machines are evaluated using the expression $(V_n^f - V_n^h)/(I_n^f - I_n^h)$ for all different fault levels, as shown in Figure 4.10. Again, Motor 2 is induced with stator turn faults.

In Figure 4.10, $(V_n^f - V_n^h)/(I_{n1}^f - I_{n1}^h)$ of the healthy machine all lie in the first quadrant of the complex plane. $(V_n^f - V_n^h)/(I_{n2}^f - I_{n2}^h)$ of the faulty machine all lie in the third quadrant, approximately symmetric with $(V_n^f - V_n^h)/(I_{n1}^f - I_{n1}^h)$ with respect to the origin of the complex plane. This observation verifies the theoretical derivation of equation (4.21). Figure 4.10 also verifies that different fault levels do not have a notable influence on the estimated negative-sequence impedance. The estimated Z_{nn1} of the healthy machines is approximately $0.5 + j0.4 \Omega$, which agrees reasonably well with the value calculated using the machine parameters in Table 4.1, about $0.64 + j0.40 \Omega$.

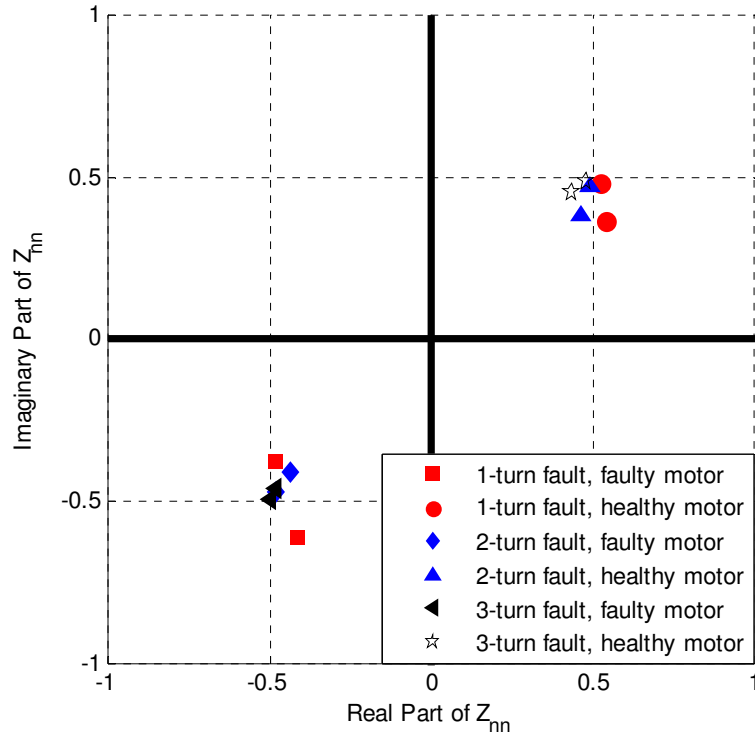


Figure 4.10: Scatter plot of Z_{nn} at 300 rpm and 0.03 slip with various fault levels.

A similar diagram can be drawn for other operating conditions as well. Figure 4.11 shows the fault-locating results still at the same 300 rpm but with zero load torque. In this plot, $(V_n^f - V_n^h) / (I_{n2}^f - I_{n2}^h)$ of the faulty machine are in the third quadrant of the complex plane, roughly symmetric with $(V_n^f - V_n^h) / (I_{n1}^f - I_{n1}^h)$ of the healthy machine. The estimated Z_{nn1} of the healthy machine, however, have changed from $0.5 + j0.5 \Omega$ to about $0.5 + j0.9 \Omega$. This is because at no load condition, the slot leakage path of the machine is less saturated by the relatively small positive-sequence current. Consequently, the inductance part of Z_{nn1} becomes larger. This phenomenon is especially obvious for small induction machines which typically have narrow slot openings.

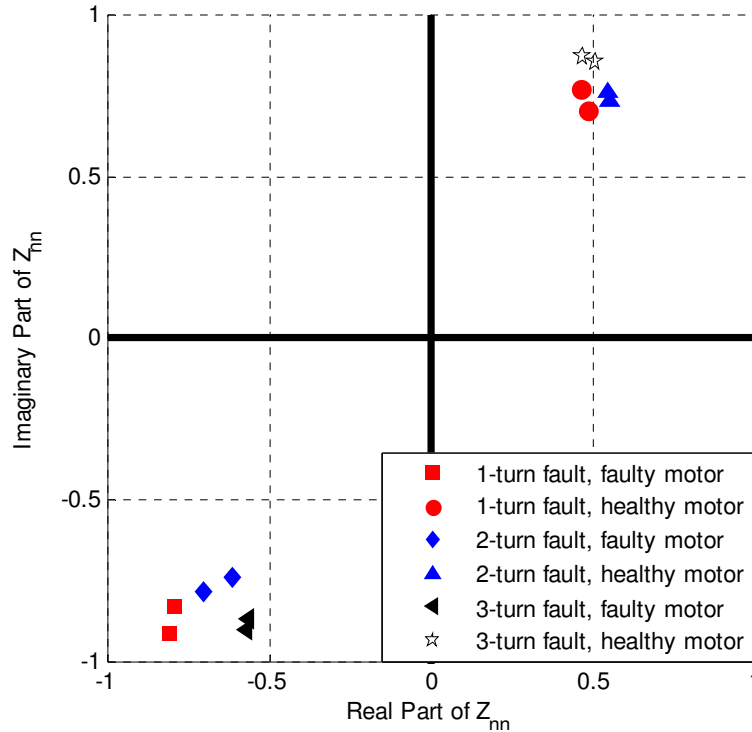


Figure 4.11: Scatter plot of Z_{nn} at 300 rpm and no load with various fault levels.

When the motor speed is increased to 600 rpm, the faulty machine can still be separated from healthy one, as shown in Figure 4.12. Since the stator frequency has

increased, the estimated Z_{nn1} of the healthy machines is now about $0.7 + j1.4 \Omega$ for no load condition and about $0.7 + j0.8 \Omega$ when the slip is 0.03.

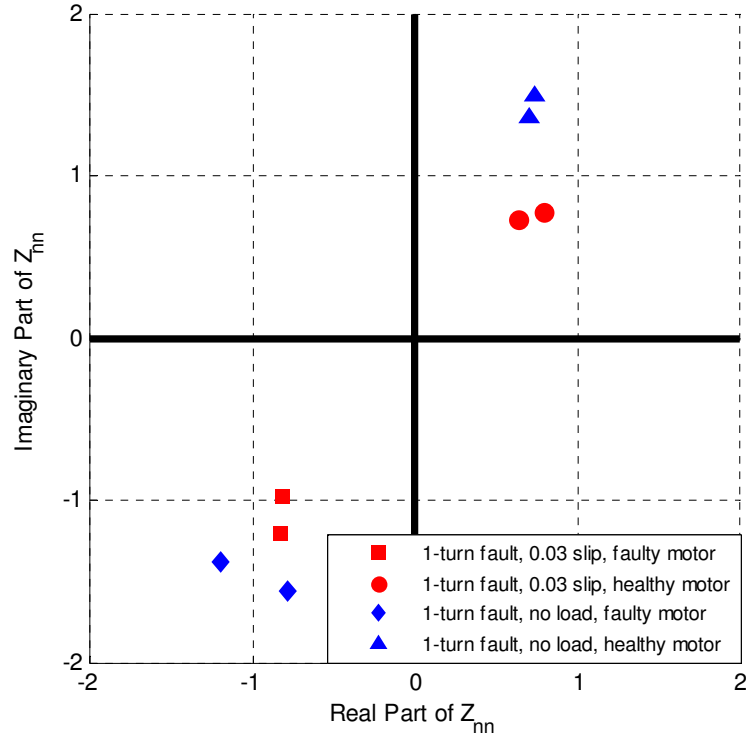


Figure 4.12: Scatter plot of Z_{nn} at 600 rpm and various load levels with 1-turn fault.

4.7 Practical Considerations for Real-time Implementation

Several practical aspects still need to be considered so that the above stator turn-fault detector can be successfully implemented in real time in a closed-loop induction motor drive.

4.7.1 Terminal Voltage Estimation

The proposed stator turn-fault detector requires terminal voltages of the induction machine fed by the closed-loop inverter. Those voltages are simply measured by voltage sensors in section 4.6. However, typical induction motor drives have no terminal voltage measurements but only a voltage sensor that measures the DC bus voltage. In this case,

the three-phase terminal voltages can be estimated using the commanded duty cycles and the measured DC bus voltage. Non-ideal behaviors of inverters, such as the dead time, the switching device voltage drop, and the switching device turn-on/off delay, can be properly compensated using the method described in detail in section 5.4. The compensation for those inverter nonidealities greatly improves the accuracy of the terminal voltage estimation and therefore improves the sensitivity of the stator turn-fault detector.

4.7.2 Bandwidth of the Current Controller

As stated in section 4.2 and 4.3, the very basic assumption of the proposed method is that the current controller can suppress any negative-sequence current of the induction machine even if there is a stator turn fault. This assumption holds very well for the specific inverter and the induction machine used in the experiment, as evidenced by Figure 4.8.

However, given many different types of closed-loop inverters and induction machines for various applications, there might be rare cases that the natural bandwidth of the current controller does not reach twice the stator frequency at certain speeds of the induction machine. In those scenarios, the current controller may not be able to fully suppress the negative-sequence current, which may result in deteriorated performance of the stator turn-fault detector.

An active negative-sequence-current suppressor can be implemented in the inverter controller to completely eliminate this concern. For field-oriented controlled induction machines, for example, the current controller is normally implemented in the synchronous rotating reference frame. The negative-sequence current thus exhibits itself

as current oscillations at twice the stator frequency in this reference frame. However, in a reference frame that rotates at the synchronous speed but in the opposite direction, the negative-sequence current become DC. Therefore, another pair of current controllers implemented in the reverse-rotating synchronous reference frame can easily suppress any remaining negative-sequence current regardless the speed of the induction motor. A diagram of the proposed negative-sequence-current suppressor is shown in Figure 4.13. In addition to the normal current control loop, the function blocks in the red box make up the optional negative-sequence current suppressor.

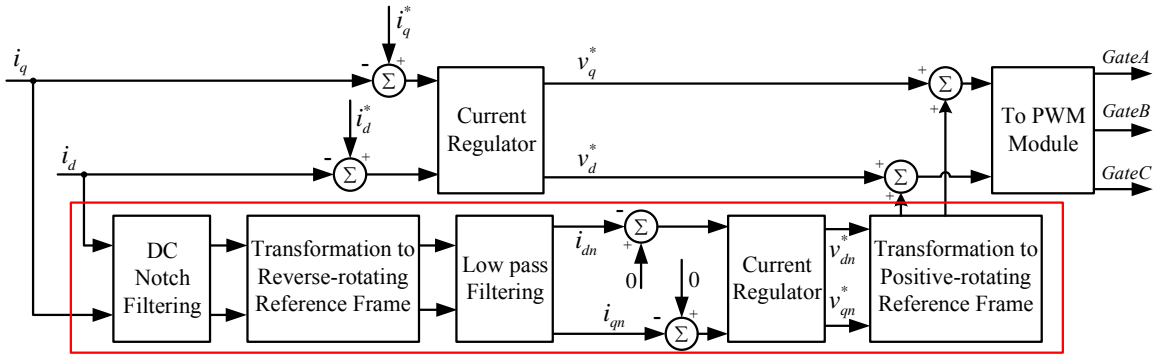


Figure 4.13: Current controller enhanced with negative-sequence-current suppressor.

Specifically, a simple DC notch filter is used to remove DC currents in the synchronous reference frame. This is equivalent to eliminate the positive-sequence current. After the notched currents are transformed to the reverse-rotating reference frame, a low-pass filter is used to extract the small DC components, which is equivalent to the negative-sequence current. A pair of current controllers is then used to drive these small DC components to zero.

4.7.3 Real-time Implementation

To demonstrate the feasibility of the method in terms of real-time implementation, a programmable inverter drive was designed and built. Two photographs of the inverter are

shown in Figure 4.14. The inverter has a quite standard setup of the power stage, consisting of a front-end rectifier, a DC-link capacitor, a choker inductor, and three standard IGBT bridges.

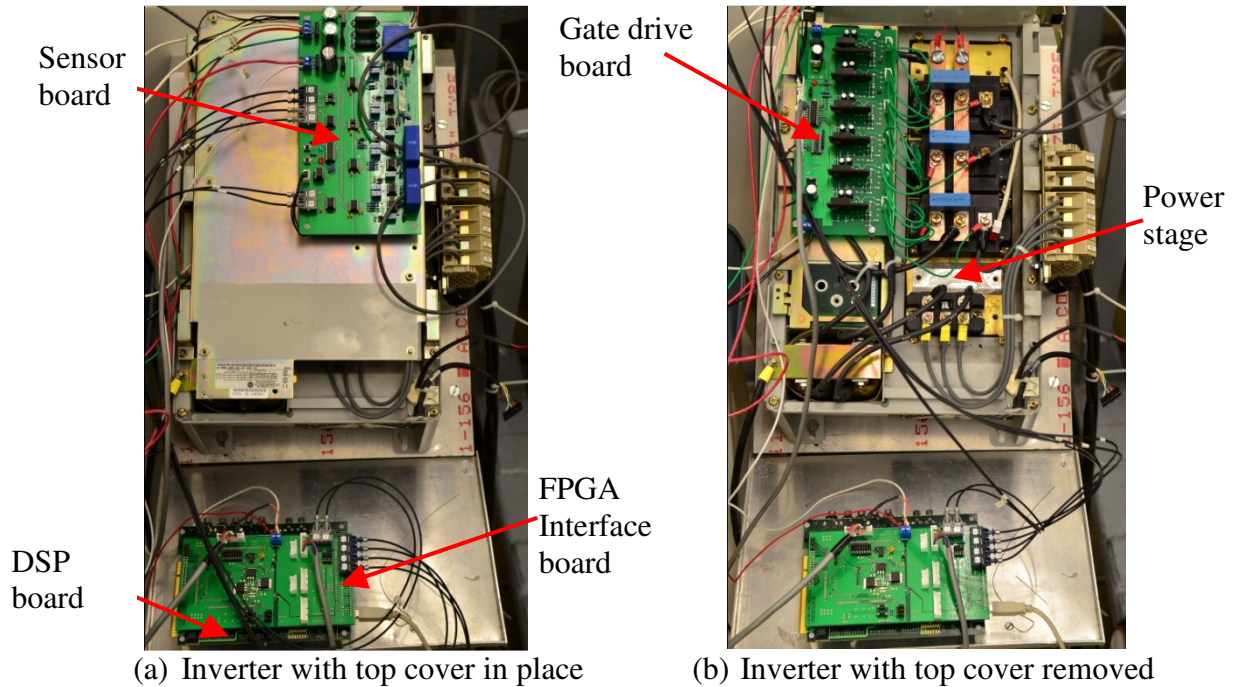


Figure 4.14: Photographs of the inverter built for validating real-time condition monitoring methods of electric machines.

The control architecture of the inverter is shown in Figure 4.15, which includes the DSP board, the FPGA interface board, the gate drive board, and the sensor board. The DSP board is a commercial ADSP-21369 evaluation board by Analog Devices©. It serves as the main processing power of the inverter. The main clock frequency of this DSP is 450 MHz. Directly mated with the DSP board is an interface board using Xilinx Spartan-3 FPGA, which handles routine tasks such as translating duty cycles from the DSP into actual gate signals, translating pulses from the speed encoder into the speed measurement, and translating serial data from the sensor board into parallel data. The gatedrive board amplifies the gate signals from the FPGA interface board and drives the

IGBT switches. Two inverter output currents and the DC link voltage are measured by the sensor board and converted into serial digital signals, which are then sent back to the FPGA interface board via optical fibre links.

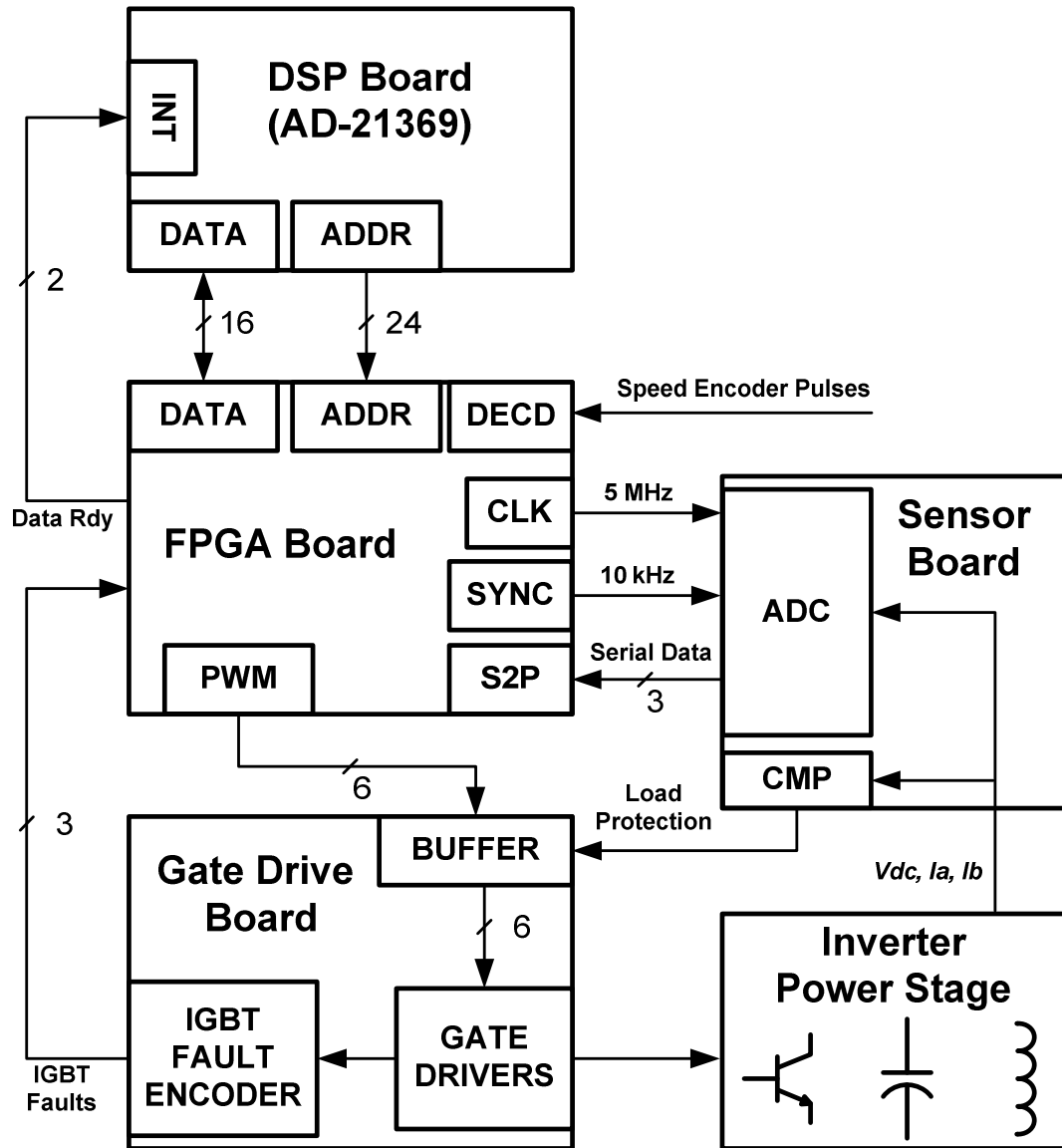


Figure 4.15: Control architecture of the inverter built for validating real-time condition monitoring methods of electric machines.

Each measurement channel employs a 12-bit A/D converter. The inverter runs at 10-kHz PWM frequency, and the duty cycle can be varied from 0 to 1 with the increment of

1/2000. An indirect field-oriented control scheme is implemented in the inverter drive with space-vector modulation (SVM). The proposed stator turn-fault detector is integrated in real time in the control algorithm using the signal processing technique described in section 4.5.2.

The real-time test results verify that the proposed stator turn-fault detector is highly computationally efficient. The entire motor controller and fault detector only takes up about 6 percent of the total computational capability of the DSP.

Some samples of the test results are shown in Table 4.3 to demonstrate the feasibility of the real-time stator turn-fault detector. Data in Table 4.3 are acquired when the induction motor is running at 900 RPM. The first two columns summarize the sequence components given by the motor controller when the induction motor is healthy. The last two columns show the sequence components given by the motor controller when the induction motor has a 1-turn fault.

Table 4.3: Sequence components extracted by the inverter controller in real time.

Sequence Component	No Fault #1	No Fault #2	1-turn Fault #1	1-turn Fault #2
$ I_n , A$	0.00277	0.00317	0.00168	0.00216
$\angle I_n^\circ$	121.5	39.3	-79.3	25.72
$ I_p , A$	11.51	11.47	11.59	11.56
$\angle I_p^\circ$	-34.87	-34.96	-34.62	-34.67
$ V_n , V$	0.1022	0.1185	0.1545	0.1865
$\angle V_n^\circ$	-82.92	-93.25	-121.40	-123.85
$ V_p , V$	74.54	74.54	74.33	74.42
$\angle V_p^\circ$	0	0	0	0

With the negative-sequence-current suppressor proposed in 4.7.2, the inverter shows very good performance in rejecting any negative-sequence current. No matter there is

fault or not, the amplitude of the negative-sequence current is always regulated below 4 mA. By compensating for inverter nonidealities, the negative-sequence voltage estimation is also accurate and consistent. The magnitude and phase angle of the negative-sequence voltage with fault is found to be clearly different from those without fault.

The experimental results given by the real-time stator turn-fault detector is similar to those obtained from the commercial closed-loop inverter. Therefore, they are not repeated in this section.

4.8 Chapter Summary

This chapter has proposed a highly sensitive stator turn-fault detector based on monitoring ΔZ_{np} of induction machines fed by closed-loop motor drives. The method is different from existing techniques in the sense that it has taken advantages of the current regulating effect of the motor controller to eliminate the learning process of machine inherent asymmetry. For multiple-motor drives, a fault-locating method has also been derived by carefully analyzing the interactions of multiple parallel motors in the presence of the stator turn fault. The limitation of the fault locator is that it requires independent current measurement of each machine.

The proposed stator turn fault detector and locator have both been validated through experimental testing. The main advantages of the proposed methods are as follows,

- (1) Sensitive: 1-turn stator fault can be reliably detected and located, even when the motor speed is as low as 300 rpm and there are as many as 216 turns per phase.
- (2) Fast: Faults can be detected and located in 5 cycles of fundamental waveform.

(3) Simple: Only one set of calibrations is required when the motors are known healthy. There is no need to vary the amount of voltage unbalance to learn the inherent asymmetry of the induction machine.

(4) Robust: The method is immune to inherent asymmetry in the motors and measurement channels.

The feasibility of implementing the stator turn-fault detector in real time in a closed-loop inverter is also discussed and tested. Some practical aspects are considered, including real-time signal processing technique, accurate terminal voltage estimation despite inverter nonidealities, and improved current control performance in suppressing negative-sequence current. The real-time experimental results show that the method is suitable for real-time implementation.

CHAPTER 5 Stator Thermal Monitoring for Induction Machines Fed by Closed-loop Inverter Drives

5.1 Overview

In addition to the above method that detects a solid stator turn fault, it is also desirable to monitor the health of the stator insulation even before a solid short circuit occurs. The thermal overload of electric machines is a major root cause to stator insulation degradation. Accurate stator thermal monitoring can prevent the machine from being thermally overloaded and thus alleviate the degradation of stator insulation [59-67]. At the same time, accurate stator temperature information also helps to boost the availability and performance of the overall drive system without being too conservative on the motor temperature.

As discussed in Chapter 2, the DC-injection-based stator temperature estimator has many advantages over the conventional thermal-model-based stator temperature estimators for AC electric machines. Over the last decade, several methods have been reported using the DC signal injected by external circuits [65] or soft starters [59] to estimate the stator winding temperature of the induction machines. However, the method has not yet been successfully extended to inverter-fed induction machines. The lack of direct terminal-voltage measurement poses the biggest challenge for stator temperature monitoring of induction motors fed by closed-loop inverter drives.

The thermal monitoring scheme proposed in this chapter overcomes this difficulty. The principle of the method is explained below and is also validated by simulation and experimental results.

5.2 Principle of Stator Winding Temperature Estimation

Figure 5.1 shows a typical closed-loop motor drive which contains an outer, low-bandwidth speed-regulating loop, which generates the current (torque) command for the inner, high-bandwidth current-regulating loop.

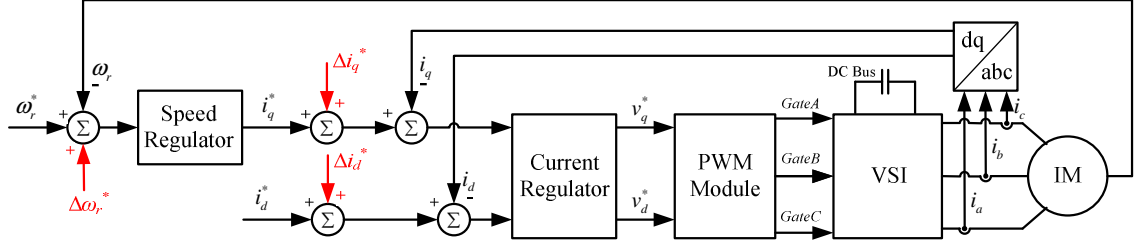


Figure 5.1: A simple method to inject DC current into induction motors fed by closed-loop inverters.

DC currents can be injected into the three-phase winding of the induction machine by superimposing a sine-wave component onto the current command i_d^* and i_q^* ,

$$\Delta i_d^* = I_{dc} \cos \theta, \Delta i_q^* = -I_{dc} \sin \theta, \quad (5.1)$$

where θ is the transformation angle of the d-q reference frame. For field-oriented controlled induction machines, θ is typically chosen as the angle between the rotor flux linkage and phase-A winding.

If the current controller has enough bandwidth to enforce such additional current components, then the following DC currents will be injected into the motor's windings,

$$\Delta i_a = I_{dc}, \Delta i_b = -0.5 I_{dc}, \Delta i_c = -0.5 I_{dc}, \quad (5.2)$$

Note that DC current cannot be injected by superimposing a sine-wave component onto the voltage command v_d^* and v_q^* , because the injected voltage reference will be quickly canceled out by the high-bandwidth current control loop. The proposed DC

current injection does not require any direct switch-level interference by the motor controller, which makes it easy to implement.

The injected DC current will inevitably produce a torque pulsation at the machine's electrical frequency. The torque oscillation can be minimized by choosing a relatively small DC current level. Moreover, due to the low-pass filtering effect of the motor mechanical inertia and the typically limited bandwidth of the speed control loop, the speed controller is not able to counteract the injected DC currents. Therefore, the effectiveness of the DC current injection is not affected. In rare cases, if the mechanical inertia of the machine and the load is relatively small and the bandwidth of the speed control loop is sufficiently high, the injected current offset could be attenuated or even canceled out by the speed controller. In this case, a small sine-wave component can be added to the speed reference to induce an oscillating i_q^* , thereby still realizing the DC current injection.

$$\Delta\omega_r^* = \omega_0 \sin \theta, \quad (5.3)$$

Once the currents in equation (5.2) have been injected into the motor's winding, the DC stator resistance can be calculated as,

$$R_s = \frac{2}{3} \cdot \frac{V_{ab}^{dc}}{I_a^{dc}}, \quad (5.4)$$

where V_{ab}^{dc} and I_a^{dc} are the DC components of v_{ab} and i_a respectively. i_a can be readily obtained from phase-current measurement. v_{ab} , on the other hand, is generally not directly measured but can be indirectly synthesized from the PWM duty cycles and the DC-link voltage measurement. Both the current sensors and DC bus voltage sensors are

commonly available in typical motor drives. Therefore, the proposed thermal monitoring method is nonintrusive.

To track the stator temperature over time, the stator resistance R_0 is first estimated at room temperature t_0 during the algorithm commissioning stage. Once the reference resistance R_0 and the reference temperature t_0 are obtained, the winding temperature t_s can then be deduced as a function of the estimated stator resistance R_s as,

$$t_s = (t_0 + k_1) \frac{R_s}{R_0} - k_1. \quad (5.5)$$

According to International Annealed Copper Standard (IACS), k_1 is 234.5 for 100% IACS conductivity copper, or 225 for aluminum, based on a volume conductivity of 62% [69]. The accuracy of the parameter-based methods is not affected by the running condition and the cooling mode of the machine.

Since the temperature of stator windings changes slowly, the DC current can be injected into the motor for a very short period of time every a few minutes so that the increased loss and torque ripple due to DC current can be minimized.

5.3 Simulation Validation

The principle of the method is validated by a simple simulation using Matlab/Simulink, as shown in Figure 5.2. A typical indirect vector control scheme is implemented with both the speed and current controllers. The current offset is added to the current reference i_d^* and i_q^* . To minimize the simulation time, the stator temperature is varied very fast as a predefined function of time.

The DC current is chosen to be 3 Amps and injected continuously after the motor is started. The stator winding temperature is calculated according to (5). as shown in Figure

5.3, the temperature estimation error is less than 2 °C. This simulation validates the basic principle of this nonintrusive thermal monitoring method.

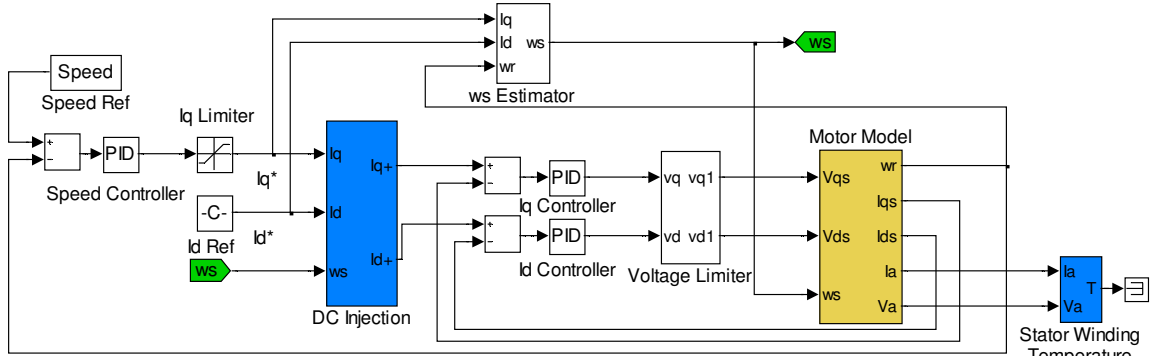


Figure 5.2: Simulink simulation of a field-oriented controlled induction motor with DC current injection.

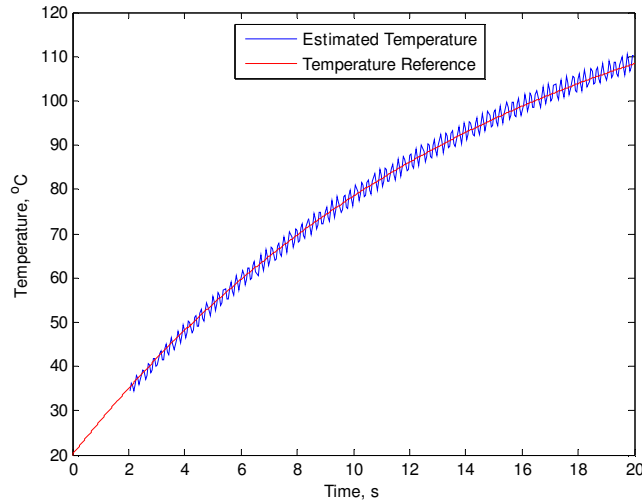


Figure 5.3: Estimated stator winding temperature given by the simulation of the DC injection method.

5.4 Terminal Voltage Estimation

Accurate extraction of the DC component in the line voltage, v_{ab} , is critical for calculating the stator resistance of the induction machine. In a typical closed-loop inverter drive, the terminal voltages are estimated from the PWM duty cycles and the measured DC bus voltage as,

$$V_{aN} = D_a \cdot V_{dc}, \quad (5.6)$$

where D_a is the phase-A duty cycle generated by the current regulator, V_{dc} is the measured DC bus voltage, V_{aN} is the phase-A voltage with respect to the negative rail of the DC bus.

The terminal voltages obtained from (5.6) are widely used for calculating the stator flux for motor control purposes. But they are not accurate enough for estimating the injected DC voltage, which is necessary for calculating the stator resistance. It is observed from experimental tests that if equation (5.6) is used for terminal voltage estimation, the estimated stator resistance will be inconsistent at different injected DC current levels, different load levels, different motor speeds, and even different DC bus voltages. Careful analysis and experimental data reveal that inverter non-idealities, namely the dead time, the device voltage drop, and the difference between the device turn-on and turn-off time delay, are the root causes for inconsistent stator-resistance estimation.

Although inverter non-idealities are well known to the power-electronic community [80-86], most research has been focused on their effects on the fundamental voltage component or the harmonic distortion. The effect of inverter non-idealities on DC voltage generation is seldom studied. The possible effect of dead time on DC voltage estimation was initially discussed in [72]. Unfortunately, the discussion in [72] is very preliminary and the effect was not analyzed quantitatively. The following sections will analyze the effect of inverter non-idealities on DC voltage estimation in detail. Several compensation techniques are also proposed to achieve consistent stator-resistance estimation.

5.4.1 Effect of Dead Time on DC Voltage Estimation

Figure 5.4 illustrates the effect of dead time with only one leg of the inverter and the DC link capacitor. The negative rail of the DC bus is chosen to be the voltage reference point, denoted as point N in Figure 5.4. The output of the inverter bridge is connected to phase A of the induction machine. The inverter bridge has a total of four legitimate operating modes depending on the direction of the machine current (inductive load assumed), as illustrated in Figure 5.4 (a) and (b). Neglecting any device voltage drop for now, the voltage of the phase A winding, V_{aN} , switches between 0 and V_{dc} , as shown in Figure 5.4 (c) and (d).

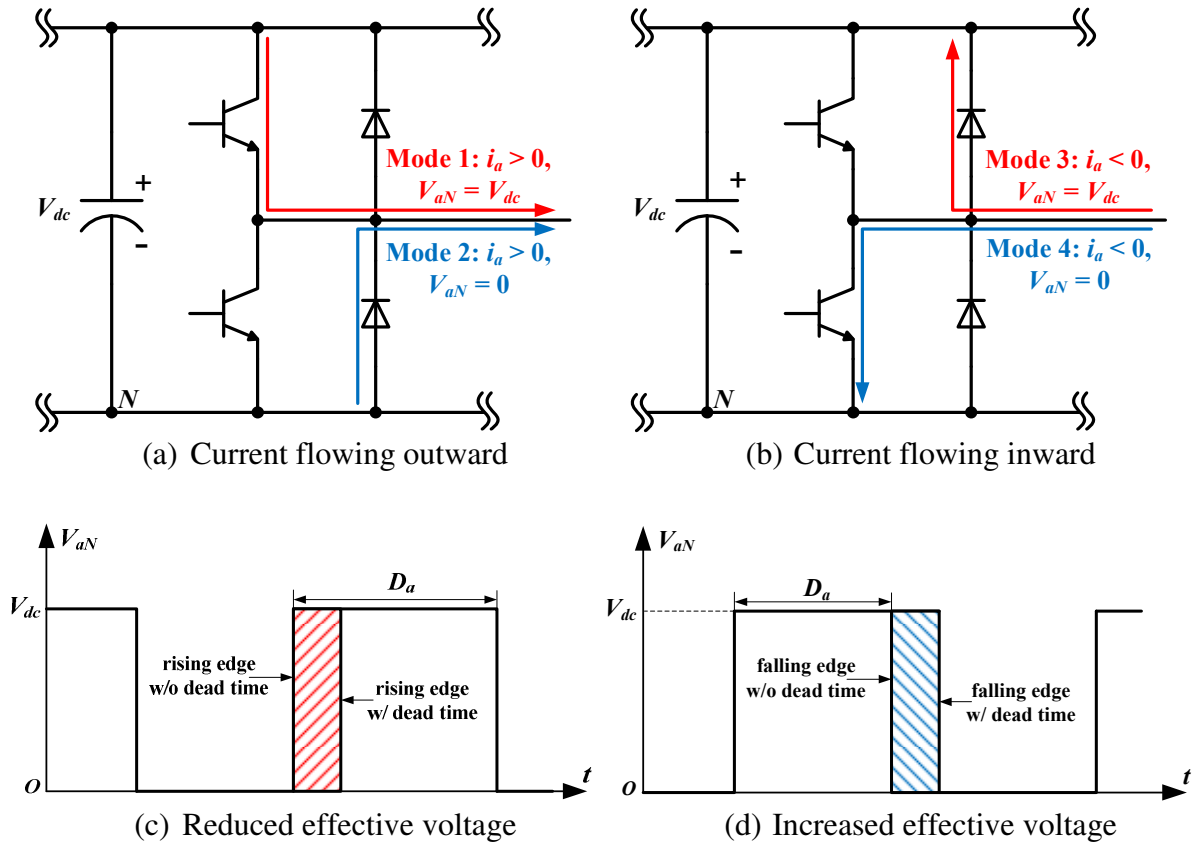


Figure 5.4: Illustration of the effect of the dead time.

The effect of the dead time makes the actual voltage applied to the phase A winding different from that calculated from (5.6). When the inverter current is flowing outward (i_a

> 0), the rising edge of the output voltage V_{aN} gets delayed by the amount of dead time as shown in Figure 5.4 (c). The falling edge of the voltage pulse, on the other hand, is not affected. Similarly, when the current is flowing inward ($i_a < 0$), the falling edge of the output voltage V_{aN} gets delayed by the amount of dead time as shown in Figure 5.4 (d). The rising edge of the voltage pulse, on the other hand, is not affected.

The impact of dead time on DC voltage estimation is graphically illustrated in Figure 5.5 through Figure 5.7. In Figure 5.5, each narrow voltage pulse represents the contribution of the dead time to the terminal voltage in each PWM cycle (number of pulses not drawn in scale). When the current is positive, the voltage pulses are negative (negative contribution). When the current is negative, the voltage pulses are positive.

During normal operation of the induction machine, i_a is sinusoidal with no DC offset. Hence, the number of negative voltage pulses equals the number positive voltage pulses. Over an entire current cycle, the dead time has no influence on the DC voltage.

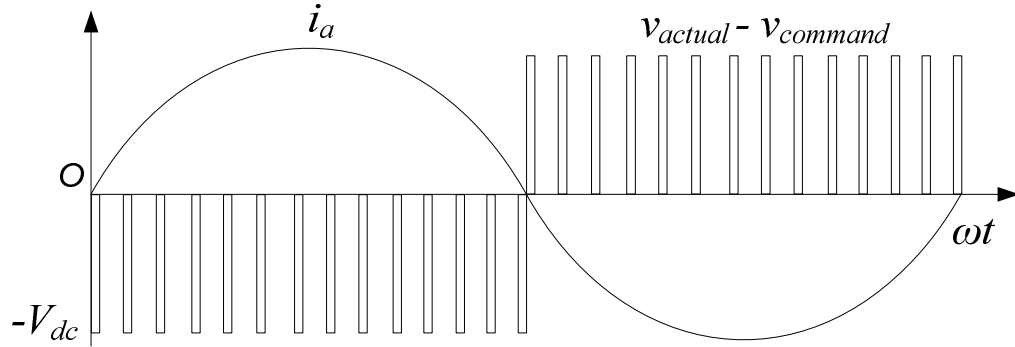


Figure 5.5: Contribution of dead time on terminal voltage – No DC current offset.

When a positive DC offset is injected into the phase-A winding, the number of negative voltage pulses is greater than the number of positive pulses, as shown in Figure 5.6. Therefore, the dead time has an overall negative contribution to the DC voltage.

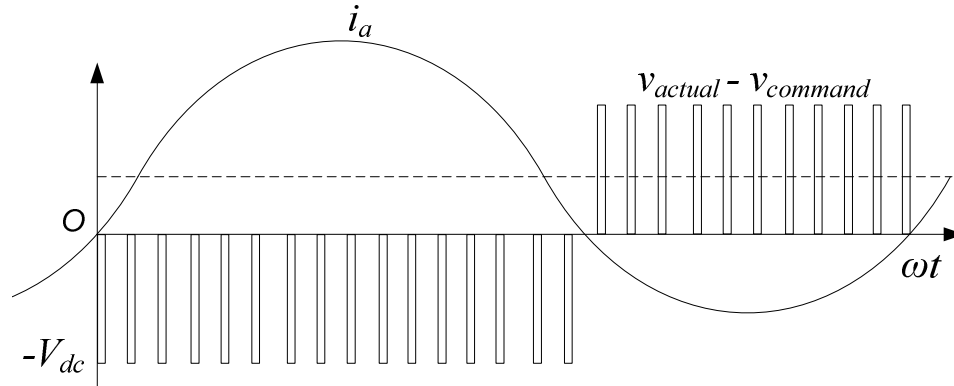


Figure 5.6: Contribution of dead time on terminal voltage – Positive DC current offset.

With the same DC current offset, if the amplitude of the fundamental current becomes smaller as shown in Figure 5.7, there will be even more negative voltage pulses and even fewer positive voltage pulses. Hence, the net negative contribution of dead time on the DC voltage will become even greater with smaller current amplitude (load level). Since the mechanical load level of an induction motor is usually dependent on the motor speed, the contribution of dead time is also speed-dependent. Moreover, if the DC bus voltage becomes higher, the height of the voltage pulses in Figure 5.7 becomes higher, which will also amplify the contribution of dead time on the DC voltage.

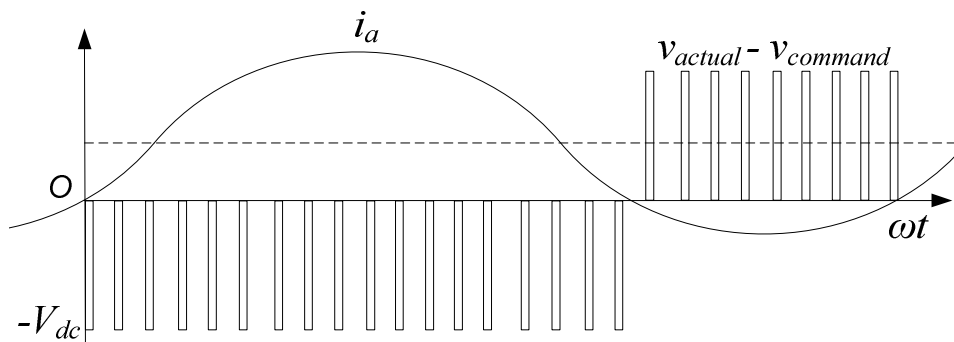


Figure 5.7: Contribution of dead time on terminal voltage – Positive DC current offset and smaller current amplitude.

Overall, the DC voltage is overestimated without considering the effect of dead time. Moreover, the DC voltage is *overestimated more* when the injected DC current is higher,

the load level is lower, the speed is lower (fan, or pump-like mechanical load), the dead time is longer, and the DC bus voltage is higher. The dependence of estimated DC voltage on so many factors is the root cause for inconsistent stator-resistance estimation, and is extremely difficult to compensate using look-up-table based methods [72, 73].

To achieve consistent DC voltage estimation, an efficient and straightforward method is to compensate the effect of dead time during each control cycle (also the PWM cycle) of the motor controller. Equation (5.6) is modified to,

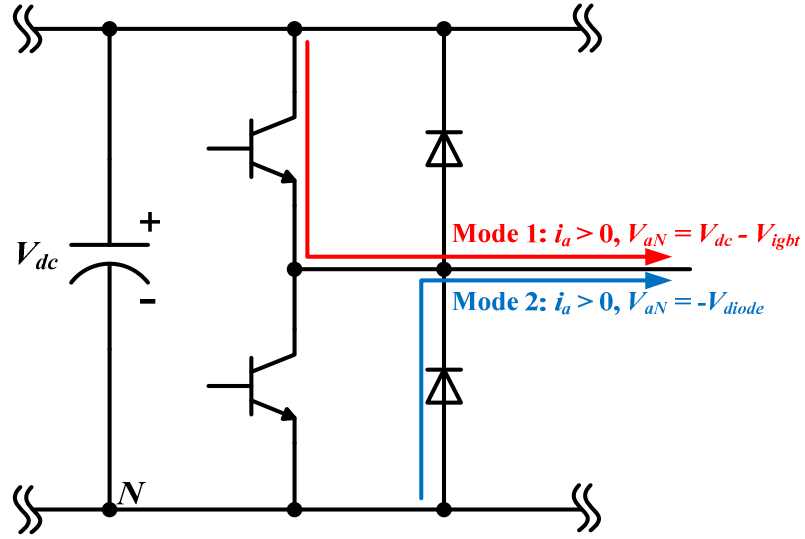
$$\begin{aligned} &\text{if } i_a > 0, \\ &\quad V_{aN} = (D_a - D_{dt}) \cdot V_{dc} \\ &\text{if } i_a < 0, \\ &\quad V_{aN} = (D_a + D_{dt}) \cdot V_{dc} \end{aligned} \quad (5.7)$$

where D_{dt} is dead time normalized by the PWM cycle. Phase-B and phase-C voltages can be estimated similarly.

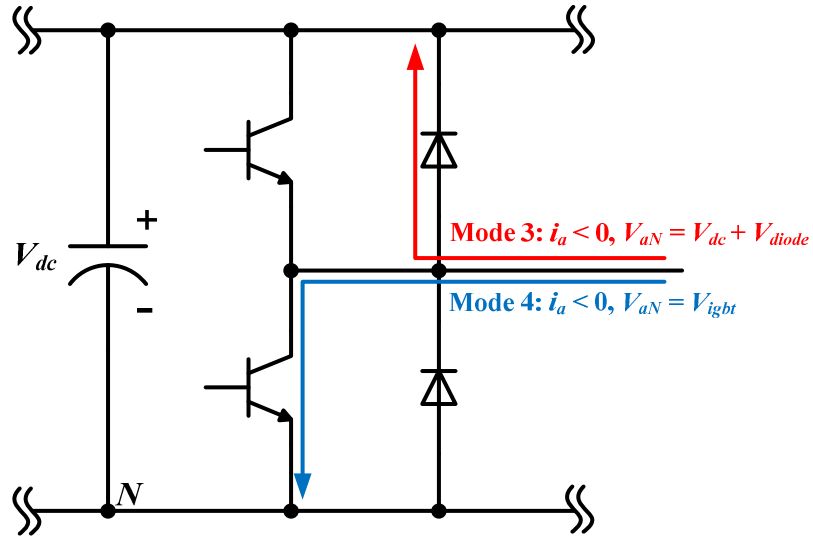
5.4.2 Effect of Device Voltage Drop on DC Voltage Estimation

In addition to the dead time, the voltage drop across the IGBT device and the diode is another inverter non-ideality that impacts the DC voltage estimation.

In Figure 5.8, the device voltage drop is analyzed with different operating modes of the inverter. When the inverter current is flowing outward ($i_a > 0$), the output voltage V_{aN} is reduced by the voltage drop across the upper IGBT and the lower diode. When the current is flowing inward ($i_a < 0$), the output voltage V_{aN} is boosted by the voltage drop across the lower IGBT and the upper diode.



(a) Current flowing outward



(b) Current flowing inward

Figure 5.8: Illustration of device voltage drop.

The impact of device voltage drops on DC voltage estimation is graphically illustrated in Figure 5.9. The voltage drop across the power devices is not constant but related to the magnitude and polarity of the current. The net contribution of the device voltage drop on the terminal voltage is negative with a positive DC current offset. The net contribution depends on the injected DC current level and the AC current amplitude.

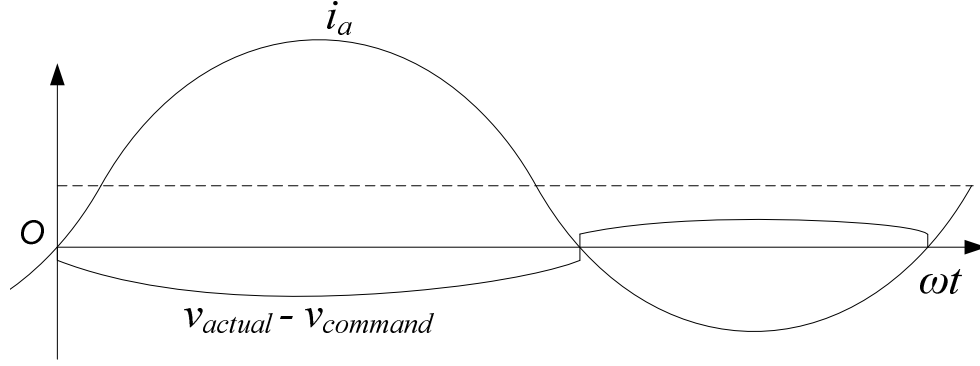


Figure 5.9: Contribution of device voltage drop on terminal voltage.

To account for the effect of device voltage drop, equation (5.7) is further improved to,

$$\begin{aligned}
 &\text{if } i_a > 0, \\
 &\quad V_{aN} = (D_a - D_{dt}) \cdot V_{dc} - (D_a - D_{dt}) \cdot V_{igbt}(i_a) - (1 - D_a + D_{dt}) \cdot V_{diode}(i_a) \\
 &\text{if } i_a < 0, \\
 &\quad V_{aN} = (D_a + D_{dt}) \cdot V_{dc} + (D_a + D_{dt}) \cdot V_{diode}(i_a) + (1 - D_a - D_{dt}) \cdot V_{igbt}(i_a)
 \end{aligned} \tag{5.8}$$

where V_{igbt} and V_{diode} are the voltage drop across the IGBT device and the diode respectively, which are readily available in the device datasheet as a function of device current, i_a . Phase-B and phase-C voltages can be estimated in a similar fashion. Strictly speaking, voltage drops across IGBT and diode also depend on the device temperature. However, such dependency is low enough that its effect on terminal voltage estimation can be neglected in practice.

5.4.3 Effect of Different Device Turn-on and Turn-off Time Delay

Any induction motor drive has some time delay between the triggering pulses generated by the logic circuit and the actual IGBT bridge output. This delay is a combined effect of the communication delay of the circuit, the gate drive dynamics, and the IGBT dynamics, which are determined by the design of the inverter.

It is found through experimental tests that for the inverter shown in Figure 5.13, the overall turn-on delay is relative constant at 800 ns, and the overall turn-off delay is approximately 1080 ns, regardless motor operating conditions. That means each IGBT stays 280 ns longer than originally expected, and the width of the generated voltage pulse can be either longer or shorter than the commanded voltage depending on the direction of the output current.

The effect of turn-on/turn-off delay difference on the terminal voltage is graphically illustrated in Figure 5.10. Figure 5.10 is very similar with Figure 5.6 except that the polarity of the voltage pulses is opposite. Overall, the DC voltage is underestimated without considering the effect of turn-on/turn-off delay difference.

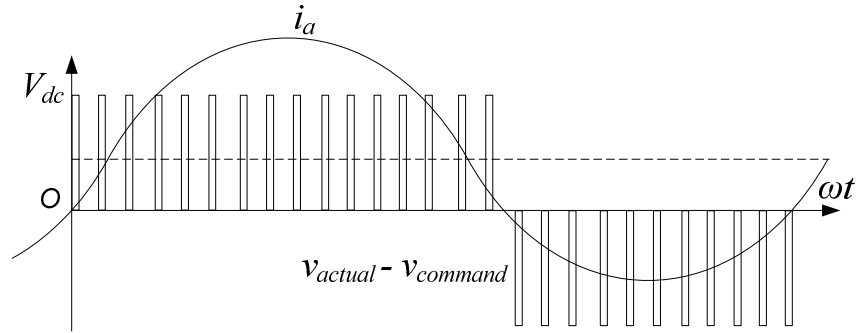


Figure 5.10: Contribution of different turn-on/turn-off delay on terminal voltage.

To account for the effect of device turn-on/turn-off time difference, equation (5.8) is further improved to,

$$\begin{aligned}
 &\text{if } i_a > 0, \\
 &\quad V_{aN} = (D_a - D_{dt} + D_{dly}) \cdot V_{dc} - (D_a - D_{dt} + D_{dly}) \cdot V_{igbt}(i_a) \\
 &\quad \quad - (1 - D_a + D_{dt} - D_{dly}) \cdot V_{diode}(i_a) \\
 &\text{if } i_a < 0, \\
 &\quad V_{aN} = (D_a + D_{dt} - D_{dly}) \cdot V_{dc} + (D_a + D_{dt} - D_{dly}) \cdot V_{diode}(i_a) \\
 &\quad \quad + (1 - D_a - D_{dt} + D_{dly}) \cdot V_{igbt}(i_a)
 \end{aligned} \tag{5.9}$$

where D_{dly} is the time difference of the turn-on and turn-off delay normalized by the PWM cycle.

5.4.4 Over Modulation and Discontinuous PWM Methods

Equation (5.9) gives an accurate estimation of the motor terminal voltage by compensating for inverter non-idealities, such as the dead time, the device voltage drop, and the different turn-on/off time delay. However, in cases when the inverter enters the over-modulation mode, or when the inverter is running with discontinuous PWM schemes (DPWM_{min}, DPWM_{max}, DPWM₀, and etc), the commanded duty cycle D_a can be clamped to either 0 or 1. In such cases, there is no physical switching of IGBT devices within that PWM cycle, and it is unnecessary to consider of the effect of dead time and different device turn-on/off time delay.

Such special cases when the duty cycle D_a is either 0 or 1 can be easily incorporated into equation (5.9) by setting both D_{dt} and D_{dly} to 0 for phase A for that specific PWM cycle. The form of equation (5.9) remains unchanged.

5.5 Real-time Signal Processing Technique

Normally, the extraction of the DC component in the voltage and current is simply a matter of low pass filtering. In this study, however, the magnitude of the DC voltage component is much smaller than that of the fundamental voltage. More importantly, the frequency of the fundamental voltage is constantly varying. It is thus difficult to design a low-order IIR filter that has sufficient high-frequency attenuation characteristic. The following signal processing technique is proposed to solve this problem, as shown in Figure 5.11.

In Figure 5.11 (a), a digital DC notch filter is first applied to the stator current in the synchronous reference frame. Then the filtered current is transformed back to the natural A-B-C reference frame. These two operations eliminate the fundamental component in the stator current and leaves the DC component intact. Finally, a low pass filter is applied to the phase current to eliminate other high-frequency harmonics, and the DC current is extracted. The DC current is then integrated for a few seconds to reduce random errors.

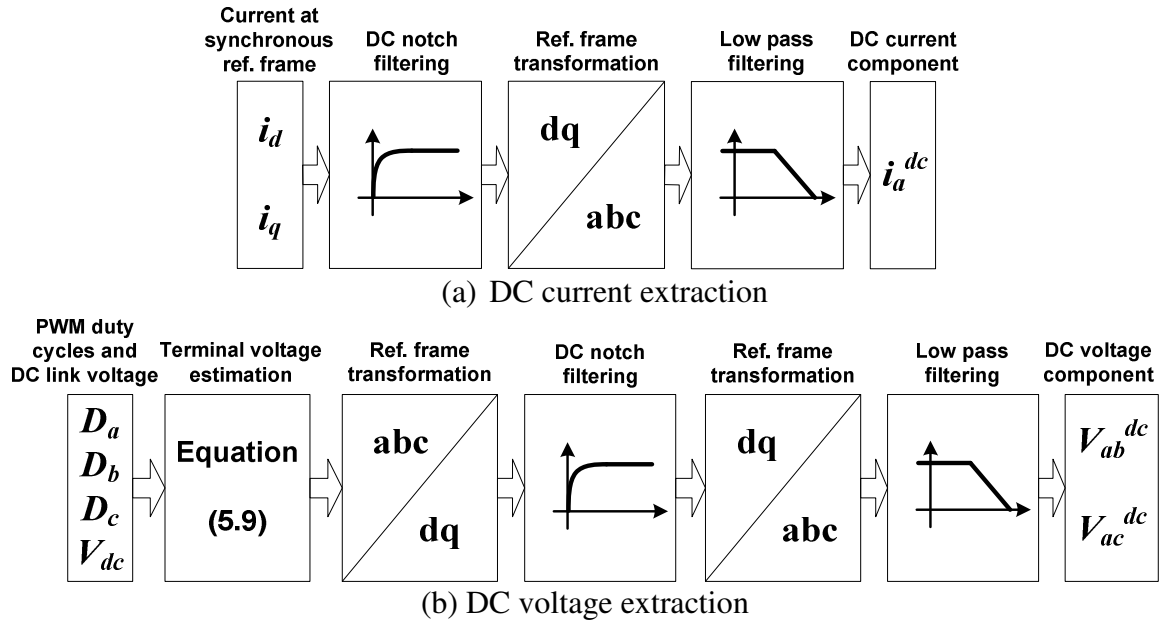


Figure 5.11: Signal process techniques for extracting DC current and voltage.

In Figure 5.11 (b), the extraction of the DC voltage component starts with the measured DC bus voltage and the commanded PWM duty cycles. The three-phase terminal voltage is estimated from these quantities using equation (5.9). After transforming the the three-phase voltages into synchronous reference frame, a DC notch filter is applied. Then the filtered voltage is transformed back to the natural A-B-C reference frame. These operations eliminate the fundamental component in the stator voltage and leaves the DC component intact. Finally, a low pass filter is applied to the terminal voltages to eliminate other high-frequency harmonics and the DC voltage is

extracted. The DC voltage is also integrated for a few seconds to eliminate random errors.

5.6 Temperature Estimation Error Analysis

The error of the estimated temperature mainly comes from the error of the current measurement and the DC voltage estimation. This section discusses several main sources of errors in the measurement system and how they propagate into the error in the final estimated winding temperature.

5.6.1 Errors Introduced by the Current Measurement

There exist two sources of errors in the current measurement channel.

The first error source is the inherent error of the analog current sensing circuit, which is consisted of a Hall Effect current sensor and the associated calibration circuit. The current sensing circuits for both phase of the experimental inverter in Figure 4.14 are calibrated to the precision of 0.15% using a Fluke 187 multimeter.

The second error source is the quantization error introduced by the analog-to-digital converter (ADC). As described in section 4.7.3, the experimental inverter uses typical 12-bit ADCs. Since the peak-to-peak measurement range of the current signal is tuned to 75 A, the quantization error of the current signal is therefore $75/2^{12+1}=0.00916$ A. However, the quantization error of the ADC is completely random. Therefore, it will be eliminated during the current integration process described in section 5.5.

Therefore, the overall relative error introduced by the current measurement is 0.15%.

5.6.2 Errors Introduced by the DC Bus Voltage Measurement

Without considering the inverter nonidealities, the terminal voltage is estimated as a fraction of the DC bus voltage measurement V_{dc} , as shown in equation (5.6). There are also two sources of errors in the DC bus voltage measurement.

The first error source is the inherent error of the analog voltage sensing circuit, which is calibrated to the precision of 0.025% using a Fluke 187 multimeter.

The second error source is the quantization error introduced by the analog-to-digital converter (ADC). Since measurement range of the DC bus voltage is tuned to 0 to 400 V, the quantization error of the current signal is therefore $400/2^{12+1}=0.0488$ V. However, the quantization error of the ADC is completely random. Therefore, it will be eliminated during the voltage integration process described in section 5.5.

Therefore, the overall relative error introduced by the DC bus voltage measurement is 0.025%.

5.6.3 Errors Introduced During Inverter-nonideality Compensation

Considering inverter nonidealities, the terminal voltage is estimated using equation (5.9). The commanded duty cycle D_a and the dead time D_{dt} are synchronized with the clock signal generated by a crystal oscillator on the FPGA board. Therefore, the error in D_a and D_{dt} can be neglected. The time difference of the IGBT turn-on/off delay is calibrated by a high-precision oscilloscope and is also highly accurate.

However, the voltage drop across the IGBT v_{igbt} and the diode v_{diode} may have some error because the voltage drop across those power semiconductors is also dependent on its junction temperature. In practice, the actual junction temperature and the one used in the motor control program may be different by as much as 20°C. To quantify the error

caused by power semiconductor temperature mismatch, assume that the on-state voltage drops across the IGBT device and diode are the same, denoted as V_{device} .

Equation (5.9) can then be simplified to,

$$\begin{aligned} &\text{if } i_a > 0, \\ &\quad V_{aN} = (D_a - D_{dt} + D_{dly}) \cdot V_{dc} - V_{device}(i_a) \\ &\text{if } i_a < 0, \\ &\quad V_{aN} = (D_a + D_{dt} - D_{dly}) \cdot V_{dc} + V_{device}(i_a) \end{aligned} \quad (5.10)$$

Figure 5.12 shows the on-state voltage drop of the IGBT anti-parallel diode under different temperature from the device datasheet. According to Figure 5.12, if the IGBT junction temperature is off by 20°C, the device voltage drop will be off by 0.087 V. With the injected DC current at 5% of peak AC current amplitude, the positive half cycle of the current waveform will be longer than the negative half cycle of the current waveform by about 3.18% of the entire current cycle. Therefore, the effective DC voltage error caused by the IGBT temperature mismatch is up to $0.087 \times 3.18\% = 0.00277$ V for one phase.

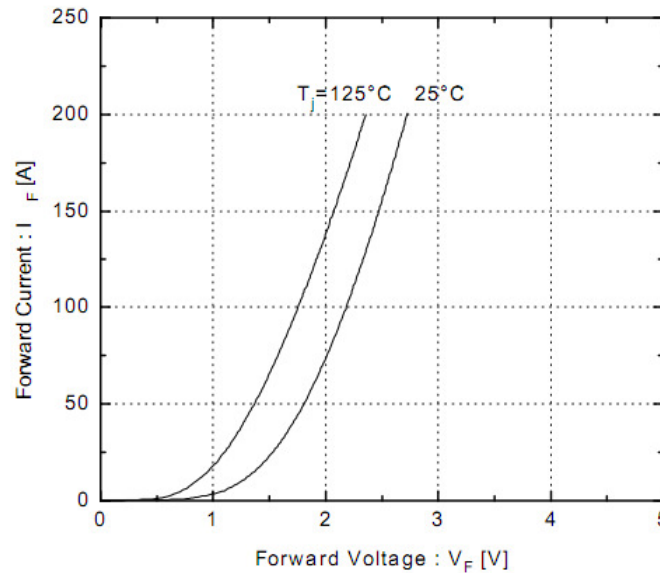


Figure 5.12: Device voltage drop curve at different temperature.

5.6.4 Errors in the Estimated Temperature

The resistance of the stator winding is calculated as the quotient of the DC component of line-to-line voltage and DC line current, as shown in equation (5.4). As discussed above, the error in the estimated DC terminal voltage is caused by DC bus measurement error and device temperature mismatch. Since these two errors are independent, the overall relative error of the estimated DC component of line-to-line voltage can be expressed as,

$$V_{ab, err}^{dc} = \sqrt{(0.025\%)^2 + \left(\frac{0.00277}{2/3 \cdot V_{ab}^{dc}}\right)^2}, \quad (5.11)$$

where $2/3 \cdot V_{ab}^{dc}$ is the DC component of the phase-A voltage.

The overall relative error of the DC current measurement is,

$$I_{a, err}^{dc} = 0.15\% . \quad (5.12)$$

Consider the error analysis rule for the quotient, the overall relative error of the estimated resistance is,

$$R_{s, err} = \sqrt{(0.025\%)^2 + \left(\frac{0.00415}{V_{ab}^{dc}}\right)^2 + (0.15\%)^2} . \quad (5.13)$$

Since the physical relationship in equation (5.5) is highly accurate [69], the relative error of the estimated temperature is also,

$$(t_s + k_1)_{err} = \sqrt{(0.025\%)^2 + \left(\frac{0.00415}{V_{ab}^{dc}}\right)^2 + (0.15\%)^2} . \quad (5.14)$$

5.7 Experimental Validation

5.7.1 Experiment Setup

The programmable inverter drive previously introduced in section 4.7.3 and Figure 4.14 is also used to validate the proposed thermal monitoring method in real time. The picture of the entire test setup is shown in Figure 5.13. The specification of the induction machine is summarized in Table 5.1. The speed of the induction machine is measured by a speed encoder and is fed back to the controller.

The fundamental principle of the proposed method determines that it can only estimate the average temperature of the stator winding. Ideally, to validate the proposed method, the average temperature of the stator winding needs to be measured. In practice, however, measuring the average temperature of the stator winding when the motor is running is quite difficult. To approximate the average winding temperature, eight thermocouples are attached to different parts of the stator winding. Four of them are attached to the drive-end stator winding while the other four are attached to the nondrive-end stator winding. On each end of the machine, two thermocouples are inserted into the stator slots and the other two are attached to the end winding. Using this setup, the average reading of all eight thermocouples can be used as an approximation of the winding average temperature for validation purposes.

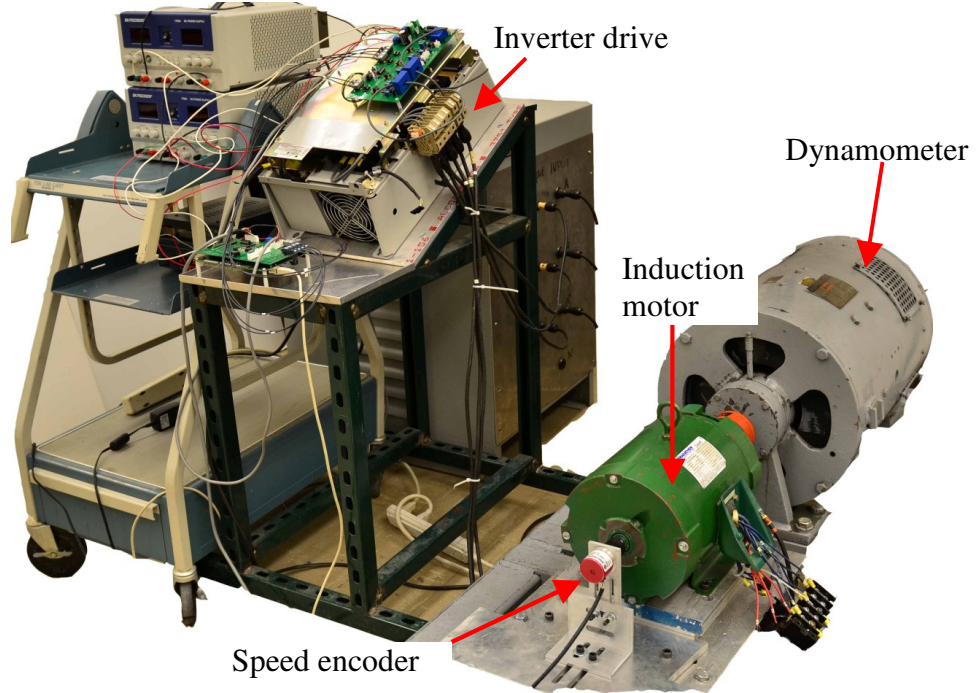


Figure 5.13: Experimental setup for DC-injection based stator resistance estimation.

Table 5.1: Parameters and ratings of the test machine for thermal monitoring

Parameter	Value
P_{rated}	5 (hp)
Poles	4
V_{rated}	230 (V)
I_{rated}	13 (A)
$N_{m,rated}$	1745 (rpm)
R_s	0.353 (ohm)
R_r	0.424 (ohm)
L_m	67.47 (mH)
L_{ls}	2.59 (mH)
L_{lr}	3.88 (mH)

5.7.2 Measured Motor Waveforms

Figure 5.14 shows the i_d and i_q currents before and during current injection. The induction motor is running at 600 rpm and 85% of rated current. The magnitude of the injected current, I_{dc} , is 1.0 Amps. It can be seen that the actual i_d and i_q follows the superimposed sine-wave reference closely.

Figure 5.15 shows i_a and v_{ab} before and during DC current injection. While the stator current has a noticeable DC offset after 0.2 seconds, the DC offset in the voltage are too small to notice due to the large amplitude of the fundamental voltage. With an 5% of additional DC current, the peak instantaneous current of the motor increases by 5%, and the peak RMS current of the motor increase by only 0.25%. Such small increase of the motor current will not affect the sizing of the inverter and power electronic components.

Using the real-time signal processing method described in Figure 5.11, the DC components of i_a and v_{ab} are extracted and shown in Figure 5.16. Note that Figure 5.16 has a longer time span compared to Figure 5.14 and Figure 5.15 so that the DC components can be shown more clearly. Both the voltage and current waveforms are smooth and clean, which allows for reliable estimation of the stator resistance.

Figure 5.17 shows the electromagnetic torque and the speed of the motor before and during DC current injection. The torque oscillation is at the stator frequency. The amplitude of the oscillation is directly related to the injected DC current level and is about 5% of rated torque. Because of the inertia of the rotating mass, and the limited bandwidth of the speed control loop, no speed oscillation is observed. The audible noises emitted by the test bench before and during DC current injection are indistinguishable by human ears as well as sound pressure level meters.

Since the thermal time constant of motors is in the range of several minutes, it is only necessary to inject DC current for a few seconds every a couple of minutes, which further minimizes the adverse effect of torque oscillations.

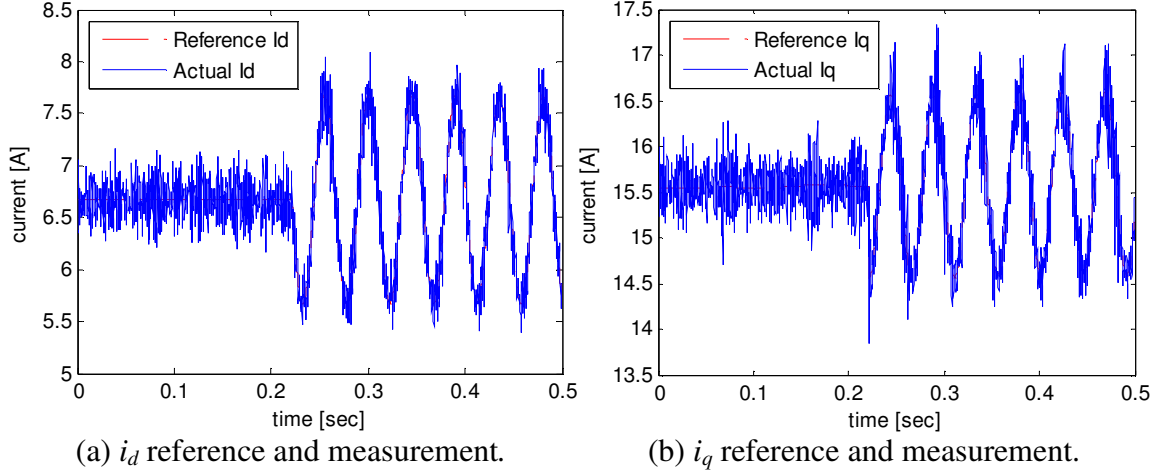


Figure 5.14: D- and Q- axis current before and during DC current injection.

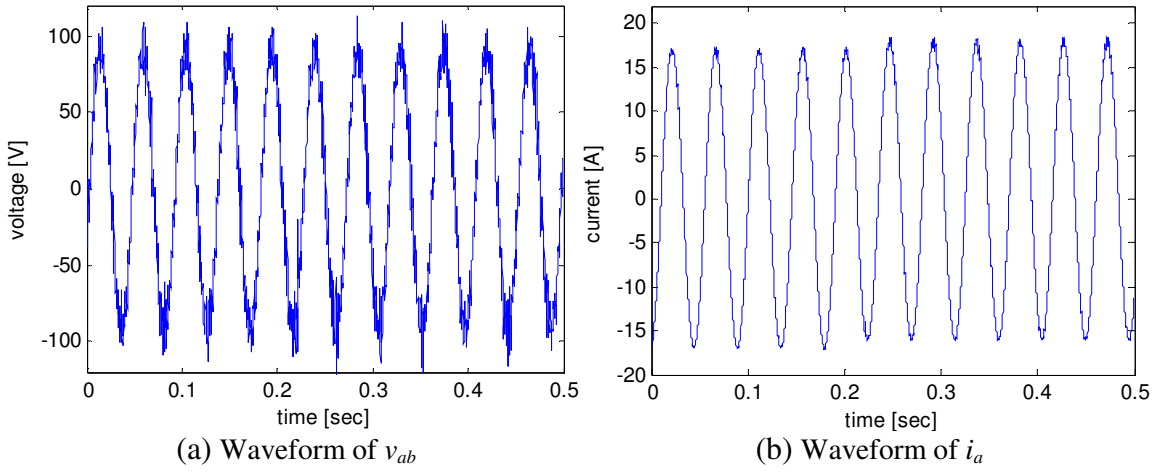


Figure 5.15: Stator voltage and current before and during DC current injection.

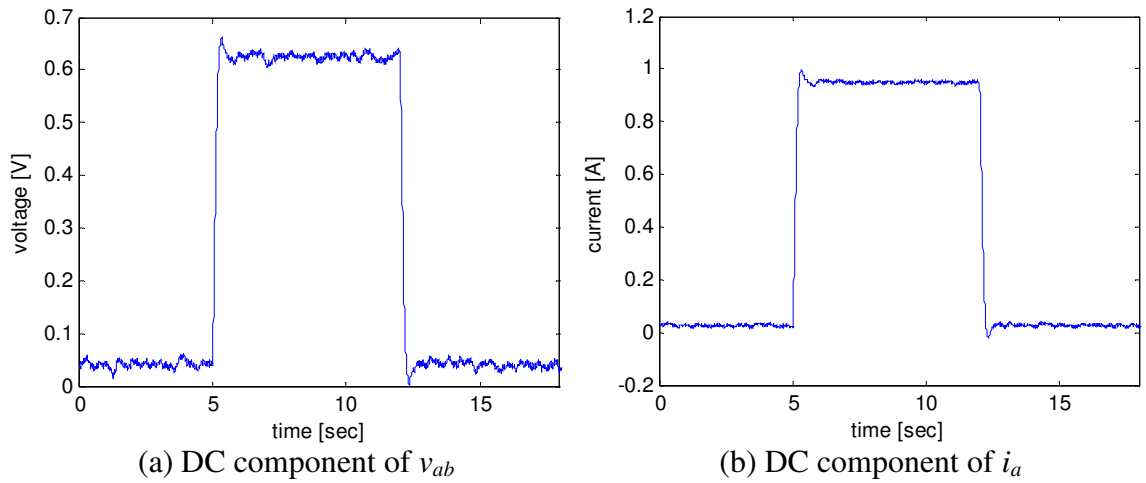


Figure 5.16: DC components of stator voltage and current.

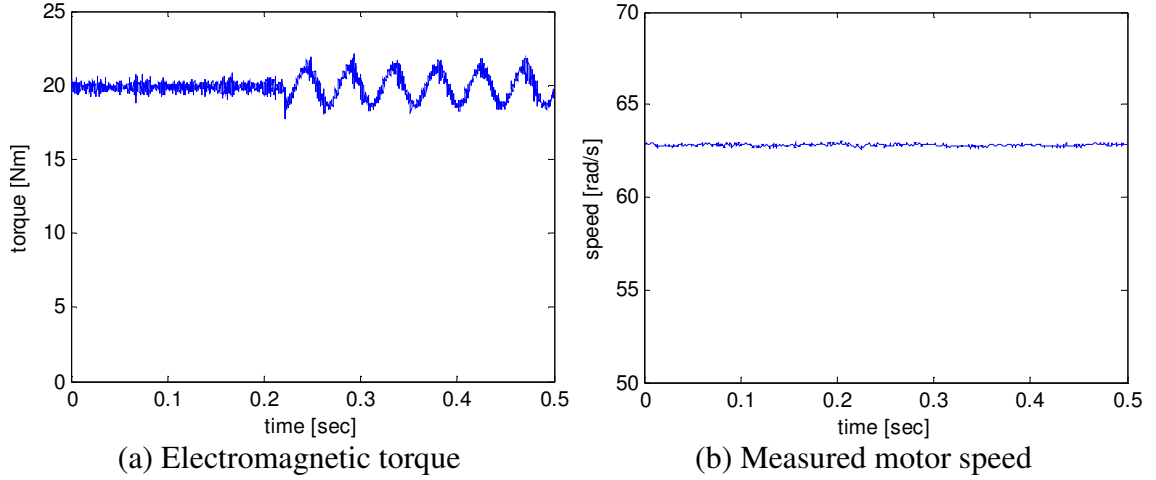


Figure 5.17: Motor torque and speed before and during DC current injection.

5.7.3 Temperature Estimation at a Single Operating Condition

To validate the proposed method, the induction machine specified in Table 5.1 is running continuously at approximately 85% of its rated current at 600 rpm for 2.5 hours. One ampere of DC current is injected into the motor winding for a few seconds every 10~15 minutes. The reference stator resistance R_0 is first estimated when the machine is at the room temperature t_0 . Then the stator winding temperature is tracked over time using (5). If necessary, the cable and contact resistances can also be compensated following procedures outlined in [60]. To emulate a change in the motor cooling condition, a thermal-insulation jacket is wrapped around the motor housing beginning at 70 minutes.

The experimental result is shown in Figure 5.18. The red dashed curve is the stator winding temperature estimated by the proposed method. The blue solid line is the average temperature measured by eight thermocouples. The estimated winding temperature tracks the average thermocouple measurement very closely regardless the changing cooling conditions. The deviation between the estimated temperature and the average thermocouple reading is less than 3 °C.

The thin black dashed lines indicate the error band of the estimated winding temperature using equation (5.14). The width of the error band increases slightly with the estimated temperature. At about 77°C, the width of the error band is about $\pm 2.45^{\circ}\text{C}$. The relative narrow error band demonstrates that the proposed method has good temperature estimation consistency.

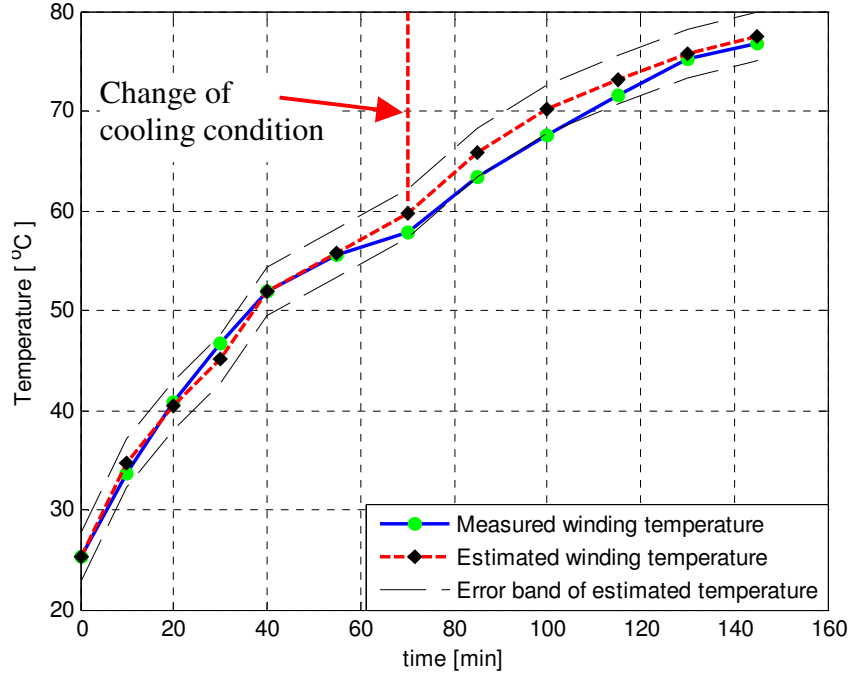


Figure 5.18: Stator winding temperature estimation at constant operating condition.

5.7.4 Temperature Estimation with Variable Operating Conditions

To verify the consistency of the method at variable operating conditions, similar temperature tracking tests are also performed with variable load level, variable motor speed, and variable DC bus voltage, as shown in Figure 5.19, Figure 5.20, and Figure 5.21, respectively.

In Figure 5.19, the induction motor is first running at 50% of its rated current for 40 minutes and then 90% of its rated current for another 85 minutes. The reference stator

resistance R_0 and the room temperature t_0 are obtained at the 50% rated current level. As shown in Figure 5.19, if the inverter non-idealities are considered as discussed in section 5.4, the estimated winding temperature tracks the measured temperature closely even after the load level has changed. The maximum temperature error is less than 5°C. However, if the inverter non-idealities are not considered, the estimated winding temperature drops significantly when the load level goes up. The maximum temperature deviation is almost 48 °C. This is because the stator resistance is more overestimated when the load level is low and relatively less overestimated when the load level is high, as discussed in section 5.4.

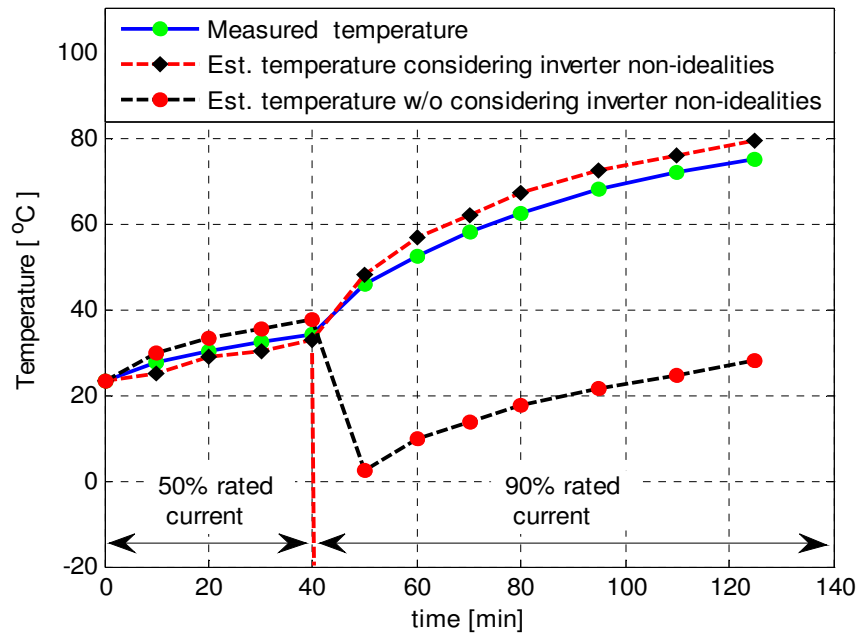


Figure 5.19: Stator winding temperature estimation with variable load level (error band of estimated temperature removed for clarity).

In Figure 5.20, the speed of the induction motor changes from approximately 600 RPM to 840 RPM. Correspondingly, the load level changes from 76% rated current to 93% rated current. With all the inverter non-idealities considered, the estimated winding temperature tracks the measured temperature closely even after the motor speed has

changed. The maximum temperature error is less than 5°C. However, if the inverter non-idealities are not considered, the estimated winding temperature drops significantly when the motor speed goes up. The reason for the sudden drop of estimated temperature is similar with that in Figure 5.19.

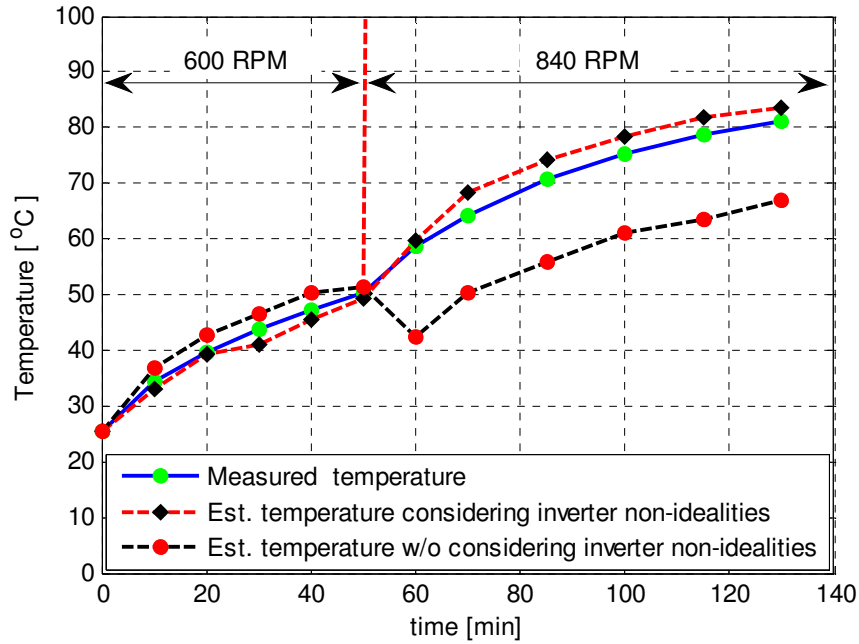


Figure 5.20: Stator winding temperature estimation with variable motor speed (error band of estimated temperature removed for clarity).

In Figure 5.21, the induction motor is running at 600 RPM with 77% of its rated current. The DC bus voltage changes from 136 V to 196 V at 30 minutes into the test. Again, with all the inverter non-idealities considered, the estimated winding temperature tracks the measured temperature closely even after the DC bus voltage has changed. The maximum temperature error is less than 5°C. If the inverter non-idealities are not considered, the estimated winding temperature increases significantly as the DC bus voltage goes up. This is because the stator resistance is less overestimated when the DC bus voltage is low and more overestimated when the DC voltage is high, as discussed in section 5.4.

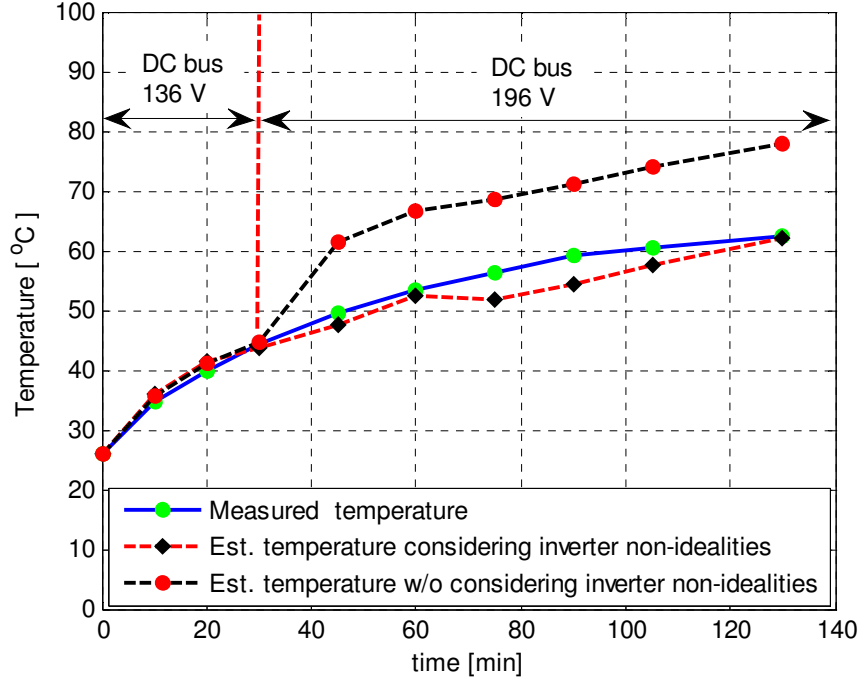


Figure 5.21: Stator winding temperature estimation with variable DC bus voltage (error band of estimated temperature removed for clarity).

5.8 Chapter Summary

This chapter proposes a nonintrusive thermal monitoring scheme for closed-loop drive-fed induction motors using DC current injection. The major contributions of this paper are as follows,

- (1) A simple method is proposed for injecting DC current into closed-loop drive-fed induction machines without interrupting its normal operation.
- (2) The major technical difficulty of DC-injection-based thermal monitoring, the inconsistency in resistance estimation, has been overcome by carefully analyzing and compensating for the effects of inverter non-idealities.

The proposed thermal monitoring scheme has the following advantages over existing methods,

- (1) Non-intrusive: The method requires no additional sensors or hardware except for those already available in closed-loop induction motor drives. Besides, only 1 Amp of DC current (about 5% of the rated current amplitude) is injected every couple of minutes into the stator winding. This results in minimal impacts on the torque smoothness and energy efficiency of the motor.
- (2) Easy-to-use: As demonstrated in the paper, the method can be easily integrated with the existing control algorithm of the closed-loop motor drive with minimal computational cost. No complicated calibrations, except for the estimated resistance under room temperature, are needed to commission the method.
- (3) Accurate: Compared to the temperature measurement taken by thermocouples, the maximum error of the proposed method is less than 3 °C at a constant operating condition and less than 5 °C with variable operating conditions for a 5-HP induction motor.

CHAPTER 6 Fundamental Aspects of Condition Monitoring of Claw-pole Generators

6.1 Overview

The claw-pole synchronous generator is the heart of virtually all automotive electric power generation and storage (EPGS) systems. Based on the literature survey presented in Chapter 3, the condition monitoring of this crucial component in vehicles remains largely unexplored.

Existing condition monitoring techniques developed for grid-connected AC synchronous machines do not directly transfer to claw-pole generators. Failure modes of claw-pole generators are different from those of conventional synchronous machines because of its special application. The complex magnetic structure of the claw-pole generator also makes the fault modeling challenging. Moreover, the AC voltage and current information of the generator are difficult to access because of the built-in rectifier.

A general discussion is performed in this chapter to better understand the fundamental aspects of claw-pole-generator condition monitoring. Common failure modes of claw-pole generators are first summarized, among which several important types of faults are selected to be investigated further in this study. The major procedures to model the claw-pole generator in finite-element simulation software are also outlined. Finally, spectral analyses are performed on the generator voltages and currents. Several important fault signatures in the voltage and current spectra are identified and discussed.

6.2 Failure Types and Failure Mechanisms

As discussed in Chapter 3, the faults of claw-pole generators can be broadly classified into two categories: the external faults (or system-related faults) and the internal faults. In an EPGS system, typical external faults include:

- 1) Serpentine belt slip
- 2) Defective serpentine belt
- 3) Loose or contaminated electrical connection
- 4) Improper mounting

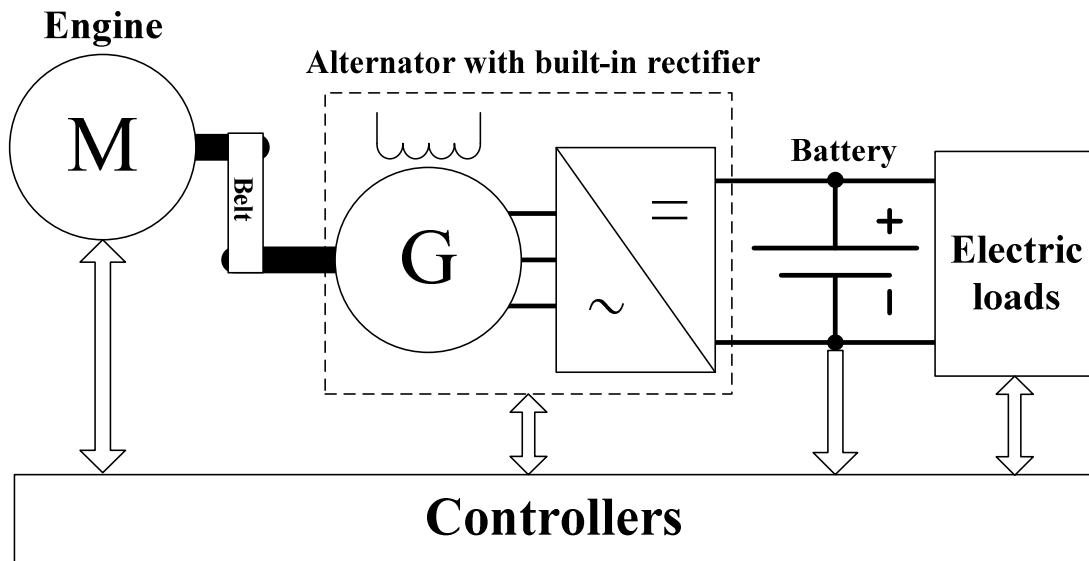


Figure 6.1: Illustration of the automotive EPGS system.

If the tension of the serpentine belt is smaller than required, slip may occur between the serpentine belt and the generator pulley especially when the generator is carrying heavy electric loads [20]. Belt slip accelerates the wearing of the belt and significantly reduces the energy conversion efficiency and the output capability of the claw-pole generator.

In addition to the belt slip, the serpentine belt may also develop defects, such as cracks or torn rubber on the grooves, as it ages over time.

If left undetected, both the belt slip and the belt defect may lead to premature breakage of the serpentine belt. The breakage of the serpentine belt is a catastrophic failure which results in loss of the electric power and all crucial accessories driven by the same belt, such as the water pump, power steering pump, A/C compressor, air pump, etc. Therefore, it is highly desirable to detect those faults in the incipient stage so that preventive maintenance can be scheduled before catastrophic belt breakage occurs.

The loose or contaminated electric connections mostly occur at the positive or negative terminal of the battery. It may cause starting problem of the vehicle.

The improper mounting will increase the vibration level of the generator. However, this is much less a problem nowadays than before because very long mounting bolts are typically used in modern designs of claw-pole generators.

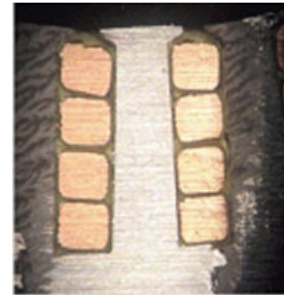
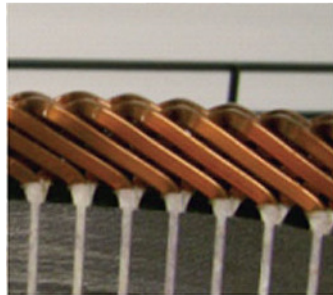
In addition to the system-related faults, the internal components of the generator are also subject to failures. A sectional view of a typical claw-pole generator is shown in Figure 6.2. The mechanical assembly of the claw-pole generator contains not only the wound-rotor synchronous machine, but also a plural of electrical and mechanical components and accessories. Possible internal faults of generator include:

- (1) Worn bearing
- (2) Stator winding fault
- (3) Short/open rectifier diode
- (4) Voltage regulator fault
- (5) Rotor winding fault
- (6) Rotor eccentricity (bent shaft)
- (7) Brush and slip ring fault

winding design, as shown in Figure 6.3. Stator turns in the bar winding have thicker insulations in the stator slot and more clearance in the winding overhang, and thus pose a lower risk of turn-to-turn short circuit. However, bar-wound windings are expensive to manufacture because they typically require threading of stator bars in the stator slots. In the foreseeable future, the dominant majority of the claw-pole generators will still be wire-wound.



(a) wire-wound stator



(b) bar-wound stator

Figure 6.3: Comparison of the bar-wound and wire-wound stator winding [88].

In addition to interviews with industry experts, some warranty data on claw-pole generators replaced by auto dealerships is also kindly provided by General Motors (GM). Due to the limited diagnostic capability at auto dealerships, the classification of failure modes in this data is far from systematic and complete. Nevertheless, the data sheds some helpful insight into short-term failure modes of claw-pole generators. A breakdown of failure modes is shown in Figure 6.4.

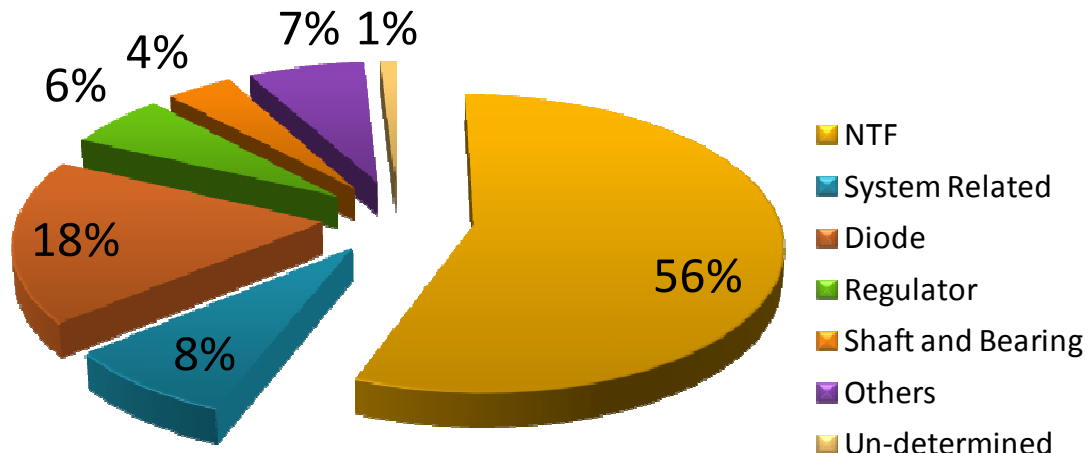


Figure 6.4: Major types of faults of generators replaced by auto dealerships under warranty (Courtesy: General Motors).

As shown in Figure 6.4, about 8 percent of failures are system-related, including loose connection and contamination of the overall charge system.

About 18 percent of failures are due to the rectifier diode damage. Diodes are typically damaged by excessive housing press and electrical stress. In particular, short diode is a much more common failure mode than open diode. When one diode becomes shorted during the operation of claw-pole generators, there will be a large fault current circulating between the phases, which quickly overheats and damages the other two diodes in the same positive or negative bank. Hence, the damage to the diode rectifier is often observed in banks.

About 6 percent of failures can be traced back to voltage regulators. The PWM switch in the voltage regulator gets “stuck” either to the high level of the supply voltage or the ground, which causes over-voltage or under-voltage problems in the generator output.

About 4 percent of generator is diagnosed of mechanical problems, such as worn bearing, bent shaft and etc, which are usually accompanied by excessive audible noises.

Other types of faults include improperly seated electronic fastener, slip ring damage, broken rotor winding and etc. Interestingly, however, about 56 percent of the claw-pole generators are replaced by trained technicians with no trouble found (NTF) afterwards. This is possibly due to misdiagnoses, or intermittent faults that are difficult to duplicate [18]. Out of the 56 percent NTF generators, large portions of consumers have complaints on increased noise level and starting/battery problem. Therefore, there may exist faults, such as worn bearing and stator turn fault, which cannot be effectively determined by the current generator diagnostic procedure at auto dealerships.

Among various types of external faults and internal faults of claw-pole generators, the following ones will be investigated in this study:

- (1) Serpentine belt slip
- (2) Serpentine belt defect
- (3) Stator turn-to-turn fault
- (4) Rotor eccentricity (bent shaft)
- (5) Worn bearing

Although some other types of faults, such as the loose electrical connection, diode fault, and voltage regulator fault, are commonly encountered in practice, the detection and isolation of these faults are relatively trivial and are therefore not included in this PhD research.

6.3 Finite-element Model of the Claw-pole Generator

Detailed models of the claw-pole generator can help greatly in understanding and analyzing the effects of various types of generator faults. Commercial finite-element software is a convenient and proven tool for detailed modeling of transient behaviors of

the electric machines [89]. It is generally more accurate and flexible than other modeling methods such as magnetic equivalent circuit or analytical modeling [90, 91]. In the proposed research, the finite-element models of the generators are built in Ansoft Maxwell 3D ©.

Unfortunately, the design information of the claw-pole generator is not provided by the manufacturer. In order to obtain the detailed design information, one of the generators is completely disassembled and reverse engineered. The 3D solid model of the generator is shown in Figure 6.5.

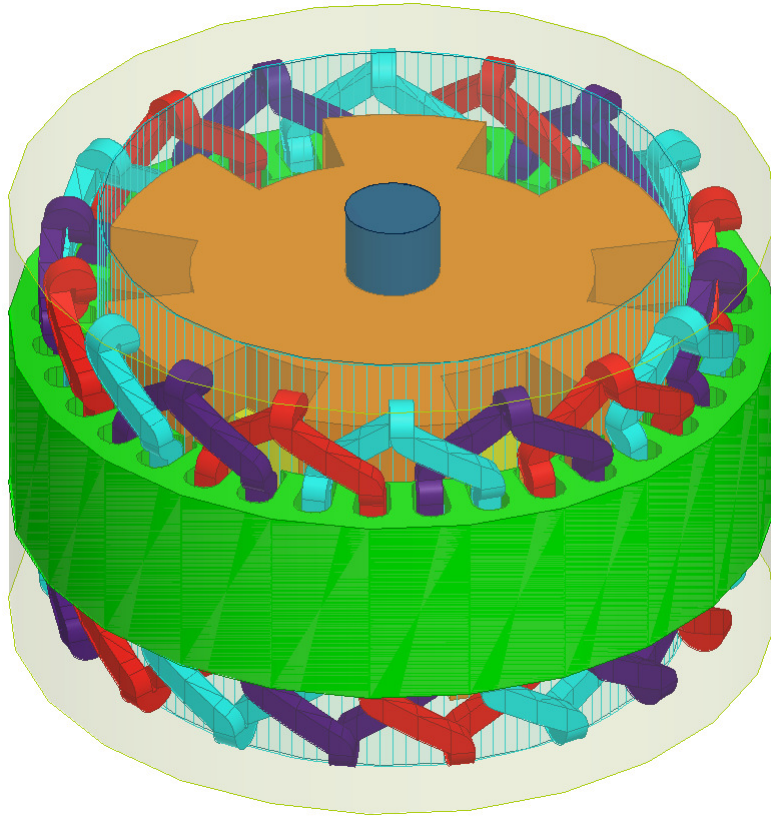


Figure 6.5: Finite-element model of the claw-pole generator.

The model in Figure 6.5 is built to the level of detail that most important features of the generator geometries are preserved. Some small geometric features are not modeled because they can slow down the simulation process significantly. The green assembly is

the stator core filled with three-phase wave-wound stator windings. The bronze assembly is the claw-pole rotor core, excited by the field winding inside the rotor core. The deep blue assembly is the rotor shaft. The model is very flexible in the sense that it can be easily modified to represent different types of generator faults, such as a stator turn fault or rotor eccentricity.

In addition to geometric dimensions, the accuracy of the finite-element model is also highly dependent on the magnetic property of the stator and rotor core materials. The material of the stator core is determined by visual inspection to be normal silicon steel (M-19). To figure out the magnetic property of the rotor core, a ring-shape sample is cut from the rotor of the disassembled generator. Two sets of coils are wound on the ring-shape sample. By injecting a series of DC currents into one set of the windings and measuring the transient-voltage responses of the other set of the winding, the DC B-H curve of the rotor material can be obtained, as shown in Figure 6.6.

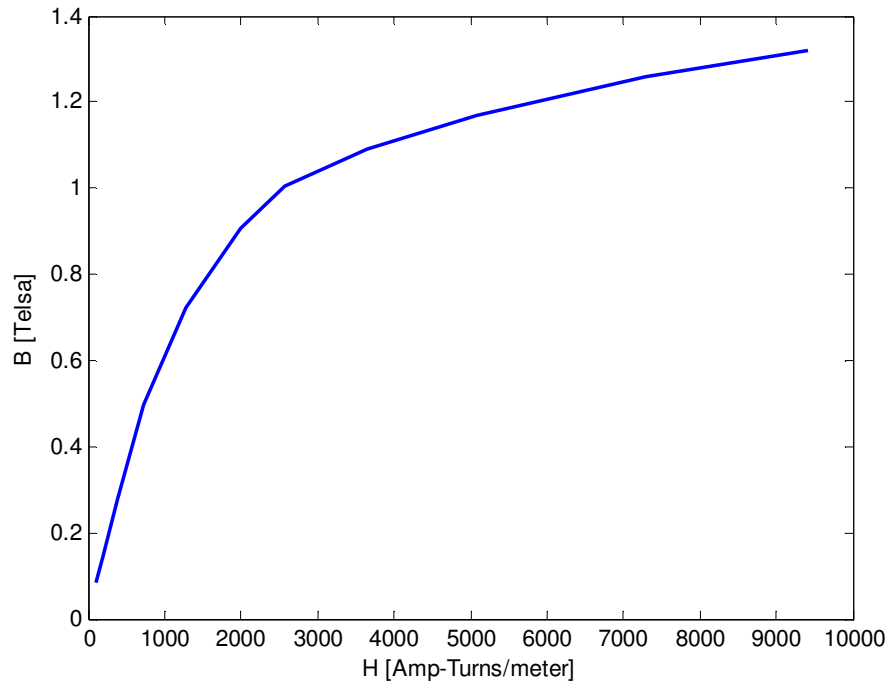


Figure 6.6: Measured DC B-H curve of the rotor material.

The finite-element model is validated by comparing the simulation results and experimental results. Specifically, Figure 6.7 shows the simulated phase voltage and measured phase voltage under the same speed and no load condition. The simulated voltage agrees well with the measured voltage.

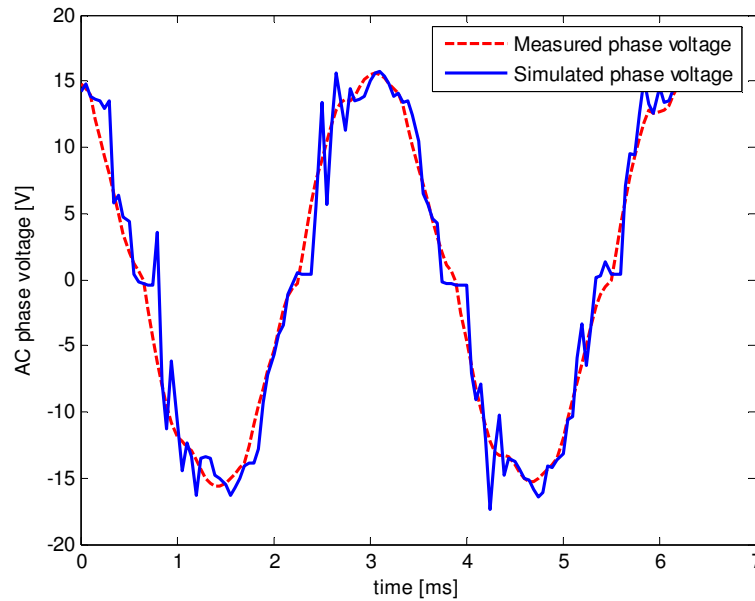


Figure 6.7: Experimental and simulated open-circuit voltage waveforms.

Figure 6.8 and Figure 6.9 shows the spatial distribution of the magnetic flux in the rotor and stator core of the generator respectively. The magnetic flux originally flows in the axial direction inside the rotor yoke, but it is then bent by the rotor claws and becomes oriented in the radial direction in the airgap. After the magnetic flux leaves one rotor pole, it enters the stator core, links a few slots of stator conductors and then enters back into the adjacent rotor pole. As can be seen in both plots, the distribution of the magnetic is truly three-dimensional and highly complex.

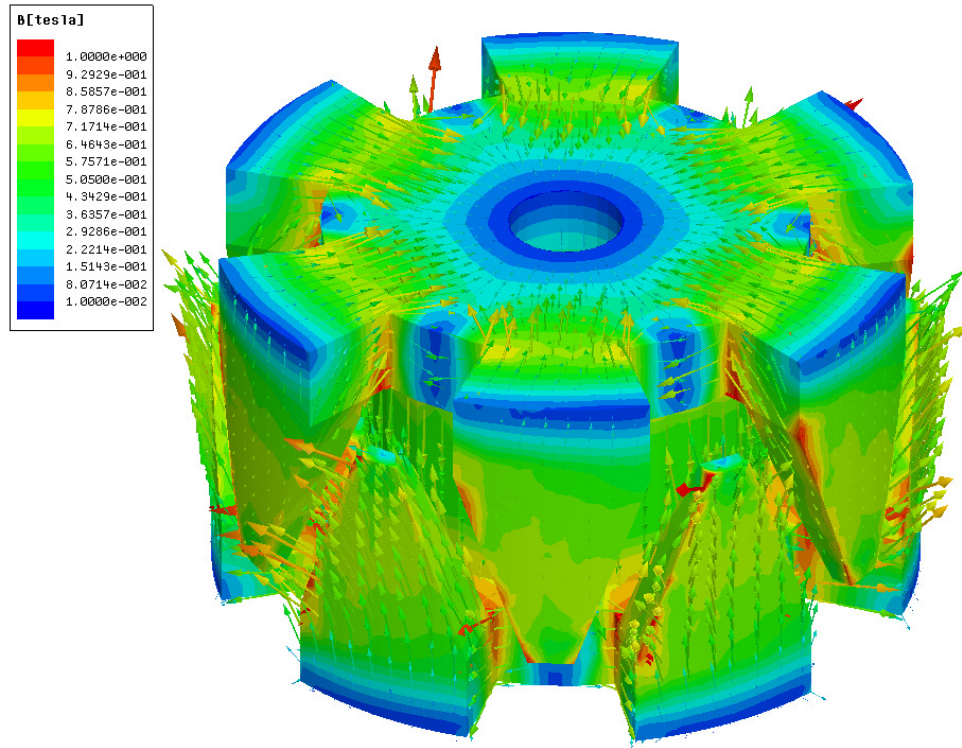


Figure 6.8: Magnetic flux distribution in the rotor core.

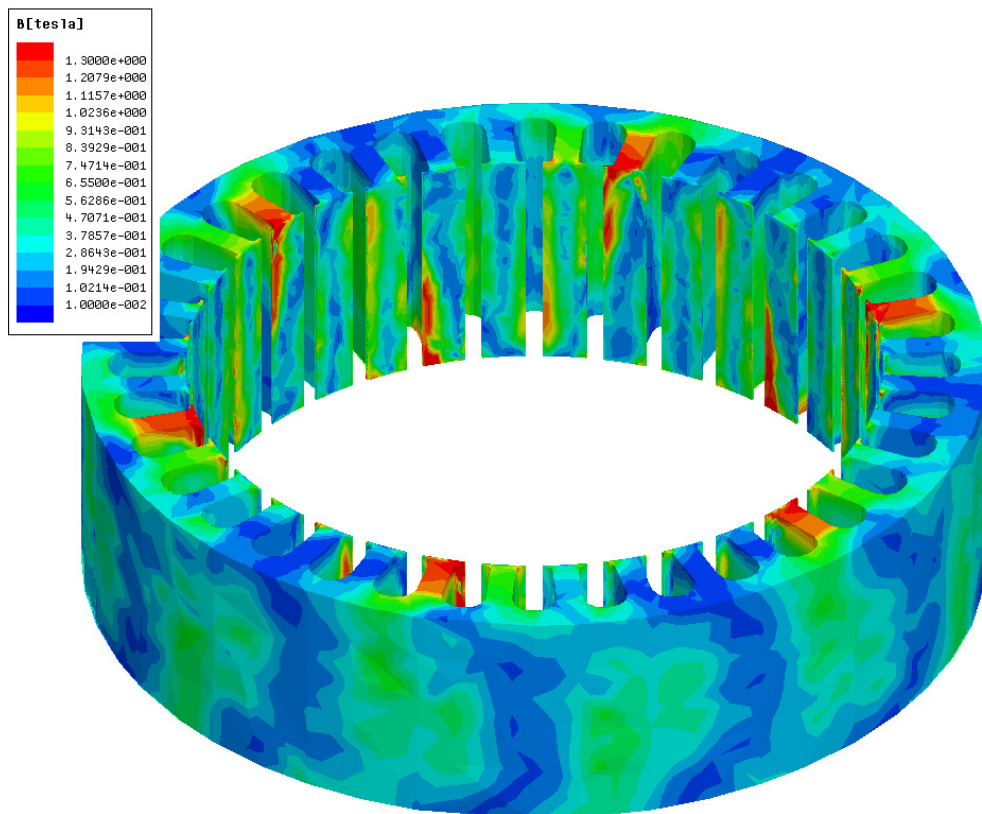


Figure 6.9: Magnetic flux distribution in the stator core.

6.4 Test Bench Setup

In terms of condition monitoring for claw-pole generators, possible physical quantities that may be monitored include, field voltage, field current, three-phase stator current, three-phase stator voltage, rectified generator current, and rectified generator voltage. Among all these quantities, some are more difficult to access than the others. Table 6.1 summarizes the intrusiveness of monitoring each of the aforementioned quantities in the vehicle EPGS environment.

Table 6.1: Physical quantities that may be monitored in a claw-pole generator

Quantities Monitored	Intrusiveness	Comments
DC output voltage	Very low	Already monitored in the EPGS system.
DC output current	Low	Already monitored in the EPGS system. But higher-bandwidth current sensor may be needed.
Rotor field voltage	Very low	Already monitored in the EPGS
Rotor field current	Very high	Major modifications to the generator voltage regulator are needed to monitor the field current. Additional current sensor is needed.
Stator three-phase voltages	High	Modifications to generator package and wirings are needed to monitor the AC voltage.
Stator three-phase currents	Very high	Major modifications to the generator stator windings are needed to monitor the AC current. Additional current sensors are needed.

Due to the stringent cost constraint in automotive applications, condition monitoring schemes for claw-pole generators should be nonintrusive and low-cost. Ideally, only the DC output voltage, DC output current, and rotor field voltage should be used for condition monitoring purposes.

In this study, special modifications have been made to the experimental generator so that all six physical quantities can be monitored. This helps better understand the effect of the built-in rectifier on generator voltages and currents during the research stage.

In order to analyze the voltage and current spectra of claw-pole generators, a generator test bench is built and shown in Figure 6.10. The “vehicle engine” is simulated by an Allen Bradley © servo motor. Controlled by a PC, the servo motor drive is able to simulate complex load profiles within a wide speed range. The servo motor is coupled to the generator through a pulley-serpentine belt assembly. The generator is electrically loaded with several high-current power resistors and one lead-acid battery. The generator voltages and currents are monitored using LEM sensors. The measured data is recorded by the National Instrument © data acquisition system.

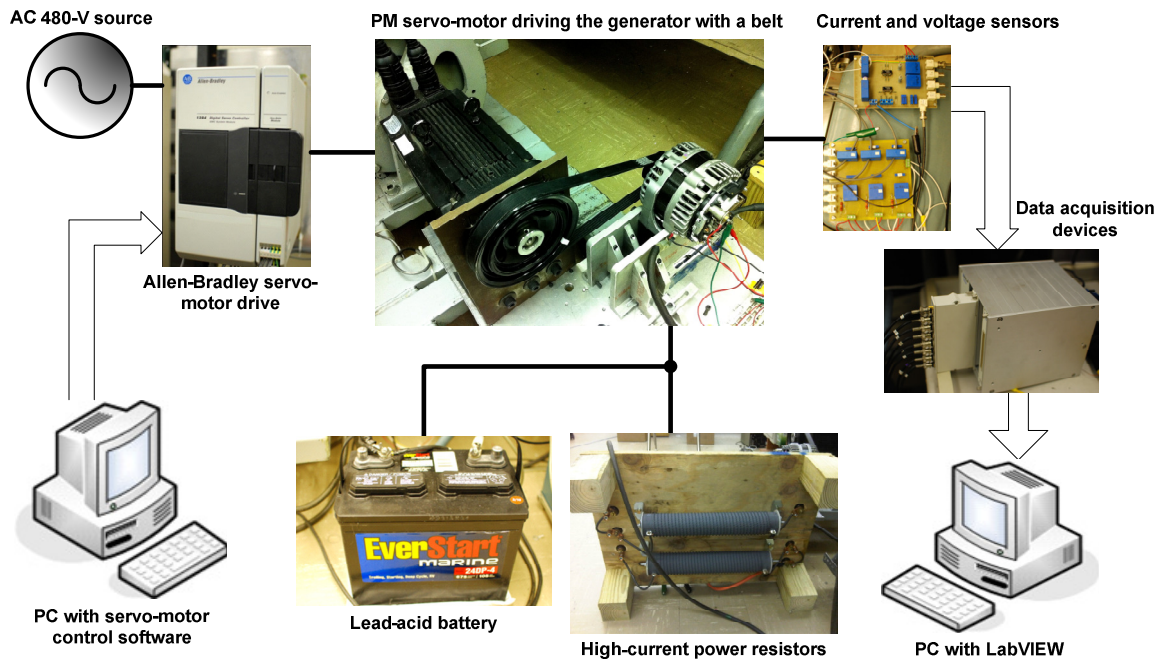


Figure 6.10: Test bench for claw-pole generators.

A similar but more advanced test bench is available for access at the GM EPGS test facility, as shown in Figure 6.11. The digitally controlled DC load bank allows for

continuous variation of the generator load level. A dSPACE © embedded processor also allows for real-time validation of the proposed condition monitoring schemes.

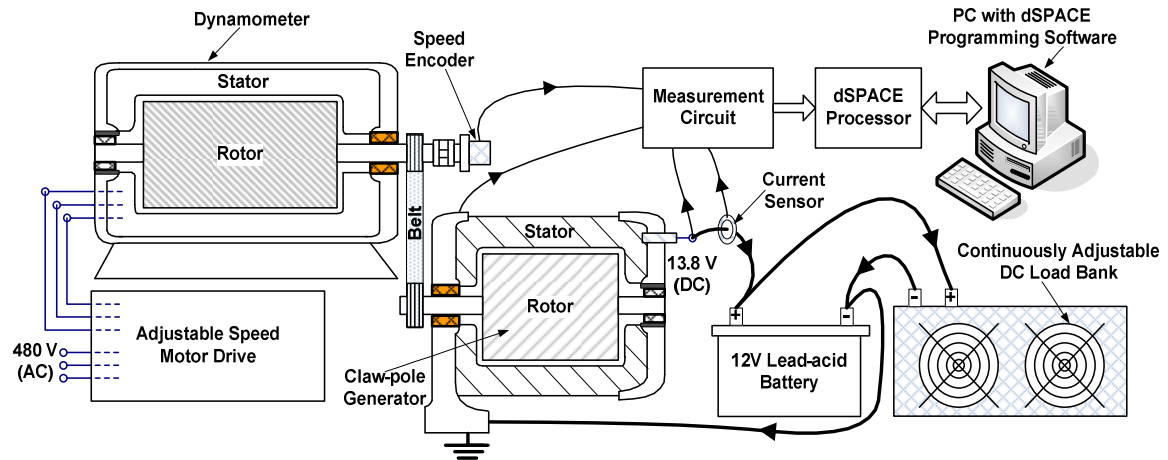


Figure 6.11: EPGS test facilities at General Motors.

A complete set of generator voltage and current waveforms obtained from above test bench is shown in Figure 6.12~Figure 6.14

As can be seen in Figure 6.12, the field voltage is a PWM signal that switches between -0.7V and the generator DC output voltage. The switching frequency is at about 400 Hz. The field current is mainly DC, with some ripples induced by the PWM switching of the voltage regulator.

The line-to-line voltage and line current are shown in Figure 6.13. The AC voltage has a somewhat flat top because of the voltage-clamping effect of the battery. Typical to a three-phase rectifier, the AC current has two small lobes on the peaks of the waveform and stays zero for a short period of time during zero crossing.

The generator output voltage and current are shown in Figure 6.14. Both the voltage and current are rich in harmonics. While the high-frequency ripples are most likely introduced by the rectifier, there are also some lower-frequency ripples in the voltage and current spectra that correspond to the switching of the voltage regulator.

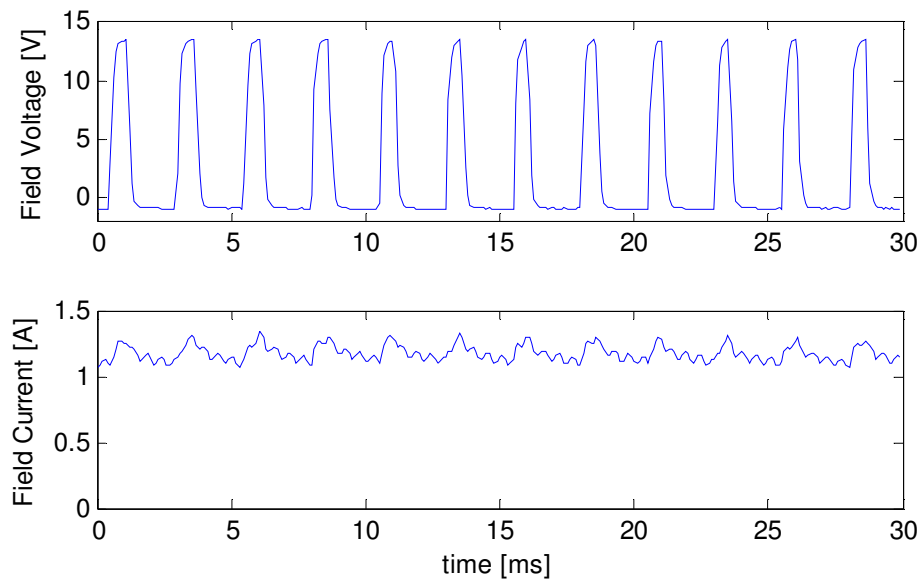


Figure 6.12: Generator field voltage and field current.

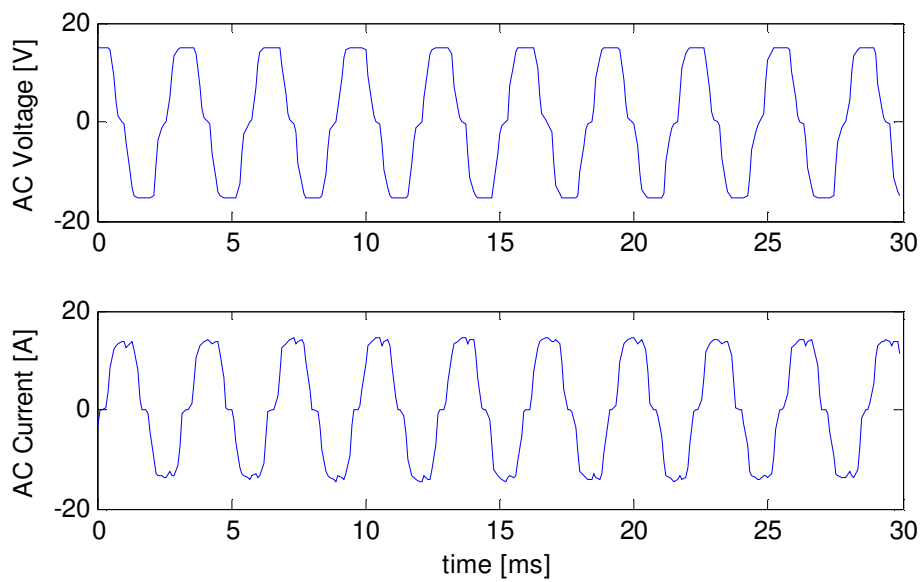


Figure 6.13: Generator line voltage and phase current.

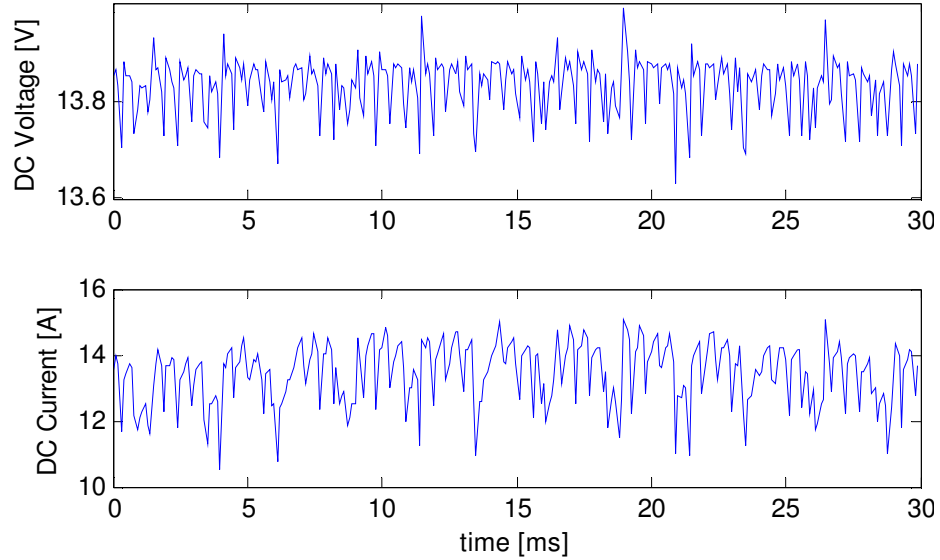


Figure 6.14: Generator output voltage and output current.

6.5 Spectral Analysis

6.5.1 Voltage-regulator Switching Harmonics

The spectrum of the generator field voltage at a certain operating condition is shown in Figure 6.15. The exact PWM switching frequency of the voltage regulator is located at 398.3 Hz. The 2nd~7th order harmonics of the PWM frequency are also presented in the field voltage spectrum. Overall, the spectral contents of the field voltage are very similar to those of a square wave.

The voltage-regulator switching harmonics are also present in the generator output voltage spectrum, as shown by the harmonics marked by red circles in Figure 6.16.

The spectrum of the generator output current is shown in Figure 6.17. The harmonic contents are similar with those in the voltage spectrum. However, the magnitudes of the current harmonics are usually much higher than the corresponding spectral bins in the voltage spectrum. This is mainly because the connected battery is a large capacitive load that has low impedance in the high-frequency range.

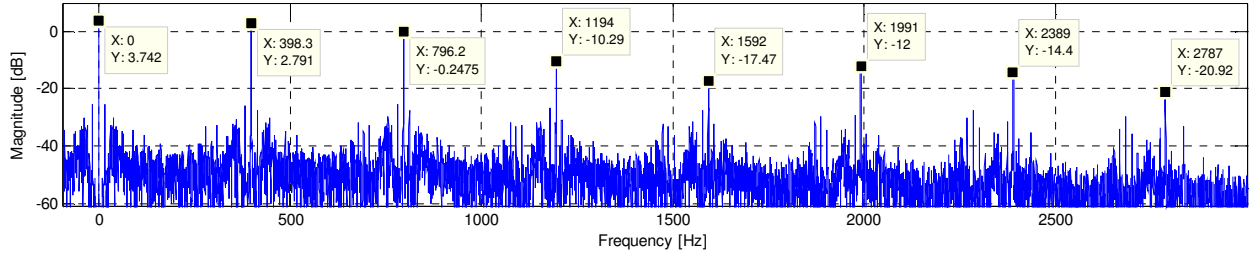


Figure 6.15: Spectrum of generator field voltage.

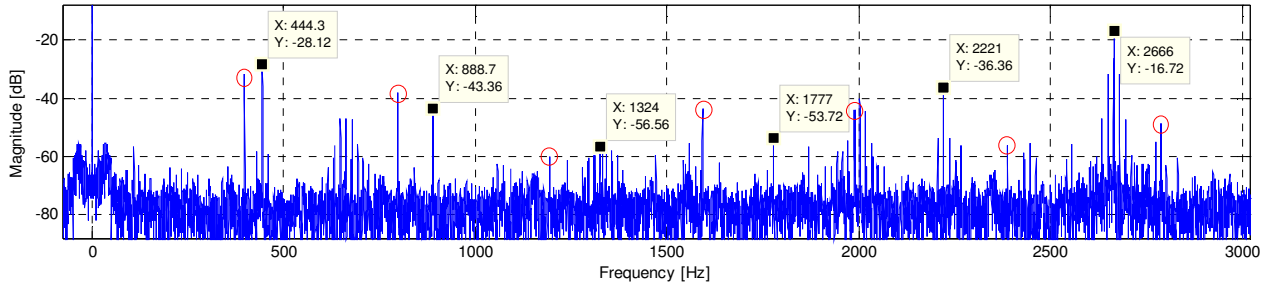


Figure 6.16: Spectrum of generator output voltage.

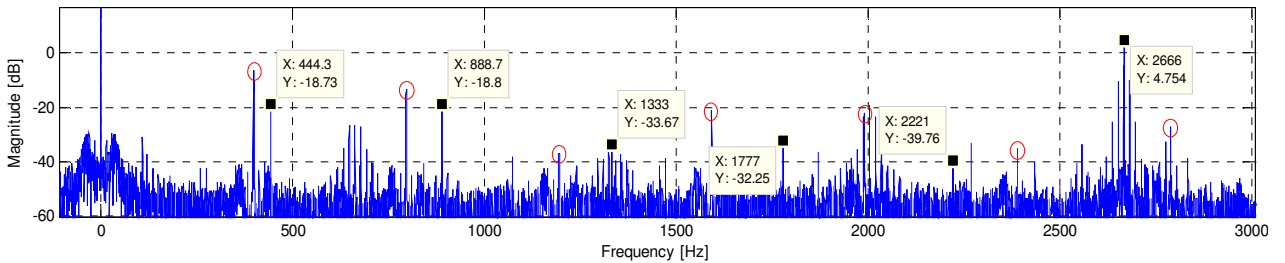


Figure 6.17: Spectrum of generator output current.

6.5.2 Rectifier Ripple Harmonic

In the current spectrum shown in Figure 6.17, the frequency component at 2666 Hz has the largest magnitude in the generator voltage spectrum except for the DC component. Since the experimental generator has 12 poles and is running at 4443 rpm, this frequency component at 2666 Hz is confirmed to be the rectifier ripple harmonic.

The frequency of the rectifier ripple harmonic, if accurately tracked over time, can be used to estimate the speed of the synchronous generator. By comparing the estimated generator speed with the engine speed, the fault of serpentine-belt slip can be effectively

detected. A real-time implementation of the belt-slip detector is described in detail in Chapter 7.

6.5.3 Harmonics at Integral Factors of the Rectifier Ripple Frequency

In addition to the rectifier ripple harmonic, the output current spectrum also contains relatively evident spectral bins at $1/6$, $1/3$, $1/2$, $2/3$ and $5/6$ of the rectifier ripple frequency, which are marked by black dots in Figure 6.16 and Figure 6.17.

Specifically, the harmonic component at $1/3$ of the rectifier ripple frequency (888.7 Hz in Figure 6.17) is an accurate indicator of the three-phase asymmetry of generator. In fact, this harmonic component in the rectifier output is the counterpart of the negative-sequence component in the three-phase system. A stator turn-fault detector based on this spectrum signature is described in detail in Chapter 8.

6.5.4 Harmonics related to the Belt Cycle

Figure 6.18 is a zoom-in plot of Figure 6.17 around 2600 Hz. The rectifier ripple frequency is located at 2665.7 Hz. Two relatively large spectral bins are located symmetrically around the rectifier ripple frequency at 2650.5 Hz and 2680.9 Hz.

These two side-band harmonic components are caused by the uneven thickness and tension of the serpentine belt, i.e. the line speed and transmitted torque vary slightly within a full cycle of the belt. The exact frequencies of the belt-cycle related harmonics can be determined as follows,

$$f_{belt} = f_{ripple} \pm \frac{f_{ripple}}{3 \cdot p_1 \cdot k_{belt}}, \quad (6.1)$$

where f_{ripple} is the rectifier ripple frequency, p_1 is generator pole number, and k_{belt} is the number of generator shaft revolutions per belt cycle.

These harmonic components can be used to detect belt defects. A detailed discussion of this topic will be presented in Chapter 7.

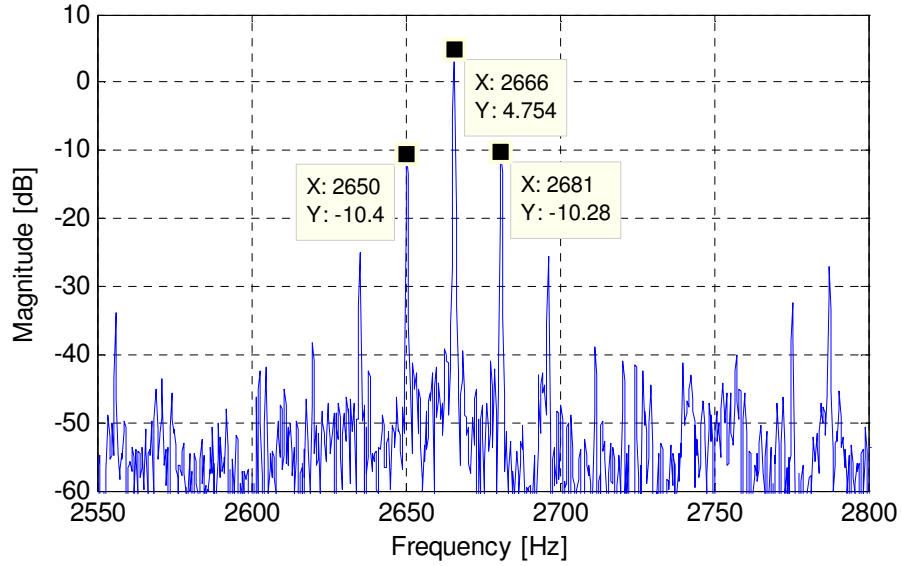


Figure 6.18: Zoom-in plot of the output current spectrum around the rectifier ripple frequency

6.5.5 Harmonics related to the Torque Oscillations of the Prime Mover

Figure 6.19 is a zoom-in plot of Figure 6.17 around 200 Hz. The frequency component at 109.9 Hz in Figure 6.19, for example, is related to the torque oscillation of the prime mover.

Generally, the frequency of the torque-oscillation-related harmonic can be determined as follows,

$$f_{osc} = \frac{p_2 \cdot f_{ripple}}{3 \cdot p_1 \cdot k_{pulley}}, \quad (6.2)$$

where f_{ripple} is the rectifier ripple frequency, p_1 is generator pole number, p_2 is the cycles of torque oscillations per mechanical revolution of the prime mover, and k_{pulley} is the pulley ratio.

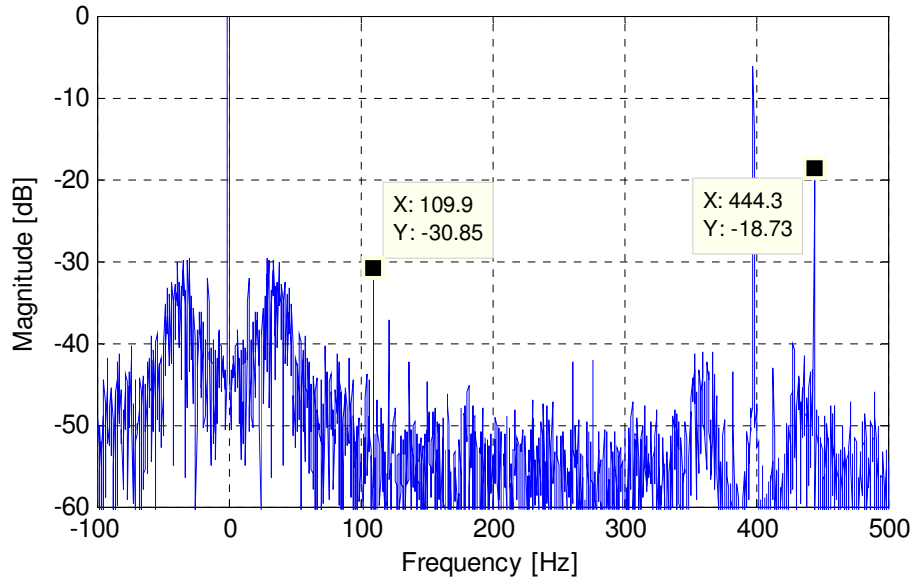


Figure 6.19: Zoom-in plot of the output current spectrum around 200 Hz.

This harmonic component can be potentially used to monitor torque oscillations of the vehicle engine or other important accessories that also have an oscillating torque characteristic, such as the air compressor and water pump. However, the problem is beyond the scope of this study and is not further investigated in this PhD study.

6.6 Chapter Summary

The claw-pole generator is a family of electric machine on its own. It has vastly different operating environment and failure modes from conventional industrial electric machines. This chapter presents an introduction to the condition monitoring of claw-pole generators. The common failure modes and failure mechanisms are thoroughly discussed, among which several important types of faults are selected for further investigation.

To better understand the effects of internal faults on the operation of the claw-pole generator, a detailed finite-element model is built using the parameters extracted from a disassembled generator.

A lab setup for testing the generator has also been built and spectrum analysis has been performed on the generator voltages and currents. All the major harmonic components in the voltage and current spectra have been identified and explained. Several important harmonic components in the voltage and current spectrum are shown to be potentially useful for,

- (1) estimating the generator speed or detecting the belt slip;
- (2) detecting the stator turn-to-turn fault in the generator;
- (3) detecting the defects in the serpentine belt;
- (4) detecting the torque oscillations in the prime mover.

The following chapters will go into more details on the detection and protection of specific generator faults.

CHAPTER 7 Detection of External Faults for Claw-pole Generators

7.1 Overview

The claw-pole generator is inherently part of the automotive EPGS system. The detection and isolation of external faults (or system-related faults) is very important to improve the overall system reliability and to reduce misdiagnoses of the claw-pole generator itself.

In this chapter, a sensorless speed estimator is proposed for claw-pole generators using only the generator output voltage information. The proposed speed estimator is further applied to the detection of serpentine belt slip. The experimental results show that the method is able to estimate the generator speed accurately even during fast mechanical transients. The belt-slip fault can thus be reliably detected within a wide speed range.

This chapter also proposes a method to detect serpentine belt defects using only the generator output current information. The signal processing technique proposed for belt-defect detection can also be applied to detections of other faults of claw-pole generators.

7.2 Generator Speed Tracking and Detection of Belt Slip

7.2.1 Principle of the Belt-slip Detector

In an automotive EPGS system, the accurate engine speed is always known to the vehicle controllers. The speed of the claw-pole generator, on the other hand, is strictly related to the frequency of the rectifier ripples as discussed in section 6.5.2.

The specific relationship can be described as follows,

$$n_{gen} = \frac{60 \cdot f_{ripple}}{P \cdot n_{diode}}, \quad (7.1)$$

where n_{gen} is the generator mechanical speed, f_{ripple} is the rectifier ripple frequency, P stands for the number of pole pairs of the generator, and n_{diode} is the number of diodes in the rectifier.

For a typical 12-pole generator with a three-phase full-bridge rectifier, the frequency of the output voltage ripple is 0.6 times of the generator speed in rpm. The serpentine belt slip is detected when the generator speed drops below the engine speed adjusted for the pulley ratio.

In addition to being used to detect belt slip, the rectifier ripple frequency is also the baseline frequency for real-time recognition and location of all other harmonics in the voltage and current spectra of the generator. Therefore, the frequency of the rectifier ripples must be estimated very accurately.

With a reasonable sampling frequency of 10 kHz, a time-frequency transform based on Hanning-window interpolated FFT is proposed in this study to accurately extract the voltage ripple frequency with relatively short sample time. Frequency-domain methods [92-94] are used because they are generally less prone to performance degradation caused by noise than time-domain methods [94].

As can be seen in Figure 6.16, the spectrum of generator output voltage contains several harmonic components with relatively large amplitudes in addition to the rectifier ripple harmonic. In order to reduce the interference from other frequency components when locating the rectifier ripple frequency, it is desirable to apply a digital notch filter to eliminate frequency components at DC and the voltage-regulator PWM frequency. The DC notch filter has a discrete-time transfer function of,

$$H(z) = \frac{1 - z^{-1}}{1 - r \cdot z^{-1}} \quad (0 < r < 1), \quad (7.2)$$

where the parameter r controls the width of the notch. The closer the value r is to 1, the sharper the notch is.

The notch filter at the PWM frequency has a discrete-time transfer function of,

$$H(z) = \frac{(1 - e^{j\omega_0} z^{-1})(1 - e^{-j\omega_0} z^{-1})}{(1 - re^{j\omega_0} z^{-1})(1 - re^{-j\omega_0} z^{-1})} = \frac{1 - 2\cos\omega_0 z^{-1} + z^{-2}}{1 - 2r\cos\omega_0 z^{-1} + r^2 z^{-2}} \quad (0 < r < 1) \quad (7.2)$$

Here, r still controls the width of the notch. $\omega_0 = \frac{398}{10000} \cdot 2\pi$, which is the normalized frequency to be rejected.

7.2.2 Interpolated FFT for Ripple Frequency Extraction

It should be noted that the spectrum in Figure 6.16 is obtained from 8192-point FFT with a 10 kHz sampling frequency. In practice, such large-scale FFT is hardly computationally feasible for embedded micro-processors in vehicles. Moreover, since the generator speed is highly dynamic in nature in a typical urban driving cycle, the long sample time (0.8192 sec) of the 8192-point FFT makes it difficult to track the generator speed reliably during fast mechanical transients.

To address these problems, FFT with a significantly narrower window size (256 points) is used to increase the time resolution (refresh rate) of the generator speed estimation. However, with such short FFT window size, the frequency resolution will suffer. In Figure 7.1, for instance, the spectrum resolution from 256-point is only 39 Hz compared to the frequency resolution of 1.22 Hz from 8192-point FFT. Whereas the largest spectral bin from 256-point FFT is located at 1523.4 Hz, the true ripple frequency

is actually at 1511 Hz. As a result, there will be larger errors in the estimated generator speed.

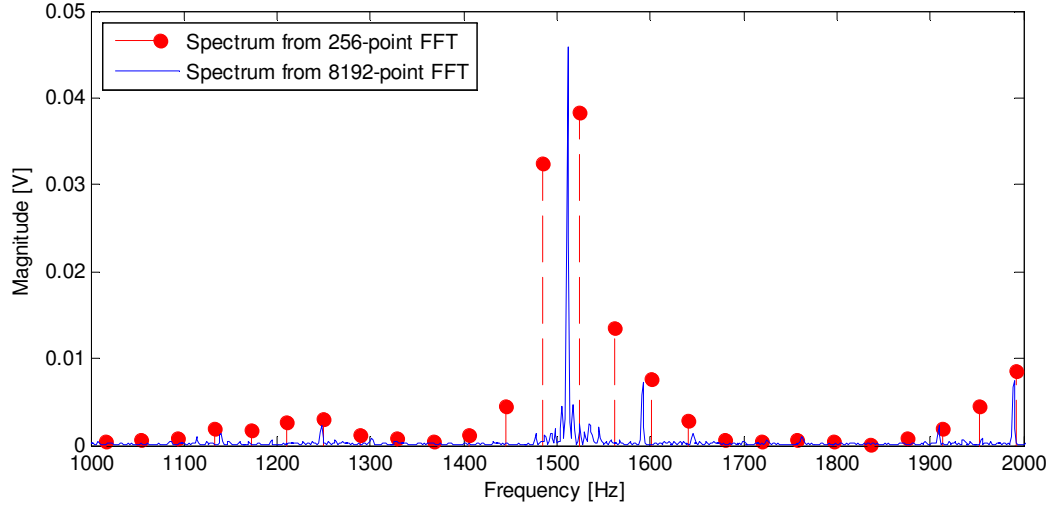


Figure 7.1: Comparison of the generator output voltage spectrum with different FFT sizes.

An interpolated-FFT method is employed [92-94] to improve the speed estimation accuracy while not increase the size of the FFT. Consider Δt is the time interval between two consecutive data samples, N is the number of data points in FFT. Then the frequency interval between the spectral bins in the current spectrum will be,

$$f_0 = \frac{1}{N\Delta t}, \quad (7.3)$$

That is, all spectral bins will be located in the FFT spectrum at the integral multiples of f_0 .

Assume f is the peak frequency that is to be located. Generally, f will fall between two adjacent spectral bins. Therefore, f will be a fractional multiple of f_0 ,

$$f = (i + \delta)f_0 = \lambda f_0 \quad (0 \leq \delta < 1), \quad (7.4)$$

where i is the integer part of λ and δ is the fractional part of λ .

The interpolated FFT algorithm [92] starts from the two adjacent spectral bins which have the largest amplitudes, denoted as $X(i)$ and $X(i+1)$ respectively, where i and $i+1$ are the indices of the two spectral bins. The true peak of the spectrum will thus be located between these two loudest frequency components. The exact location of the peak can be estimated from the frequencies and amplitudes of the two loudest spectral bins given a certain window function.

For FFT that uses a Hanning window, there exist very simple analytical equations for calculating δ ,

$$\delta = \frac{2\alpha - 1}{\alpha + 1}, \quad (7.5)$$

where,

$$\alpha = \frac{|X(i+1)|}{|X(i)|}. \quad (7.6)$$

Once δ is determined, the frequency of the true peak can therefore be obtained from equation (7.4). In the example shown in Figure 7.1, the peak frequency located using interpolated 256-point FFT is 1509 Hz, which is now very close to the 1511 Hz given by the 8192-point FFT.

7.2.3 Frequency Locking

In practice, it is found that even if the DC component and the 398-Hz PWM switching harmonic are eliminated from the voltage spectrum as shown in Section II, there are still chances that the algorithm may occasionally snap to an incorrect frequency such as the 2nd order harmonic of the ripple harmonic.

To solve this problem completely, the characteristic of the ripple frequency must be further investigated. The generator speed cannot change abruptly due to the inertia of the rotating machinery and nor does the rectifier ripple frequency. Therefore, every time the ripple frequency needs to be updated, it won't be too far away from the previously located ripple frequency. This means that instead of searching the whole spectrum for peak voltage harmonic, it is only necessary to search for the peak voltage harmonic within a small neighborhood of the previously extracted frequency. During the very first time of the peak frequency location, when no information of previously located ripple frequency is available, the engine speed and pulley ratio can be used to initialize the search range.

7.2.4 Spectrum Aliasing

Reliable detection of belt slip also requires accurate and continuous tracking of the generator speed within a wide speed range. Typical claw-pole generators have a speed range from 1800 rpm to 16,000 rpm due to the rather wide speed range of the vehicle engine. With a sampling frequency of 10 kHz, the maximum frequency component that can be detected in theory is 5 kHz, which corresponds to a generator speed of 8333 rpm. For any ripple frequency higher than 5 kHz, the effect of spectrum aliasing kicks in and the ripple frequency actually folds back to the region below 5 kHz. This introduces ambiguity when interpreting the generator speed. For example, if the rectifier ripple harmonic appears to be at 4.5 kHz, the generator speed may be either 7500 rpm or 9167 rpm without any further information.

This limitation of the generator speed estimation can be properly overcome with the prior information of the engine speed. When the belt-slip detector senses a mismatch

between the estimated generator speed and the engine speed, it takes a step further to determine whether the mismatch is caused by belt slip or merely by the spectrum aliasing. This effectively doubles the speed range of belt slip detector all the way up to 16667 rpm using the same 10 kHz sampling frequency. In the following experimental results, the estimated speed is not corrected just to show the effects of spectrum aliasing.

Complete procedures to detect belt slip are summarized in a flowchart in Figure 7.2.

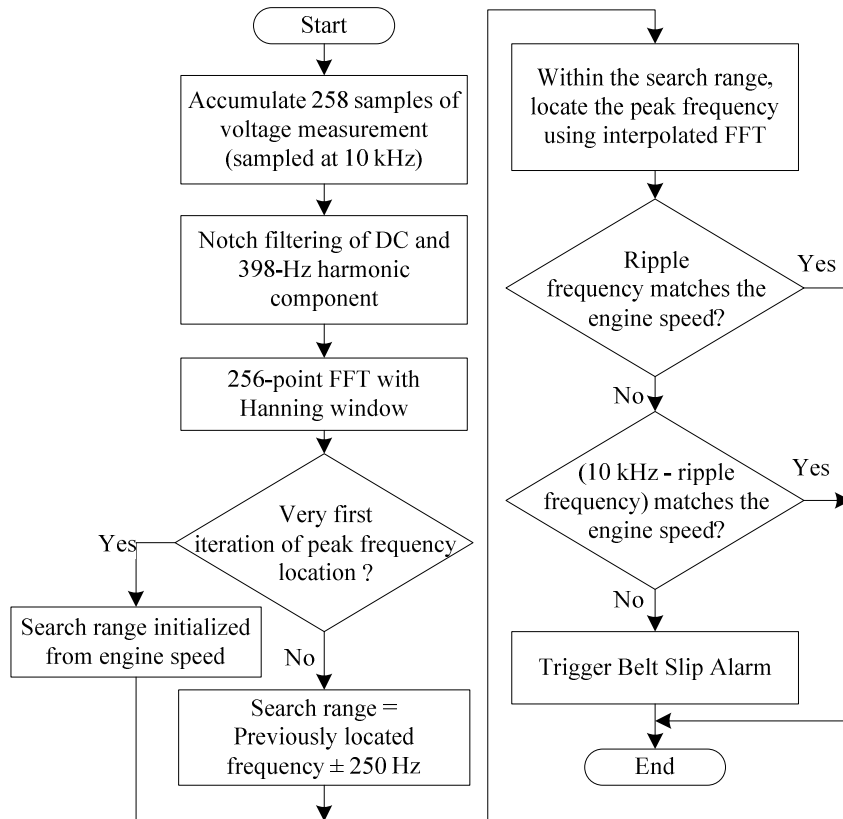


Figure 7.2: Major procedures for generator speed tracking and belt-slip detection.

7.2.5 Experimental Results

The above algorithm for detecting belt slip is implemented in real time in dSPACE© and is experimentally validated in the GM EPGS test facility shown in Figure 6.11. The

belt connecting the generator and the prime mover is intentionally made loose so that the belt slippage can be induced when the load torque is sufficiently high.

Figure 7.3 demonstrates the performance of the proposed method on generator speed tracking and belt-slip detection. In the middle subplot of Figure 7.3, the blue curve is the measured engine speed, the green curve is the measured generator speed, and the red curve is the estimated generator speed. When there is no belt slippage, the generator speed is exactly 3.162 times of the engine speed because of the pulley ratio. The estimated generator speed in green agrees very well with the true generator speed in red even when generator speed is varying.

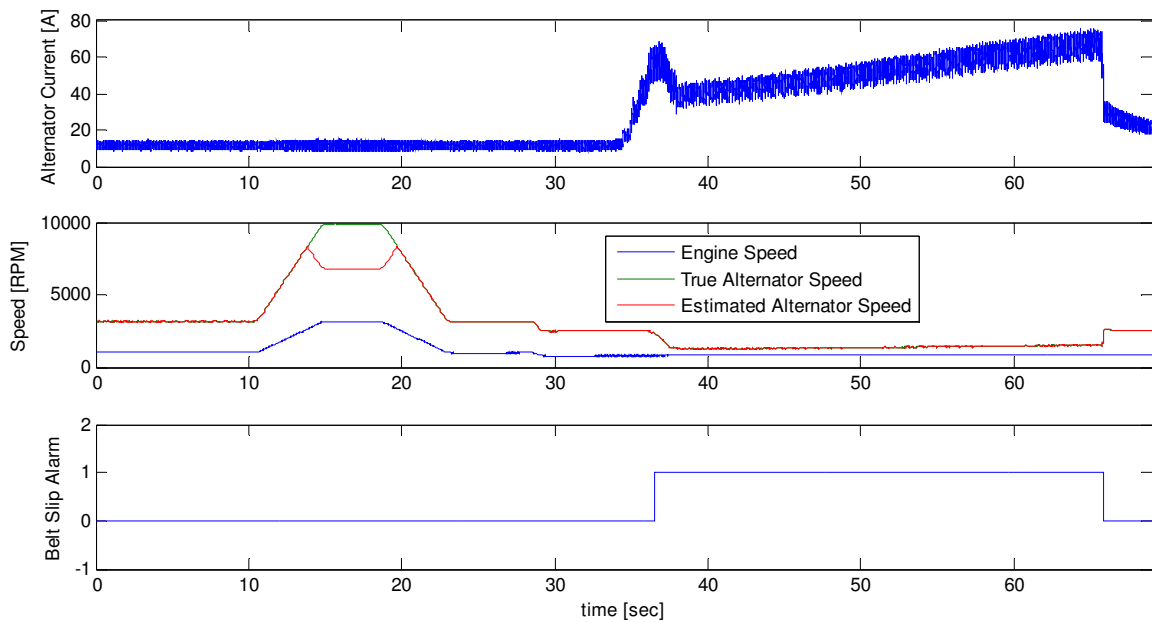


Figure 7.3: Experiment results of generator speed tracking and belt-slip detection.

Between the 13th seconds and the 22nd seconds in Figure 7.3, when the generator speed exceeds 8333 rpm, the speed estimator is not able to track the generator speed any more due to the limit in the sampling frequency. However, the fault detection logic cleverly recognizes that the mismatch between the estimated generator speed and the

engine speed are merely caused by the spectrum aliasing. Therefore, the belt slip alarm in the bottom subplot of Figure 7.3 is not triggered, and the false alarm is avoided.

Beginning around the 37th seconds, the load current in the top subplot of Figure 7.3 is increased substantially to more than 60 A. The belt thus begins to slip. The estimated generator speed drops significantly while the engine speed remains constant. The fault detection logic senses the mismatch between these two speeds, and the belt slip alarm is triggered.

Around the 66th seconds in Figure 7.3, the load current is suddenly reduced back to around 20 A. The belt quickly recovers from slip and the generator speed rises back extremely fast. Even during such fast mechanical transient, the estimated generator speed still has no problem tracking the true generator speed. The fault detection logic then clears the belt slip alarm.

7.3 Detection of Belt Defects

7.3.1 Principle of the Belt-defect Detector

In passenger vehicles, it is common for aged serpentine belts to develop defects such as torn rubbers in the grooves, as shown in Figure 7.4. Such defects are early signs of a failing belt, and it is highly recommended to replace the serpentine belt soon to prevent unexpected loss of electric power and crucial accessories that are driven by the same belt.

The belt defect will change the effective thickness of the serpentine belt at the place of defect. When the belt defect makes contact with the pulley of a running claw-pole generator, it will slightly change the generator speed or transmitted torque every belt revolution. This modulation of the generator speed will give rise to the harmonic

components that are related to the belt cycle. The exact frequencies of these belt-cycle related harmonics are given in section 6.5.4., as,

$$f_{belt} = f_{ripple} \pm \frac{f_{ripple}}{3 \cdot p_1 \cdot k_{belt}}, \quad (7.7)$$

where f_{ripple} is the rectifier ripple frequency, p_1 is generator pole number, and k_{belt} is the number of generator shaft revolutions per belt cycle. Hence, by monitoring the magnitude of the belt-cycle related harmonics, the belt defect can be detected.

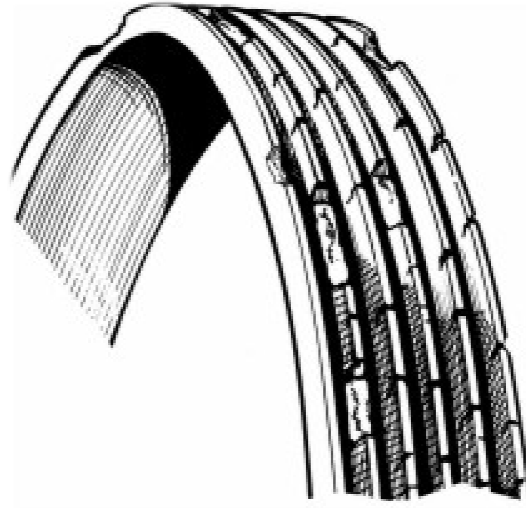


Figure 7.4: Illustration of aging serpentine belt with torn rubber in the grooves

A 2-cm defect is created on one groove of the experimental serpentine belt, as shown in Figure 7.5.



Figure 7.5: Artificially induced belt defect

Figure 7.6 and Figure 7.7 compares the generator output current spectra near the rectifier ripple frequency before and after the defect is induced. Note that the defect is induced *in situ*, and the belt is never taken off the pulley between the two tests. Magnitudes of side-band harmonics have increased after the defect was induced, and the magnitude of the rectifier ripple harmonic has slightly decreased.

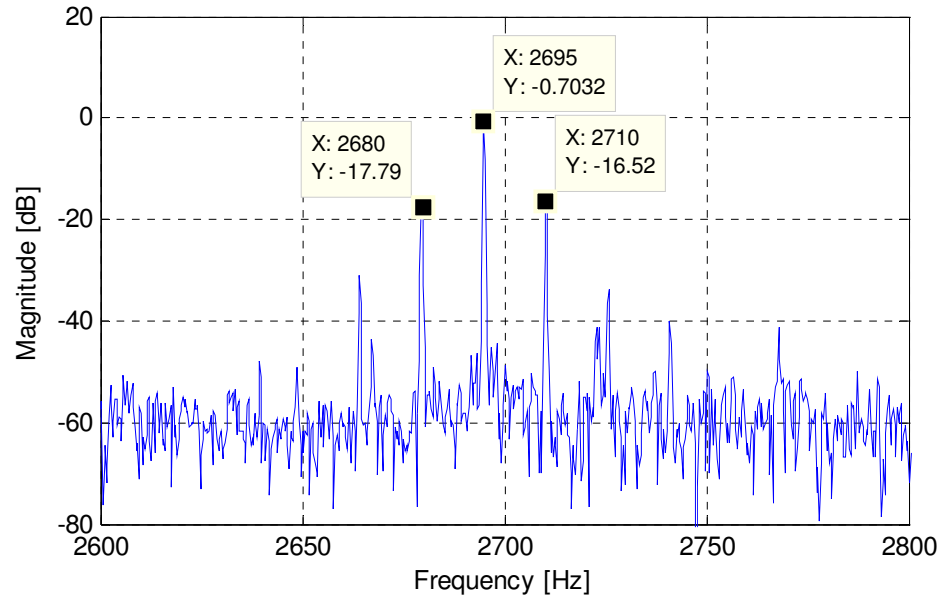


Figure 7.6: Generator current spectrum around the rectifier ripple frequency without any belt defect

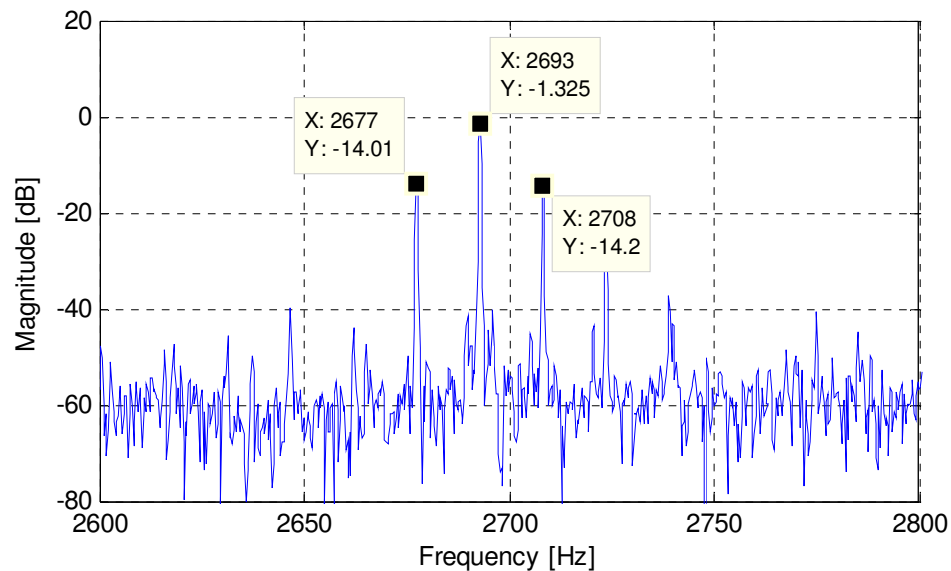


Figure 7.7: Generator current spectrum around the rectifier ripple frequency with the belt defect

To eliminate the effect of load change on the magnitude of the belt-cycle related harmonic, the following expression is proposed as the fault signature of serpentine belt defect,

$$\text{Fault signature} = \frac{|X_{belt1}| + |X_{belt2}|}{2 \cdot |X_{ripple}|}, \quad (7.8)$$

where magnitudes of belt-cycle related harmonics, $|X_{belt1}|$ and $|X_{belt2}|$, are normalized by the magnitude of rectifier ripple harmonic $|X_{ripple}|$. Since frequencies of these current harmonics are very close to each other, the variation of the load impedance has almost the same effect on all three harmonics. Therefore, the normalized magnitude in (7.8) is independent of the load impedance variation and is thus a robust indicator of the severity of the belt-defect fault.

7.3.2 Real-time Signal Processing Technique

The magnitudes of all current harmonics in section 7.3.1 are determined by high-resolution FFT spectrum. To avoid using FFT and to implement the belt-defect detector in real time, this section proposes the following signal processing technique consisted of three steps:

Step One: Locate the rectifier ripple frequency using the method outlined in Figure 7.2 in a real-time fashion.

Step Two: Use equation (7.7) to calculate the exact frequencies of current harmonic that are related to the generator belt cycle.

Step Three: Use the Goertzel algorithm to calculate the magnitudes of belt-cycle related current harmonics at the predetermined frequencies in a sample-by-sample fashion.

Unlike FFT that performs calculations on a block of data, the Goertzel algorithm calculates the spectral bins in a sample-by-sample fashion using recursive difference equations,

$$s(n) = x(n) + 2 \cos(2\pi\omega)s(n-1) - s(n-2), \quad (7.9)$$

$$y(n) = s(n) - e^{-2\pi i\omega}s(n-1), \quad (7.10)$$

where $x(n)$ is the input signal in the time domain, ω is the frequency of interest, in cycles per sample, $s(n)$ is an intermediate sequence and $y(n)$ is the spectral bin at the frequency ω .

By setting the frequency ω at exactly the belt-cycle related frequency, the final fault signature can be calculated with trivial computational efforts and virtually no additional memory requirement.

Not only is the proposed signal processing technique useful for identifying belt-cycle related harmonic, but it can also be used to identify other harmonics of interest in a real-time fashion. The only thing needs to be changed is the frequency of interest ω in the above procedure.

7.3.3 Experimental Results

Using the above signal processing technique, fault signatures from the healthy belt and the defective belt are compared in Figure 7.8 over a wide range of different speeds. The proposed signature does not vary with the load level at a certain speed. Whereas the fault signature does vary with the motor speed, the fault signature of the defective belt is always higher than the fault signature of the healthy belt at all test speeds, which demonstrates the effectiveness of the proposed method.

In practice, due to manufacturing imperfections, serpentine belts may exhibit some uneven thickness even when they are brand new. Figure 7.9 shows the measured signatures for one defective serpentine belt and four brand new serpentine belts of the same type.

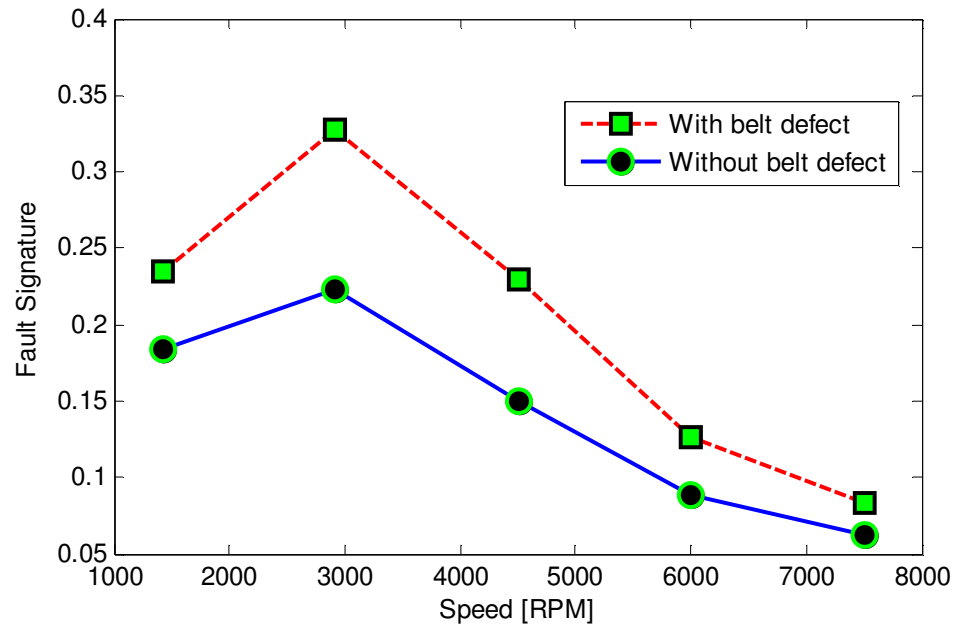


Figure 7.8: Experimental results of belt-defect detection at different speeds

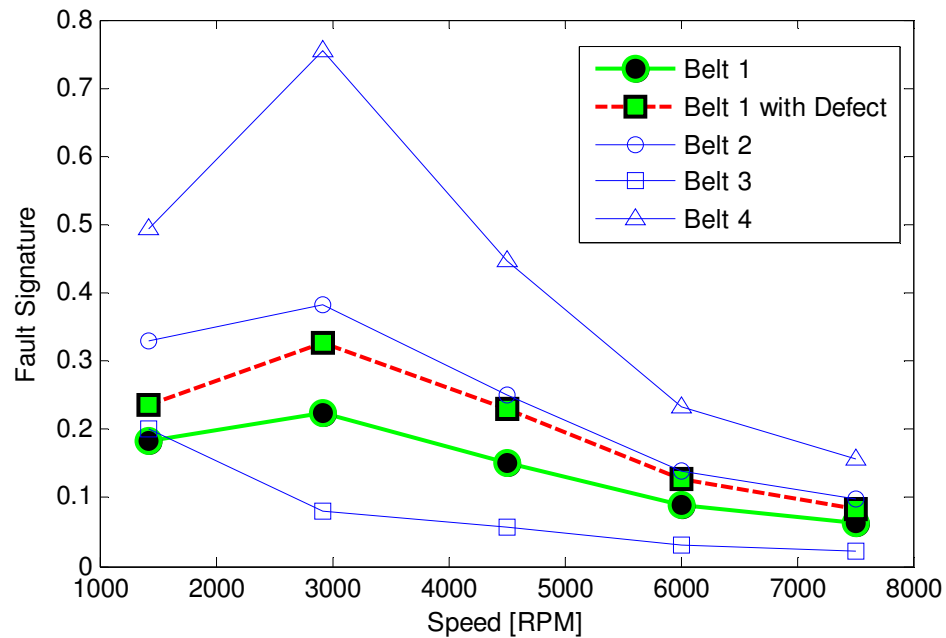


Figure 7.9: Fault-signature variations between different serpentine belts

As can be seen in Figure 7.9, observed fault signatures caused by belt sample variations may well exceed the fault signature caused by belt defect. This observation rules out the possibility for setting up a universal fault threshold for all belts of the same type. Instead, the belt defect should be detected based on the *change* of the fault signature for the specific serpentine belt that is being monitored.

7.4 Chapter Summary

This chapter addresses the early detection of system-related faults for claw-pole generators with built-in rectifiers.

Specifically, a novel speed estimator is proposed for claw-pole generator based on ripple frequency detection in the generator output voltage. Notable features of the generator speed estimator include,

- (1) Nonintrusive: Only the existing generator output voltage measurement is used to estimate the generator speed;
- (2) Fast: Highly responsive real-time speed estimation is achieved through the use of 256-point FFT;
- (3) Accurate: The speed estimation accuracy is not sacrificed through proper interpolation of FFT results;

Although the speed estimation method is originally developed for claw-pole generators, it is essentially applicable to any wound-rotor or permanent-magnet synchronous generators with rectified output voltage and current.

The proposed speed estimator is applied to the detection of belt slip. Non-ideal effects such as spectrum aliasing and harmonic interference are also properly taken care

of, which results in a highly responsive and reliable belt-slip detector within a wide speed range.

An incipient belt-defect detector is also proposed in this chapter. It is discovered that the defective serpentine belt will modulate the generator speed every belt revolution, which will give rise to specific side-band current harmonics close to the rectifier ripple frequency. The proposed belt-defect detector is based on monitoring belt-cycle related harmonics and is validated experimentally over a wide generator speed range. The real-time signal processing technique proposed for belt-defect detection can also be used for detecting various internal faults in Chapter 8.

CHAPTER 8 Detection of Internal Faults for Claw-pole Generators

8.1 Overview

Unlike external faults that only change the input or output conditions of the claw-pole generator, internal faults occur inside the mechanical assembly of the generator and can fundamentally impact the way how the generator operates.

Internal faults investigated in this chapter include the stator turn fault, the rotor eccentricity, and the generalized bearing roughness of claw-pole generators.

The stator turn fault is first studied. To detect the stator turn fault using only the limited available sensor information, a detailed analytical model of the claw-pole generator with stator turn faults is derived to analyze the effect of the stator fault on generator output voltage and current. The analysis leads to the discovery of a highly robust fault signature, which is further validated by finite-element analysis and experimental results. Following the detection of the stator turn fault, the proposed generator model is also shown capable of predicting the fault current accurately from the observed fault signature. Using a database generated by this model, the severity of the stator turn fault can be evaluated at various operating conditions and well-informed post-fault protection strategies can be designed.

The rotor eccentricity is also studied in this chapter. A finite-element model of the generator with rotor eccentricity is constructed to help find the fault signature for rotor eccentricity. The proposed rotor-eccentricity detector is validated by experimental results.

Finally, the detection of generalized bearing roughness fault is investigated. Multiple accelerated bearing aging tests and control tests are performed. Existing noise-cancelling methods are not very effective in detecting worn bearing in claw-pole generators, mainly

because of the small bearing size and large per-unit airgap. However, careful analysis of experimental data reveals that the frequency deviation of the rectifier ripple harmonic is strongly correlated to the bearing wear in claw-pole generators and can be used as an indicator of the generalized bearing roughness.

8.2 Detection of the Stator Turn-to-turn Fault

The stator winding failure in the claw-pole generator usually starts with a short circuit between adjacent turns in the stator windings. Large circulating current will then flow in the shorted turns, overheating or even melting adjacent winding insulations. If left undetected, the incipient stator turn fault can develop into severe stator winding or stator core failures that result in sudden loss of vehicle electric power and increased risk of electric fire.

In conventional poly-phase AC electric machines, a stator turn fault introduces some negative sequence components into the current or voltage of the electric machine [95-97]. For claw-pole generators with built-in rectifiers, the three-phase asymmetry cannot be quantified by negative sequence components any more. The question then becomes, what can be used as an alternative to measure the three-phase unbalance in the rectified generator output voltage or current.

To detect the stator turn fault using only the available sensor information, a dynamic model of the claw-pole generator with stator turn faults is derived in this chapter to analyze how the fault would interact with the connected battery and the static full-bridge rectifier, and how it would affect the generator's output voltage and current. It is found that despite the connected lead-acid battery, the generator output current harmonic at one third of the rectifier ripple frequency is a robust signature of the stator turn fault. The

performance of the stator turn-fault detector is demonstrated by extensive experimental results. The same fault-detection method can also be extended to many other AC generators with a DC link rectifier.

8.2.1 Modeling of Claw-pole Generator with Stator Turn Faults

The delta-connected stator winding of a claw-pole generator can be represented by a simplified circuit as shown in Figure 8.1. In Figure 8.1, e_{0A} , e_{0B} and e_{0C} represent the back-EMFs produced by the field winding in phase A, B, and C respectively. Experimental measurements confirm that waveforms of open-circuit voltages e_{0A} , e_{0B} and e_{0C} are approximately sinusoidal and 120 degrees out of phase. L_{ar} is the armature reaction inductance, L_{ls} is the stator leakage inductance, and R_s is the winding resistance of each phase. Note that armature reaction inductance L_{ar} is an aggregated per-phase parameter that not only accounts for the self inductance of phase-A winding, but also the mutual inductances between different phases.

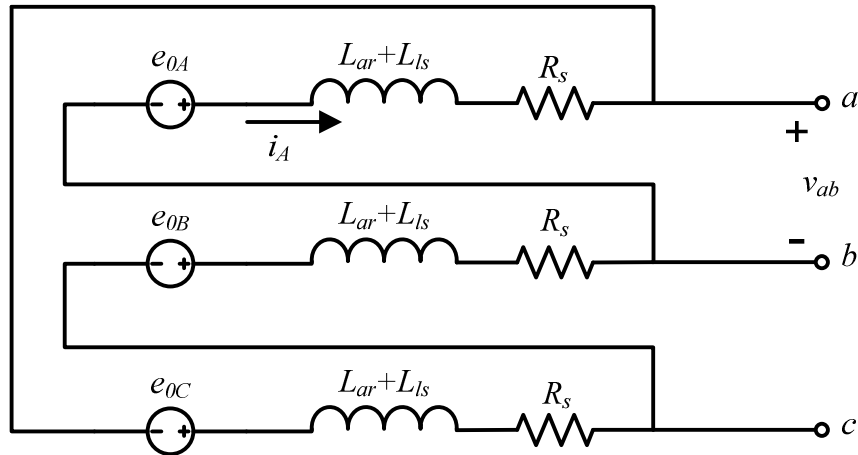


Figure 8.1: Circuit representation of a healthy claw-pole generator.

The line-to-line voltage of the generator is expressed as,

$$v_{ab} = e_{0A} - (L_{ar} + L_{ls}) \frac{d}{dt} i_A - R_s i_A, \quad (8.1)$$

where i_A is the phase-A current, v_{ab} is the phase-A voltage. The phasor form of (8.1) has been used extensively for analyzing conventional synchronous machines. However, as will be shown later, the line-to-line voltages of claw-pole generators are far from sinusoidal because of the output rectifier. Hence, equation (8.1) in its more generalized form is used in this study.

The voltage can also be expressed in terms of the magnetic flux as,

$$v_{ab} = N \frac{d\phi_A}{dt} - R_s i_A, \quad (8.2)$$

where ϕ_A is the total flux that links the entire phase-A winding, which includes the airgap flux, the slot leakage flux, and the end-winding leakage flux.

Assume that a stator turn fault occurs in phase-A winding, shorting m turns out of the total N serial turns. If $m \ll N$, the circulating current in the shorted path can be calculated using a simple equivalent circuit as shown in Figure 8.2. A rigorous derivation of this equivalent circuit is given in Appendix A.

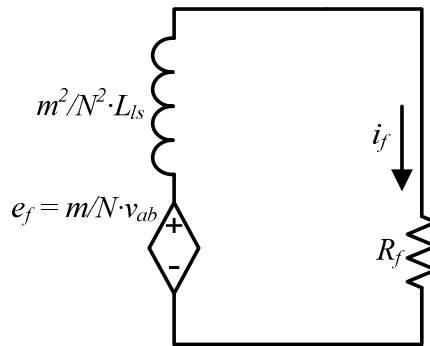


Figure 8.2: Simplified equivalent circuit of the short-circuit path.

In Figure 8.2, $m^2/N^2 \cdot L_{ls}$ is the leakage inductance of the m shorted turns, and R_f is the short-circuit resistance. As will be derived in Appendix A, the magnitude of the back-EMF e_f in the equivalent circuit is proportional to the phase-A voltage and the number of shorted turns,

$$e_f = \frac{m}{N} v_{ab} \quad (8.3)$$

The equivalent voltage source e_f will push a circulating current flowing in the short-circuit path in Figure 8.2. The fault current i_f will further impact the three-phase voltages of the generator through magnetic couplings (mutual inductance) between the shorted turns and three-phase windings. The circuit representations of fault-induced voltages in three windings are shown in Figure 8.3. L_{Af} is the mutual inductance between the phase-A winding and the short-circuit path, and vice versa for L_{Bf} and L_{Cf} .

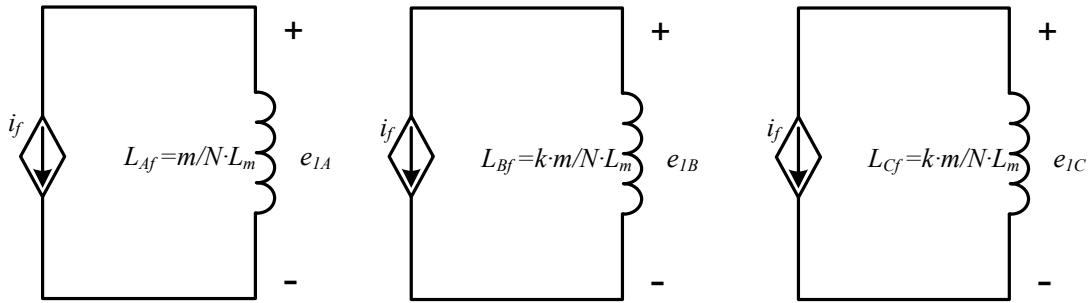


Figure 8.3: Circuit representations of fault-current-induced back-EMFs in three-phase windings.

If the self inductance of phase-A winding is defined as $L_m + L_{ls}$, then the mutual inductance between different phases is $k \cdot L_m$, where k is a constant coefficient that typically has a negative value. The inductance L_m is related to the armature reaction inductance L_{ar} as,

$$L_m = \frac{L_{ar}}{1-k} \quad (8.4)$$

With wave-wound stator windings, L_{Af} , L_{Bf} and L_{Cf} can be easily expressed in terms of L_m . The fault-current induced back-EMFs can therefore be written as,

$$e_{1A} = -\frac{d}{dt}(L_{Af}i_f) = -L_{Af} \frac{d}{dt}i_f = -\frac{m}{N}L_m \frac{d}{dt}i_f, \quad (8.5)$$

$$e_{1B} = -\frac{d}{dt}(L_{Bf}i_f) = -L_{Bf} \frac{d}{dt}i_f = -\frac{m}{N}(kL_m) \frac{d}{dt}i_f, \quad (8.6)$$

$$e_{1C} = -\frac{d}{dt}(L_{Cf}i_f) = -L_{Cf} \frac{d}{dt}i_f = -\frac{m}{N}(kL_m) \frac{d}{dt}i_f. \quad (8.7)$$

For non-salient pole electric machines with a sinusoidally-distributed airgap flux, k is typically $\cos(120^\circ)$ or -0.5. For the claw-pole generator, however, k is not -0.5 because of the irregular shapes of the rotor poles and consequently the non-sinusoidal distribution of the airgap flux. The identification of parameter k is outlined later in section 8.2.2.

The short-circuit current in the phase-A winding will also result in an additional voltage drop across the leakage inductance of the shorted turns (the inductor in Figure 8.2). However, this voltage drop is small compared to the voltage drop given by equation (8.5), and is therefore neglected during the analysis of phase-A voltage.

Combining Figure 8.1 ~ Figure 8.3, the output rectifier, the lead-acid battery, and the electric load, a complete model for a claw-pole generator with stator turn faults is finally shown in Figure 8.4.

In Figure 8.4, all voltage and current sources with red shades are controlled sources, with control inputs labeled next to them. R_{cable} and L_{cable} are the resistance and inductance of the cable connecting the generator and the battery. R_{load} represents the electric loads in the vehicles. The battery is simply represented by a constant DC voltage source V_{batt} in series with an internal resistance R_{batt} . The model can be implemented in any major circuit simulation software with transient analysis capability.

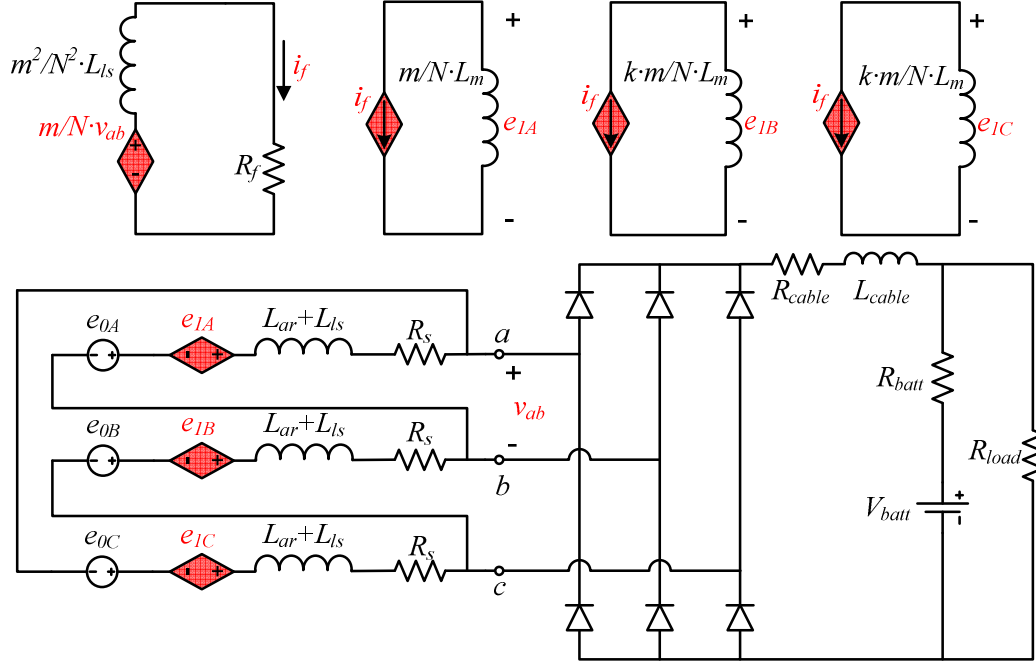


Figure 8.4: A circuit model of claw-pole generator with stator turn faults.

The lead-acid battery in Figure 8.4 may be represented by a more complicated and realistic model, such as the Thevenin model [98-101] as shown in Figure 8.5. However, as will be shown later, only fast electrical transients (at least several hundred Hertz) are concerned in detecting the stator turn fault. In such frequency range, the over-voltage capacitor (C_2) in the Thevenin model can be treated as a short circuit, and the energy storage capacitor (C_1) can be treated as a constant voltage source. Therefore, the Thevenin model collapses to the simple model in Figure 8.4 in the high-frequency range.

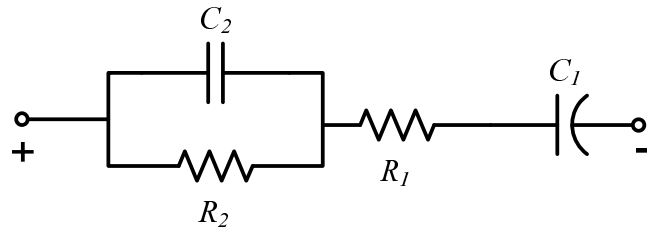


Figure 8.5: Thevenin model of a lead-acid battery.

8.2.2 Parameter Identification for the Generator Model

Various parameters in Figure 8.4 need to be properly identified before the generator model can be used to analyze the stator turn-to-turn short circuit. Table 8.1 briefly summarizes how these parameters are identified.

Table 8.1: Identified parameters for the generator model.

Parameter	Value	Unit	Identification Method
$L_{ar} + L_{ls}$	5.2724e-4	H	Experimentally measured via open-circuit and short-circuit tests. See Figure 8.6 for details.
L_{ar}	5.0088e-4	H	$0.95 * (L_{ar} + L_{ls})$
L_{ls}	2.6362e-5	H	$0.05 * (L_{ar} + L_{ls})$
k	-0.2625		Calculated from finite-element simulation (Ansoft Maxwell 3D ©). See Figure 8.7 for details.
L_m	3.9674e-4	H	$L_{ar} / (1 - k)$
R_s	0.0537	Ω	Experimentally measured using Baker Tester.
R_{cable}	0.0124	Ω	Inferred from experimental data for stator turn-fault detection.
L_{cable}	5.686e-6	H	Calculated using analytical formula based on cable dimension.
R_{batt}	0.0102 (typical)	Ω	Experimentally measured via battery charging and discharging tests
R_{load}	varying	Ω	Inferred from experimental data for stator turn-fault detection.
R_f	0.131, 0.230	Ω	Artificially induced; exact values inferred from experimental data for stator turn-fault detection.
V_{batt}	varying	V	Directly measured during experiment. (voltage drop across R_{batt} neglected)
m	1		Artificially induced.
N	9		Manually counted. Two wave-wound 9-turn coils connected in parallel in each phase.
e_{0A}, e_{0B}, e_{0C}	varying	V	Manually adjusted until the model reaches the same operating condition as the experiment.

Specifically, the identification of the synchronous inductance $L_{ar} + L_{ls}$ involves open-circuit and short-circuit tests of the claw-pole generator. The results of the open-circuit and short circuit tests are shown in Figure 8.6. The field current is first increased to 1.2 Amp and then decreased back to 0.

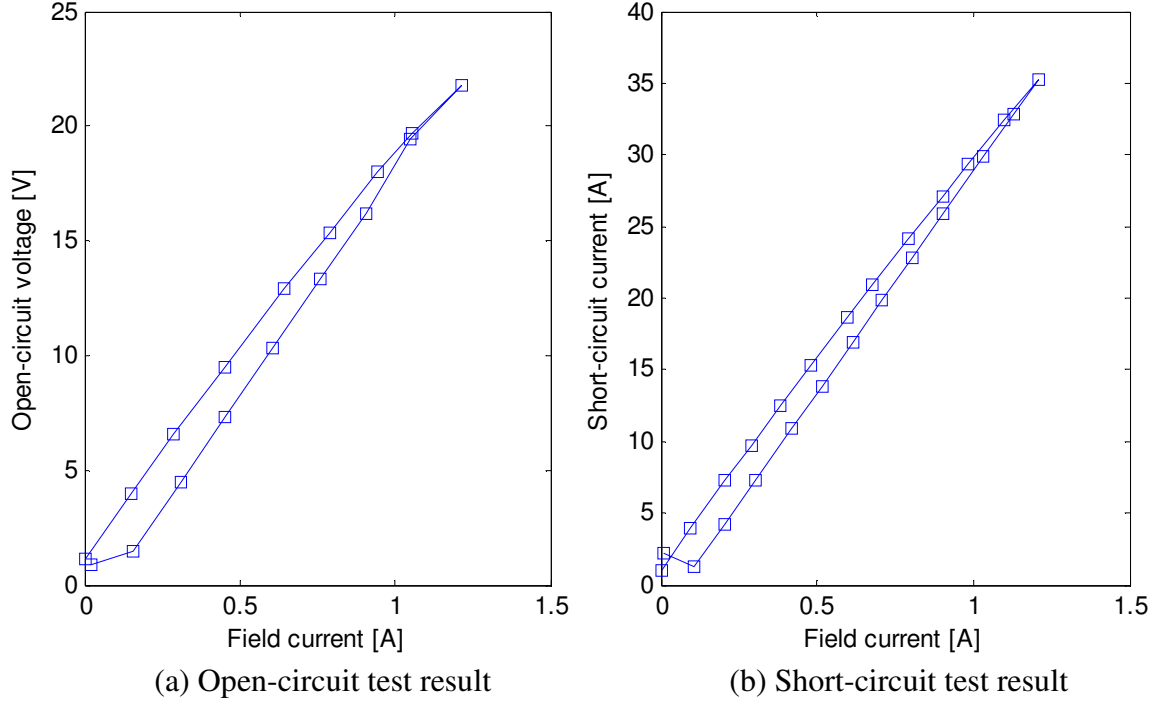


Figure 8.6: Claw-pole generator test results.

The coefficient for mutual inductance, k , is identified using the finite-element model in Figure 6.5. A sinusoidal current with amplitude of 10 Amp and a frequency of 300 Hz is injected into the phase-C winding. Three-phase voltages are then measured and recorded for various rotor angles. As shown in Figure 8.7, all three-phase voltages vary with the rotor angle due to the irregular shape (saliency) of the rotor. The coefficient k is the ratio between the phase-A voltage and phase-C voltage. Ideally, it should be set up as a function of the rotor angle. In this study, the average value of k at different rotor positions is used in the final generator model for simplicity.

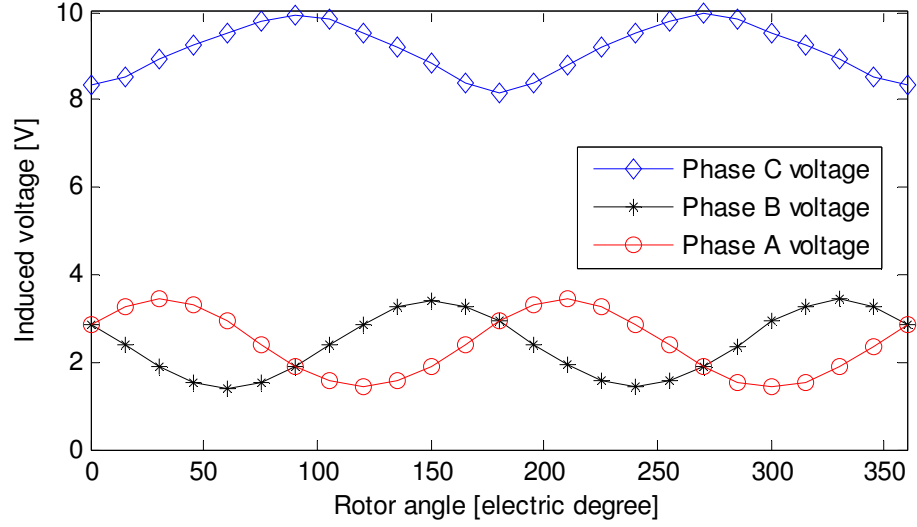


Figure 8.7: Finite-element simulation result for calculating mutual inductances.

8.2.3 Fault Signature

The proposed generator model with stator turn faults is implemented using SimPowerSystem in Matlab/Simulink ©, as shown in Figure 8.8 and Figure 8.9. To find out how the stator turn fault impacts the generator output voltage and current, a 1-turn fault is seeded in the model with a small fault-current limiting resistor.

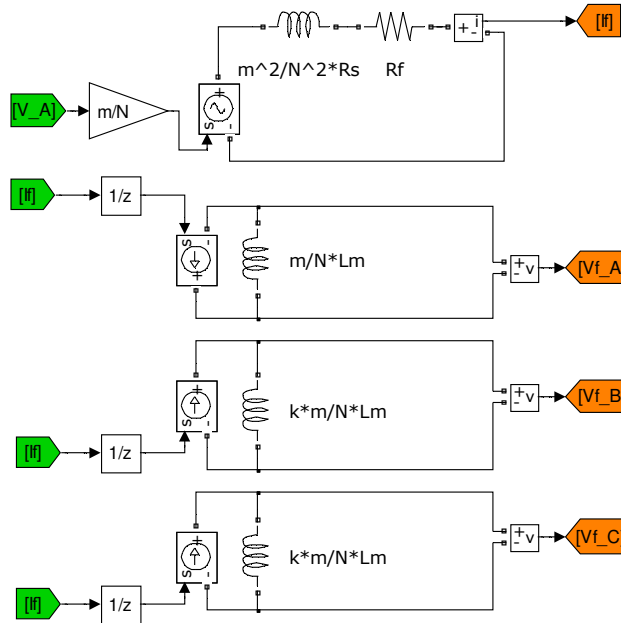


Figure 8.8: Simulink model of the generator with stator turn fault – part 1.

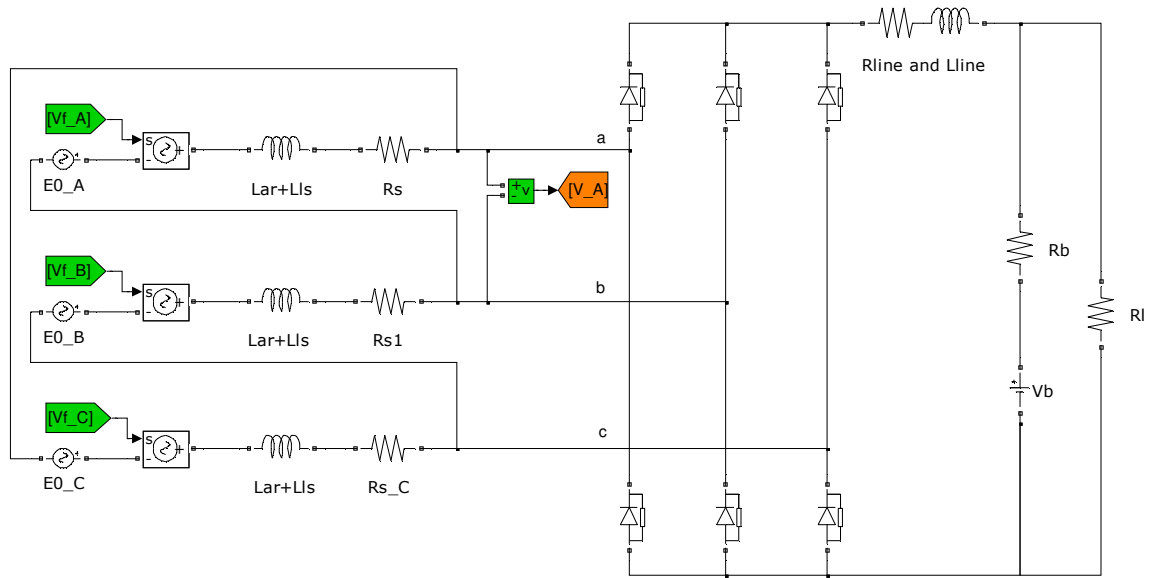


Figure 8.9: Simulink model of the generator with stator turn fault – part 2.

Meanwhile, in the automotive EPGS test bench shown in Figure 6.11, the same stator turn fault is induced experimentally for comparison purposes. The generator is modified so that four taps are attached to four adjacent turns in the stator winding, as shown in Figure 8.10. These taps are then brought out of the stator housing and can be shorted to create different levels of stator turn faults. In practice, a small resistor is put in series of the shorted path to limit the fault current.

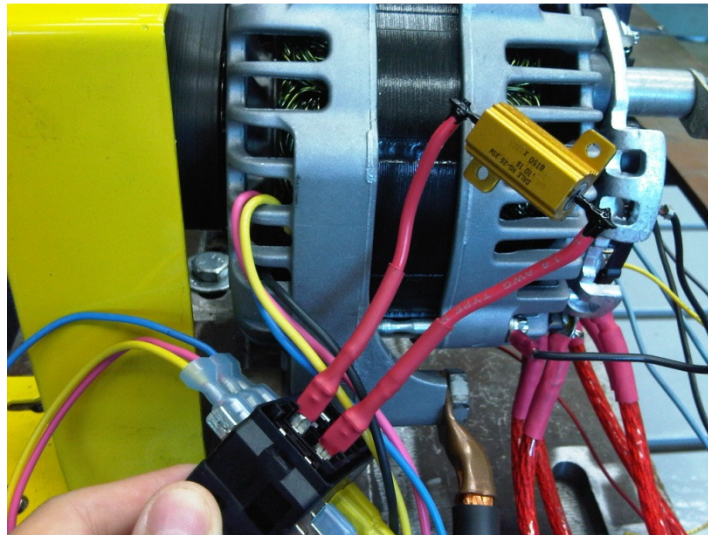


Figure 8.10: Experimental generator with artificially induced stator turn fault

Figure 8.11 compares the fault current given by the circuit model of the generator and the fault current measured from experiments. The claw-pole generator is running at 3000 RPM with approximately 48 Amps of DC load current, and the fault-current limiting resistor is $0.230\ \Omega$. The simulated current agrees closely with the measured one and manages to capture the distortion caused by the full-bridge rectifier in the fault current very accurately.

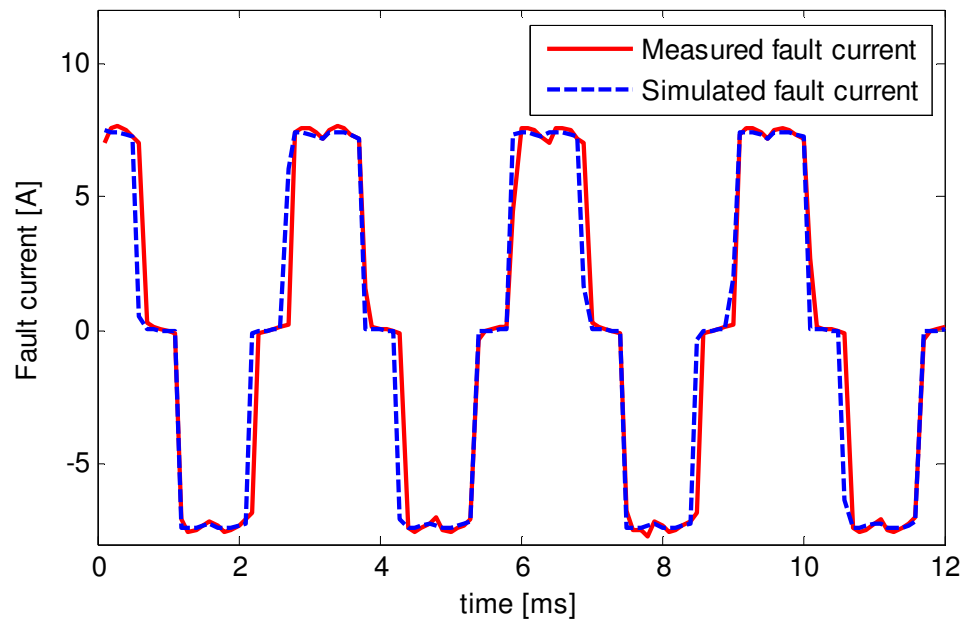


Figure 8.11: Comparison of the simulated and measured fault currents in the shorted path.

Figure 8.12 compares the line current given by the circuit model of the generator and the line current measured from experiments. Again, the simulated current agrees very closely with the measured one and even manages to capture small features of the measured current near its peak, which are caused by natural current switching between diodes.

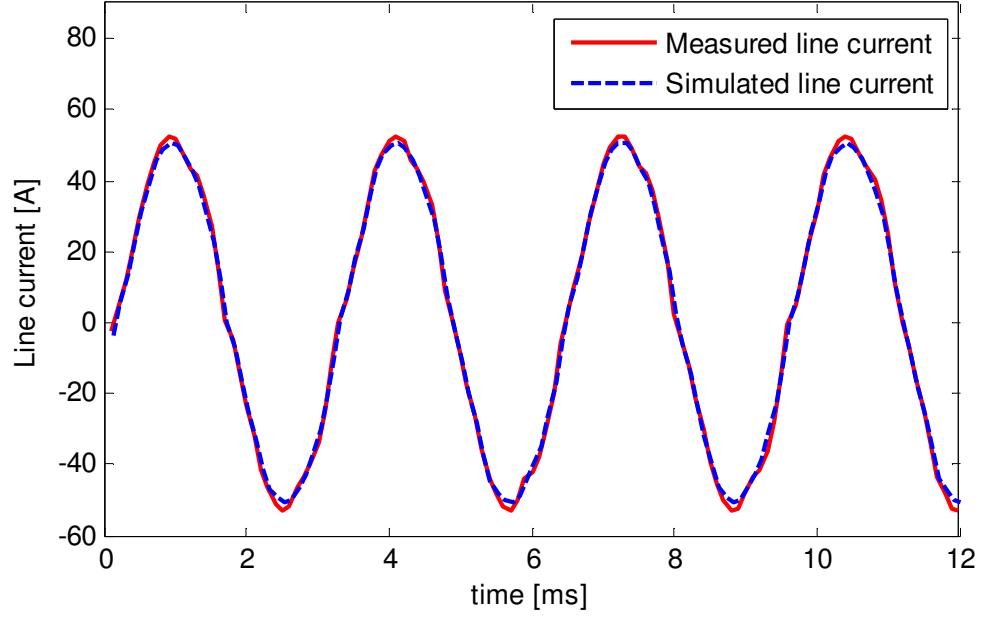


Figure 8.12: Comparison of the simulated and measured line currents.

Since the proposed model can accurately emulate the behavior of the faulty claw-pole generator, it is used to study the fault signature in the generator output current and voltage. Figure 8.13 compares the simulated output current of generator with and without the 1-turn stator fault and a $0.230\ \Omega$ current-limiting resistor.

When the generator is healthy, all the output current ripples have identical magnitudes. When the generator has a stator turn fault, however, a clear repetitive pattern of a large current ripple followed by two small current ripples appears in the output current of the rectifier. The period of this repetitive pattern is three times of the period of a regular current ripple. Therefore, the stator turn fault gives rise to the *current harmonic at one third of the rectifier ripple frequency*. The primary root cause for this phenomenon is that the fault-current induced back-EMFs, e_{IA} , e_{IB} and e_{IC} , have different magnitudes and relative phase angles in different phase windings. Figure 8.14 graphically illustrate how unbalanced rectifier inputs can lead to rectifier output harmonic at one third of the rectifier ripple frequency.

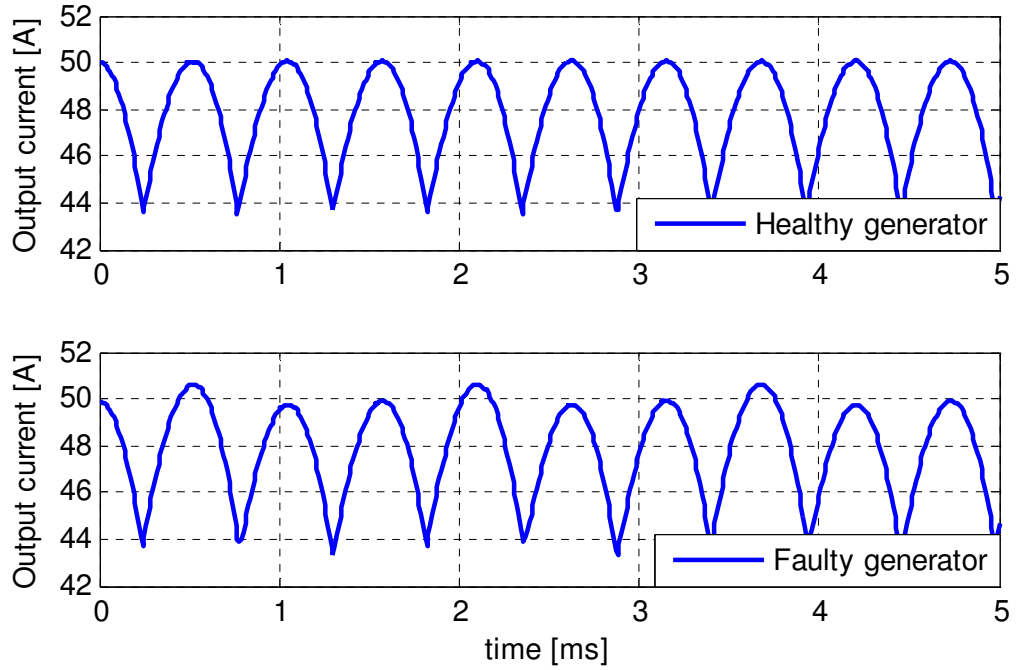


Figure 8.13: Comparison of the simulated generator output current without and with stator turn fault.

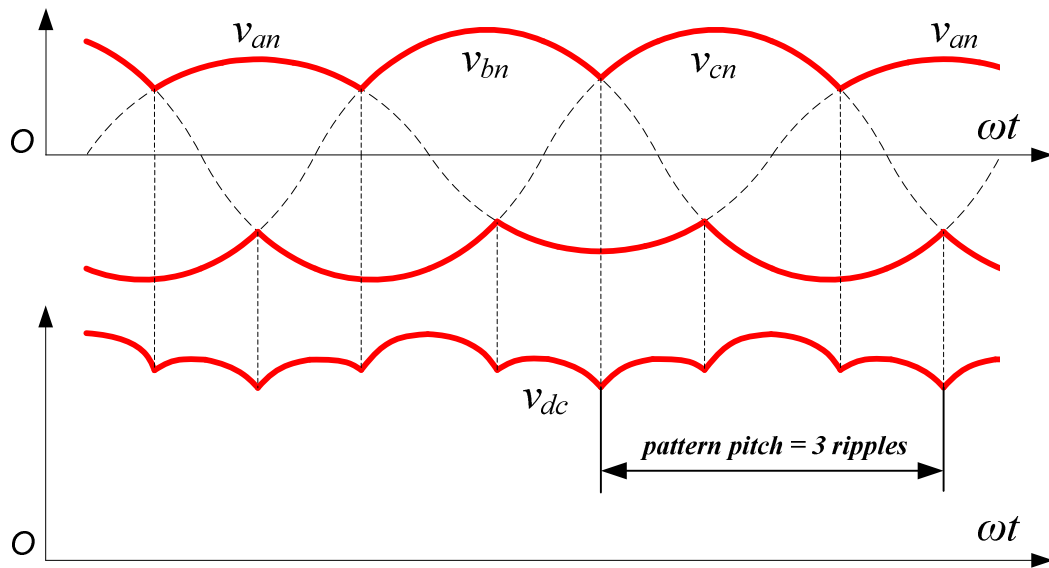


Figure 8.14: Illustration of harmonic at one third of rectifier ripple frequency caused by unbalanced rectifier inputs.

The frequency of the fault-related current harmonic is at least a few hundred Hertz given the typical speed range of 2400~12000 rpm of the claw-pole generator. In the

generator model in Figure 8.4, the synchronous reactance of the generator is dominating the cable impedance and battery resistance in this frequency range. Hence, the magnitude of the current harmonic at one third of the rectifier ripple frequency is mainly determined by the generator synchronous reactance and the fault-current-induced back-EMFs. It is almost independent of the battery internal resistance.

Similar repetitive pattern can also be observed in the generator output voltage waveform. However, since the cable impedance and the battery internal resistance are much smaller than the internal synchronous reactance of the generator, the output voltage of the generator is largely clamped by the battery voltage, and the magnitude of the voltage harmonic at one third of the rectifier ripple frequency is small and heavily dependent on the battery internal resistance. Since the battery internal resistance varies considerably with battery state of charge and temperature, the voltage harmonic at one third of the rectifier frequency is not a consistent signature of the stator turn fault in claw-pole generators.

Figure 8.15 shows how the magnitudes of the fault-related current harmonic and fault-related voltage harmonic vary with the battery internal resistance value in the simulation. With the same 1-turn fault and the 0.230- Ω resistor, the magnitude of fault-related current harmonic stays practically constant while the magnitude of fault-related voltage harmonic doubles as the battery internal resistance is changed from 25% to 400% of its typical.

The final choice of the stator turn-fault signature is therefore *the current harmonic at one third of the rectifier ripple frequency*.

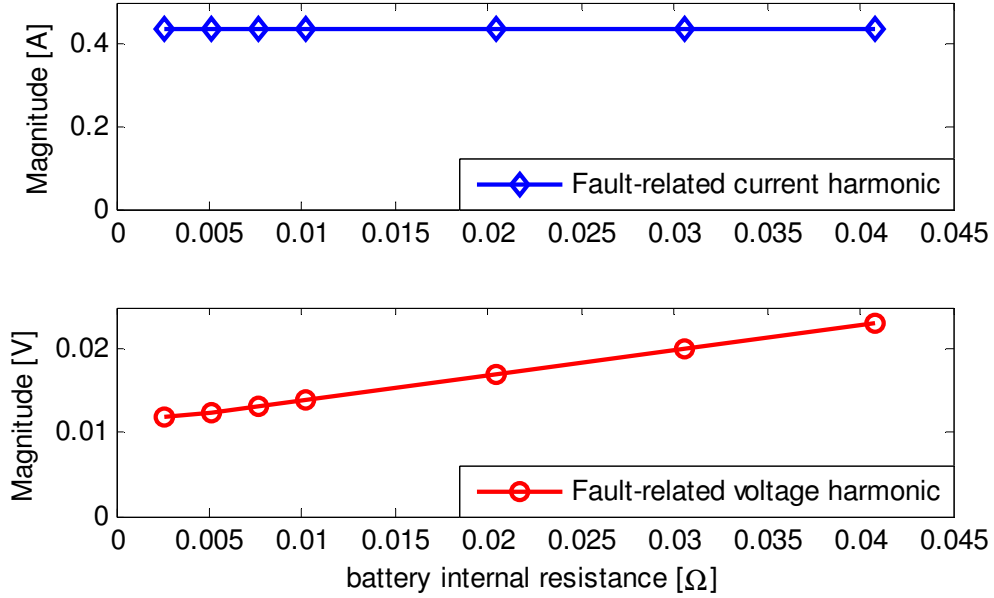
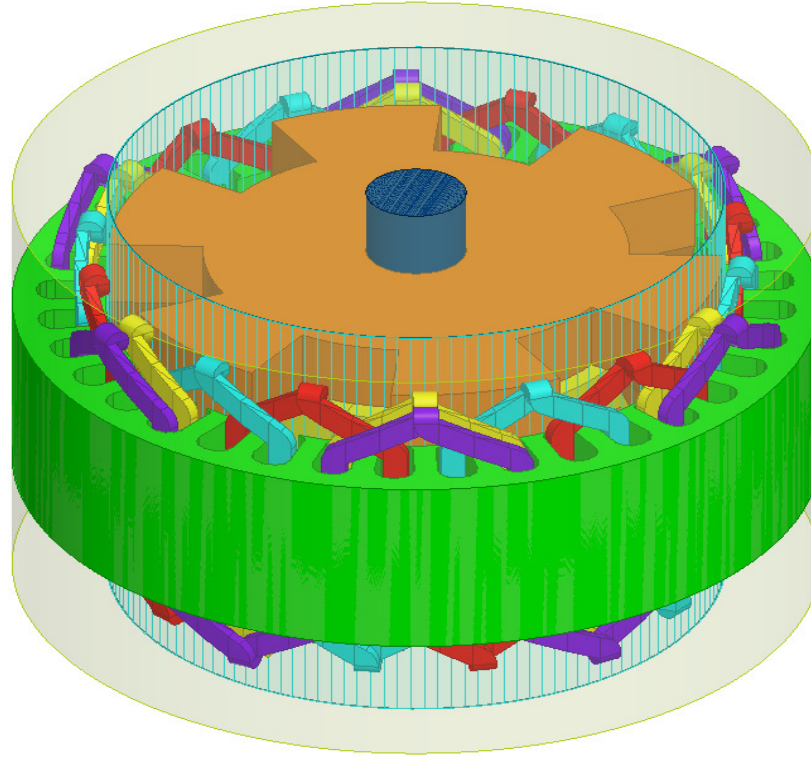


Figure 8.15: Dependencies of fault-related current and voltage harmonics on battery internal resistance.

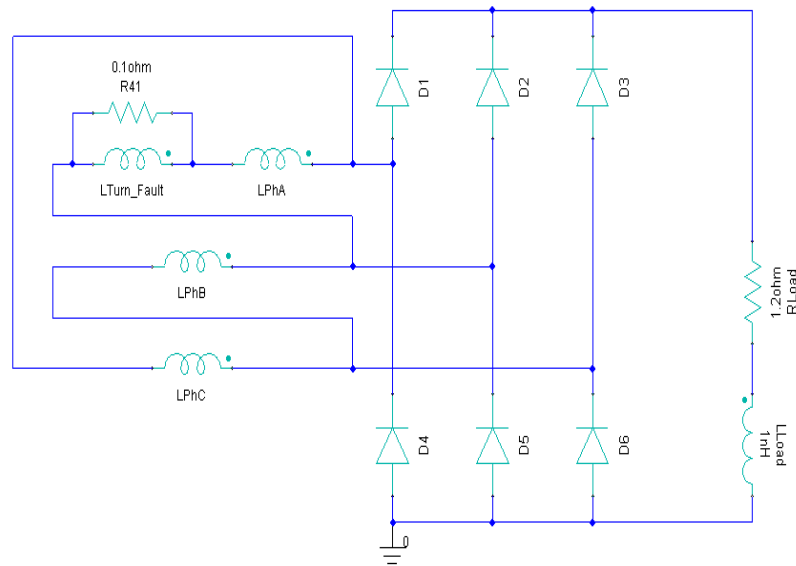
8.2.4 Finite-element Model of Generators with Stator Turn Faults

To further validate the proposed fault signature, a generator with stator turn fault is modeled and simulated in Ansoft Maxwell ©. Figure 8.16 (a) shows the 3D finite element model the claw-pole generator. The Phase-A winding is split into two sub windings. One of the sub winding is short-circuited to itself through a small resistor to simulate the stator turn fault.

The winding connections are illustrated more clearly in Figure 8.16 (b). In Figure 8.16 (b), the three-phase windings are connected in delta. A fraction of turns in Phase A (depending on the severity of the turn fault) is split from the entire winding and is shorted through a small resistor. The shorted winding is still electrically connected in series with the rest part of Phase A, and is still magnetically coupled with all three phases as shown in the 3D model in Figure 8.16 (a).



(a) 3-D finite-element model



(b) Winding connection

Figure 8.16: Finite-element model for a generator with stator turn faults.

Figure 8.17 shows the waveform of generator output current obtained from the finite-element simulation. Running at 3139 rpm, the generator has a ripple frequency of 1883

Hz. It is clear in Figure 8.17 that there exists a repeating pattern of a large ripple followed by two small ripples, which agree well with the analytical analysis in section 8.2.3. When the short circuit in the simulation is removed, the generator output current is shown again in Figure 8.18. The repeating pattern is much reduced. Therefore, the current harmonic component at $1/3$ of the rectified ripple frequency is verified to be the fault signature for the stator turn fault.

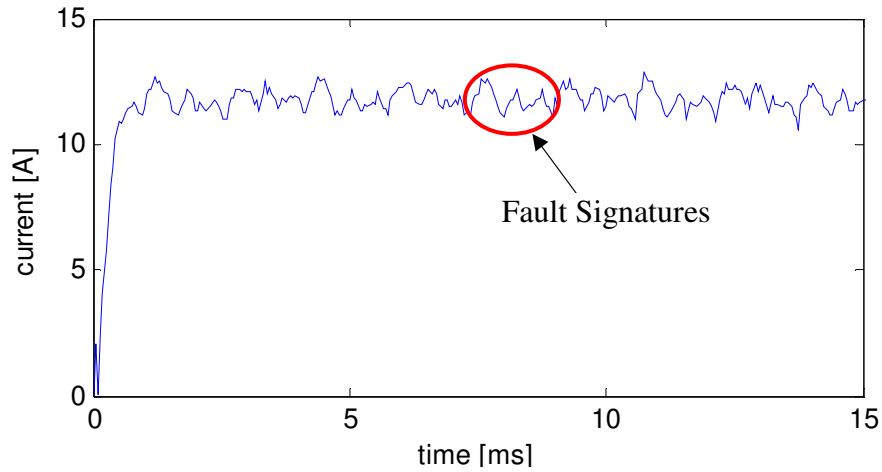


Figure 8.17: Simulated generator output current with stator turn fault.

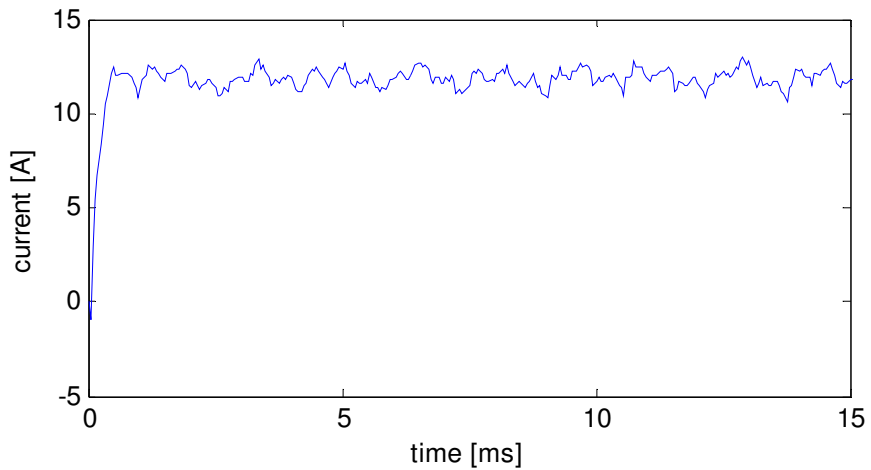


Figure 8.18: Simulated generator output current without stator turn fault.

Although the finite-element analysis helps to confirm the signature of the stator turn fault, it has several major limitations for quantitative analysis of stator turn fault. Firstly,

the finite-element simulation is very slow. It is not very suitable for analyzing stator turn faults for a wide variety of operating conditions. More importantly, due to numerical calculation artifacts, such as the asymmetrical meshing of the three-phase winding, the three-phase AC currents are slightly asymmetrical even if no stator turn fault exists. This also makes it difficult to use finite-element model to accurately predict magnitudes of fault signatures.

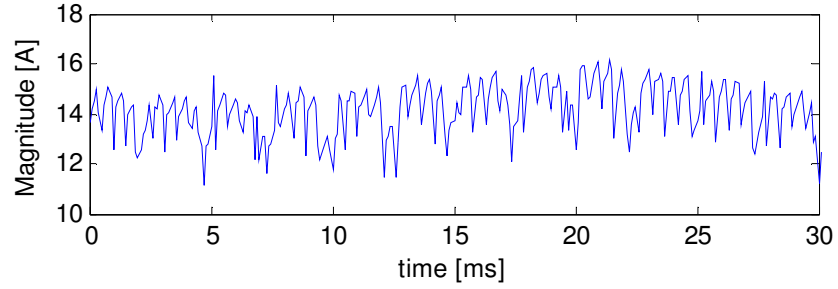
8.2.5 Experimental Validation of the Stator Turn-fault Detector

A. Comparison of Generator Current Spectra

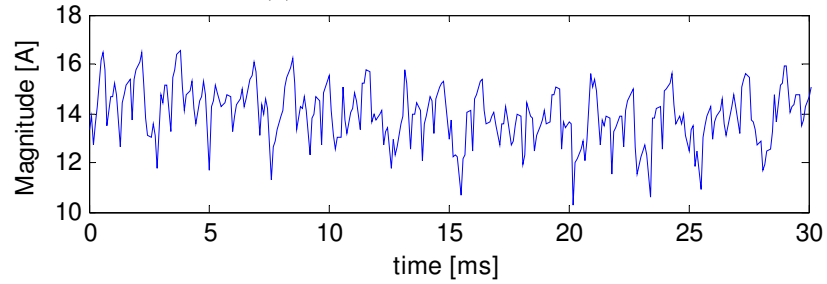
Using the automotive EPGS test bench shown in Figure 6.11, the proposed stator turn-fault detection method is validated experimentally. The method to induce the fault is previously described in Figure 8.10.

Figure 8.19 (a) and (b) compares the generator output current waveforms when the generator is healthy and when the generator is induced with a 1-turn fault (roughly $0.1\text{-}\Omega$ current-limiting resistor) at 3163 RPM with a light electric load. There is a noticeable difference in the pattern of current ripples between the two plots. The current waveforms generally look much noisier than the simulated current waveforms in Figure 8.13 because of the lower sampling rate (10 kHz) in the experiment and other factors that are not modeled in the generator model (such as the PWM switching of the voltage regulator).

The corresponding spectra for above current waveforms are shown in Figure 8.20 (a) and (b) respectively. The rectifier ripple harmonic is at 1898 Hz and the fault-related current harmonic is therefore located at 632.3 Hz. In Figure 8.20 (a), the magnitude of the fault signature is merely -25.61 dB with no stator turn fault. In Figure 8.20 (b), the magnitude of the fault signature increases to -10.11 dB with the stator turn fault.

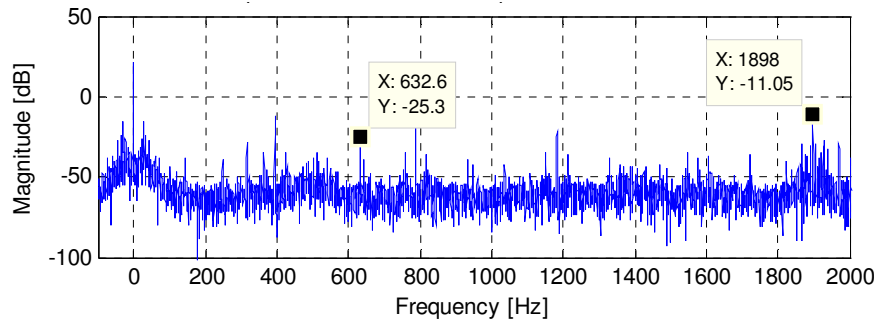


(a) Without stator turn fault

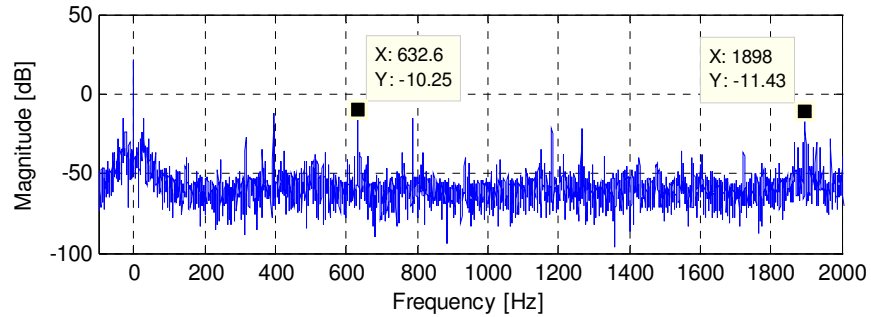


(b) With stator turn fault

Figure 8.19: Generator output current waveforms.



(a) Without stator turn fault



(b) With stator turn fault

Figure 8.20: Generator output current spectrum.

B. Real-time Signal Processing for Detecting Stator Turn Faults

As shown in section A, the rectifier ripple frequency is the prerequisite to determine the location of the current harmonic related to stator turn faults. The magnitude of the

current harmonic is then determined by high-resolution FFT spectrum. To avoid using FFT, signal processing techniques similar with that described in section 7.3.2 is also used to detect stator turn faults. The only difference is that the predetermined frequency for Goertzel algorithm is now one third of the rectifier ripple frequency.

C. Experimental Results at Various Operating Conditions

In practice, the magnitude of the fault signature is not only related to the fault level, but also varies significantly with different load levels and generator speeds. In order to provide complete protection coverage of the generator against stator turn faults, the fault-related current harmonic needs to be calibrated under various operating conditions.

Figure 8.21 shows the magnitude of the fault signature at various operating conditions. The test covers the speed ranges from 1580 rpm to 7930 rpm and load levels from 0A to approximately 48 A. The bottom deep blue surface shows the magnitude of the fault signature resulting from the inherent asymmetry of the healthy machine. The surface in the middle is the magnitude of the fault signature when two physically-adjacent turns are shorted through a 0.2-Ohm resistor. The top surface is the magnitude of fault signature when two physically-adjacent turns are shorted through a 0.1-Ohm resistor. Evidently, there is a clear separation between all three surfaces, which demonstrate the effectiveness of the method at various operating conditions.

The magnitude of the fault signature is not constant over the specified region. The general trend is that the fault signature increases as the load level and generator speed go up. This trend is the combined effect of several factors and will be explained by the proposed generator model in section 8.3.

The surface of fault signatures with 0.1 Ohm serial resistance is usually 4~5 times higher than the healthy surface and the surface with 0.2 Ohm serial resistance is roughly 2~3 times higher than the healthy surface. Given the large clearance between the surfaces, a threshold surface can be easily set up to determine when to trigger the alarm of the stator turn fault for this specific generator.

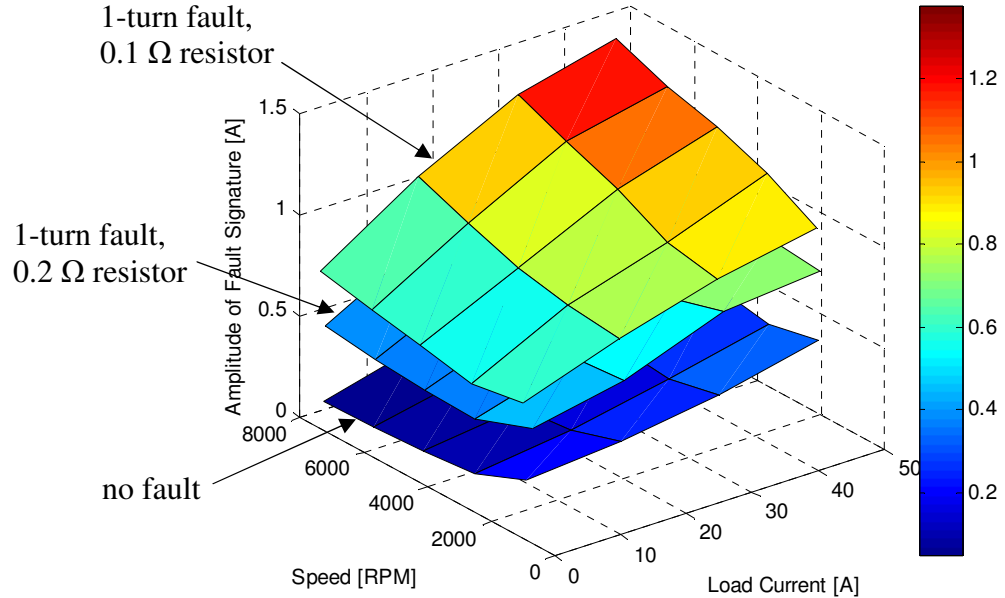


Figure 8.21: Fault signatures at various operating conditions.

To set up a fault threshold surface, the fault-related current harmonics are calibrated for two more healthy generators of the same specification. As can be seen in Figure 8.22, the fault signatures for all three healthy generators are quite small and do not vary too much from each other.

In Figure 8.23, the three surfaces from top to bottom are the fault signatures with 1-turn stator short circuit, the fault threshold, and the healthy characteristic of the claw-pole generator. The fault-threshold surface is statistically calculated from the measured signatures from three randomly selected healthy generators of the same type. The statistical confidence of the threshold is 90%, which means that for another claw-pole

generator outside of the test group, there is 90% confidence that a stator turn fault exists if the monitored fault signature is higher than the fault-threshold plane. The actually monitored fault signature is clearly above the fault threshold, which means that the confidence to conclude the existence of a stator turn fault is much higher than 90%.

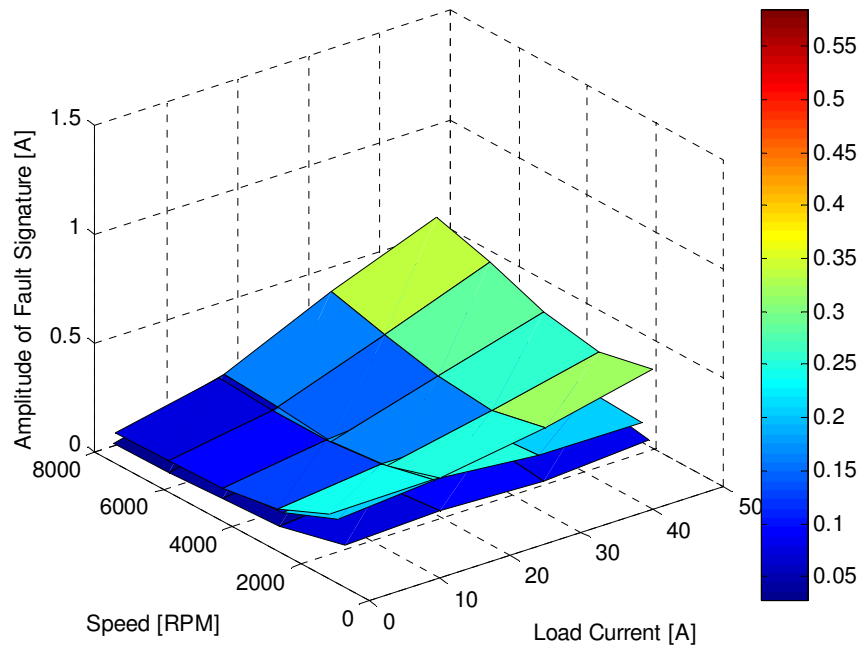


Figure 8.22: Fault signatures for three healthy generators.

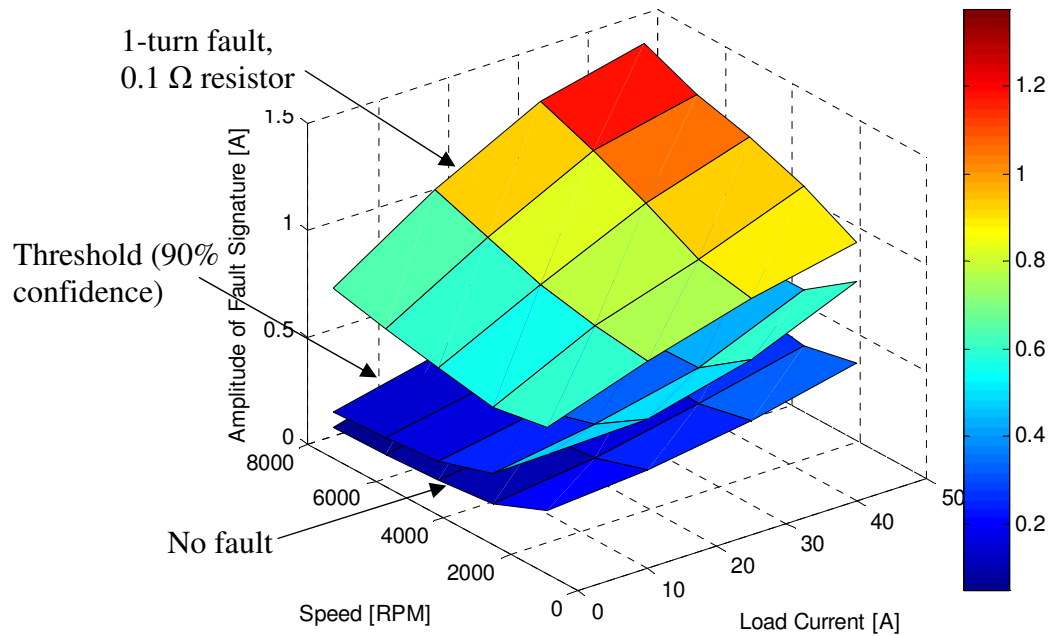


Figure 8.23: Fault signatures and the fault threshold.

D. Discussion of the Experimental Results

In conventional AC machines, a subtle 1-turn stator fault is generally not easy to detect. Successful detection of a 1-turn fault usually involves clever ways to account for the inherent asymmetry of the electric machine and delicate signal processing techniques [44, 56, 102].

In claw-pole generators, however, a 1-turn stator fault seems easy to detect. The fault signature rises 4~5 times even with a 0.1 Ohm current limiting resistor. There are two reasons for this:

(1) Conventional induction and synchronous machines are usually lap-wound, which means the physically-adjacent conductors are also usually electrically-adjacent. Hence, when conductors become shorted, only a small fraction of the total conductors in that phase are affected. For automotive generators, most stator windings are wave-wound. As a result, the physically-adjacent conductors are not electrically adjacent. They are electrically apart by at least a full round of wave winding. Therefore, when conductors become shorted in claw-pole generators, a much larger fraction of the total conductors in that phase are affected. For the specific generator studied in this paper, a 1-turn fault is equivalent to 6-turn fault if the machine is lap-wound.

(2) To detect stator turn faults for conventional three-phase AC machines, at least two current sensors are needed to monitor the three-phase current. The slight unbalance in the measurement channels may artificially exaggerate the inherent asymmetry of those machines. For the claw-pole generator, however, only one current sensor is used to monitor the output current and to detect the asymmetry in current ripples. Therefore,

there is no additional asymmetry introduced by the measurement channel. This also increases the sensitivity of stator turn-fault detection.

8.3 Fault-severity Evaluation and Post-fault Protection of the Stator Turn-to-turn Short Circuit

Once the stator turn fault has been detected in the claw-pole generator, the next question then becomes what protection measures should be taken to deal with the fault. In addition to standard procedures to notify the vehicle controller of the fault and to generate appropriate diagnostic code, the post-fault protection of stator short circuits should also meet the following two objectives.

- (1) The post-fault protection should prevent or at least slow down the stator turn fault from progressing into catastrophic stator-winding or stator-core failures, because such failures would result in total loss of electric power and increased risk of electric fire.
- (2) The post-fault protection should still allow some limp-home capability of the vehicle, because simply shutting off the claw-pole generator may result in a stranded-motorist situation soon after the battery charge is depleted.

Apparently, these two objectives are sometimes conflicting with each other. A good post-fault protection strategy should be able to make a well-informed decision based on the actual severity of the fault.

For example, in the case of very severe stator turn fault, it may be required to shut off the generator field immediately to prevent severe damage to the generator or the vehicle. In the case of less severe stator turn fault, the claw-pole generator may still be

operational but at a reduced current rating, so that the thermal limit of the winding insulations is not violated.

To enable such well-informed post-fault protection, the severity of the stator turn fault must be accurately evaluated from the observed fault signature.

As previously discussed in 8.2, the signature of stator turn faults is the generator output current harmonic at $1/3$ of the rectifier ripple frequency.

The severity of the fault, on the other hand, is best defined as the circulating current in the shorted turns. Not only is the circulating current a direct result of the stator turn fault, but it is also the root cause for further stator-insulation thermal degradations. Therefore, accurate knowledge of the circulating current can help determine the appropriate protection measure to be taken.

8.3.1 Validation of the Generator Model for Fault-severity Evaluation

In section 8.2, the proposed generator model shown in Figure 8.4 has been used to qualitatively analyze the fault signature of stator turn-to-turn short circuits. In this section, it will be shown that the fault signature given by the derived model is also quantitatively accurate.

With a $0.230\text{-}\Omega$ fault-current limiting resistor, Figure 8.24 compares fault signatures given by the generator model and fault signatures measured from experiments at various operating speeds and load levels of the claw-pole generator. Overall, fault signatures given by the proposed generator model agree very closely with measured fault signatures when the inherent asymmetry is taken out. Note that fault signatures given by the generator model manage to capture the trend of measured fault signatures over different generator speeds and load levels very well.

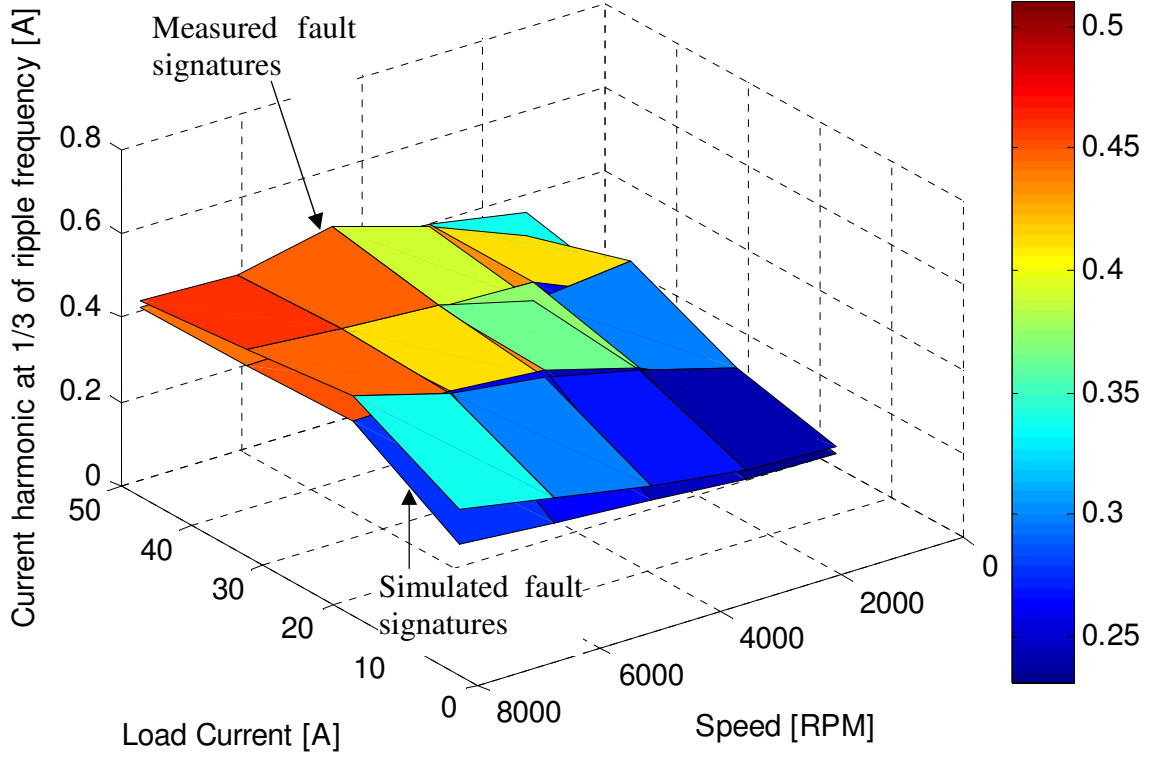


Figure 8.24: Simulated and measured fault signatures with a 0.230- Ω current-limiting resistor.

The same comparison with a different fault severity is also shown in Figure 8.25. The fault-current limiting resistor in this case is reduced to 0.131 Ω . Again, fault signatures given by the circuit model of the generator agree closely with measured fault signatures when the inherent asymmetry is taken out. Fault signatures given by the circuit model accurately capture the trend of measured fault signatures with respect to varying motor speed and load level.

To sum up, comparisons in Figure 8.24 and Figure 8.25 verify that the proposed generator model gives accurate quantitative estimation of the fault signature of the stator turn-to-turn short circuits over various motor speed and load levels. This experimentally-validated generator model can be used to establish a mapping relationship between the fault current and the fault signature. This enables us to predict the fault current from the

fault signature without resolving to exhaustive and sometimes infeasible experimental tests.

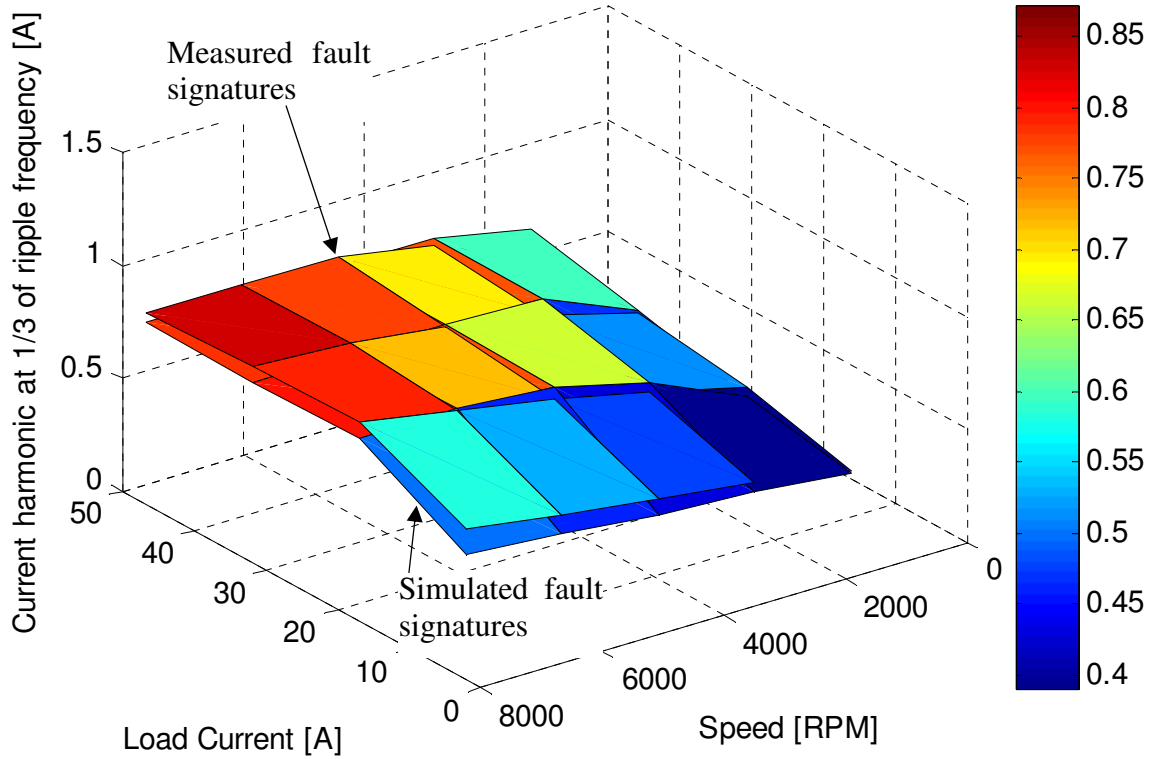


Figure 8.25: Simulated and measured fault signatures with a $0.131\text{-}\Omega$ current-limiting resistor.

8.3.2 Fault-severity Evaluation

The experimentally-validated generator model enables us to study many cases of stator turn faults that are previously too complicated or even infeasible to study experimentally. The following two sections describe how the model can be used for evaluating the severity of the stator turn fault and more importantly, for designing appropriate post-fault protection strategies.

The model of the claw-pole generator are seeded with more severe stator turn faults than those shown in Figure 8.24 and Figure 8.25 by reducing the fault-current-limiting resistor to $0.066\text{ }\Omega$, $0.033\text{ }\Omega$, and $0.016\text{ }\Omega$. The fault resistor is not reduced further

because $0.016\ \Omega$ is already very close to the natural resistance of the shorted path under normal operating temperature.

While short-circuit currents can be directly measured from the generator model, fault signatures are extracted from the output current of the generator model using FFT. Therefore, the fault signature can be set up as a function of the short-circuit current given a specific generator speed and load level. However, this functional relationship involves four quantities and is thus difficult to illustrate directly in a single three-dimensional plot.

To visualize this mapping relationship between fault signatures and short-circuit currents, two 3-D plots are made.

Figure 8.26 shows simulated fault signatures at different generator speeds, different load levels, and with different fault severities. Due to the smaller current-limiting resistor, magnitudes of fault signatures in Figure 8.26 are significantly higher than those shown in Figure 8.24 and Figure 8.25.

Figure 8.27 shows RMS values of simulated short-circuit currents with exactly the same operating conditions as those in Figure 8.26.

Whenever a certain fault signature is observed, the corresponding short-circuit current can be looked up using the database represented by Figure 8.26 and Figure 8.27. Hence, the severity of the stator turn-to-turn fault can be evaluated.

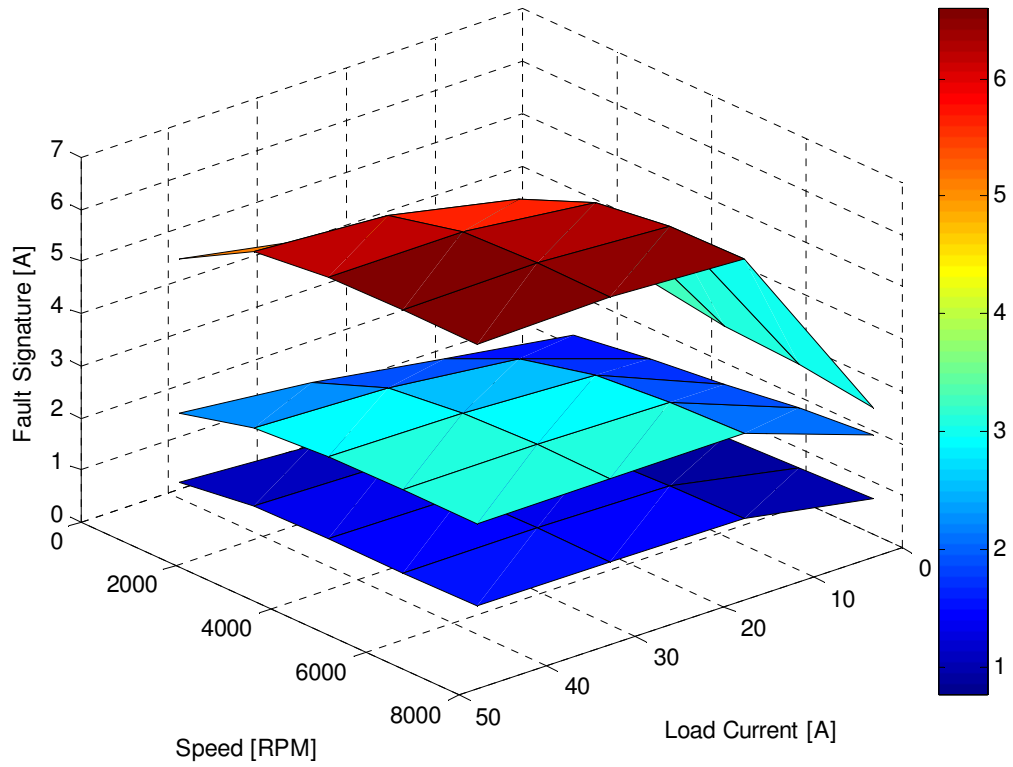


Figure 8.26: Additional Fault signatures given by the generator model (from top surface to bottom surface, current-limiting resistors are 0.066 Ω , 0.033 Ω , and 0.016 Ω).

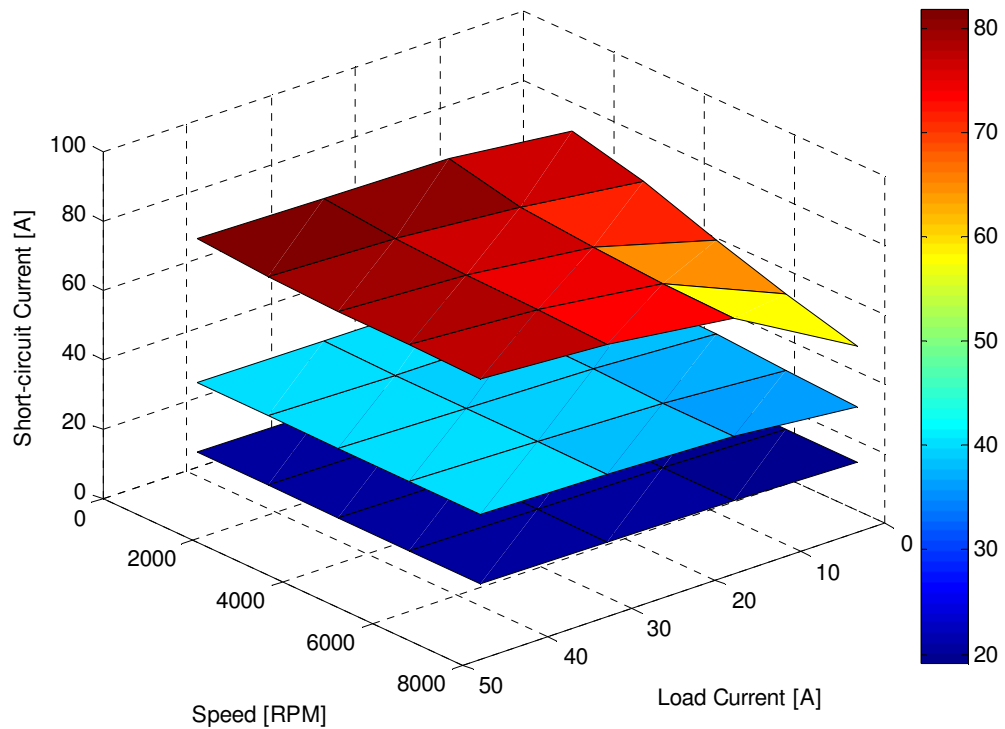


Figure 8.27: RMS short-circuit currents given by the generator model (from top surface to bottom surface, current-limiting resistors are 0.066 Ω , 0.033 Ω , and 0.016 Ω).

8.3.3 Post-fault Protection Strategy

The main objective of the post-fault protection is to prevent or slow down further thermal degradations of the winding insulation while preserving as much limp-home capability of the claw-pole generator as possible.

The root cause for the propagation of stator turn faults is the insulation thermal degradation resulted from the current overloading. In the case of a stator-turn short circuit, the current in the shorted turns is the superposition of the normal winding current and the circulating current in the shorted path. The circulating current and the normal winding current are found to be generally in phase with each other using the proposed generator model. Hence the RMS values of these two currents can be directly summed to calculate the overall RMS current in the shorted turns.

For the specific type of generator used in this study, the absolute maximum DC current rating is 145 A, which is equivalent to a maximum RMS current of 54 A in each parallel strand of the generator's delta-connected winding. To simply demonstrate the following post-fault protection strategy, it is conservatively assumed that the current limit in the shorted turns is also dictated by the maximum strand current of 54 Amp. The actual thermal current limit is likely to be slightly higher than 54 Amp because the shorted path is only a local heat source.

The overall current in the shorted turns can be limited by either reducing the short-circuit current or reducing the normal load current of the stator winding. On the one hand, the load current can be reduced by shedding non-critical electric loads in the vehicles. On the other hand, the short-circuit current can be reduced by weakening the field flux of the claw-pole generator. However, when the flux is weakened in the claw-pole generator, the

output voltage of the generator will soon drop below the battery voltage, and the claw-pole generator will not be able to output any energy. Thus, it is better to simply shut off the field.

Based on the above analysis, the following rules are designed for post-fault protection of claw-pole generators. Once a stator turn fault is detected, the short-circuit current is looked up using Figure 8.26 and Figure 8.27.

- (1) If the stator turn fault is so severe that the short-circuit current alone has exceeded the preset current limit, it is necessary to turn off the generator field immediately to prevent the fault from propagating into catastrophic winding and core failures and thus to reduce the risk of electric fire.
- (2) If the short-circuit current is lower than the current limit but the overall current in the shorted turns is higher than the limit, it is not absolutely necessary to turn off the generator field. But it is mandatory to shed non-critical electric loads in the vehicle so that the overall current can be kept at least within the current limit.
- (3) If the sum of short-circuit current and winding load current is below the current limit, there is no immediate risk of further thermal degradations of adjacent winding insulations. However, it is still a sound practice to shed unnecessary electric loads.

The post-fault protection strategy is illustrated below with the visual aid of Figure 8.28. Figure 8.28 is the same with Figure 8.26 except that the observed fault signatures are labeled with red, yellow, and green markers.

For fault signatures labeled with red markers, it means that the corresponding short-circuit current alone has exceeded the current limit. Once such fault signatures are

detected, the field of the claw-pole generator needs to be shut off immediately. For fault signatures labeled with yellow markers, the total current in the shorted turns is violating the current limit. But by reducing the load current of the generator, the overall current in the shorted turns can still be kept below the current limit. For fault signatures labeled with green markers, the total current in the shorted turns is below the current limit even if a stator turn fault exists. In such scenarios, it is still advisable to shed unnecessary electric loads, and the driver should be notified of the fault for timely repair.

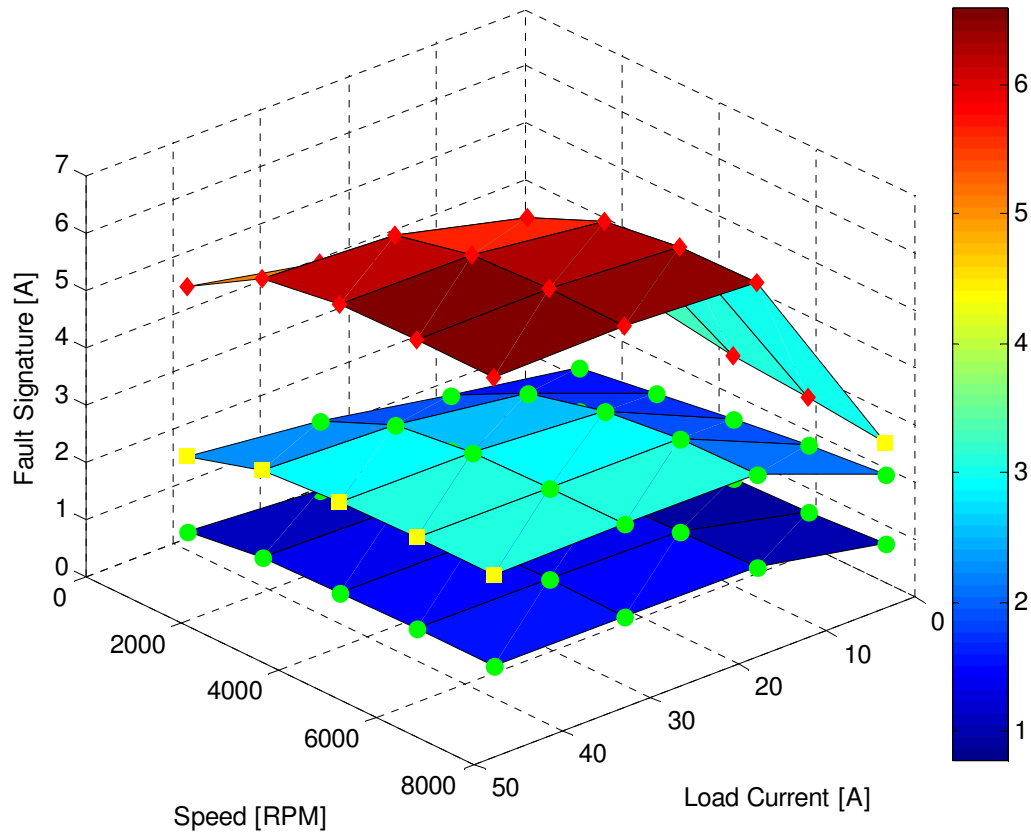


Figure 8.28: Illustration of the post-fault protection strategy with fault signatures classified into three categories.

8.4 Detection of the Rotor Eccentricity

The rotor eccentricity is another important type of internal fault for claw-pole generators. The eccentricity in the claw-pole generator will produce an unbalanced

magnetic pull (UMP) on the rotor, greatly increasing the bearing wear. If left undetected, the rotor eccentricity may eventually develop into stator-to-rotor rub.

8.4.1 Fault Signature

In general, eccentricity faults of an electric machine can be classified into three types: the static eccentricity, the dynamic eccentricity, and the mixed eccentricity. The differences between these three types of eccentricity are illustrated in Figure 8.32 through Figure 8.34. In all three plots, the outer ring represents the stator core of the claw-pole generator; the inner circle represents the rotor core; the green dot marks the geometric center of the stator core; the red dot marks the geometric center of the rotor core; and the cross label marks the rotational center of the rotor. For an ideal electric machine with no eccentricity, the stator geometric center, the rotor geometric center, and the rotational center should perfectly overlap.

Static eccentricity is normally caused by manufacturing imperfections and misalignment of the bearing and the rotor shaft. In the case of static eccentricity in Figure 8.32, the stator geometric center deviates from the rotational center. As a result, the length of the airgap is no longer uniform around the peripheral of the rotor, but the position of the minimum airgap is still fixed in space.

Dynamic eccentricity is mostly caused by bent rotor shaft. In the case of dynamic eccentricity in Figure 8.33, the rotor's geometric center deviates from the rotational center. As a result, the length of the airgap is not uniform around the peripheral of the rotor, and position of the minimum airgap rotates with the rotor. The length of the minimum airgap, however, does not change.

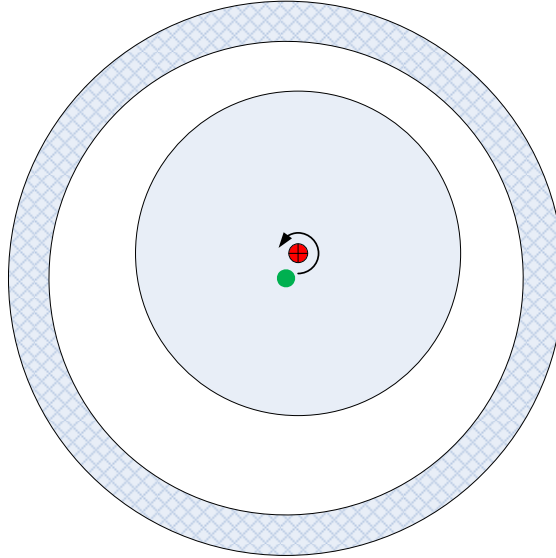


Figure 8.29: Illustration of the static eccentricity.

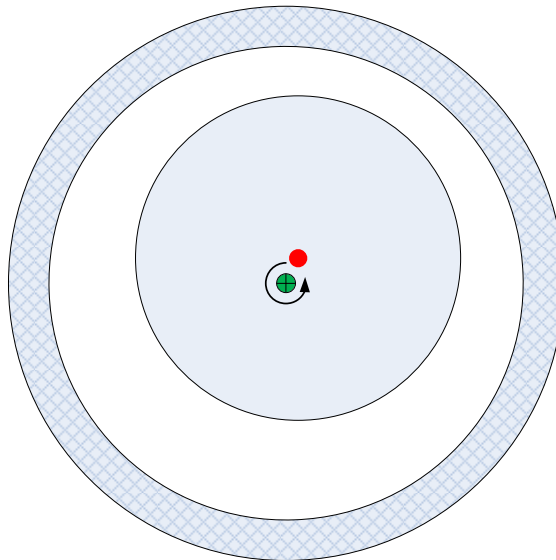


Figure 8.30: Illustration of the dynamic eccentricity.

In practice, most machine eccentricity is a mix of the static and dynamic eccentricities. As shown in Figure 8.34, geometric centers of the stator and the rotor both deviate from the rotational center. As a result, the airgap length is not uniform around the peripheral of the rotor, and position of the minimum airgap rotates with the rotor. Moreover, the length of the minimum airgap also varies as the rotor rotates.

As the length of the minimum airgap varies periodically as the rotor rotates, the eccentric claw-pole generator will develop an oscillating reluctance torque at the mechanical shaft frequency of the claw-pole generator. Moreover, since the rotor center is deviated from its rotational center, the gravity will also exert an additional oscillating torque on the rotor also at the generator shaft frequency. In an electric machine, the torque and current are strongly correlated. Hence the torque oscillation will also exhibit itself in the output current waveform. Therefore, the output current harmonic at the shaft frequency can be used as the fault signature for detecting rotor eccentricity.

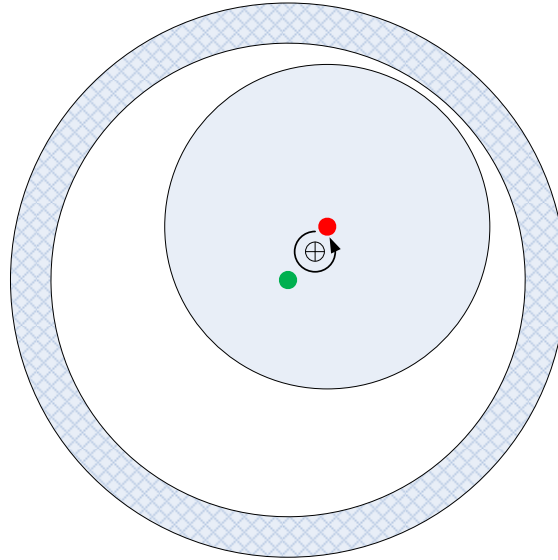


Figure 8.31: Illustration of the mixed eccentricity.

8.4.2 Finite-element Simulation

To verify the proposed fault signature for the rotor eccentricity, a 3-D finite-element model of the generator is built in Ansoft Maxwell © with a mix of static and dynamic rotor eccentricity. While the model is similar with that in Figure 6.5, the stator assembly is offset slightly in the radial direction to create the static eccentricity, and the geometric center of the rotor assembly is offset slightly away from its rotational center to create the

dynamic eccentricity. When both eccentricities co-exist, it is called a mixed rotor eccentricity that represents the most realistic type of eccentricity in real-world electric machines.

The torque and output current waveforms given by the finite-element model are shown in Figure 8.32 and Figure 8.33 respectively. Once smoothed by a low-pass filter, both the torque and current waveforms exhibit clear low-frequency oscillations. The frequency of the torque and current oscillation is verified to be the mechanical shaft frequency of the claw-pole generator. The oscillation frequency is related to the rectifier ripple frequency as follows,

$$f_{ecc} = \frac{f_{ripple}}{P \cdot n_{diode}} \quad (8.8)$$

where P equals the number of pole pairs of the alternator, and n_{diode} equals the number of diodes in the rectifier.

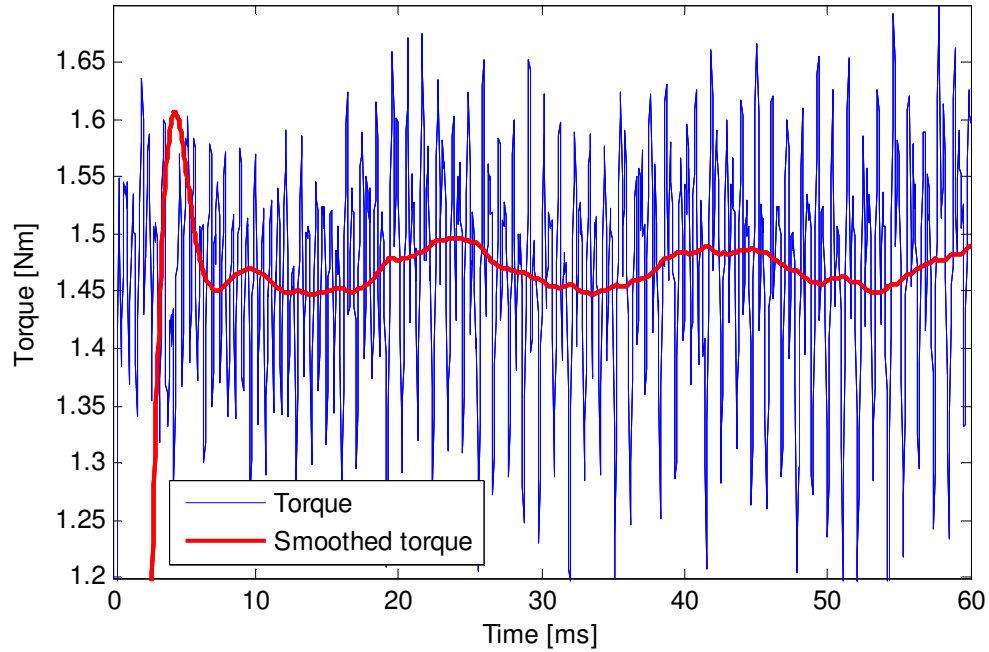


Figure 8.32: Simulated electromagnetic torque of a generator with mixed eccentricity.

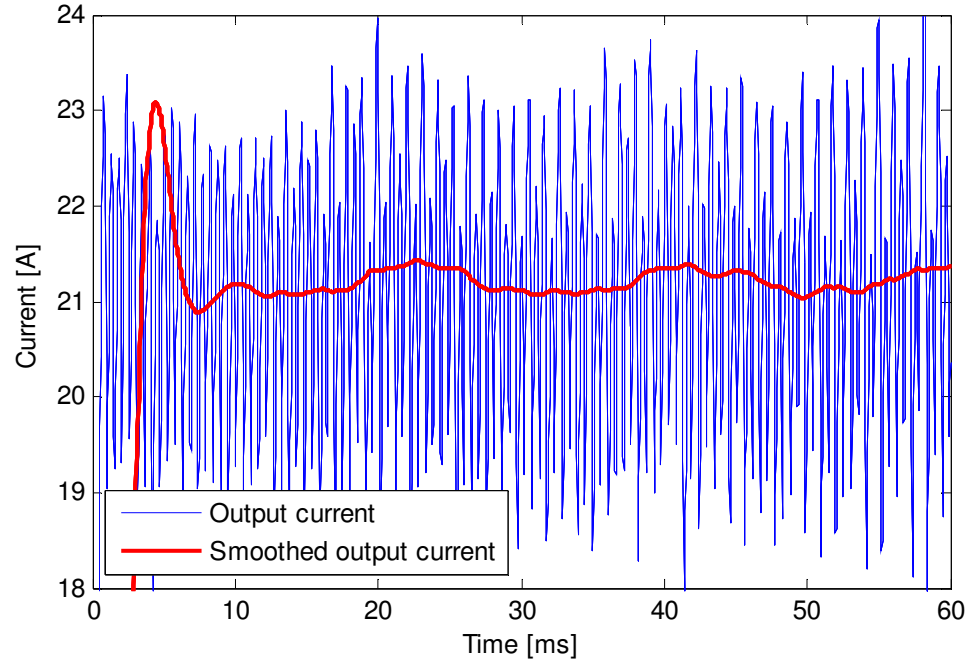


Figure 8.33: Simulated output current of a generator with mixed eccentricity.

8.4.3 Experimental Validation

The fault signature is further validated by experimental results. A claw-pole generator has been prepared with artificially induced mixed rotor eccentricity. The stator is offset by 0.15 mm at the drive-end bearing. The rotor has been offset from its rotational center by 0.15 mm by asymmetrical machining of the rotor core surface. The low-frequency current spectra of the generator without and with eccentricity are shown in Figure 8.34 (a) and (b) respectively. The generator is running at 3222 RPM which corresponds to a shaft frequency of 53.71 Hz. The generator output current is about 27 Amp. As can be seen in Figure 8.34 (a) and (b), the fault signature is significantly higher in the current spectrum of the eccentric generator.

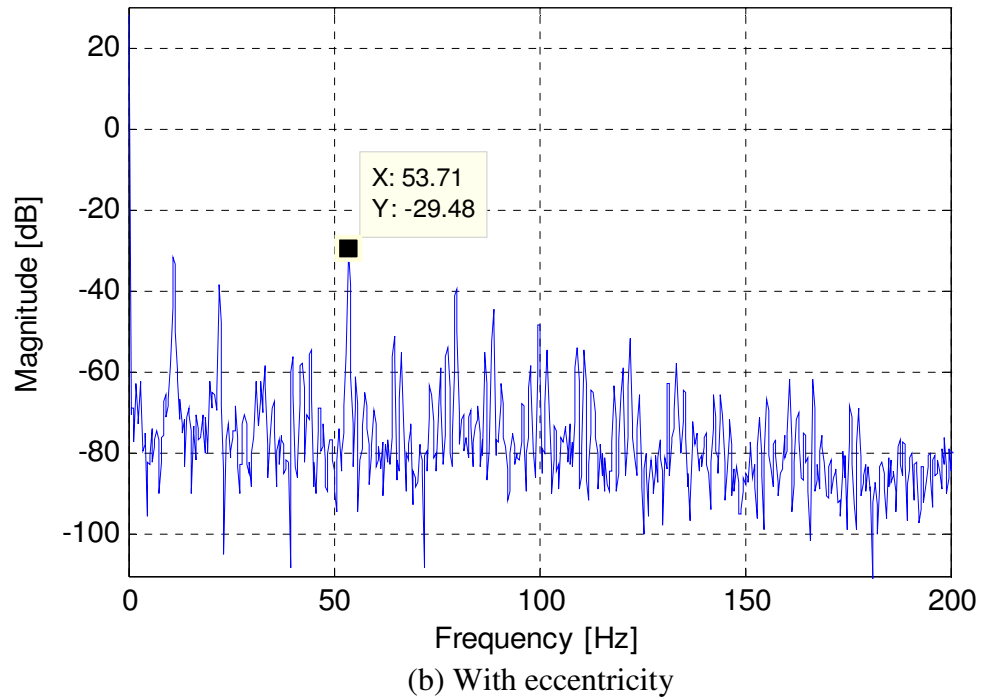
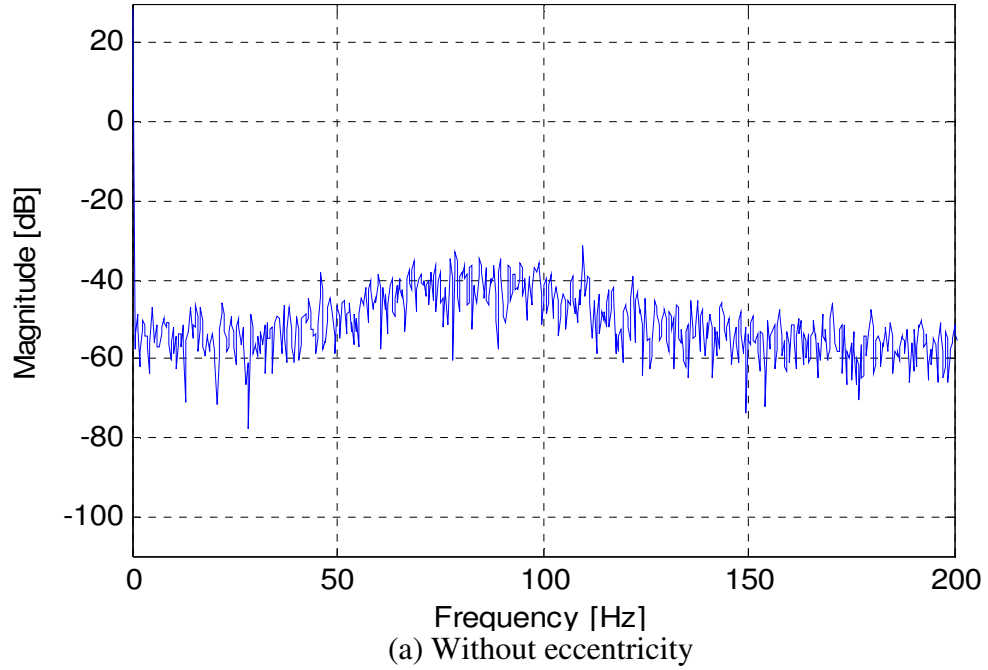


Figure 8.34: Low-frequency spectrum of the generator output current.

An important difference between the stator turn fault and the rotor eccentricity is that the rotor eccentricity is a slowly progressing fault. Contrary to the detection of the stator turn fault, it is unnecessary to monitor the eccentricity fault continuously.

Instead, the existence of rotor eccentricity fault can be tested, for example, every time the engine starts and is in its idle speed. Therefore, there is no need to record fault signatures at various generator speeds or load levels for detecting the rotor eccentricity fault.

8.5 Detection of the Generalized Bearing Roughness Fault

The worn bearing is one of the most common internal faults in claw-pole generators. The faulty bearing increases the noise level and vibration of the vehicle. A generator bearing-fault detector can help quickly identify the noise source and reduces misdiagnosis on claw-pole generators.

Unlike many other electric machines that are coupled to the load by a mechanical coupling or a gear set [103], the claw-pole generator is driven by a serpentine belt and a multi-rib pulley attached to the rotor shaft. As a result, the drive-end bearing of the claw-pole generator is subject to a strong side pull from the serpentine belt along a fixed direction. This large bearing side load has a profound impact on the fault mechanism and fault behavior of the generator drive-end bearing.

Whereas the developing bearing roughness can be easily detected by an accelerometer mounted on the generator housing, the objective of this study is to detect the bearing roughness using only the generator output current or voltage.

8.5.1 Accelerated Bearing Aging Tests

The generalized bearing roughness fault is induced in an online fashion using the experimental setup shown in Figure 8.35. An accelerometer is mounted on the drive-end housing of the claw-pole generator to monitor the vibration. A brass disk is installed on the extended generator shaft. A carbon brush is pressed against the brass disk so that a

current can flow into the generator shaft, pass through the drive-end bearing, and return from the outer housing while the generator is rotating.

During bearing aging tests, the speed of the prime mover (a PM servo motor) is precisely controlled at a constant 848 rpm. The generator speed is therefore around 2680 rpm. The DC load of the claw-pole generator is kept constant at 28 Amp. Accelerated bearing aging tests have been performed on three claw-pole generators. By passing about 10 Amp of current through the generator drive-end bearing, the bearing can develop roughness very quickly. It takes between 25 ~ 100 hours before the vibration and noise of the generator become unacceptable and the experiment needs to be stopped.

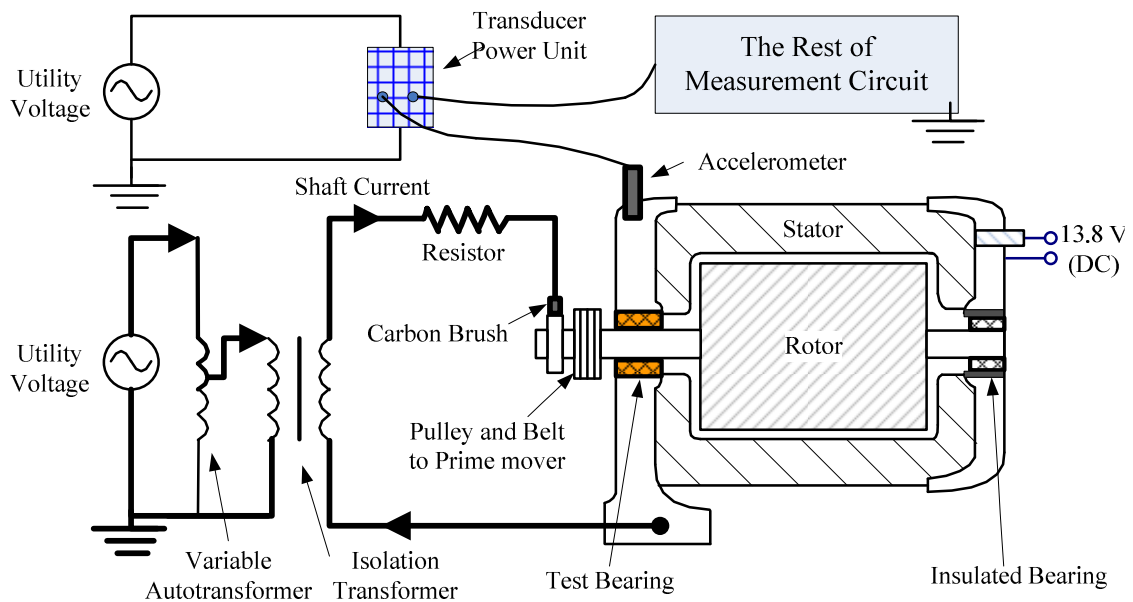


Figure 8.35: Experimental setup for accelerated bearing aging.

In addition to bearing aging tests, control tests have been performed on two claw-pole generators, where generators are running at the same operating condition with exactly the same setup just without the bearing current. Generators in control tests can run for a long time without producing increased audible noise or vibration.

Figure 8.36 shows several pictures of inner and outer races of generator bearings damaged by accelerated aging tests. Bearing 1 is manufactured by NSK with the model number of B17-102DG46. Bearing 2 and 3 are manufactured by SKF with the model number of BB1-3065DD. All bearings are deep groove ball bearings.



(a) Inner race of Bearing 1



(b) Outer race of Bearing 1



(c) Inner race of Bearing 2



(d) Outer race of Bearing 2



(e) Inner race of Bearing 3



(f) Outer race of Bearing 3

Figure 8.36: Pictures of bearings after the aging tests.

In Figure 8.36 (a), (c), and (e), generalized roughness caused by electric pitting can be observed in inner ring raceway surfaces for all bearings. Electric pitting is a phenomenon in which the bearing surface is partially melted by sparks when electric current enters the bearing and passes through an extremely thin oil film at the rolling contact point. For Bearing 1, some fluting patterns can also be observed in the inner race in addition to the electric pitting. Fluting patterns are not observed on Bearing 2 and 3 probably because of the bearing material difference.

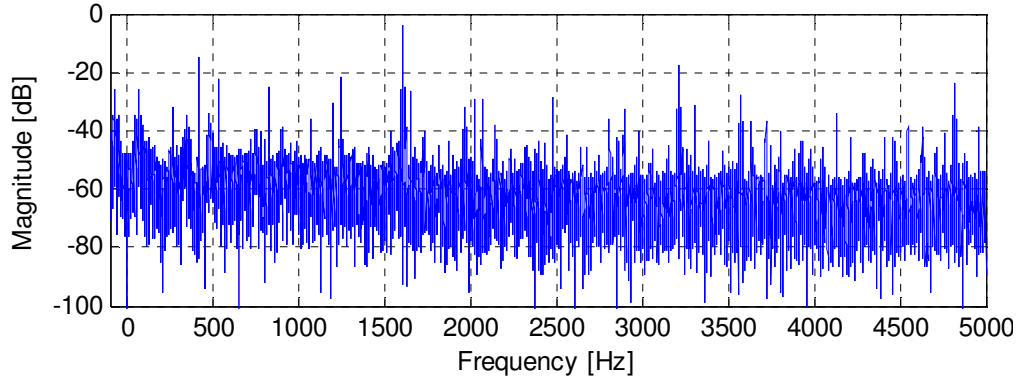
Generalized roughness can also be observed in outer ring raceway surfaces for all bearings, but only on one side of the outer races. This is because the serpentine belt is always pulling the generator shaft against one side of the bearing outer race. For Bearing 1, some fluting patterns can also be observed in the outer race in addition to the electric pitting.

8.5.2 Evaluation of Noise-cancellation Methods for Bearing Roughness Detection

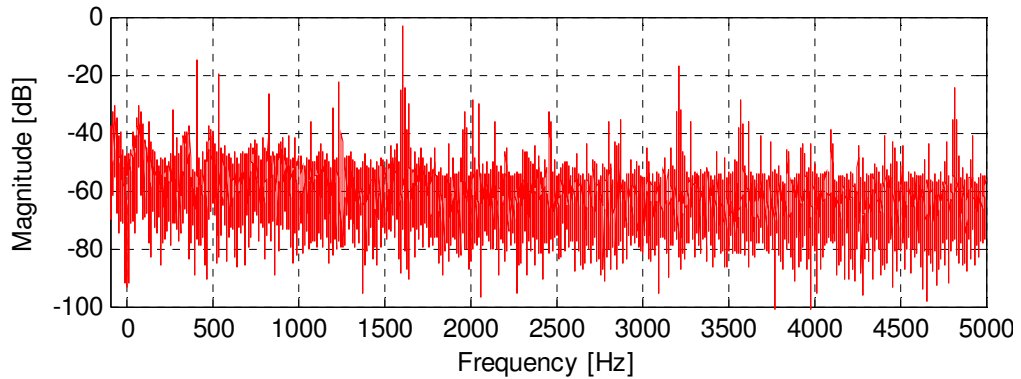
Conventionally, it is believed that shaft vibrations caused by generalized bearing roughness faults will modulate the airgap of the electric machine irregularly [103, 104]. The random variation of the airgap length does not give rise to specific harmonic components. Rather, it levitates the noise floor of the machine current spectrum in a broad frequency range. An adaptive notch-filtering method (or noise-cancellation method) based on Wiener filter was previously proposed in [104]. The energy in the noise floor of the current spectrum can be extracted using this method and is monitored over time as a condition indicator of the electric machine bearing

To evaluate the effectiveness of the method in detecting generalized bearing roughness in claw-pole generators, Figure 8.37 first compares the output current spectra

of Generator 3 before and after the bearing aging test. As expected, the generalized bearing roughness does not result in significant increase in specific current harmonics. All major harmonics in Figure 8.37 (b) can also be found in Figure 8.37 (a). However, a somewhat unexpected observation of Figure 8.37 is that the noise floors of two current spectra also do not show much difference.



(a) Generator output current spectrum when Bearing 3 is healthy



(b) Generator output current spectrum when Bearing 3 is worn

Figure 8.37: Comparison of generator current spectra before and after Bearing 3 develops roughness.

Using the Wiener-filter based adaptive notch filtering technique proposed in [104], the energy in the noise floor of the current spectrum is monitored over time. The experimental result for Bearing 3 is shown in Figure 8.38. Even though the vibration has increased substantially over the test period, the energy in the current noise floor remains

practically unchanged. The noise-cancelled (NC) current fails to indicate the developing bearing roughness.

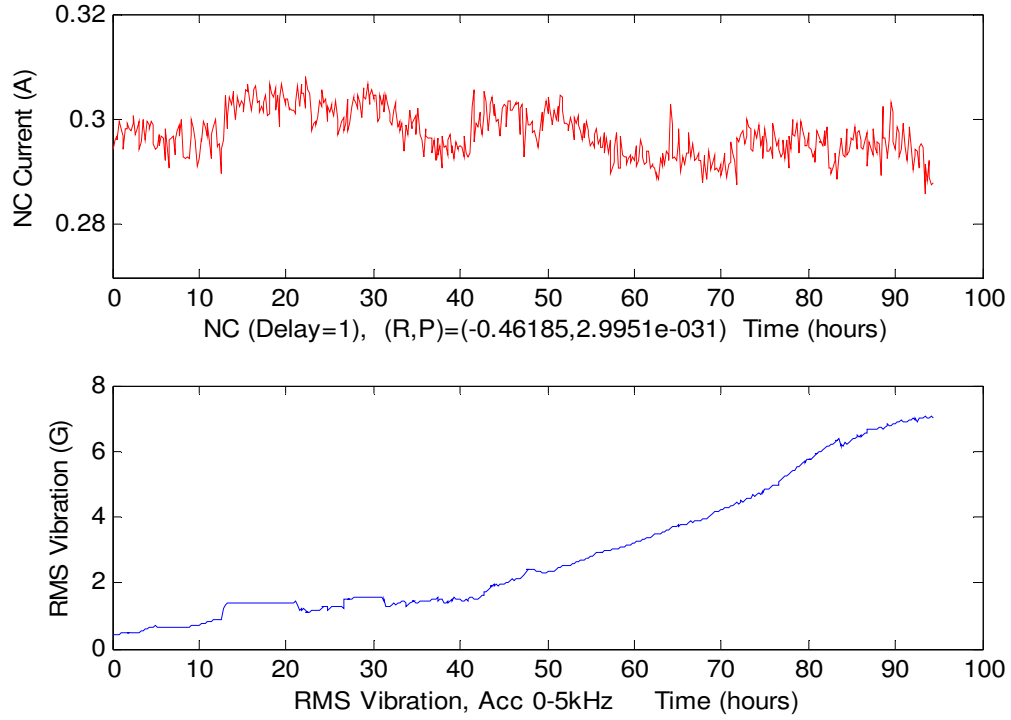


Figure 8.38: Notch-filtering-based bearing fault detection for Bearing 3.

The poor performance of noise-cancellation method applied to claw-pole generators can be largely attributed to the bearing size and the winding structure of claw-pole generators. Bearings in claw-pole generators are much smaller in size compared to those in typical induction machines (15~30 HP). The airgap length (0.44 mm) of the claw-pole generator, however, is comparable to typical induction machines. Hence, the claw-pole generator sees a much smaller percentage variation of airgap length when its bearing develops roughness. Moreover, the claw-pole generator used in this study has 12 poles. A large pole number also reduces the effect of an eccentric airgap on the generator current.

Therefore, to detect the generalized bearing roughness, a different fault indicator other than the energy in current noise floor has to be proposed.

8.5.3 Shift of Rectifier Ripple Frequency Caused by the Bearing Fault

Through multiple bearing aging tests and control tests, it is found that a worn bearing will result in slight frequency shift of the rectifier ripple harmonic in the generator output current. Experimental evidences for this phenomenon will be presented in detail in section 8.5.4. To understand why the worn bearing will lead to the shift of the rectifier ripple frequency, several possible mechanisms are analyzed and discussed in this section.

A. *Change of Contact Force Direction due to Skewed Rotor Shaft*

As shown in Figure 8.36, the wear on the bearing inner and outer races will leave some additional space between the bearing balls and bearing races. With the serpentine belt pulling the rotor shaft towards one direction, the bearing inner race and the drive end of the rotor shaft are likely to be offset slightly, as shown in Figure 8.39 (b). Since only the drive end of the shaft is offset and the non-drive end is fixed, the generator rotor shaft and the attached pulley are going to be skewed slightly towards the belt length direction, as shown in Figure 8.40.

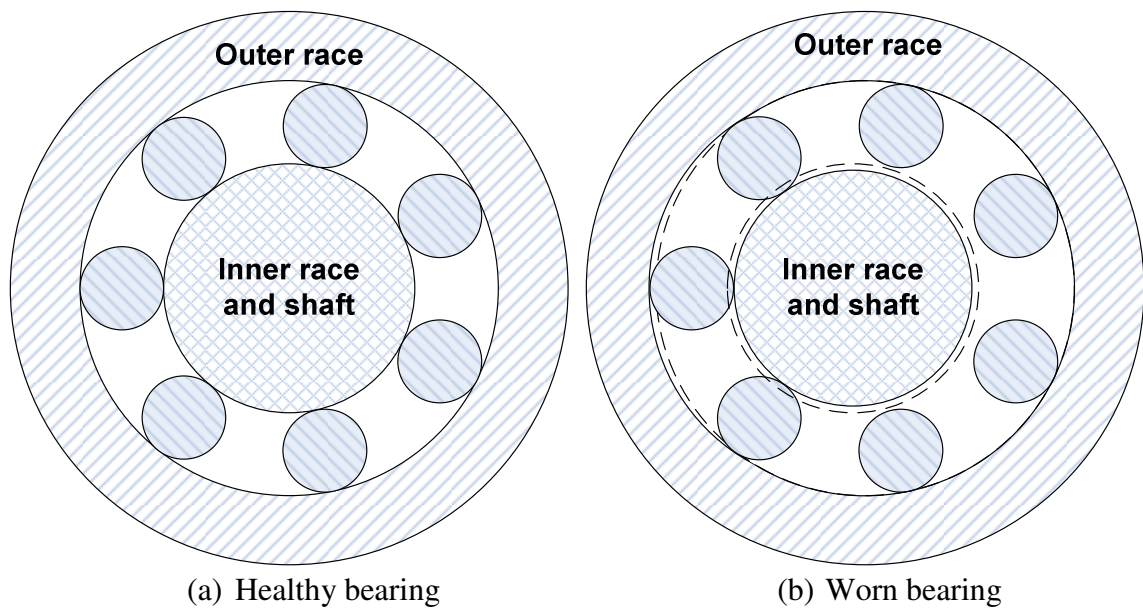
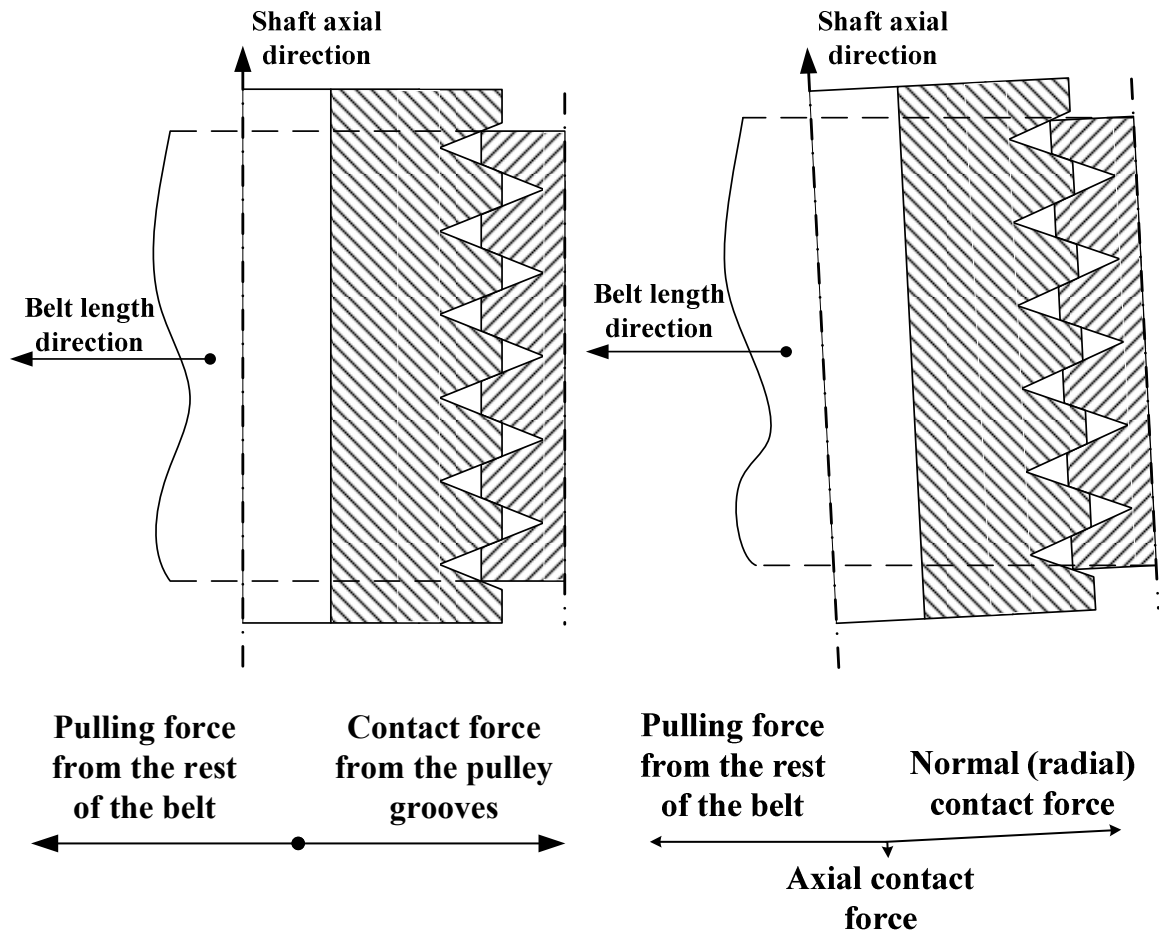


Figure 8.39: Pictures of bearings after the aging tests.



(a) Healthy bearing

(b) Worn bearing

Figure 8.40: Generator shaft positions and belt-segment force analysis with and without bearing fault.

With the rotor shaft slightly skewed, the contact force between the pulley grooves and serpentine belt ribs is going to be different. In Figure 8.40 (a), the small segment of serpentine belt that makes contact with the generator pulley has two forces on it. One is the pulling force from the rest of belt. The other is the contact force from the pulley grooves. These two forces are both in normal (radial) directions with respect to the belt (shaft) and balance out with each other. In Figure 8.40 (b), because of the skewed rotor shaft, the direction of the contact force has changed slightly with respect to the serpentine

belt. The contact force from the pulley grooves can now be divided into two components: One in the normal direction (or radial direction), and the other in the axial direction.

The directional change of the contact force on the serpentine-belt segment is likely to affect which part of the soft rubber rib is effectively contacting the pulley groove [105]. As a result, the contact area between the serpentine belt ribs and pulley grooves is shifted slightly. Consequently, the effective diameter of the generator pulley is changed.

Since the speed of the prime mover (a PM servo motor) is precisely maintained at a constant 848 rpm, the change of the effective pulley diameter is going to change the generator speed slightly. Moreover, the rectifier ripple frequency of the claw-pole generator is strictly proportional to the generator speed. Therefore, slight shift in rectifier ripple frequency may be observed during the bearing aging test.

In addition to the mechanism explained above, several other factors may also contribute to the change of effective diameter ratio between the generator pulley and the prime-mover pulley.

B. Uneven Contact Force Distribution due to Skewed Rotor Shaft

In addition to the directional change of the contact force, skewed rotor shaft may also result in uneven distribution of the contact force across different belt ribs.

In Figure 8.40 (b), for example, the bottom belt rib in the skewed rotor shaft may have a larger contact force than the top belt rib. If the total contact force remains unchanged, the bottom rubber rib may deform more into the pulley groove compared to the case where the rotor shaft is not skewed. Hence, the effective diameter of the generator pulley is changed.

C. Change of Belt Tension

As the bearing wears over time, the tension of the serpentine belt may be slightly reduced because the distance between the rotor shaft and the prime-mover shaft is slightly reduced. This change of belt tension is reversely proportional to the overall length of the belt and is typically very small. With a different belt tension, the compression force between the rubber belt rib and the pulley groove may also be different. This is likely to slightly shift the contact area between the belt ribs and pulley grooves and thus change the effective diameter of the generator pulley.

D. Increased Vibration

As the generator bearing wears over time, it leaves some additional space between the bearing balls and bearing races, as shown in Figure 8.39 (b).

The vibration of the bearing also increases substantially as the bearing wears. The excessive vibration of the bearing and the rotor shaft may move the position of the rotor shaft around irregularly given the available space between the bearing balls and bearing races. The average effect of the bearing vibration may move the contact area between the rubber belt ribs and pulley grooves. As a result, the effective diameter of the generator pulley may be changed.

E. Temperature Rise due to Increased Bearing Friction

The increased friction and vibration due to the bearing fault is likely to increase the temperature of the bearing and the generator pulley higher than that of the prime-mover pulley. Before reaching the thermal steady state, the temperature rise of the generator pulley may also contribute slightly to the effective diameter change of the generator pulley.

To sum up, the frequency shift of the rectifier ripple harmonic is caused by the change in the effective diameter of the generator pulley. The change of generator pulley diameter is further caused by the bearing wear through one or more of the introduced fault mechanisms.

The directional change of the contact force between the belt ribs and pulley grooves due to the skewed rotor shaft is likely the main reason for the diameter change of the generator pulley. But other factors, such as the uneven contact force distribution, changed belt tension, and etc, may also contribute to the change of effective diameter of the generator pulley.

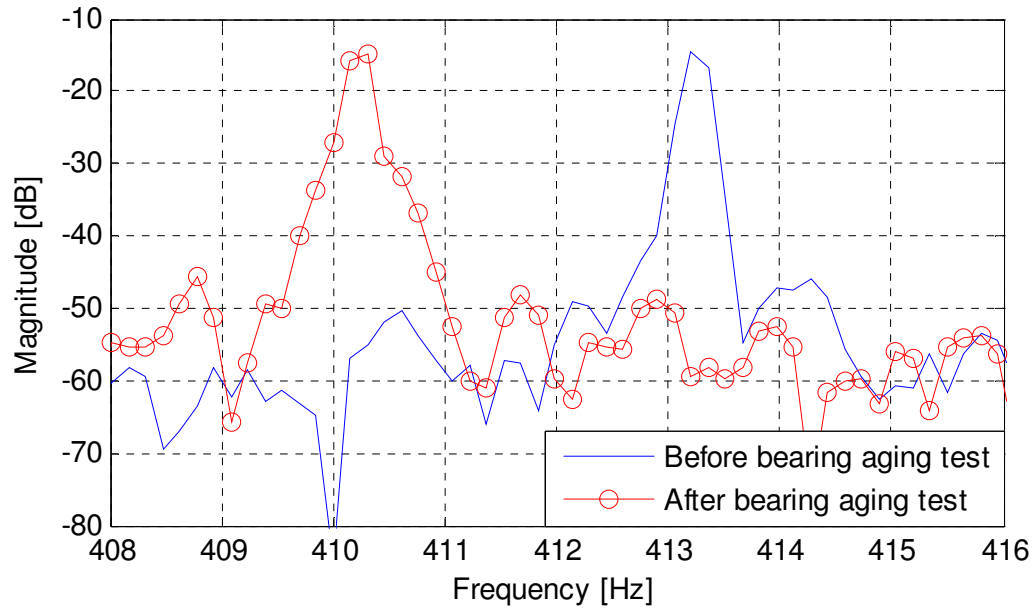
Nevertheless, no matter which mechanisms cause the diameter change of the generator pulley, the frequency shift of the rectifier ripple harmonic is the result of the worn bearing and is thus proposed as the new condition indicator for bearings in belt-driven claw-pole generators.

8.5.4 Experimental Validation

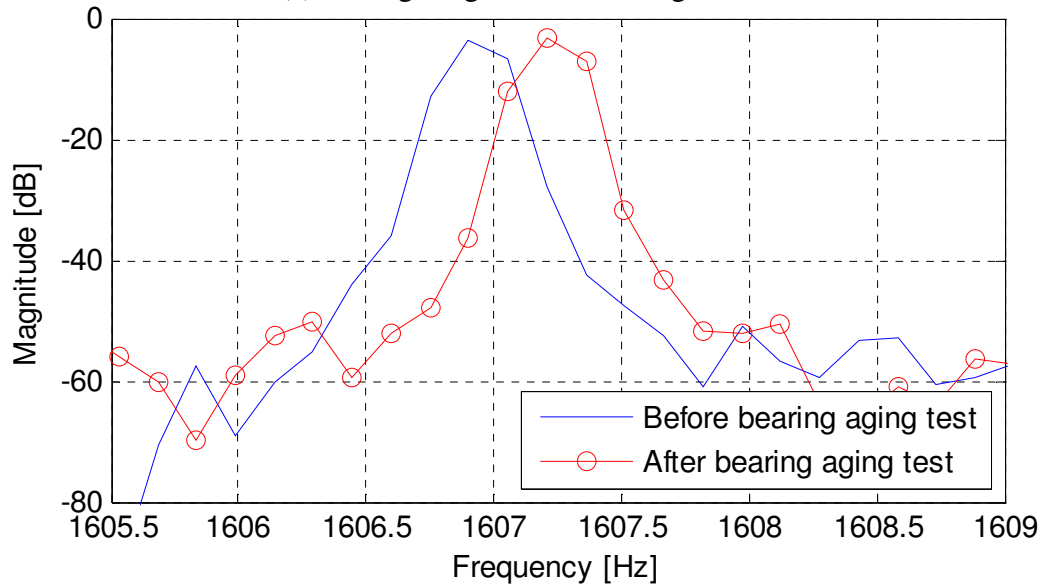
Upon careful comparison between Figure 8.37 (a) and (b), it is found that some current harmonics in Figure 8.37 (b) have indeed shifted slightly in frequency compared to Figure 8.37 (a).

Figure 8.41 shows two zoom-in plots of Figure 8.37 around the voltage-regulator PWM frequency and the rectifier ripple frequency. The PWM harmonic produced by the voltage regulator has decreased by 3 Hz. Datasheets of the voltage-regulator control chip confirm that the range of PWM frequency is between 360 Hz and 440 Hz, and the frequency shift of 3Hz is quite normal.

On the other hand, the rectifier ripple frequency has increased by about 0.35 Hz. Since the rectifier ripple frequency is strictly related to the generator speed, this indicates a slight speed change of the claw-pole generator by 0.022%.



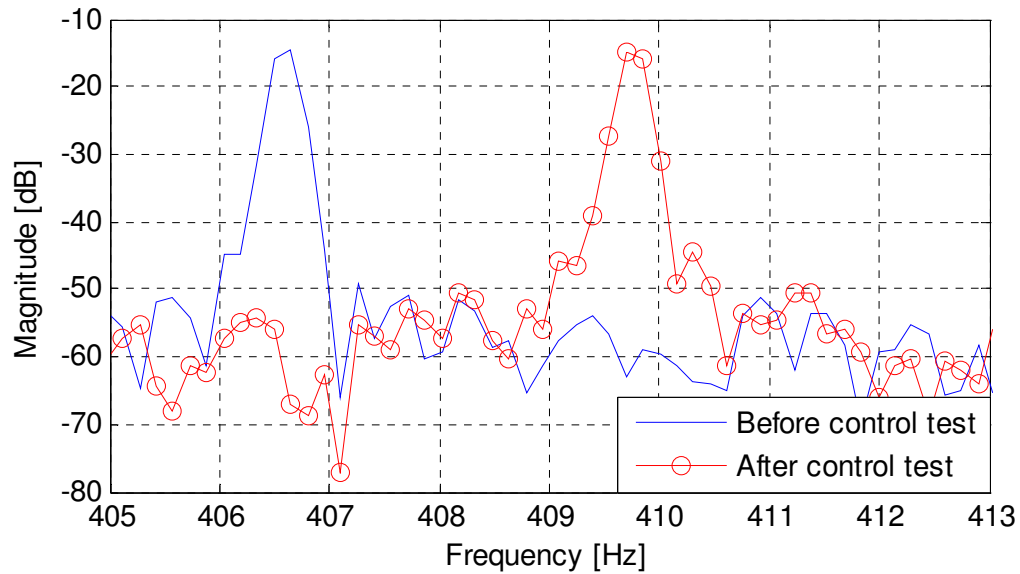
(a) Voltage-regulator switching harmonic



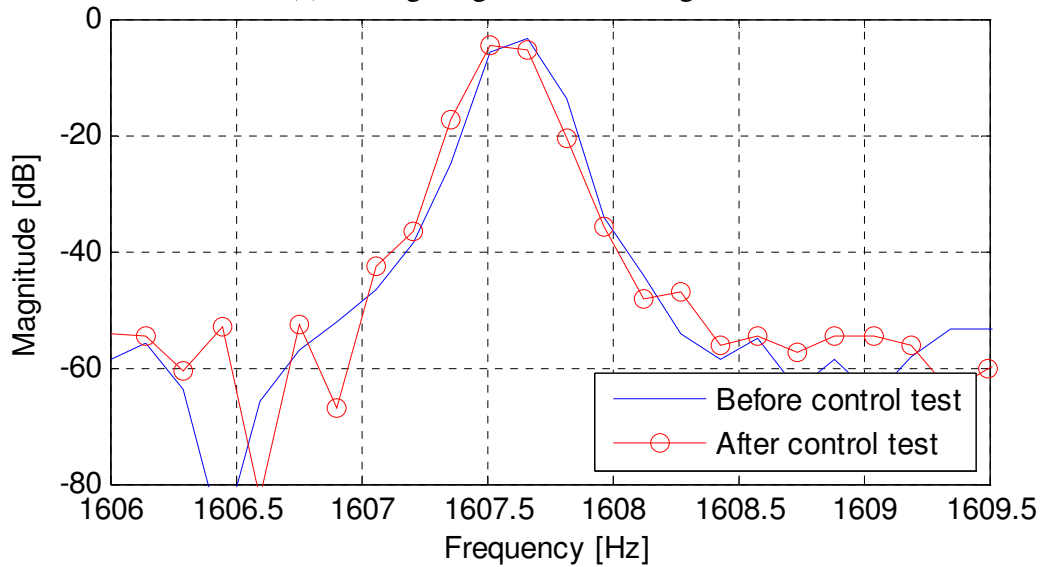
(b) Rectifier ripple harmonic

Figure 8.41: Frequencies of major current harmonics before and after the bearing aging test.

Similarly, Figure 8.42 compares the voltage-regulator PWM harmonics and the rectifier ripple harmonics before and after a *bearing control test* that lasts for 63 hours. The PWM frequency has increased by about 3 Hz. Hence, the frequency shift of the PWM frequency is not unique to the bearing aging test.



(a) Voltage-regulator switching harmonic



(b) Rectifier ripple harmonic

Figure 8.42: Frequencies of major current harmonics before and after the control test.

Interestingly, the rectifier ripple frequency stays practically constant before and after the control test, as shown in Figure 8.42 (b). This is different from the phenomenon observed during the bearing aging test in Figure 8.41 (b). Therefore, the bearing generalized roughness may be related to the frequency shift of the rectifier ripple harmonic, or the slight speed change of the claw-pole generator.

To further verify the above observation that the worn bearing causes frequency shift of the rectifier ripple harmonic in claw-pole generators, the rectifier ripple frequency is estimated accurately using the interpolated FFT technique (see section 7.2.2) and plotted over time for all three bearing aging tests and two control tests, as shown in Figure 8.42~Figure 8.47.

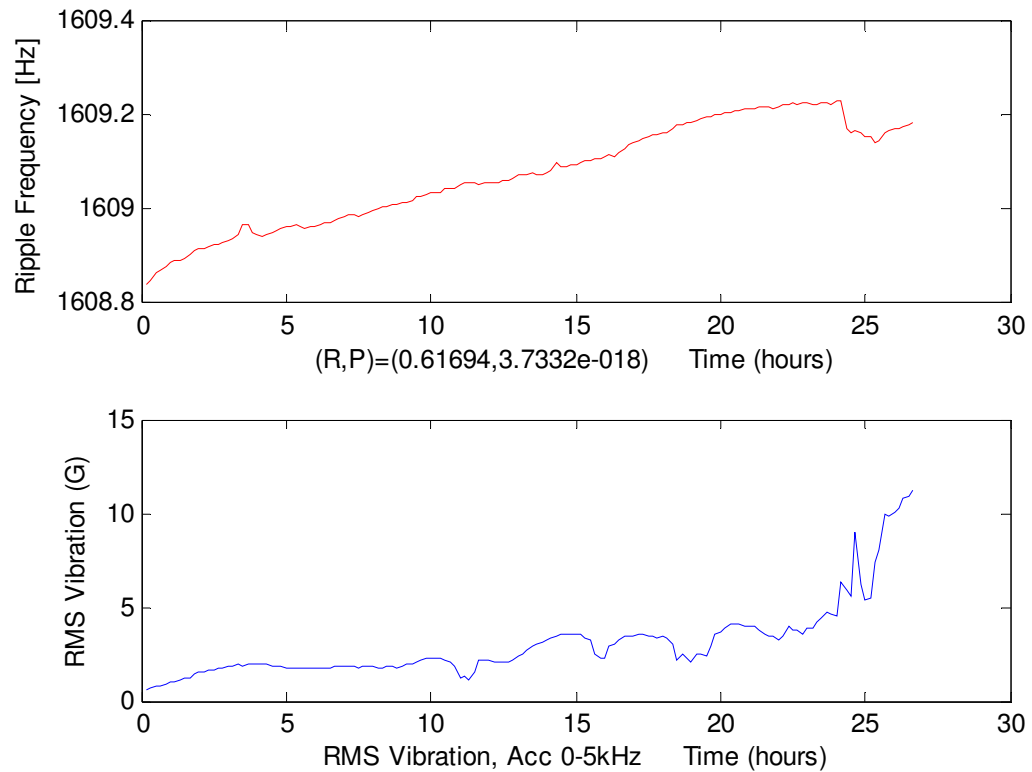


Figure 8.43: Ripple frequency and vibration during aging test on Bearing 1.

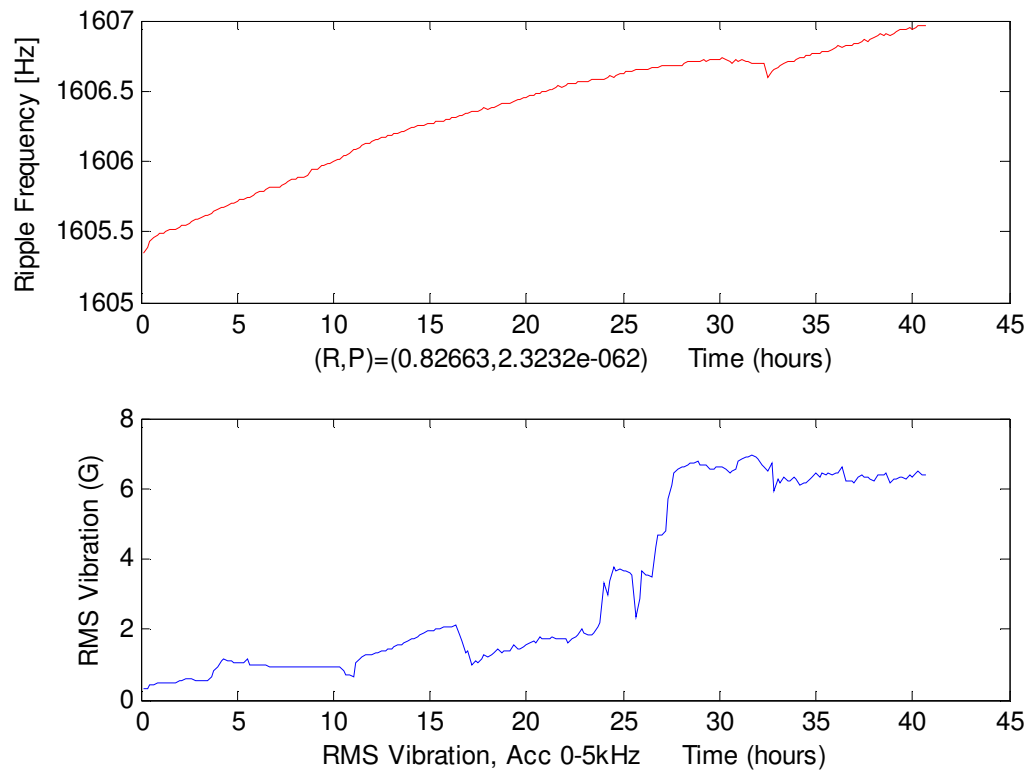


Figure 8.44: Ripple frequency and vibration during aging test on Bearing 2.

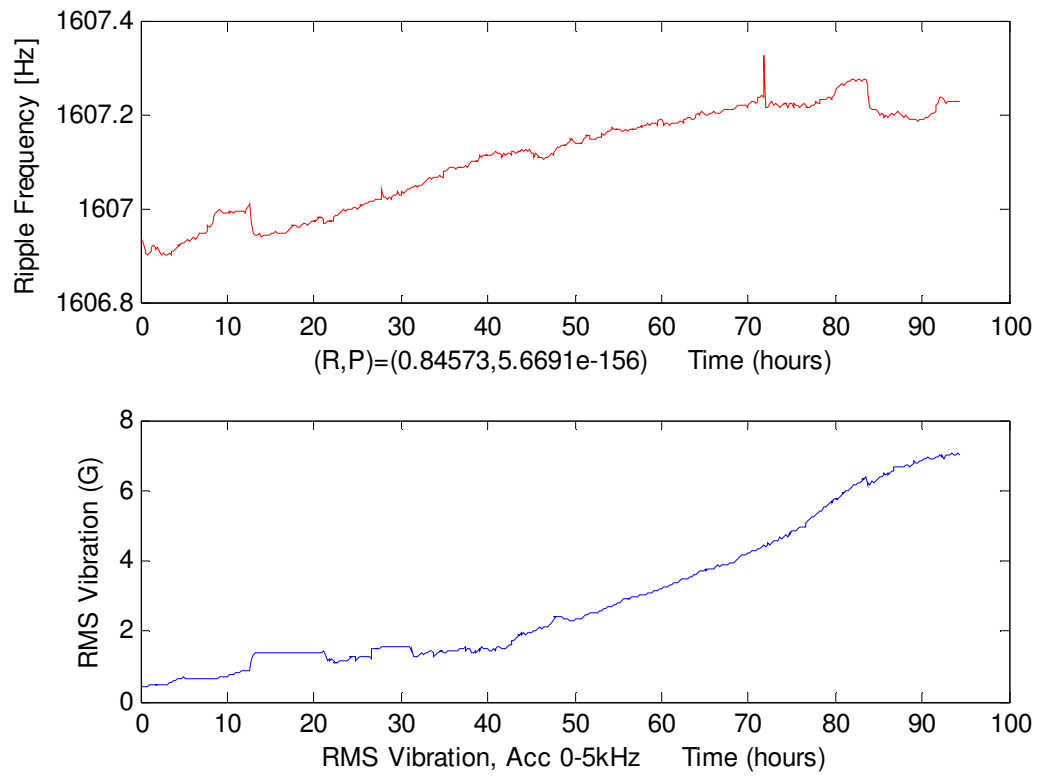


Figure 8.45: Ripple frequency and vibration during aging test on Bearing 3.

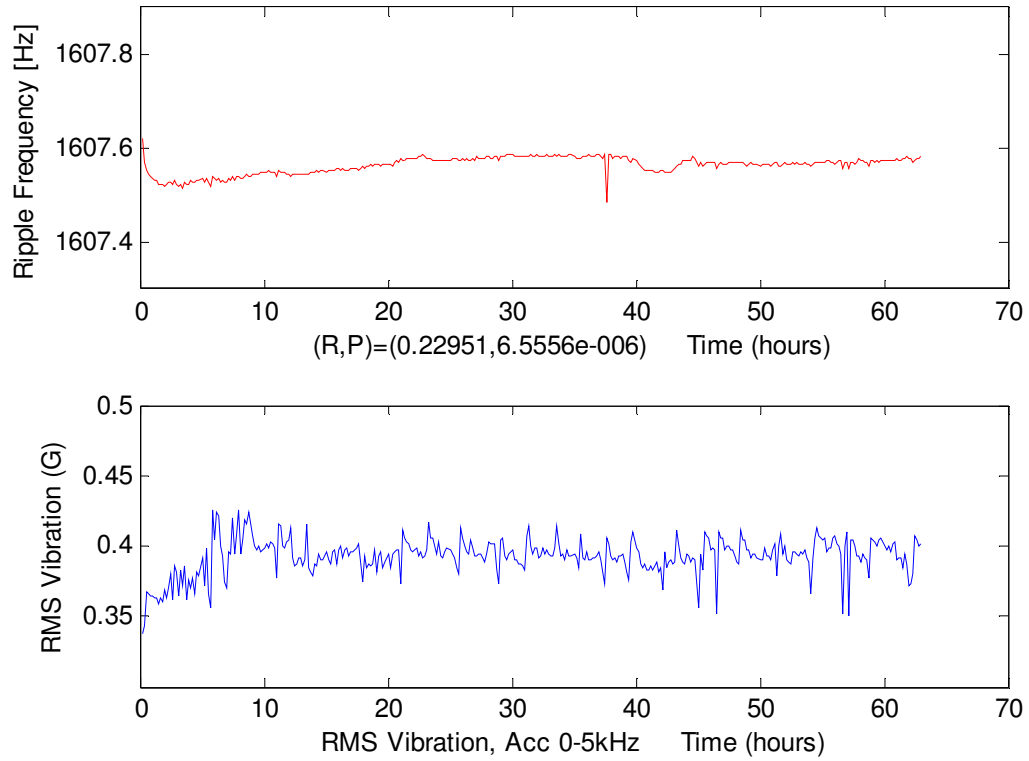


Figure 8.46: Ripple frequency and vibration during control test on Bearing 4.

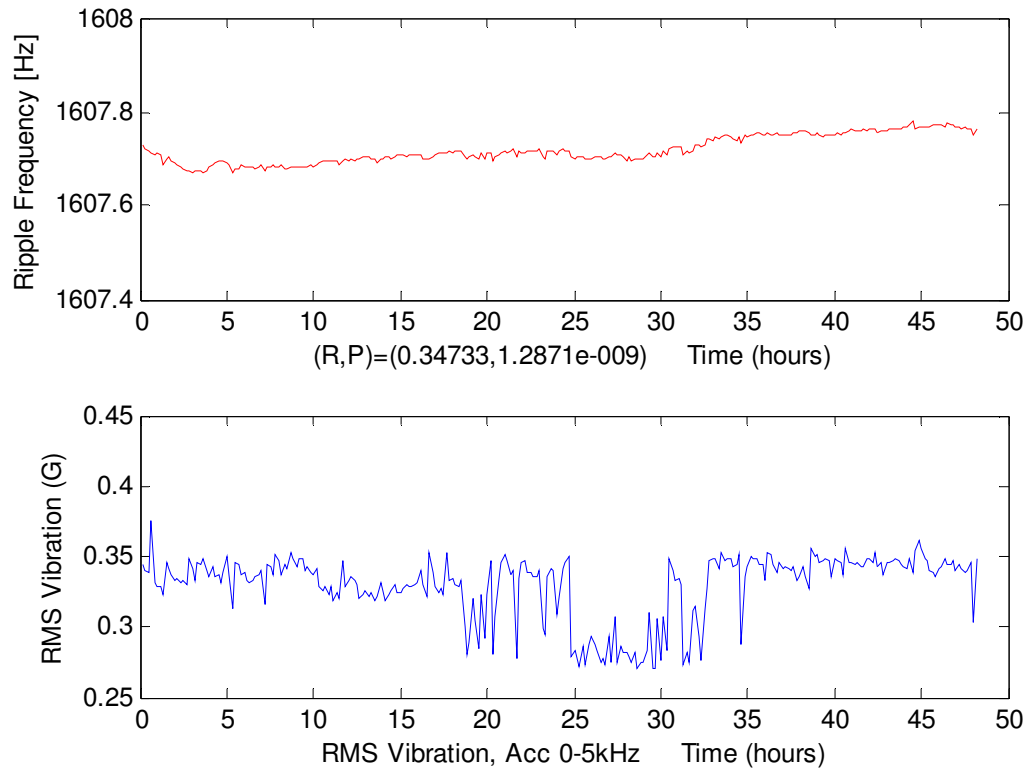


Figure 8.47: Ripple frequency and vibration during control test on Bearing 5.

As can be seen in Figure 8.42~Figure 8.47, the rectifier ripple frequency stays within a 0.1 Hz band during two control tests.

During bearing aging tests, the rectifier ripple frequency has increased over time by at least 0.35 Hz and by as much as 1.62 Hz. This corresponds to a speed change of the claw-pole generator of 0.022%~0.09%.

As discussed in section 8.5.3, the speed change of the claw-pole generator is caused by the change in the effective pulley diameter ratio. The diameter of the generator pulley is measured to be 59 mm. From observed frequency deviations during accelerated bearing aging tests, the change of the effective pulley radius is estimated in the range of 6.5 μm ~26.5 μm .

The frequency deviations, correlation coefficients between the ripple frequency and the vibration, and P-value of the correlation for all tests are finally summarized in Table 8.2.

Table 8.2: Experimental results for bearing aging tests and control tests.

Test No.	Ripple Frequency Deviation (Hz)	Correlation with Vibration Measurement	P-value of Correlation
<i>Aging Test 1</i>	0.35	0.6169	3.733e-18
<i>Aging Test 2</i>	1.62	0.8266	2.323e-62
<i>Aging Test 3</i>	0.35	0.8457	0.669e-156
<i>Control Test 4</i>	0.092	0.2295	6.555e-6
<i>Control Test 5</i>	0.095	0.3473	1.287e-9

The correlation coefficients between the ripple frequency and the vibration are noticeably larger for the bearing aging tests. The p-values for the bearing aging tests are also much more significant than those for the control tests.

Therefore, the frequency deviation of the rectifier ripple harmonic is proved to be strongly related to the bearing wear in claw-pole generators and can be used as a fault indicator for detecting generalized bearing roughness fault.

8.6 Chapter Summary

This chapter addresses the early detection of internal faults for claw-pole generators with built-in rectifiers.

Specifically, the chapter first investigated the effect of a full-bridge rectifier on the three-phase electric machine with stator turn fault. Theoretic and finite-element analyses show that the output current harmonic at $1/3$ of the rectifier ripple frequency can be used as an alternative of the negative sequence component to quantify the level of unbalance in a rectified three-phase system. A novel stator turn fault detector for claw-pole generators is proposed based on this principle. The performance of the stator turn-fault detector is demonstrated by extensive experiment results.

In addition to detection of the stator turn fault, this chapter also analytically derives a dynamic model of claw-pole generator with stator turn faults. This model, when implemented in its equivalent-circuit form, is able to accurately predict the fault current from the observed fault signature. Using a database generated by this model, a well-informed post-fault protection strategy is proposed to prevent the insulation from further thermal degradation while preserving as much limp-home capability of the claw-pole generator as possible. To the best knowledge of the author, this is first successful attempt to evaluate the severity of the stator turn fault for any type of electric machine.

Another internal fault investigated in this chapter is the rotor eccentricity. Finite-element simulation shows that the rotor eccentricity will give rise to the output current

harmonic at the mechanical shaft frequency of the generator. The fault signature is theoretically explained and is also experimentally verified on a claw-pole generator with artificially induced eccentricity fault.

Although the above condition monitoring methods are originally proposed for claw-pole alternators, they can also be easily applied to many other poly-phase AC generators with a rectified DC link.

Finally, the detection of bearing generalized roughness is investigated. It is found that the bearing wear in a belt-driven claw-pole generator can lead to slight change of effective generator pulley diameter through one or more of the introduced fault mechanisms. The change of effective generator pulley diameter is going to further shift the frequency of rectifier ripple harmonic in the generator output current. Through multiple accelerated bearing aging tests and control tests, it is confirmed that the frequency deviation of the rectifier ripple harmonic is strongly correlated to the bearing wear in claw-pole generators and can be used as a fault indicator of the generalized bearing roughness.

CHAPTER 9 Conclusions, Contributions, and Recommended Future Work

9.1 Conclusions

The dissertation has proposed several advanced sensorless thermal, mechanical, and insulation monitoring methods for induction motors and claw-pole generators by smartly utilizing special features and capabilities of the connected power electronic converter.

Chapter 1 has introduced the background information related to the sensorless condition monitoring of power-electronics-converter fed electric machines. The scope of the study is refined to induction motors fed by closed-loop inverters and claw-pole generators with built-in rectifiers.

Chapter 2 has presented a comprehensive literature survey on methods to detect stator turn faults and methods to estimate the stator temperature of induction machines. The literature survey concludes that the major limitation of existing stator turn-fault detectors for closed-loop induction motor drives is that they require intrusive and complicated calibration of machines' inherent asymmetry. The major challenge for signal-injection-based temperature monitoring of inverter-fed induction machines is that motor terminal voltage sensors are not available in typical inverter drives.

Chapter 3 has summarized the previous work on condition monitoring of claw-pole generators with built-in rectifiers. However, the limited literature reveals that the condition monitoring of claw-pole generators remains largely unexplored. The major challenge for condition monitoring of claw-pole generators is that the built-in rectifier makes it difficult to access the three-phase voltage and current measurements that are essential in the condition monitoring of conventional AC electric machines.

Chapter 4 has presented a highly sensitive stator turn-fault detector for induction machines fed by closed-loop motor drives. The major innovation of the method is that it eliminates the intrusive learning process of machine inherent asymmetry by taking advantage of the current regulator in the closed-loop inverter. For the special case of a single inverter driving multiple motors, a fault-locating method has also been proposed by analyzing the interactions between multiple parallel motors in the presence of the stator turn fault.

Experimental results demonstrate the method can reliably detect a subtle 1-turn short circuit in a 5-HP induction motor within 5 fundamental cycles, even when the motor speed is as low as 300 rpm and there are as many as 216 turns per phase. Moreover, only one set of baseline calibration is required to commission the method. Hence, there is no need to vary the amount of voltage unbalance to learn the inherent asymmetry of the induction machine.

The method is also implemented in a general-purpose inverter designed and built from the ground up. The real-time experimental results prove that the method is suitable for embedded implementation.

Chapter 5 has proposed a nonintrusive thermal monitoring scheme for closed-loop drive-fed induction motors using DC current injection. With no available terminal voltage sensors in inverter drives, the main contribution of the work is the proposed theory on how the DC component of the terminal voltage can be accurately estimated despite inverter non-idealities.

The method is implemented in real time in the home-built inverter drive without any additional sensors or hardware. The temperature estimation error for a 5-HP induction

motor is less than 3°C at a constant operating condition and less than 5°C even with varying load level, motor speed, and DC bus voltage of the induction motor drive. At the same time, the injected DC current level is kept within a record-low 5% of motor's rated current to minimize adverse effects such as torque oscillation.

In Chapter 6, a general analysis has been performed to better understand the fundamental aspects of claw-pole-generator condition monitoring. Common failure modes of claw-pole generators are identified and summarized, among which several important types of faults are selected to be investigated further in this study. One claw-pole generator is reverse engineered and modeled in finite-element simulation software. Finally, spectral analyses are performed on the generator voltages and currents. Several harmonics in the generator output voltage and current spectra are identified to be related to different faults in the claw-pole generator.

Chapter 7 addresses the early detection of system-related faults for claw-pole generators with built-in rectifiers. Specifically, a novel generator speed estimator is proposed based on ripple frequency detection in the generator output voltage using 256-point interpolated FFT. The typical speed estimation error is in the order of 0.1% with a quick 25 ms response time, which makes the method effective even during fast mechanical transients. The proposed speed estimator is applied to the detection of belt slip. The experimental results prove that the belt-slip fault can be reliably detected within a wide speed range.

An incipient belt-defect detector is also proposed in this chapter based on monitoring the belt-cycle related harmonics in the generator output current spectrum. Experimental

results demonstrate that belt defects, such as torn rubber in the grooves, can be reliably detected over a wide speed range.

In Chapter 8, several important internal faults of claw-pole generators, such as the stator turn fault, the rotor eccentricity, and the generalized bearing roughness fault are investigated. Specifically, the stator turn fault is studied in detail. Theoretic and finite-element analyses show that the output current harmonic at $1/3$ of the rectifier ripple frequency can be used to quantify the level of unbalance in a rectified three-phase system. A novel stator turn fault detector for claw-pole generators is proposed based on this principle. Extensive experiment results demonstrate that the method can reliably detect a 1-turn stator short circuit at various operating conditions even with a $0.2\ \Omega$ current-limiting resistor.

This chapter also analytically derives a dynamic model of claw-pole generator with stator turn faults, which is shown capable to accurately predict the fault current from the observed fault signature. Using a database generated by this model, a well-informed post-fault protection strategy is proposed to prevent the insulation from further thermal degradation while preserving as much limp-home capability of the claw-pole generator as possible. To the best knowledge of the author, this is first successful attempt to evaluate the severity of the stator turn fault for any type of electric machine.

Another internal fault investigated in this chapter is the rotor eccentricity. Finite-element simulation shows that the rotor eccentricity will give rise to the output current harmonic at the mechanical shaft frequency of the generator. The fault signature is theoretically explained and is then experimentally verified on a claw-pole generator with artificially induced eccentricity fault.

Finally, the detection of worn bearing is investigated. It is found that that the bearing wear in a belt-driven claw-pole generator can lead to slight change of effective generator pulley diameter through one or more of the introduced fault mechanisms. The change of effective generator pulley diameter is going to further shift the frequency of rectifier ripple harmonic in the generator output current. Through multiple accelerated bearing aging tests and control tests, it is confirmed that the frequency deviation of the rectifier ripple harmonic is strongly correlated to the bearing wear in claw-pole generators and can be used as a fault indicator of the generalized bearing roughness. The proposed fault indicator is clearly superior to the conventional noise-cancellation method when applied to belt-driven claw-pole generators

9.2 Contributions

The main contributions of this research are summarized as following:

1. A comprehensive literature survey of stator turn-fault detectors for closed-loop inverter-fed induction motors is presented. Various methods are compared in terms of detection sensitivity and implementation complexity.
2. A simple and highly-sensitive stator turn-fault detector is proposed for induction motors fed-by closed-loop inverter drives. The proposed method eliminates the need of learning the inherent asymmetry of the induction motors, and is sensitive enough to detect 1-turn stator fault out of 216 turns per phase even at low motor speed.
3. A sensorless thermal-monitoring method is proposed for induction motors fed by closed-loop inverters. The major difficulty met by the existing methods, the inconsistency in terminal-voltage estimation, is overcome in the

proposed method by carefully analyzing and compensating for the effects of inverter non-idealities. Even with only 5% of injected DC current, the method achieves a temperature estimation error less than 5°C for varying load, varying speed, and varying DC bus voltage operation of the induction motor drive.

4. A general-purpose programmable inverter is co-designed and co-built from the ground up by the author and a visiting professor. The inverter drive allows for real-time integration of condition monitoring schemes with the motor control algorithms. It is a valuable asset towards future study of condition monitoring of drive-fed motors.
5. A flexible and detailed finite-element model has been built for the claw-pole generator. The model can be easily modified to simulate various types of generator faults so that better understanding of the fault behaviors can be obtained.
6. A comprehensive spectral analysis has been performed on the voltage and current waveforms of the claw-pole generator. Several important harmonic components in the generator output voltage and current are identified to be useful in detecting various faults of the claw-pole generator.
7. A dynamic model of the claw-pole generator with stator turn faults is derived to analyze how the stator turn fault would interact with the connected battery and the static full-bridge rectifier, and how it would affect the generator's output voltage and current. A robust stator turn fault detector is proposed based on the model-based analysis. Moreover, the fault signature given by

the generator model is so accurate that quantitative evaluation of the fault severity can be performed. To the best knowledge of the author, this is first successful attempt to evaluate the severity of the stator turn fault for any type of electric machine without resorting to exhaustive experimental testing.

8. A novel fault indicator for detecting generalized bearing roughness is proposed for belt-driven claw-pole generators. The proposed fault indicator is validated by multiple accelerated bearing aging tests and control tests, and is shown to have superior performance compared to conventional noise-cancellation method when applied to claw-pole generators.

The research work presented in this dissertation has resulted in the following publications:

Journal Papers

- [1] **S. Cheng**, P. Zhang, T. G. Habetler, "An Impedance Identification Approach to Sensitive Detection and Location of Stator Turn-to-Turn Faults in a Closed-Loop Multiple-Motor Drive," *IEEE Transactions on Industrial Electronics*, vol. 58, pp. 1545-1554, 2011.
- [2] **S. Cheng**, Y. Du, J. A. Restrepo, P. Zhang, T. G. Habetler, "A Nonintrusive Thermal Monitoring Method for Induction Motors fed by Closed-loop Inverter Drives," *IEEE Transactions on Power Electronics*, accepted for publication.
- [3] **S. Cheng**, T. G. Habetler, "Using Only the DC Current Information to Detect Stator Turn Faults in Automotive Claw-pole Generators," *IEEE Transactions on Industrial Electronics*, accepted for publication.

Conference Papers

- [1] **S. Cheng**, T. G. Habetler, "A new method to detect stator turn-to-turn faults in a closed-loop multiple-motor drive system," in *Proceedings of the 7th IEEE International Symposium on Diagnostics for Electrical Machines, Power Electronics & Drives (SDEMPED'09)*, Cargese, France, Sept. 2009, pp. 1-6.
- [2] **S. Cheng**, P. Zhang, T. G. Habetler, "Detecting and locating the stator turn-to-turn faults in a closed-loop multiplemotor drive system," in *Proceedings of the*

2009 IEEE Energy Conversion Congress and Exposition (ECCE 2009), San Jose, CA, Sep. 2009, pp. 3247-3254.

- [3] J. Kunz, **S. Cheng**, Y. Duan, J. R. Mayor, R. G. Harley, T. G. Habetler, "Design of a 750,000 rpm switched reluctance motor for micro machining," in *Proceedings of the 2010 IEEE Energy Conversion Congress and Exposition (ECCE 2010)*, Atlanta, GA, Sep. 2010, pp. 3986-3992.
- [4] **S. Cheng**, Y. Zhang, S. Nawrocki, T. G. Habetler, and M. Salman, "Interpolated FFT for Real-time Detection of Belt Slip in Automotive Electric Power Generation and Storage System," in *Proceedings of the 2011 IEEE International Conference on Prognostics and Health Management. (PHM 2011)*, Denver, CO, Jun. 2011, pp. 1-6.
- [5] **S. Cheng**, Y. Du, J. Restrepo, P. Zhang, and T. G. Habetler. "A Nonintrusive Thermal Monitoring Method for Closed-loop Drive-fed Induction Machines," in *Proceedings of the 2011 IEEE Energy Conversion Congress and Exposition (ECCE 2011)*, Phoenix, AZ, Sep. 2011, pp. 714-721.
- [6] **S. Cheng**, Y. Zhang, S. Nawrocki, T. G. Habetler, and M. Salman, "An Analysis and Discussion of the Voltage and Current Spectrum of Claw-pole Alternators for Fault Detection Purposes," in *Proceedings of the 8th IEEE International Symposium on Diagnostics for Electrical Machines, Power Electronics & Drives (SDEMPED'11)*, Bologna, Italy, Sept. 2011, 606-611.
- [7] **S. Cheng**, Y. Zhang, S. Nawrocki, T. G. Habetler, and M. Salman, "Using Only the DC Current Information to Detect Stator Turn Faults in Automotive Claw-pole Alternators," in *Proceedings of the 8th IEEE International Symposium on Diagnostics for Electrical Machines, Power Electronics & Drives (SDEMPED'11)*, Bologna, Italy, Sept. 2011, pp. 119-125.
- [8] **S. Cheng**, H. Zhang, T. G. Habetler, "Fault Severity Evaluation and Post-fault Protection for Claw-pole Generators with Stator Turn-to-turn Short Circuits," in *Proceedings of the 2012 IEEE Energy Conversion Congress and Exposition (ECCE 2012)*, Raleigh, NC, Sep. 2012, under review.

9.3 Recommended Future Work

While this PhD dissertation has presented contributions to various aspects of condition monitoring of power-converter-fed electric machines, there are several directions in which further research could build upon the results presented in this work.

9.3.1 Stator Turn-fault Detection during Transient Operation of Induction Motors

Due to its fast-propagating nature, the stator turn-to-turn fault in induction machines needs to be continuously monitored so that timely protection measures can be taken to avoid catastrophic machine failures. Chapter 4 has proposed and demonstrated an effective stator turn-fault detection method during steady state operation of induction machines. Induction machines fed by inverters, however, may frequently operate in mechanical transients for extended period of time. To provide complete protection coverage of inverter-fed machines, the condition of stator windings should ideally be monitored even when the induction machine is in mechanical transients.

To achieve this goal, the definitions of negative-sequence components used in Chapter 4 may need to be extended to incorporate instantaneous representations of three-phase asymmetry. Similar with the definition of instantaneous reactive power for active filtering applications, proper definitions of instantaneous sequence components may greatly simplify the detection of machine asymmetry even in transient or quasi-steady-state operations.

9.3.2 Fault-severity Evaluation of Stator Turn-to-turn Short circuits for Inverter-fed Induction Machines

Once a stator turn fault is detected in inverter-fed induction machines, possible measures to limit the overall current in the shorted turns include,

- (1) Reducing the circulating current in the shorted turns by reducing the magnetization current (reducing the voltage)
- (2) Reducing the torque-producing current (shedding mechanical load)

However, successful execution of both measures requires accurate information of the fault current. Therefore, it is highly desirable to know the actual severity of the stator turn fault so that the most appropriate post-fault operating strategy can be taken.

It is shown in Chapter 8 that with detailed modeling of claw-pole generators and proper parameter identifications, it is possible to accurately evaluate the severity of the stator turn fault using only the generator output current.

For induction machines, accurate fault modeling has traditionally not been a problem. The main difficulty of fault-severity evaluation lies in the fact that the small and time-varying unbalance in measurement channels may have artificially distorted the observed fault signature. Therefore, methods must be developed to compensate for the time-varying sensor mismatch in inverter-fed induction machines.

Once the severity of the fault can be evaluated accurately in inverter-fed induction machines, safer post-fault operation and better limp-home capability of induction machines can be achieved.

9.3.3 Thermal Monitoring of Induction Motors with Direct Torque Control (DTC)

Chapter 5 has proposed a nonintrusive thermal monitoring method for induction machines fed by closed-loop inverters using DC current injection. The specific control scheme implemented in the inverter drive is the indirect rotor-field-oriented control. The injection of DC current is straightforward with this control scheme because there exist explicit current control loops in the field-oriented control.

Another major category of control schemes for inverter-fed induction machines is the so-called direct torque control (DTC). In DTC, there exist no explicit current control loops. The only available control loops are the flux control loop and the torque control

loop. Hence, the injection of DC current requires a different strategy such that the existing torque and/or flux controllers can be utilized to inject DC current noninvasively.

Moreover, since most DTC drives have controllers of the hysteresis type, there may be different considerations in estimating the terminal voltage.

Overall, DC-injection based thermal monitoring for induction machines with DTC may be an interesting research topic.

9.3.4 Further Study and Verification of the Mechanism for Pulley Diameter Change

In Chapter 8, the detection of the generalized bearing roughness fault is investigated. The shift of the rectifier ripple frequency is identified as a result of the effective diameter change of the generator pulley, which is further caused by the bearing wear through one or more of the introduced fault mechanisms. Although the shift of the rectifier ripple frequency is validated as an effective bearing fault indicator by multiple experimental tests, further research is still needed to verify the introduced fault mechanisms in explaining the effective diameter change of the generator pulley.

Detailed mechanical modeling of the pulley-belt contact and clever experimental designs are therefore needed to further understand and verify the fundamental mechanism of the contact-point shift between pulley grooves and belt ribs. Dynamics of the belt-drive system and vibration modes of the serpentine belt under both skewed and aligned pulley positions may also need to be investigated. This work requires profound expertise in mechanical engineering and thus requires close collaboration between different disciplines.

APPENDIX A

Derivation of the Equivalent Circuit of the Short-circuit Path

Figure A.1 shows a physical representation of the generator winding with the turn-to-turn fault. The lower coil is consisted of m turns of the phase-A winding shorted through a fault resistor R_f . The upper coil contains the remaining $N-m$ turns.

Since ϕ_A is defined in Chapter 8 as the magnetic flux that links the entire phase-A winding, it will induce back-EMFs in both the shorted coil and the non-shortcd coil, as shown by the upper two voltage sources in Figure A.1.

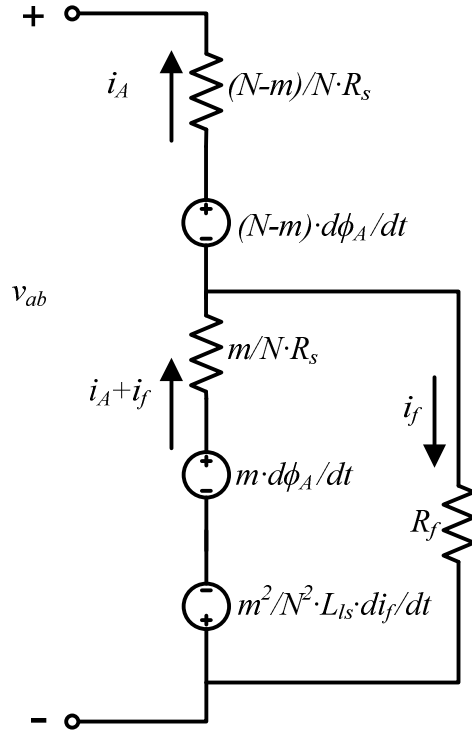


Figure A.1: Stator winding with turn-to-turn faults.

As for the shorted coil, assume that the magnetic flux produced by the fault current i_f either enters the rotor as part of the airgap flux or only links the shorted coil itself. With this simplified assumption, the effect of the leakage flux produced by the fault-current i_f

can be represented as an inductive voltage drop in the shorted coil, as shown at the bottom of Figure A.1.

The phase voltage v_{ab} is the sum voltage of the two coils,

$$v_{ab} = (N - m) \frac{d\phi_A}{dt} - \frac{N - m}{N} R_s i_A + m \frac{d\phi_A}{dt} - \frac{m}{N} R_s (i_A + i_f) - \frac{m^2}{N^2} L_{ls} \frac{di_f}{dt}. \quad (\text{A.1})$$

Combining and reorganizing terms in equation (A.1) yields,

$$N \frac{d\phi_A}{dt} - R_s i_A = v_{ab} + \frac{m}{N} R_s i_f + \frac{m^2}{N^2} L_{ls} \frac{di_f}{dt}. \quad (\text{A.2})$$

In the short-circuit path, the fault current i_f can be calculated as,

$$m \frac{d\phi_A}{dt} - \frac{m}{N} R_s (i_A + i_f) - \frac{m^2}{N^2} L_{ls} \frac{di_f}{dt} = R_f i_f. \quad (\text{A.3})$$

Reorganizing terms in equation (A.3) yields,

$$\frac{m}{N} \left(N \frac{d\phi_A}{dt} - R_s i_A \right) - \frac{m}{N} R_s i_f - \frac{m^2}{N^2} L_{ls} \frac{di_f}{dt} = R_f i_f. \quad (\text{A.4})$$

To get rid of the flux ϕ_A and the phase current i_A , substitute equation (A.2) into (A.4),

$$\frac{m}{N} \left(v_{ab} + \frac{m}{N} R_s i_f + \frac{m^2}{N^2} L_{ls} \frac{di_f}{dt} \right) - \frac{m}{N} R_s i_f - \frac{m^2}{N^2} L_{ls} \frac{di_f}{dt} = R_f i_f. \quad (\text{A.5})$$

Combining terms in equation (A.5) yields,

$$\frac{m}{N} v_{ab} - \left(1 - \frac{m}{N} \right) \frac{m}{N} R_s i_f - \left(1 - \frac{m}{N} \right) \frac{m^2}{N^2} L_{ls} \frac{di_f}{dt} = R_f i_f. \quad (\text{A.6})$$

Equation (A.6) establishes a direct relationship between v_{ab} and i_f . Equation (A.6) can be described by an equivalent circuit, as shown in Figure A.2.

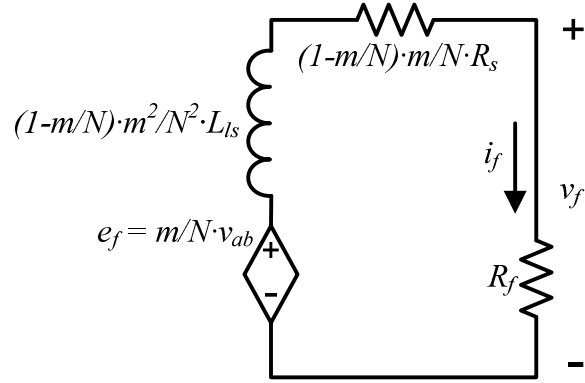


Figure A.2: Equivalent circuit of the short-circuit path.

The equivalent circuit in Figure A.2 can be used to simulate the fault current i_f regardless the number of shorted turns. In the case that $m \ll N$, the term $1-m/N$ in Figure A.2 can be simply replaced by 1. The resistance term can also be absorbed into the fault resistor R_f . Consequently, the equivalent circuit in Figure A.2 can be further simplified to the equivalent circuit in Figure 8.2 when $m \ll N$.

BIBLIOGRAPHY

- [1] "Report of Large Motor Reliability Survey of Industrial and Commercial Installations, Part I," *Industry Applications, IEEE Transactions on*, vol. IA-21, pp. 853-864, 1985.
- [2] A. Bellini, F. Filippetti, C. Tassoni, *et al.*, "Advances in Diagnostic Techniques for Induction Machines," *Industrial Electronics, IEEE Transactions on*, vol. 55, pp. 4109-4126, 2008.
- [3] S. Nandi, H. A. Toliyat and L. Xiaodong, "Condition monitoring and fault diagnosis of electrical motors-a review," *Energy Conversion, IEEE Transactions on*, vol. 20, pp. 719-729, 2005.
- [4] P. Zhang, Y. Du, T. G. Habetler, *et al.*, "A Survey of Condition Monitoring and Protection Methods for Medium-Voltage Induction Motors," *Industry Applications, IEEE Transactions on*, vol. 47, pp. 34-46, 2011.
- [5] P. Neti and S. Nandi, "Stator Interturn Fault Detection of Synchronous Machines Using Field Current and Rotor Search-Coil Voltage Signature Analysis," *Industry Applications, IEEE Transactions on*, vol. 45, pp. 911-920, 2009.
- [6] Y. Jangho, L. Kwanghwan, L. Kwang-Woon, *et al.*, "Detection and Classification of Stator Turn Faults and High-Resistance Electrical Connections for Induction Machines," *Industry Applications, IEEE Transactions on*, vol. 45, pp. 666-675, 2009.
- [7] S. A. McInerny and Y. Dai, "Basic vibration signal processing for bearing fault detection," *Education, IEEE Transactions on*, vol. 46, pp. 149-156, 2003.
- [8] A. Bellini, F. Filippetti, G. Franceschini, *et al.*, "Closed-loop control impact on the diagnosis of induction motors faults," *Industry Applications, IEEE Transactions on*, vol. 36, pp. 1318-1329, 2000.
- [9] P. F. Albrecht, J. C. Appiarius, R. M. McCoy, *et al.*, "Assessment of the Reliability of Motors in Utility Applications - Updated," *Energy Conversion, IEEE Transactions on*, vol. EC-1, pp. 39-46, 1986.
- [10] "Report of Large Motor Reliability Survey of Industrial and Commercial Installations, Part II," *Industry Applications, IEEE Transactions on*, vol. IA-21, pp. 865-872, 1985.
- [11] "Report of Large Motor Reliability Survey of Industrial and Commercial Installations: Part 3," *Industry Applications, IEEE Transactions on*, vol. IA-23, pp. 153-158, 1987.

- [12] O. V. Thorsen and M. Dalva, "A survey of faults on induction motors in offshore oil industry, petrochemical industry, gas terminals, and oil refineries," *Industry Applications, IEEE Transactions on*, vol. 31, pp. 1186-1196, 1995.
- [13] M. Melfi, A. M. J. Sung, S. Bell, *et al.*, "Effect of surge voltage risetime on the insulation of low-voltage machines fed by PWM converters," *Industry Applications, IEEE Transactions on*, vol. 34, pp. 766-775, 1998.
- [14] D. J. Perreault and V. Caliskan, "Automotive power generation and control," *Power Electronics, IEEE Transactions on*, vol. 19, pp. 618-630, 2004.
- [15] J. M. Miller, "Multiple voltage electrical power distribution system for automotive applications," in *Energy Conversion Engineering Conference, 1996. IECEC 96. Proceedings of the 31st Intersociety*, 1996, pp. 1930-1937 vol.3.
- [16] A. Scacchioli, G. Rizzoni and P. Pisu, "Model-based fault detection and isolation in automotive electrical systems," in *2006 ASME International Mechanical Engineering Congress and Exposition, IMECE2006, November 5, 2006 - November 10, 2006*, Chicago, IL, United states, 2006.
- [17] A. Scacchioli, G. Rizzoni and P. Pisu, "Hierarchical model-based fault diagnosis for an electrical power generation storage automotive system," in *2007 American Control Conference, ACC, July 9, 2007 - July 13, 2007*, New York, NY, United states, 2007, pp. 2991-2996.
- [18] Y. Zhang, G. W. Gantt, M. J. Rychlinski, *et al.*, "Connected Vehicle Diagnostics and Prognostics, Concept, and Initial Practice," *Reliability, IEEE Transactions on*, vol. 58, pp. 286-294, 2009.
- [19] M. Abbas, A. A. Ferri, M. E. Orchard, *et al.*, "An Intelligent Diagnostic/Prognostic Framework for Automotive Electrical Systems," in *Intelligent Vehicles Symposium, 2007 IEEE*, 2007, pp. 352-357.
- [20] Y. Zhang, S. Rajagopalan and M. Salman, "A practical approach for belt slip detection in automotive electric power generation and storage system," in *2010 IEEE Aerospace Conference, March 6, 2010 - March 13, 2010*, Big Sky, MT, United states, 2010, p. Aerospace and Electronics Systems Society.
- [21] Y. Zhang, M. Salman, H. S. Subramania, *et al.*, "Remote vehicle state of health monitoring and its application to vehicle no-start prediction," in *AUTOTESTCON, 2009 IEEE*, 2009, pp. 88-93.
- [22] B.-x. Xiao, T.-l. Lou, F.-q. Guo, *et al.*, "The research of fault diagnosis system based-on fuzzy neural network for vehicle alternator," *Journal of System Simulation*, vol. 16, pp. 1001-4, 2004.
- [23] Y. Zhang, G. W. Gantt, M. Rychlinski, *et al.*, "Vehicle Design Validation via Remote Vehicle Diagnosis: A feasibility study on battery management system," in

Prognostics and Health Management, 2008. *PHM 2008. International Conference on*, 2008, pp. 1-6.

- [24] R. J. Streifel, R. J. Marks, II, M. A. El-Sharkawi, *et al.*, "Detection of shorted-turns in the field winding of turbine-generator rotors using novelty detectors-development and field test," *Energy Conversion, IEEE Transactions on*, vol. 11, pp. 312-317, 1996.
- [25] Y. Han and Y. H. Song, "Using improved self-organizing map for partial discharge diagnosis of large turbogenerators," *Energy Conversion, IEEE Transactions on*, vol. 18, pp. 392-399, 2003.
- [26] H. A. Darwish, A. M. I. Taalab and T. A. Kawady, "Development and implementation of an ANN-based fault diagnosis scheme for generator winding protection," *Power Delivery, IEEE Transactions on*, vol. 16, pp. 208-214, 2001.
- [27] M. E. H. Benbouzid and G. B. Kliman, "What stator current processing-based technique to use for induction motor rotor faults diagnosis?," *Energy Conversion, IEEE Transactions on*, vol. 18, pp. 238-244, 2003.
- [28] S. B. Lee, K. Younsi and G. B. Kliman, "An online technique for monitoring the insulation condition of AC machine stator windings," *Energy Conversion, IEEE Transactions on*, vol. 20, pp. 737-745, 2005.
- [29] P. Pillai, B. G. Bailey, J. Bowen, *et al.*, "Grounding and ground fault protection of multiple generator installations on medium-voltage industrial and commercial power systems - Part 3: Protection Methods Working Group Report," *Industry Applications, IEEE Transactions on*, vol. 40, pp. 24-28, 2004.
- [30] G. B. Kliman, W. J. Premerlani, R. A. Koegl, *et al.*, "A new approach to on-line turn fault detection in AC motors," in *Industry Applications Conference, 1996. Thirty-First IAS Annual Meeting, IAS '96., Conference Record of the 1996 IEEE*, 1996, pp. 687-693 vol.1.
- [31] S. Williamson and K. Mirzoian, "Analysis of Cage Induction Motors with Stator Winding Faults," *Power Apparatus and Systems, IEEE Transactions on*, vol. PAS-104, pp. 1838-1842, 1985.
- [32] M. Bouzid, G. Champenois, N. M. Bellaaj, *et al.*, "An Effective Neural Approach for the Automatic Location of Stator Interturn Faults in Induction Motor," *Industrial Electronics, IEEE Transactions on*, vol. 55, pp. 4277-4289, 2008.
- [33] A. M. da Silva, R. J. Povinelli and N. A. O. Demerdash, "Induction Machine Broken Bar and Stator Short-Circuit Fault Diagnostics Based on Three-Phase Stator Current Envelopes," *Industrial Electronics, IEEE Transactions on*, vol. 55, pp. 1310-1318, 2008.

- [34] A. J. Marques Cardoso, S. M. A. Cruz and D. S. B. Fonseca, "Inter-turn stator winding fault diagnosis in three-phase induction motors, by Park's vector approach," *Energy Conversion, IEEE Transactions on*, vol. 14, pp. 595-598, 1999.
- [35] S. M. A. Cruz and A. J. M. Cardoso, "Stator winding fault diagnosis in three-phase synchronous and asynchronous motors, by the extended Park's vector approach," *Industry Applications, IEEE Transactions on*, vol. 37, pp. 1227-1233, 2001.
- [36] S. M. A. Cruz, H. A. Toliyat and A. J. M. Cardoso, "DSP implementation of the multiple reference frames theory for the diagnosis of stator faults in a DTC induction motor drive," *Energy Conversion, IEEE Transactions on*, vol. 20, pp. 329-335, 2005.
- [37] S. M. A. Cruz and A. J. M. Cardoso, "Multiple Reference Frames Theory: A New Method for the Diagnosis of Stator Faults in Three-Phase Induction Motors," *Energy Conversion, IEEE Transactions on*, vol. 20, pp. 611-619, 2005.
- [38] J. L. Kohler, J. Sottile and F. C. Trutt, "Alternatives for assessing the electrical integrity of induction motors," *Industry Applications, IEEE Transactions on*, vol. 28, pp. 1109-1117, 1992.
- [39] J. Cusido, L. Romeral, J. A. Ortega, *et al.*, "Fault Detection in Induction Machines Using Power Spectral Density in Wavelet Decomposition," *Industrial Electronics, IEEE Transactions on*, vol. 55, pp. 633-643, 2008.
- [40] O. A. Mohammed, N. Y. Abed and S. Ganu, "Modeling and Characterization of Induction Motor Internal Faults Using Finite-Element and Discrete Wavelet Transforms," *Magnetics, IEEE Transactions on*, vol. 42, pp. 3434-3436, 2006.
- [41] R. Maier, "Protection of squirrel-cage induction motor utilizing instantaneous power and phase information," *Industry Applications, IEEE Transactions on*, vol. 28, pp. 376-380, 1992.
- [42] J. S. Hsu, "Monitoring of defects in induction motors through air-gap torque observation," *Industry Applications, IEEE Transactions on*, vol. 31, pp. 1016-1021, 1995.
- [43] R. M. Tallam, T. G. Habetler and R. G. Harley, "Self-commissioning training algorithms for neural networks with applications to electric machine fault diagnostics," *Power Electronics, IEEE Transactions on*, vol. 17, pp. 1089-1095, 2002.
- [44] S. B. Lee, R. M. Tallam and T. G. Habetler, "A robust, on-line turn-fault detection technique for induction machines based on monitoring the sequence component impedance matrix," *Power Electronics, IEEE Transactions on*, vol. 18, pp. 865-872, 2003.

- [45] M. A. Cash, T. G. Habetler and G. B. Kliman, "Insulation failure prediction in AC machines using line-neutral voltages," *Industry Applications, IEEE Transactions on*, vol. 34, pp. 1234-1239, 1998.
- [46] G. M. Joksimovic and J. Penman, "The detection of inter-turn short circuits in the stator windings of operating motors," *Industrial Electronics, IEEE Transactions on*, vol. 47, pp. 1078-1084, 2000.
- [47] B. Mirafzal, R. J. Povinelli and N. A. O. Demerdash, "Interturn Fault Diagnosis in Induction Motors Using the Pendulous Oscillation Phenomenon," *Energy Conversion, IEEE Transactions on*, vol. 21, pp. 871-882, 2006.
- [48] B. Mirafzal and N. A. O. Demerdash, "On innovative methods of induction motor interturn and broken-bar fault diagnostics," *Industry Applications, IEEE Transactions on*, vol. 42, pp. 405-414, 2006.
- [49] S. Nandi, "Detection of Stator Faults in Induction Machines Using Residual Saturation Harmonics," *Industry Applications, IEEE Transactions on*, vol. 42, pp. 1201-1208, 2006.
- [50] S. Nandi and H. A. Toliyat, "Novel frequency-domain-based technique to detect stator interturn faults in induction machines using stator-induced voltages after switch-off," *Industry Applications, IEEE Transactions on*, vol. 38, pp. 101-109, 2002.
- [51] C. S. Kallesoe, R. Izadi-Zamanabadi, P. Vadstrup, *et al.*, "Observer-Based Estimation of Stator-Winding Faults in Delta-Connected Induction Motors: A Linear Matrix Inequality Approach," *Industry Applications, IEEE Transactions on*, vol. 43, pp. 1022-1031, 2007.
- [52] S. Bachir, S. Tnani, J. C. Trigeassou, *et al.*, "Diagnosis by parameter estimation of stator and rotor faults occurring in induction machines," *Industrial Electronics, IEEE Transactions on*, vol. 53, pp. 963-973, 2006.
- [53] F. Briz, M. W. Degner, A. Zamarron, *et al.*, "Online stator winding fault diagnosis in inverter-fed AC machines using high-frequency signal injection," *Industry Applications, IEEE Transactions on*, vol. 39, pp. 1109-1117, 2003.
- [54] F. Briz, M. W. Degner, P. Garcia, *et al.*, "High-Frequency Carrier-Signal Voltage Selection for Stator Winding Fault Diagnosis in Inverter-Fed AC Machines," *Industrial Electronics, IEEE Transactions on*, vol. 55, pp. 4181-4190, 2008.
- [55] A. Bellini, F. Filippetti, G. Franceschini, *et al.*, "Closed loop control impact on the diagnosis of induction motors faults," in *Industry Applications Conference, 1999. Thirty-Fourth IAS Annual Meeting. Conference Record of the 1999 IEEE*, 1999, pp. 1913-1921 vol.3.

- [56] R. M. Tallam, T. G. Habetler and R. G. Harley, "Stator winding turn-fault detection for closed-loop induction motor drives," *Industry Applications, IEEE Transactions on*, vol. 39, pp. 720-724, 2003.
- [57] S. M. A. Cruz and A. J. M. Cardoso, "Diagnosis of stator inter-turn short circuits in DTC induction motor drives," *Industry Applications, IEEE Transactions on*, vol. 40, pp. 1349-1360, 2004.
- [58] S. Grubic, T. G. Habetler, B. Lu, *et al.*, "Investigation on surge testing for winding insulation fault detection in an online environment," in *Energy Conversion Congress and Exposition, 2009. ECCE 2009. IEEE*, 2009, pp. 3255-3261.
- [59] P. Zhang, Y. Du, B. Lu, *et al.*, "A DC Signal Injection-Based Thermal Protection Scheme for Soft-Starter-Connected Induction Motors," *Industry Applications, IEEE Transactions on*, vol. 45, pp. 1351-1358, 2009.
- [60] P. Zhang, B. Lu and T. G. Habetler, "A Remote and Sensorless Stator Winding Resistance Estimation Method for Thermal Protection of Soft-Starter-Connected Induction Machines," *Industrial Electronics, IEEE Transactions on*, vol. 55, pp. 3611-3618, 2008.
- [61] D. W. Novotny and T. A. Lipo, *Vector Control and Dynamics of AC Drives*. New York: Oxford Univ. Press, 1996.
- [62] J. F. Moreno, F. P. Hidalgo and M. D. Martinez, "Realisation of tests to determine the parameters of the thermal model of an induction machine," *Electric Power Applications, IEE Proceedings-*, vol. 148, pp. 393-397, 2001.
- [63] P. H. Mellor, D. Roberts and D. R. Turner, "Lumped parameter thermal model for electrical machines of TEFC design," *Electric Power Applications, IEE Proceedings B [see also IEE Proceedings-Electric Power Applications]*, vol. 138, pp. 205-218, 1991.
- [64] S. B. Lee, T. G. Habetler, R. G. Harley, *et al.*, "A stator and rotor resistance estimation technique for conductor temperature monitoring," in *Industry Applications Conference, 2000.*, 2000, pp. 381-387 vol.1.
- [65] S. B. Lee and T. G. Habetler, "A remote and sensorless thermal protection scheme for small line-connected ac machines," *Industry Applications, IEEE Transactions on*, vol. 39, pp. 1323-1332, 2003.
- [66] A. Bousbaine, M. McCormick and W. F. Low, "In-situ determination of thermal coefficients for electrical machines," *Energy Conversion, IEEE Transaction on*, vol. 10, pp. 385-391, 1995.

- [67] A. Boglietti, A. Cavagnino, M. Lazzari, *et al.*, "A simplified thermal model for variable-speed self-cooled industrial induction motor," *Industry Applications, IEEE Transactions on*, vol. 39, pp. 945-952, 2003.
- [68] S. F. Farag, R. G. Bartheld and T. G. Habetler, "An integrated on-line motor protection system," *Industry Applications Magazine, IEEE*, vol. 2, pp. 21-26, 1996.
- [69] "IEEE Standard Test Procedure for Polyphase Induction Motors and Generators," *IEEE Std 112-2004 (Revision of IEEE Std 112-1996)*, pp. 1-79, 2004.
- [70] K. D. Hurst and T. G. Habetler, "A thermal monitoring and parameter tuning scheme for induction machines," in *Industry Applications Conference, 1997.*, 1997, pp. 136-142 vol.1.
- [71] F. Briz, M. W. Degner, J. M. Guerrero, *et al.*, "Temperature Estimation in Inverter-Fed Machines Using High-Frequency Carrier Signal Injection," *Industry Applications, IEEE Transactions on*, vol. 44, pp. 799-808, 2008.
- [72] J. Plotkin, M. Stiebler and D. Schuster, "A novel method for online stator resistance estimation of inverter-fed ac-machines without temperature sensors," in *Optimization of Electrical and Electronic Equipment, 2008. OPTIM 2008. 11th International Conference on*, 2008, pp. 155-161.
- [73] P. Zhang, B. Lu and T. G. Habetler, "An Active Stator Temperature Estimation Technique for Thermal Protection of Inverter-Fed Induction Motors With Considerations of Impaired Cooling Detection," *Industry Applications, IEEE Transactions on*, vol. 46, pp. 1873-1881, 2010.
- [74] P. Zhang, "Active thermal protection for induction motors fed by motor control devices," Georgia Institute of Technology Ph.D., Georgia Institute of Technology, United States -- Georgia, 2010.
- [75] P. M. Kelecy and R. D. Lorenz, "Control methodology for single inverter, parallel connected dual induction motor drives for electric vehicles," in *Power Electronics Specialists Conference, PESC '94 Record., 25th Annual IEEE*, 1994, pp. 987-991 vol.2.
- [76] K. Matsuse, H. Kawai, Y. Kouno, *et al.*, "Characteristics of speed sensorless vector controlled dual induction motor drive connected in parallel fed by a single inverter," *Industry Applications, IEEE Transactions on*, vol. 40, pp. 153-161, 2004.
- [77] L. Wu, X. Huang, T. G. Habetler, *et al.*, "Eliminating Load Oscillation Effects for Rotor Eccentricity Detection in Closed-Loop Drive-Connected Induction Motors," *Power Electronics, IEEE Transactions on*, vol. 22, pp. 1543-1551, 2007.

- [78] Z. Gao, T. G. Habetler and R. G. Harley, "A Complex Space Vector Approach to Rotor Temperature Estimation for Line-Connected Induction Machines With Impaired Cooling," *Industrial Electronics, IEEE Transactions on*, vol. 56, pp. 239-247, 2009.
- [79] R. M. Tallam, T. G. Habetler and R. G. Harley, "Transient model for induction machines with stator winding turn faults," *Industry Applications, IEEE Transactions on*, vol. 38, pp. 632-637, 2002.
- [80] S. Bolognani, L. Peretti and M. Zigliotto, "Repetitive-Control-Based Self-Commissioning Procedure for Inverter Nonidealities Compensation," *Industry Applications, IEEE Transactions on*, vol. 44, pp. 1587-1596, 2008.
- [81] N. Urasaki, T. Senjyu, K. Uezato, *et al.*, "An adaptive dead-time compensation strategy for voltage source inverter fed motor drives," *Power Electronics, IEEE Transactions on*, vol. 20, pp. 1150-1160, 2005.
- [82] K. Hyun-Soo, M. Hyung-Tae and Y. Myung-Joong, "On-line dead-time compensation method using disturbance observer," *Power Electronics, IEEE Transactions on*, vol. 18, pp. 1336-1345, 2003.
- [83] A. R. Munoz and T. A. Lipo, "On-line dead-time compensation technique for open-loop PWM-VSI drives," *Power Electronics, IEEE Transactions on*, vol. 14, pp. 683-689, 1999.
- [84] H. Zhao, Q. M. J. Wu and A. Kawamura, "An accurate approach of nonlinearity compensation for VSI inverter output voltage," *Power Electronics, IEEE Transactions on*, vol. 19, pp. 1029-1035, 2004.
- [85] L. Chen and F. Z. Peng, "Dead-Time Elimination for Voltage Source Inverters," *Power Electronics, IEEE Transactions on*, vol. 23, pp. 574-580, 2008.
- [86] T. Itkonen, J. Luukko, A. Sankala, *et al.*, "Modeling and Analysis of the Dead-Time Effects in Parallel PWM Two-Level Three-Phase Voltage-Source Inverters," *Power Electronics, IEEE Transactions on*, vol. 24, pp. 2446-2455, 2009.
- [87] *Automotive electric/electronic systems*, 2nd ed. ed. Stuttgart :: R. Bosch ;, 1994.
- [88] R. Frank. Hybrid Vehicle Symposium Addresses Improvements for Efficiency, Performance and Cost [Online]. Available: http://electronicdesign.com/article/power/hybrid_vehicle_symposium_addresses_improvements_for_efficiency_performance_and_cost.aspx
- [89] I. Ramesohl, G. Henneberger, S. Kuppers, *et al.*, "Three dimensional calculation of magnetic forces and displacements of a claw-pole generator," *Magnetics, IEEE Transactions on*, vol. 32, pp. 1685-1688, 1996.

- [90] B. Hua, S. D. Pekarek, J. Tichenor, *et al.*, "Analytical derivation of a coupled-circuit model of a claw-pole alternator with concentrated stator windings," *Energy Conversion, IEEE Transactions on*, vol. 17, pp. 32-38, 2002.
- [91] V. Ostovic, J. M. Miller, V. K. Garg, *et al.*, "A magnetic-equivalent-circuit-based performance computation of a Lundell alternator," *Industry Applications, IEEE Transactions on*, vol. 35, pp. 825-830, 1999.
- [92] J. Schoukens, R. Pintelon and H. Van Hamme, "The interpolated fast Fourier transform: a comparative study," *Instrumentation and Measurement, IEEE Transactions on*, vol. 41, pp. 226-232, 1992.
- [93] C. Offelli and D. Petri, "Interpolation techniques for real-time multifrequency waveform analysis," *Instrumentation and Measurement, IEEE Transactions on*, vol. 39, pp. 106-111, 1990.
- [94] P. M. Ramos and A. Cruz Serra, "Comparison of frequency estimation algorithms for power quality assessment," *Measurement: Journal of the International Measurement Confederation*, vol. 42, pp. 1312-1317, 2009.
- [95] L. Romeral, J. C. Urresty, J. R. Riba Ruiz, *et al.*, "Modeling of Surface-Mounted Permanent Magnet Synchronous Motors With Stator Winding Interturn Faults," *Industrial Electronics, IEEE Transactions on*, vol. 58, pp. 1576-1585, 2011.
- [96] J. Pons-Llinares, J. A. Antonino-Daviu, M. Riera-Guasp, *et al.*, "Induction Motor Diagnosis Based on a Transient Current Analytic Wavelet Transform via Frequency B-Splines," *Industrial Electronics, IEEE Transactions on*, vol. 58, pp. 1530-1544, 2011.
- [97] A. Gandhi, T. Corrigan and L. Parsa, "Recent Advances in Modeling and Online Detection of Stator Interturn Faults in Electrical Motors," *Industrial Electronics, IEEE Transactions on*, vol. 58, pp. 1564-1575, 2011.
- [98] Z. M. Salameh, M. A. Casacca and W. A. Lynch, "A mathematical model for lead-acid batteries," *Energy Conversion, IEEE Transactions on*, vol. 7, pp. 93-98, 1992.
- [99] M. Ceraolo, "New dynamical models of lead-acid batteries," *Power Systems, IEEE Transactions on*, vol. 15, pp. 1184-1190, 2000.
- [100] M. Cugnet, J. Sabatier, S. Laruelle, *et al.*, "On Lead-Acid-Battery Resistance and Cranking-Capability Estimation," *Industrial Electronics, IEEE Transactions on*, vol. 57, pp. 909-917, 2010.
- [101] F. Zhang, G. Liu, L. Fang, *et al.*, "Estimation of Battery State of Charge With Hoo Observer: Applied to a Robot for Inspecting Power Transmission Lines," *Industrial Electronics, IEEE Transactions on*, vol. 59, pp. 1086-1095, 2012.

- [102] S. Cheng, P. Zhang and T. G. Habetler, "An Impedance Identification Approach to Sensitive Detection and Location of Stator Turn-to-Turn Faults in a Closed-Loop Multiple-Motor Drive," *Industrial Electronics, IEEE Transactions on*, vol. 58, pp. 1545-1554, 2011.
- [103] W. Zhou, "Incipient bearing fault detection for electric machines using stator current noise cancellation," Georgia Institute of Technology Ph.D., Georgia Institute of Technology, United States -- Georgia, 2007.
- [104] L. Bin, M. Nowak, S. Grubic, *et al.*, "An adaptive noise-cancellation method for detecting generalized roughness bearing faults under dynamic load conditions," in *Energy Conversion Congress and Exposition, 2009. ECCE 2009. IEEE*, 2009, pp. 1091-1097.
- [105] G. Cepon, L. Manin and M. Boltezar, "Experimental identification of the contact parameters between a V-ribbed belt and a pulley," *Mechanism and Machine Theory*, vol. 45, pp. 1424-1433, 2010.

VITA

Siwei Cheng was born in the city of Wuhan, China in a hot, steamy summer in 1985. With his father being an electrical engineer and his mother being a writer, Siwei was cultivated with both science and liberal arts at an early age. It was not until the latter half of high school that Siwei realized he was much better at Physics and Math, and decided to pursue science and engineering for undergraduate study.

While Siwei studied electric engineering in Tsinghua University, he became attracted towards the field of power electronics and electric machines. He worked with Prof. Wenlong Qu on electric vehicles for his senior design. Siwei graduated with the highest distinction from Tsinghua University in the summer of 2007.

To further his study and to experience the American culture and society, Siwei enrolled at Georgia Tech in the fall of 2007 as a PhD student under the supervision of Professor Thomas G. Habetler. At Georgia Tech, Siwei worked on a good number of different projects on the design, control, and condition monitoring of electric machines. Through the process, Siwei have expanded his knowledge base and sharpened his skill sets in the field of power electronics and electric machines.

Siwei often regards himself as a young engineer who loves building real stuffs and solving real-world problems. Therefore, he decided to work on hybrid/electric vehicles upon graduation. Having been at the school for almost his entire life, Siwei is eager to begin his new adventure outside universities.